Investigation of optoelectronic and photonic properties of ZnO nanoscale systems fabricated via physico-chemical routes

A thesis submitted in partial fulfillment of the requirements for the degree of Doctor of Philosophy

Mr. Sayan Bayan
Reg. No. 006 of 2012

Department of Physics,
School of Sciences
Tezpur University
Napaam, Tezpur-784028
Assam, India

September 2012

Dedicated to my parents

Abstract

In recent times, a great deal of interest has been extended in exploiting the nanoscale systems that ensure numerous application in cutting edge science and technology. The advancement in fabrication and processing techniques has offered the possibility of obtaining a wide variety of nanostructured materials (both metallic and semiconducting) with regard to morphology and organization. Essentially, the semiconductor nanostructured materials are believed to be the building blocks for high performance photonic and optoelectronic devices. The nanostructures based on semiconductor materials exhibit dimension dependent optical and electronic properties. Zinc oxide (ZnO) is a versatile material which can be processed in the form of nanorods, nanorings, nanoflowers etc. Owing to the wide band gap (~ 3.3 eV at 300 K) and higher exciton binding energy (60 meV), ZnO system is regarded as one of the most suitable candidates for application in UV light emitting diodes (LEDs), lasers, sensors etc.

In the present study, the luminescence response of spherical and elongated nanostructures of ZnO fabricated via different routes has been explored. In particular, the effect of introduction of Eu^{3+} ions into ZnO nanostructures of different structural organization is being considered. Further, ZnO nanostructure systems were subjected to both low (~ keV) and high (~ MeV) energetic ion irradiation to modify the emission characteristics. Theoretical justification has also been provided in support of the irradiation induced modification of the nanostructures. On the other hand, the transport property of ZnO nanorod based MS and metal-insulator-semiconductor (MIS) junctions have been studied. Also, the UV detection aspect of the ZnO nanostructures in MS configuration is countered. Finally, the photonic band gap tuning of ZnO embedded natural photonic crystals of peacock feather is demonstrated by analyzing alteration of reflectance spectra.

The thesis focuses on the synthesis, characterization and study of the photonic and optoelectronic properties of ZnO nanostructures with a special emphasis on the one dimensional (1D) patterns. It comprises of nine chapters including the chapters that discuss the introduction and future directions.

The **Chapter 1**, is an introductory chapter that highlights the recent development in the field of nanoscience and nanotechnology. It deals with the discussion on semiconductor nanostructures both in spherical form as well as in elongated morphology. Several important optoelectronic properties of II-VI semiconductor nanostructures are being discussed in the light of the existing literature. This chapter also describes the ZnO based various nanostructures in terms of the photonic and optoelectronic properties exhibited by them. At the end, the objectives of the present investigation are stated in this chapter.

In **Chapter 2**, description on synthesis and structural organization of ZnO nanostructures are presented. It includes the detailed explanation of various chemical and physico-chemical fabrication techniques adopted to synthesis undoped and Eu^{3+} doped ZnO nanostructures. In addition, natural peacock feather assisted growth of ZnO nanostructures is highlighted. The visible impression of different nanostructures like nanoparticles, nanorods, nanorod based urchins and nanorod arrays etc, along with their structural and compositional analysis have been presented.

The **Chapter 3** focuses on the optical properties of the ZnO nanostructures analyzed through room temperature absorption and photoluminescence (PL) spectroscopy. It has been possible to extract various native defect states of ZnO from the Gaussian fitting of the emission response of the nanostructures. The variation of the emission features of different nanostructures has been correlated with the crystallographic properties of the nanostructures. In contrast, the Eu^{3+} related intra *4f* transition is also found in the Eu^{3+} doped ZnO nanostructures. All these aspects are highlighted in this chapter.

The consequences of 80-MeV N^{4+} and 80-keV Ar^{+} ion irradiation on the emission response of the ZnO nanostructures are presented in **Chapter 4**. The irradiation led alteration of the emission patterns has been correlated with the electronic loss led modification of the subatomic system. Again, the nuclear energy loss led creation, annihilation and ionization of the defects is found to be responsible for the modification of the luminescence response of ZnO nanorods. Relevant theoretical justification is also supplied to support the experimental results.

The **Chapter 5** deals with the theoretical investigation that highlights conditions necessary for nanostructure growth and elongation. Theoretical study on surface energy assisted unidirectional growth of nanoparticles to nanorods is also included in this chapter. Furthermore, ion fluence dependent structural deformation of ZnO nanoparticles has been associated with the suppression of the effective cohesive energy of the nanoparticles during irradiation. The calculation of fluence dependent effective cohesive energy of the nanoparticles is the main theme of the chapter.

The current transport mechanism in ZnO nanorod based MS and MIS junctions are introduced in **Chapter 6**. The dependence of current transport features of Ag/ZnO Schottky nano-junctions on the native defects of ZnO has been explored. Ion irradiation induced improvement in the Schottky properties of the nano-junctions is also included in the chapter. The observation of significant Fowler-Nordheim (FN) tunneling of electrons across $Al/Al_2O_3/ZnO$ junction is an important aspect of this chapter.

The **Chapter 7** demonstrates the UV sensing of ZnO urchins and nanorod arrays studied at room temperature. The faster photoresponse of the urchins (as compared to the nanorod arrays) is assigned to the unique crystallographic properties of the two types of the nanostructured systems. The photoconductive response of the nanorod arrays reveals the presence of substantial amount of persistence photoconductivity (PPC) in each cycle of the UV light on/off

conditions. The slower electron-hole recombination process owing to the presence of trap states within the band gap of ZnO is believed to be the chief reason behind the display of PPC.

In **Chapter 8**, tuning of photonic band gap of ZnO nanostructure loaded natural peacock feather is coherently demonstrated. As evident from the reflectance spectra, the PBG of the photonic crystals present in the barbules of the feather was found to get modified upon ZnO loading and was witnessed in different coloured barbules. The alteration in effective refractive index of the hybrid system was shown to be the reason for the modification of the photonic characteristics.

Finally, in **Chapter 9**, the conclusions drawn from the present study and the scope of future work are discussed.

Declaration

I hereby declare that the thesis entitled "**Investigation of optoelectronic and photonic properties of ZnO nanoscale systems fabricated via physico-chemical routes**", being submitted to the Department of Physics, Tezpur University, Napaam, Tezpur, Assam (India) in fulfillment of the requirements for the award of the degree of Doctor of Philosophy, has previously not formed the basis for the award of any degree, diploma, associateship, fellowship or any other similar title or recognition.

Napaam, Tezpur

Sayan Bayan

(Sayan Bayan)
Department of Physics
Tezpur University
Tezpur- 784028
Assam, India

TEZPUR UNIVERSITY

Certificate

This is to certify that the thesis entitled "**Investigation of optoelectronic and photonic properties of ZnO nanoscale systems fabricated via physico-chemical routes**", submitted to the School of Sciences, Tezpur University in part fulfillment for the award of the degree of Doctor of Philosophy in Physics is a record of research work carried out by Mr. Sayan Bayan under my supervision and guidance.

All help received by him from various sources have been duly acknowledged.

No part of this thesis has been submitted elsewhere for award of any other degree.

Signature of Supervisor:

(D. Mohanta)

Designation: Associate professor

School: Sciences

Department: Physics

Date: 03 September 2012

Acknowledgements

In the preceding four years, I am fortunate enough to pursue research in Nanoscience and Soft Matter Laboratory, Tezpur University. Regarding this I offer my humblest and sincerest words of gratitude to my Ph.D. supervisor Dr. Dambarudhar Mohanta, who conferred me the chance to avail this opportunity. I am highly grateful not only for his insight inspiration, encouragement and invaluable guidance, but also for being a mentor for building up my future carrier.

I extend my sincere and hearty gratitude to Prof. Amarjyoti Choudhury, for devoting his valuable time through constant encouragement and stimulating discussions to carry out my research. Again, I am obliged to Prof. Ashok Kumar, for his expertise comments and suggestions on my research work.

I would like to express my acknowledgements to the Material Science group as well as the Pelletron team of Inter University Accelerator Centre (IUAC), New Delhi, for providing me the opportunity to perform the irradiation experiments. I also state gratitude to IUAC for availing the Low energy ion beam facility (LEIBF). The useful discussions with Dr. D. K. Avasthi, Dr. D. Kanjilal, Dr. A. Tripathi, Dr. P. Kumar are highly acknowledged.

The financial support received from IUAC (UFUP-44314/2008) and UGC (Rajiv Gandhi National Fellowship) is highly appreciated.

I would like to thank my lab senior Dr. Upamanyu Das, who has assisted me in diverse aspects of research both in laboratory experiments and in the tea-time discussions to solve many riddles during my Ph. D. time.

Sincere thanks to SAIF, North-East Hill University, Shillong and Saha Institute of Nuclear Physics, Kolkata for giving me the opportunity and extending their co-operation in providing the electron microscopy facility.

I am extremely thankful to the technical staff of the University for their helping hands during my research work. I am grateful to the teachers and staff-members of Department of Physics and also to the other fellows for their support.

I am grateful to my lab senior Ms. Manasi Devi for her assistance and invaluable suggestions to perform my research work. I also thank my lab-mates Runjhun, Nibedita, Manjit, Samiran, Rizwin for their valuable efforts and helping attitude to maintain an ideal atmosphere for research.

Words fail to acknowledge the indivisible love, affection and continuous support provided by my friends like Sikha, Bondita, Biswajit, Madhulekha, who lighted my heavy mind during my Ph. D. life. I am thankful to the senior people like Ghosh Babu, Sudhir Bhaiya for their priceless help and suggestions in times of need and recruitments during this period.

Finally, I thank the almighty for conferring me the strength and ability to move forward and pursue the research work.

Sayan Bayan

Contents

Chapter 3

Chapter 4

Chapter 5

Chapter 6

Abbreviations

0D	zero dimensional
1D	one dimensional
2D	two dimensional
3D	three dimensional
CCD	charged coupled devices
CL	cathodoluminescence
cm	centimeter
CTAB	cetyltrimethylammonium bromide
EBG	electronic band gap
EDS	energy dispersive spectroscopy
EL	electroluminescent
eV	electron volt
FWHM	full width half maxima
gm	gram
HOMO	highest occupied molecular orbital
HRTEM	high resolution transmission electron microscopy
IFBL	image force barrier lowering
IR	Infra red
JCPDS	joint committee on powder diffraction standards
LED	light emitting diode
LUMO	lowest unoccupied molecular orbital
MIS	metal-insulator-semiconductor
mL	milliliter
MS	metal-semiconductor
nm	nanometer
PBG	photonic band gap
PL	photoluminescence
PPC	persistent photoconductivity

PVA	polyvinyl alcohol
QD	quantum dot
rpm	round per minute
SCLC	space charge limited current
SEM	scanning electron microscopy
SPM	surface probe microscope
SWNT	single wall nanotube
TCLC	trap charge limited current
TEM:	transmission electron microscopy
UV	ultra-violet
VLS	vapour–liquid–solid
XRD	X-ray diffraction
ZAD	zinc acetate dihydrate

List of Figures

List of Tables

Chapter 1

Introduction

According to Ralph Merkle, a renowned researcher and director of Alchor Life Extension Foundation, *"Today's manufacturing methods move atoms in great thundering statistical herds"*.

In the past two decades, the scientific community showed keen interest in the field of advanced material processing and technology. Such immense concern in this field has led to the most significant contributions to nanoscale research. Consequently, a new field of modern research, coined as 'Nanoscience and Technology' has evolved. Originating from the Greek word 'nanos', the word 'nano' refers to 'dwarf'. Nano signifies to the one billionth or 10^{-9} power. In this sense one nanometer refers to one billionth of a meter or 10^{-9} m. The atomic scale dimension can be expressed interms of a unit 'nanometer'. The field of Nanoscience and Technology deals with the ability to fabricate, characterize and manipulate artificial structures that are controllable at the level of several atomic dimensions or, nanometer (10^{-9} m). Owing to the extremely high surface to volume ratio (>> 1), the nanostructured materials manifest unique properties compared to the bulk counterpart. The transition from the bulk or macroscopic systems to nanostructured systems is governed by quantum mechanical laws along with adequate selection rules meant for conventional atomic/molecular systems.

Although the study of nanoscale materials has become a topic of rapid scientific curiosity in the recent time, the concept was initiated 50 years ago. In a classic talk in the annual meeting of the American Physical Society held at the California Institute of Technology (Caltech, 29th December, 1959), the American theoretical physicist, Prof. Richard Feynman expressed the likelihood of fabrication of materials by manipulating individual atoms [1]. The term 'nanotechnology' was first introduced by the Japanese scientist Prof. Norio Taniguchi in an international conference on Production Engineering held at Tokyo in 1974. The term gained serious attention after its use by K. Eric Drexler in his book 'Engines of Creation: The coming era of Nanotechnology' [2]. In the early 1980s, the rapid

advancement of fabrication techniques and microscopic characterization tools have fueled up research in nanoscience and nanotechnology. For the first time in the history of science, the invention of scanning tunneling microscope at IBM-Zurich furnished the ability to see individual atoms and atomic planes. The recent trends of Nanotechnology are the direct reflection of such novel conceptual and experimental developments. The advanced microscopic techniques have offered the opportunity to gather information related to structural details and surface properties. The application and commercialization of different nanoscale materials have already been realized in day-to-day life. For instance antibacterial agents, sunscreen lotions have become a part of reality. The compact and fast non-silicon based chips for processor, quantum computation, micro-electro-mechanical systems, and other nanoelectronic devices are some of the forthcoming aspects that can be developed through proper exploitation of the nanomaterials. Low threshold current, higher thermal stability, higher differential gains etc, are some of the interesting characteristic properties of the miniaturized devices [3, 4].

The capability of manufacturing different category of nanostructured materials (metallic, semiconducting) has directed immense application in drug delivery, lasers, memory devices etc [3-6]. Among the different kinds of materials the semiconductor nanostructured materials (e.g. Si, Ge, GaAs, GaN, ZnO, InGaAsN etc.) are especially interesting owing to the existence of band gap (or forbidden gap: an energy range where no electronic states exists) which can be varied with size. The development in various processing techniques has offered the opportunity to engineer the band gap of the semiconducting nanostructured systems across the whole electromagnetic spectrum. This fact is accountable for considering the semiconducting materials as the building blocks for future nanophotonic and nanoelectronic devices [7-10]. This thesis is focused on exploring the optoelectronic and photonic properties of ZnO based nanostructured systems.

1.1 Semiconductor nanostructures

The rapid development of the modern electronic devices is facilitated by the improvement of the integrated circuit technology based on semiconducting materials. Whether it is an elementary semiconductor (e.g. Si, Ge) or a compound semiconductor (e.g. ZnS, InGaAsN), each one has its own advantages and limitations in practical applications. The semiconductor based nanostructured materials exhibit dimension dependent optical and electronic properties. As a result, their physical properties, to a large extent are tunable between molecular phase and bulk phase. In this category of nanostructured materials, the departure from the bulk behavior arises owing to the enhancement in band gap (alongwith the discreteness of energy levels), excitonic binding energy and oscillator strength of the material [10-12]. The reduction of geometric dimension in any direction to an amount comparable with the de Broglie wavelength of the carriers could lead to the spatial confinement of the carrier motion. The confinement of electron wave function in a region having a dimension smaller than the electron mean free path is an example of such phenomenon. The situation of quantum confinement can be experienced upon restricting the motion of electrons, holes and excitons (bound state of electron-hole pair) in one or more directions of the semiconductor system. The extent of quantum confinement along a particular direction, can be realized in two major regimes; weak and strong confinement regime, as proposed by A. L. Efros and Al. L. Efros [12]. Denoting the average dimension of a nanostructured system as R, the weak quantum confinement regime corresponds to the case of $R > a_B$, where a_B is the exciton Bohr radius of the bulk semiconductor. Whereas the situation of $R < a_B$ refers to the strong confinement regime where the confined electron and hole have no bound state. Consequently, the structures known as quantum well (2D), quantum wire (1D) and quantum dot (0D) originate from the carrier confinement in one, two or in three directions of the nanostructures respectively. Compared to the bulk counterpart, most of the unique electronic properties of the above mentioned quantum structures are explained in terms of abrupt change in density of states (DOS). Figure 1.1 depicts

the variation of density of states, D(E), for different quantum structures. As one moves from the bulk to the quasi-zero dimensional structures, DOS changes drastically giving rise to narrower carrier distribution and enhanced oscillator strength (the probability of transition from lower energy state to a higher energy state).

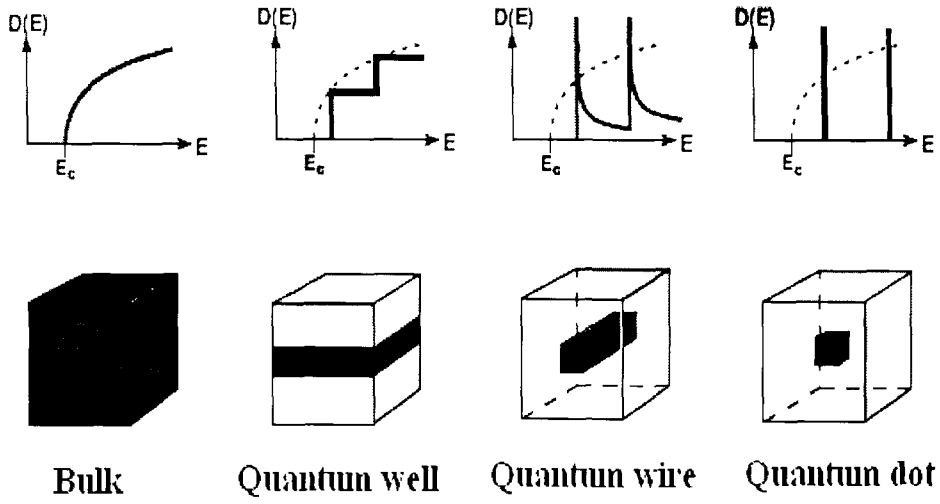

Figure 1.1: Schematic of structures and density of states for 3D, 2D, 1D and 0D systems.

1.1.1 Spherical semiconductor nanostructures

The structures which appear in the form of tiny particles and having typical diameter of 1-100 nm, are commonly known as nanoparticles or nanospheres. The quasi zero dimensional nanostructures or, quantum dots (QDs) under strong quantum confinement effect, can be achieved by restricting the diameter of the semiconductor nanoparticles to a few nm, in all the directions. Transmission electron microscopy (TEM) and High resolution transmission electron microscopy (HRTEM) images of fairly spherical CdS nanoparticles are shown in Figure 1.2 [13]. Over the years, the stability of the nanoparticles had been a matter of concern as far as the technological application is concerned. The high surface-to-volume ratio (>> 1) of the nanoparticles has led to very high surface energy and hence, surface reactivity making there by thermodynamically unstable. In order to reduce overall surface energy the nanoparticles tend to grow

in size or agglomerate. There is an urgent need to select an efficient fabrication/processing technique so that nanoparticle agglomeration can be arrived to a great extent.

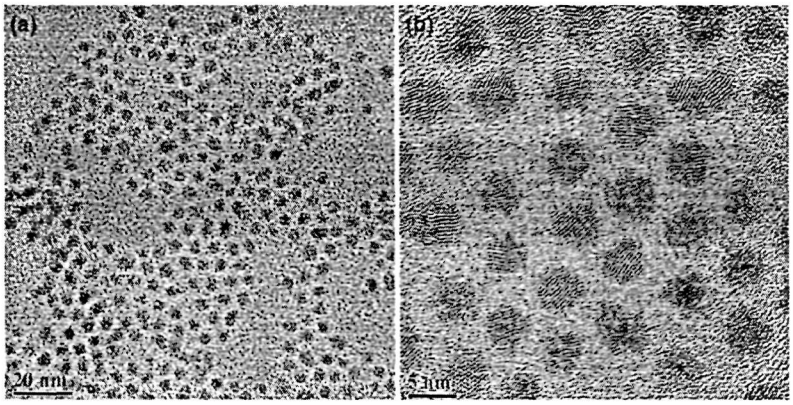

Figure 1.2: (a) TEM and (b) HRTEM images of CdS nanoparticles [13].

Previously, the semiconductor nanoparticles have been developed using a number of techniques under different environments. The various techniques were found to affect the size distribution as well as the diverse physical and chemical characteristics of the nanoparticles. The synthesis of the semiconductor nanoparticles in the presence of surfactant, capping agents or some soft templates has been employed several times to overcome the problem of agglomeration or to stabilize the system [13-16]. The synthesis of water-soluble and biocompatible fluorescent QDs by the encapsulation of surfactant/lipid micelles has been reported [14]. Again the utilization of polymers for controlling the assembly of nanoparticles is also found in the literature [15]. Murray and the co-workers presented a simple route to produce CdE (E = S, Se, Te) nanoparticles having high monodispersity [17]. The reaction involves the pyrolysis of the organometallic reagent by injecting into a hot coordinating solvent which leads to discrete nucleation and restricted growth leading to uniformed sized nanoparticles. A similar approach was found to be useful to synthesize well-crystallized nanoparticles of InP, GaP, $GaInP_2$, and GaAs [18]. The fabrication of SiO_2 embedded GaAs nanoparticles by radio frequency sputtering method has also been reported [19, 20].

Sol-gel process is one of the common techniques for the synthesis of oxide based nanoparticles. This process involves the typical precursor as metal alkoxides and metal salts, which could undergo hydrolysis and condensation reactions. The fabrication of SnO_2, TiO_2, ZnO nanoparticles using sol-gel technique have been reported by many workers [21-24]. Apart form the conventional nanoparticle systems, recent interest has grown in the processing of core-shell nanostructures. The fabrication and adequate surface passivation of semiconductor-semiconductor core-shell QDs are found to be quite effective in terms of production mechanism and various optoelectronic applications [25]. In this situation, the shell material acts as an extension of the core in the form of capping/coating layer but with different chemical composition and band gap. In these nanostructures drastic reduction of non-radiative surface recombination of charge carrier is highly attainable.

1.1.2 Elongated semiconductor nanostructures

The elongated structures having electron motion confined in two directions are considered as one dimensional (1D) nanostructures. Typically, the elongated semiconductors having diameter range 1 to 400 nm and lengths upto several micrometers are perhaps the most adaptable nanoscale building blocks for optoelectronic and nanoelectronic application. In contrast to the spherical nanoparticles, the use of 1D semiconductor nanostructures (in the form of nanorods, nanowires, nanotubes, nanobelts etc. as schematically shown in Figure 1.3) have their own advantage in specific elements/components. Basically, nanowires are solid state systems characterized by a radius which is negligible as compared to their length. On the other hand, the nanorods are usually much shorter in length than nanowires. The nanorods are often recognized as straight wires. Figure 1.4 shows the scanning electron microscopy (SEM) image of

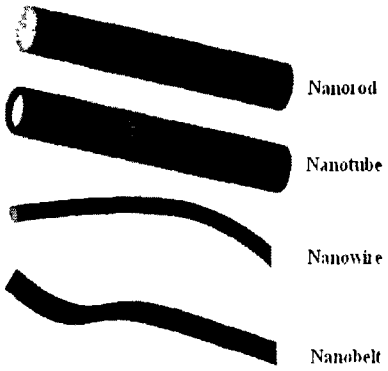

Figure 1.3: Schematic representation of various 1D nanostructures.

chemically grown ZnS nanowires [26]. The 1D structures in the form of nanobelts belong to special class of nanowires. The nanobelts are the nanowires that have well defined geometrical shape and side-surfaces. The cross section of the nanobelts is of rectangular shape having typical width-to-thickness ratio of the magnitude ~ 5 to 10. The ultranarrow nanobelts are rather narrow and smaller in length which can be characterized by a width that is comparable to the Bohr excition radius of the system under study [27]. 1D nanostructures in the form of nanotubes, differ from solid nanorods and nanowires with the internal structure being mostly unfilled. The nanotubes emerge in the form of hollow cylinders whereas nanorods and nanowires have solid cores. Generally, the cross section of nanorods and nanowires resembles to a filled circle or hexagon.

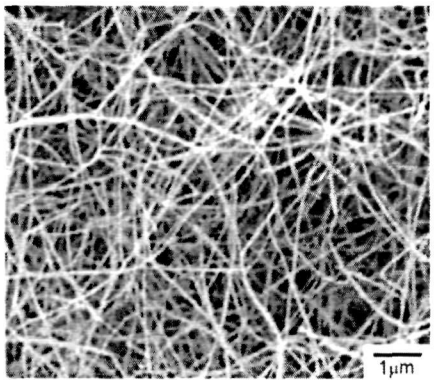

Figure 1.4: SEM image of ZnS nanowires [26].

In the recent decades, a great deal of interest was shown with regard to the fabrication of different types of 1D semiconductor nanostructures adopting a number of procedures and protocols. The fabrication of semiconductor nanorods or nanowires via vapour–liquid–solid (VLS) approach in presence of a metal catalyst (e.g. Au, Ag) is one of the most popular techniques [28-30]. The catalyst in the form of a liquid droplet serves as a superior spot for absorption of the gas phase reactant and, the nucleation site for crystallization upon supersaturation of the reactants. The direction of growth is directed by the catalyst droplet and hence, the nanowires obtained from such VLS process typically possess a solid catalyst nanoparticle at one end. Figure 1.5(a) shows the schematic representation of nanowire formation in VLS process. Based on the VLS approach, binary and ternary III-V, II-VI, and IV-IV group semiconductor nanowires (using laser-assisted catalytic growth (LCG) method) have been efficiently synthesized [28, 29]. As an alternative approach, the physico-chemical synthesis of 1D

nanostructures using some kind of surfactant or capping agents was proven to achieve a variety of elongated patterns like nanotubes, nanowires, and nanorods

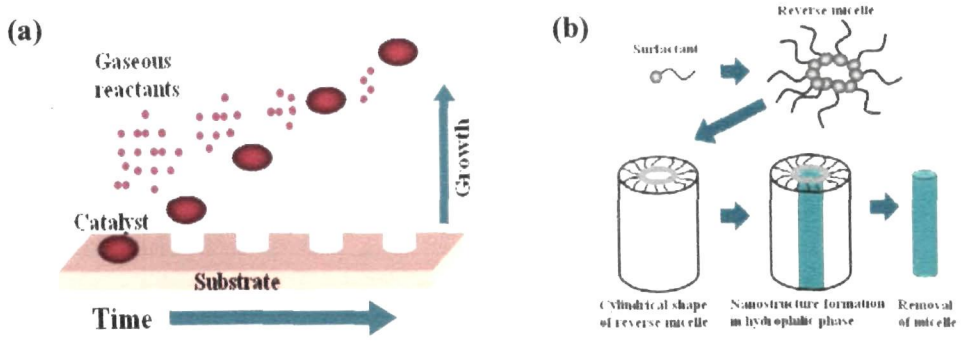

Figure 1.5: Schematic representation of (a) VLS and (b) surfactant assisted growth mechanism.

[31, 32]. The formation of nanorods via a reverse micelle route in the presence of non-polar solvent can also be realized, as depicted in the scheme below (Figure 1.5(b)). In a similar way, the solution based growth technique was employed to synthesize nanowires of II-VI and the elementary semiconductors [33-35]. In particular, the nanowires of elementary semiconductors (e.g. Si and Ge) were grown from the supercritical fluid precursors [34, 35].

Nanopatterning, depicts assembling nanowires/nanorods on suitable substrates in a systematic way. It can cater to various needs of industrial relevance in packaging, storing etc. In this regard, electron beam lithography (EBL) is a proven technique to fabricate semiconductor nanowires/nanorods mostly on Au-dot arrays [36-38]. Though such technique is appreciable for the fabrication of quality nanostructures, the technique requires cost, plentiful sophistication and machine complexities. The heterostructure/superlattice configurations are quite impressive for designing low threshold and high gained optoelectronic devices. In this regard, the fabrication of single crystalline nanowires with Si/SiGe superlattice structure has been demonstrated [39]. Again, the influence of shell thickness on the luminescence feature of TiO_2/CdS core-shell nanowires has also been studied [40]. The use of hybrid pulsed laser ablation/chemical vapor deposition (PLA/CVD) is useful to achieve quality superlattice structures. The

development of such heterojunctions based 1D nanostructures has immense potential in light emitting, photoconductive and photovoltaic devices [39-41].

1.2 Optoelectronic properties of the II-VI semiconductor based nanostructures:

The II-VI semiconductor compounds are suitable combination of group II and VI elements of the periodic table (e.g. CdS, ZnS, ZnO etc.). They are especially promising for optoelectronics devices such as light-emitting diode (LED), laser diode (LD) that operate in the blue or the ultraviolet spectral range. The nanostructures based on compound semiconductors, are expected to play crucial role in obtaining high-performance of these devices. Figure 1 6(a) depicts a block diagram related to the application of these nanostructures. A relevant section of periodic table is also shown on the right hand side of the scheme (Figure 1.6(b)).

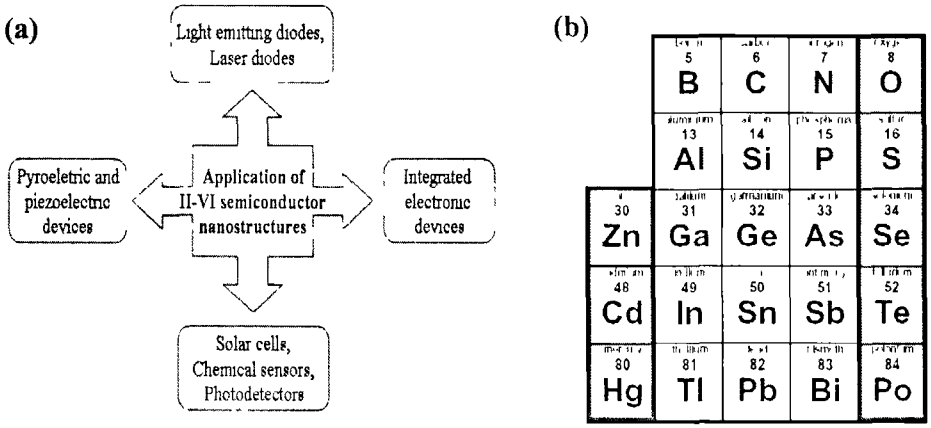

Figure 1.6: (a) Possible application of semiconductor nanostructures, (b) section of the periodic table.

Lakowicz and the co-workers have reported the blue luminescence response of CdS nanoparticles observed in the presence of an amine-terminated dendrimer [42]. The nanoparticle system displayed polarized emission with the anisotropy rising progressively from 340 to 420 nm excitation wavelength, reaching a maximal value in excess of 0.3. Whereas, polyphosphate stabilized CdS

nanoparticles exhibited red emission maximum and displayed zero anisotropy for all the excitation wavelengths [42]. Again, the electroluminescence (EL) displayed by the thin film structure containing close-packed CdS nanoparticles sandwiched between ITO and Ag contacts was found to emit light visible to unaided eye above a bias of 15 V [43]. The observed tunability of the EL was attributed to the excitation of different deep traps by electron transport across neighboring CdS nanocrystals. The ZnS and ZnO based nanostructures are quite well-known for the light emission in the ultra-violet (UV) and visible region [44-47]. Intensive UV light emission, at room temperature was revealed by ZnO nanowires and can be assigned to the dominance of emission from the free exciton over the native defect related emission [45]. Whereas, the variation of the excitonic and the defect related emission of ZnS QDs, was found to depend on the concentration of point defects that vary with synthesis parameters [44]. The ZnS nanowire arrays and aligned nanoribbons have also been grown on micrometer-wide single-crystal ZnS ribbon substrates via a homoepitaxial growth [47]. In this case, the photoluminescence (PL) spectra indicate that the cross arrays of nanowires can serve as Fabry–Perot cavities, which leads to the band gap lasing emission in two specific directions. Again, cathodoluminescence (CL) measurements show more intense green emission from the <210> ZnS nanowire cross arrays than the [001] ones and reveals that the orientation dependency of CL emission. As a remarkable step towards semiconductor nanocrystal based lasers, Chan and the co-workers have demonstrated the precise tunablity in amplified spontaneous emission and lasing action of blue light emitting in core-shell CdS/ZnS nanosystems [48].

Again, doping of the wide band gap II-VI semiconductor nanoparticles, with transition metals (Mn, Cu etc.) or, rare-earth elements (Eu, Tb, Er etc.) is of practical interest owing to the selective luminescence transitions and that is why they are widely used as phosphors and lasing media. Several semiconductor host materials such as ZnS, CdS, and ZnSe have been used for Mn-doped nanocrystals with different synthesis techniques [49, 50, 51]. Bhragava et. al. have reported

that Mn doped ZnS nanocrystals can yield efficient Mn^{2+} related orange-yellow luminescent emission alongwith life time shortening due to radiative processes [49]. The complete suppression of surface state related emission, upon Mn-doping, was found in CdS nanoparticle system [50]. The optical studies of Mn doped CdS, showed the dominance of Mn^{2+} related $^4T_1$-$^6A_1$ transition (which corresponds to 2.12 eV) with no distinguishable surface state related emission. The schematic view of the luminescence mechanism is shown in Figure 1.7 [50]. Again, ZnS:Mn and CdS:Mn/ZnS core/shell based luminescent semiconductor nanocrystals have been actively studied as electroluminescent (EL) components and luminescent biomarkers [51]. On the other hand, upon doping of Cu in ZnS QDs, emission of light in the green region of visible spectrum was witnessed [52]. In this case, the luminescence spectra of Cu-doped ZnS QDs have showed redshift with an emission response peaking at ~480 nm (green), in contrast to the undoped one, exhibiting luminescence maxima at ~424 nm (blue). The rare earth doped II-VI semiconductors are interesting because of the sharp intra 4*f* transitions in the visible and IR regions. It has been possible to fabricate quality Eu^{3+} and Tb^{3+} doped ZnS nanocrystals with the characteristic emission of the rare-earth ions in the visible region [53, 54]. Owing to the sharp characteristic emission in the red and blue-green region of the visible spectrum, the Eu^{3+} and Tb^{3+} doped semiconductor nanomaterials are very attractive as phosphor candidates. Whereas, the emission at ~ 1.54 μm of Er^{3+}-doped II-VI semiconductors are interesting due to the potential application in IR lasers. Schmidt and the co-workers have demonstrated strong enhancement in the ~ 1.54 μm fluorescence in Er^{3+} doped II-VI semiconductor QD systems [55]. Adopting a new synthesis strategy, they were able to incorporate upto 20 at.%

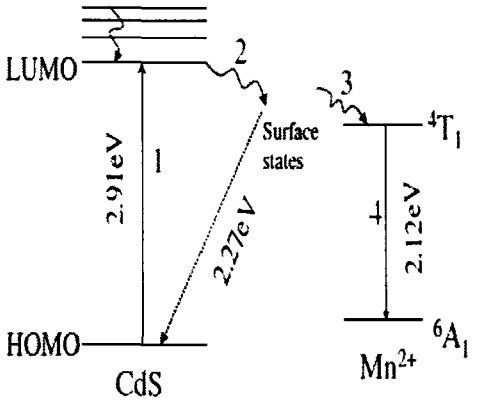

Figure 1.7: Scheme of luminescence mechanism scheme of CdS:Mn nanoparticles. HOMO and LUMO represent the highest and lowest occupied molecular orbitals [50].

Er^{3+} into ZnS, CdS, and CdSe as well as in ZnO semiconductor clusters and nanocrystals with an average size range 1.5-5 nm.

It is worth mentioning here that the performance of the optoelectronic devices depend on the quality of the metal/semiconductor contact. It has been possible to fabricate reliable Ohmic contacts out of metallic contacts of Al, Ti, In/Au etc. with nanostructures based on II-VI semiconductors like CdSe, ZnTe etc. [56-58]. The fabrication of Schottky contacts with metals (having high work function) has several technological advantages. The rectifying nature of the current-voltage (*I-V*) characteristics of a Schottky contact with less leakage current and low turn-on voltage makes its performance better than the conventional *pn* junction diodes. The formation of high-quality Schottky contacts has become an essential part of various optoelectronic components and integrated devices [56-60].

Usually, the direct band-gap of II-VI semiconductors varies from 1.5 eV (CdTe) to 3.7 eV (ZnS). This can be further extended via quantum confinement effects when they exist in nanostructured form. Therefore, compared to the conventional II-VI bulk systems, the II-VI semiconductor nanostructures will be more promising for making photodetectors that work from NIR to UV region [56]. Earlier, devices based on individual CdO nanoneedles were fabricated and efficient IR light detection was studied [61]. It was found that the CdO nanoneedle based devices that absorb IR light via the indirect band gap of CdO, could show an on/off ratio of 8.6 at 1.2 K between the illuminated on state and the dark off state. Similarly, ZnSe nanowire was shown to be a promising material for visible light detection, where the shape of the spectral response strongly reflects the absorption coefficient of ZnSe [62]. Single-crystalline ZnS nanobelts with sharp UV emission at RT have been demonstrated to act as UV sensors dictated by high spectral selectivity combined with high photosensitivity and fast response time [46]. Such experimental observations substantiate the utilization of the ZnS nanobelts as visible-blind UV photodetectors in different areas. Field effect transistors (FETs) are the fundamental elements in most of the optoelectronic

devices. Amongst different configurations of FETs, the metal-oxide-semiconductor FETs (MOSFETs) perform a major task in the existing IC techniques [63]. MOSFET configuration with a single elongated nanostructure (Figure 1.8) has been tested for several applications. The fabrication of FET devices for detection of photons having energy above the semiconductor band gap has been reported. The design of single CdSe nanoribbon based FET structure with high sensitivity and fast response was previously reported by Jie *et. al.* [64]. Further, the photoconductivity study using p-type ZnSe:Bi nanowire (with MOSFET configuration) has been successfully demonstrated [59].

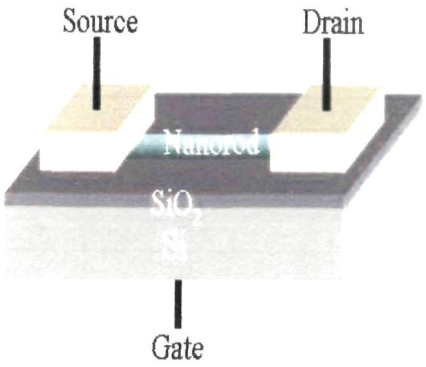

Figure 1.8: Schematic representation of a single nanorod based MOSFET.

Moreover, the semiconductors nanostructures can be used as gas sensors due to their high surface-to-volume ratio and confined charge carrier concentration. The nanostructures of ZnS, CdO, CdSe, ZnO have a selective, but pronounced sensitivity to gases, such as H_2, O_2, NO_x and other species [65-69]. The gas sensing mechanism had been explored using highly porous CdO nanowires, which has demonstrated good response owing to the porous structures and carrier site selectivity to NO_x [67]. In a similar way, room-temperature O_2 sensing under ultraviolet illumination was observed for individual ZnS nanobelts [66], whereas sound performance in H_2 sensitivity was realized in self-assembled oriented 1D ZnS nanostructures [65]. The, high-quality CdSe nanocrystals incorporated into polymer thin films were also found to respond reversibly and rapidly to environmental changes depending on the nature of the gases [68].

The fabrication of high-sensitivity LEDs, photo-detectors, gas sensors, chemical and biological detectors count on the surface-sensitive properties of these II-VI nanostructures. However, the fabrication of quality devices has been challenging

to meet the technical reliability and reproducibility of the device performance. Therefore, the drawbacks related to the basic understanding of the nanostructure interfaces with metals, dielectric, and with other nanostructures, must be addressed for controlled performance of nanostructure-based devices.

1.3 Zinc oxide (ZnO) based nanostructures and nanopatterns

Amongst the II-VI semiconductor systems, ZnO based nanostructures have gained a good deal of attention due to their extensive application in the field of optoelectronics, photonics and light harvesting devices. The novel optical, electrical and mechanical properties of ZnO have fueled numerous opportunities to meet the technological demands. ZnO, a direct band gap semiconductor, exists in two forms: hexagonal wurtzite and zinc blende (Appendix 1). However, the wurtzite phase of ZnO is the most stable one which comprises of hexagonal unit cells as the building blocks and lattice parameters as $a \sim 0.3296$ and $c \sim 0.5206$ nm [70]. Figure 1.9 illustrates the crystal structure of ZnO, as several alternating planes compiled of tetrahedrally coordinated O^{2-} and Zn^{2+} ions, stacked alternately along the *c*-axis. The piezoelectricity and pyroelectricity in ZnO originates from the non-central symmetric structure, due to the tetrahedral coordination in ZnO. The wide band gap (3.37 eV) and large exciton binding energy (~ 60 meV at RT) of ZnO, account for the potential application in making proto-type UV laser and other optoelectronic components. As far as the practical application is concerned, the bio-compatibility and environmental related aspects need to be addressed assuring safety and reliability.

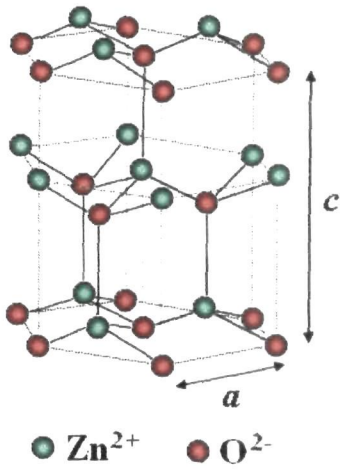

Figure 1.9: A schematic view of hexagonal unit cell of ZnO.

ZnO nanostructures may appear in diverse form: from spherically symmetric nanoparticles to asymmetric nanostructures such as 1D nanorods, nanobelts, nanopillars, nanosprings nanocombs, nanorings etc. Hierarchical structures like flowers, stars can also be synthesized. The variation in the thermodynamic equilibrium conditions is responsible for the anisotropic growth of ZnO. The control over various synthesis parameters like precursor concentration, chamber pressure and temperature or any other external stimuli, can lead to various kinds of nanostructures of ZnO. The chemical synthesis of ZnO nanoparticles using soft templates and surfactants, is often found in the literature. To avoid agglomeration of nanoparticles, the use of polymer matrix such as polyvinyl alcohol (PVA) has been reported [71, 72]. Previously, the growth of spherical nanoparticles to 1D nanorods of ZnO was also achieved, by varying the precursor molar ratio or the synthesis time [73, 74]. Again, the fabrication of ZnO nanorods or, nanowires using variety of physicochemical methods like thermal evaporation, VLS process, and catalyst free metal-organic chemical vapour deposition (MOCVD) etc. have been reported [75, 76]. Figure 1.10 shows the SEM image of ZnO nanorods/nanowires grown using Au catalyst on a polycrystalline alumina substrate [70]. While, ZnO nanobelts as presented in Figure 1.11, were fabricated by sublimation of ZnO powder without introducing any catalyst [77]. A nanobelt dominated by a polar surface can be approximated as a capacitor with two

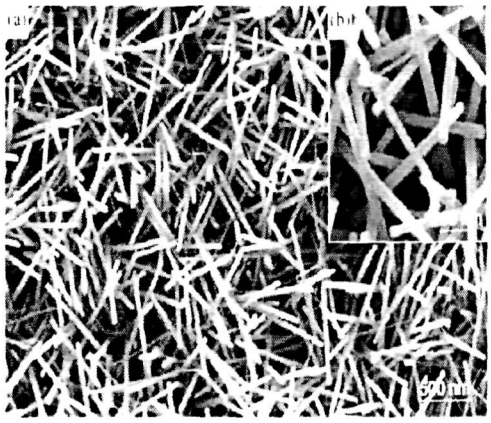

Figure 1.10: SEM image of ZnO nanorods at (a) low and (b) high magnification [70].

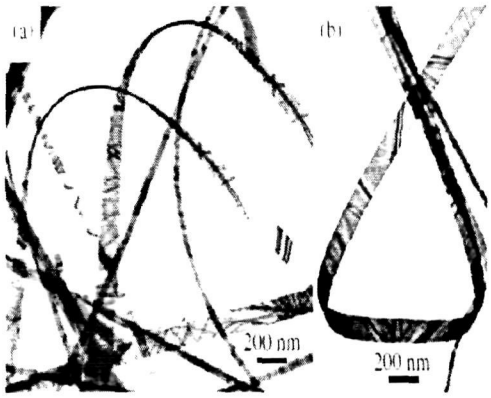

Figure 1.11: (a,b) TEM image of ZnO nanobelts [70].

charged parallel plates. In such a situation, in order to minimize the electrostatic energy, the polar nanobelt tends to roll over into an enclosed ring shape or into a spiral shape. Therefore the formation of nanoring, nanohelix or nanospring shape of ZnO can be understood from the nature of the polar surfaces [78, 79]. In contrast to such nanostructures, the formation of comb-like cantilever arrays of ZnO is also reported [80]. In absence of any foreign catalyst, during a self catalyzed process the surface polarization induced growth due to the chemically active (0001) Zn clusters was correlated to the origin of the formation of comb-like structures of ZnO. Again, the synthesis condition dependent structural organizations such as urchins, nanoflowers, multipods etc are also reported [81, 82]. Figure 1.12 depicts the SEM image of such flower like structures of ZnO [83]. The fabrication of more complex and hierarchical structures of ZnO are also found in the literature [70, 84]. The morphological view of hierarchical nanostructures of ZnO on In_2O_3 core nanowires can be seen in Figure 1.13 [84].

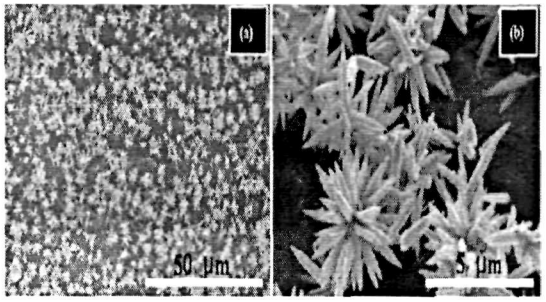

Figure 1.12: SEM image of ZnO nanoflowers at (a) low and (b) high magnification [83].

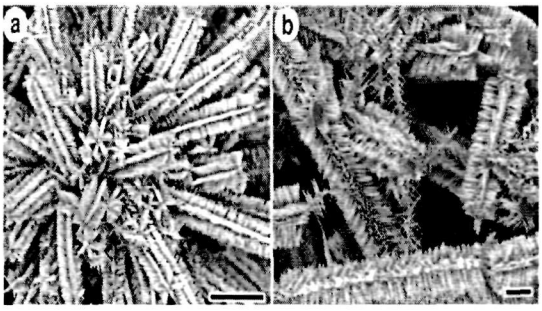

Figure 1.13: SEM image of ZnO hierarchical nanostructures at (a) low and (b) high magnification. The scale bar represents (a) 10 μm and (b) 1 μm [84].

In crystals the common imperfections arise in the form of chemical impurities, vacant lattice sites and extra atoms situated at an irregular lattice position and are called as defects [85]. The presence of various native point defect states in ZnO nanostructures is one of the most discussed issues in the area of condensed matter

systems. The point defects in ZnO include Zn or O, vacancies (missing atoms at regular lattice positions), interstitials (atoms occupying interstices in the lattice) and antisites (a Zn atom occupying an O lattice site or vice versa). Understanding of the origin and behavior of these point defects in ZnO is quite essential while fabricating and operating nanostructured based devices. However, the origin and the existence of various Zn and O related defects in ZnO have been controversial among different group of workers [86-90]. The presence of different defect levels in ZnO is responsible for the green, yellow and red emission in the electro-magnetic spectrum. Whereas, the performance of a ZnO based Ohmic and Schottky contacts are largely affected by these charged defects. Several attempts have been made to locate the electronic energy levels of the different defects within the band gap of ZnO. Based on different reports a tentative draft of the energy levels of the defects can be summarized as in Figure 1.14 [86, 90]. Using the Kröger Vink notation as i ~ interstitial site, Zn ~ zinc, O ~ oxygen, and V ~ vacancy; the chief native defects in ZnO are denoted as V_{Zn}, Zn_i, V_O, O_i, O_{Zn} etc. Generally, the defects like V_{Zn}, O_i, O_{Zn} are regarded as acceptor types, whereas Zn_i, and V_O^+ are considered as donor type defects in ZnO [90]. Hence the variation of any one these types of defects would lead to the alteration in the electronic properties including carrier transport, scattering and recombination characteristics.

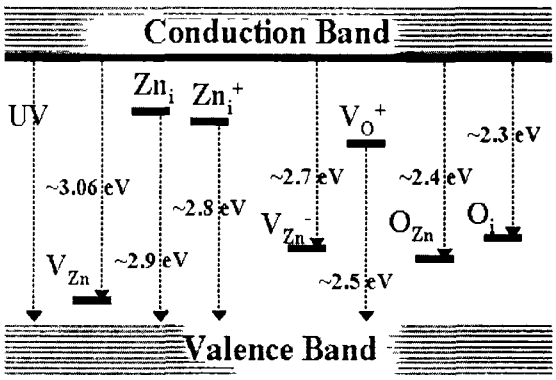

Figure 1.14: The energy levels of different defect states of ZnO.

The concentration and kind of native defects of the nanostructures are very sensitive to the synthesis parameters and environments. Consequently, the nature of luminescence spectra of the ZnO nanorods can be drastically affected by various factors (e.g. reactant quantity, substrate nature, reaction temperature, time,

etc.) involved in a particular process. The post fabrication treatments like thermal annealing, UV-curing, energetic ion irradiation etc. are also beneficial to achieve variation in the emission response. The change in precursor ratio, solvent concentration, synthesis temperature, time etc could influence the growth kinetics of the nanostructures and hence the native defect states [91-93]. Again, in case of substrate assisted fabrication of elongated nanostructures of ZnO, the crystallinity of the nanostructures largely depend on the lattice parameter of the substrates and hence on the defect concentration and defect dynamics associated with them [94]. It has been witnessed that annealing at varying temperatures and under different environmental conditions can have profound control over the defect related emission of ZnO nanorods [86, 94, 95]. The fast moving ions, while traversing through a material system, are capable of modifying atomic arrangements via deposition of a huge amount of energy in the system. During ion-matter interaction, ions carrying energy in the keV and MeV scale are capable of producing point defects or columnar defects in the solids. Again nanostructure growth, splitting and directed growth are prominent for ion energy in the MeV range [96, 97], while ion implantation and ripple formation are observed for ions carrying energy in the keV scale [98]. Ion irradiation induced such structural and crystallographic alteration can influence the various physical properties exhibited by the materials [99-101]. In this regard, irradiation of ZnO nanostructures with energetic ions has been established to be an alternative approach to tune the emission pattern of ZnO [71].

Doping with suitable impurities has its own importance when the tunabilty of a specific optical or electrical property is desired. It was shown that the band gap of ZnO nanocrystals can be tuned from 2.9 to 3.8 eV depending on the inclusion of specific dopants like Cd, Mg, Mn and Fe ions [102]. Bhargava et. al. have demonstrated that the quantum confined ZnO nanocrystals doped with Mn^{2+} and Eu^{2+} ions could show efficient broad-band emission at room temperature [103]. The PL emission of Mn doped ZnO nanocrystals exhibit emission in the green region (520 nm) and can be assigned to the $^4T_1$–$^6A_1$ transition. The well-known

Mn^{2+} orange-emission in ZnS, was found to get shifted to the green region in ZnO due to the change of Mn^{2+} position from octahedrally coordinated to tetrahedrally coordinated system [103]. Whereas, in Eu^{2+} doped ZnO system, the observed broad emission band was correlated to the intra-ion transition of $4f^6 5d^1 - 4f^7$. The intra $4f$ transition led sharp and selective emission upon doping of different rare earth ions (Eu^{3+}, Tb^{3+} etc) in ZnO nanostructures has been reported satisfactorily [101, 104]. Figure1.15 shows a simplified scheme of the different energy levels of Eu^{3+} ion in the host ZnO system and the radiative emission energy lines [104]. However, indepth investigation with regard to underlying mechanism of such emission and the role of host ZnO nanostructure in the frame work of a theoretical model is still under preview. Apart from these studies, introduction of *p*-type ZnO nanostructures by a suitable doping (with various ions such as N, As, P etc) has been achieved using ion implantation, hydrothermal method etc. [105-107]. The technological viability of achieving *p*-type conductivity of ZnO lies in the fabrication of *p-n* junction or homojunction based light emitting diodes.

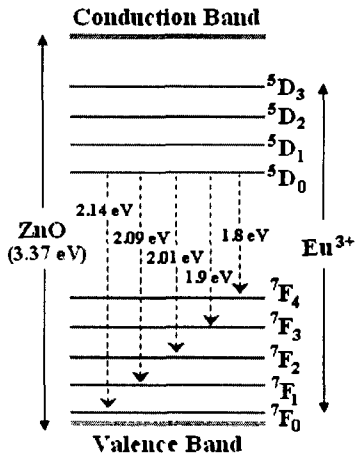

Figure 1.15: Scheme of the different energy levels of Eu^{3+} ion in the host ZnO system alongwith the radiative emission energy lines [104].

The exciton binding energy of ZnO (~ 60 meV) is much higher than that of GaN (25 meV), and that is why the room temperature thermal energy (K_BT ~ 26 meV) would give rise to the efficient excitonic emission at room temperature in the former case. This fact accounts for the potential candidature of ZnO as the room temperature UV emission source. Earlier the room temperature UV lasing in ZnO nanowire arrays grown on sapphire substrates has been demonstrated [108]. The UV light emission from ZnO nanowire and nanobelt structures has also been discussed in literature [45, 109]. On the other hand, the EL study of ZnO nanorods supported on Si and GaN substrates has revealed the superior

applicability as LED and other EL devices [110, 111]. Furthermore, it has been demonstrated that both the UV emission and the defect related visible emission can be highly polarized in case of vertically aligned ZnO nanorods [112]. The intensities of both of these emissions vary with the polarization angle by the relation of a square cosine function as predicted by the group.

Photonic crystals are well-known for their ability to enhance the useful optical characteristics of the opto-electronic devices. A photonic crystal is a periodic dielectric structure of two different materials and exhibits a photonic band gap (PBG). A PBG is the characteristic feature of a periodically arranged alternate structure and is comparable to the electronic energy band gap (EBG) that arises in semiconductors [113]. The lasing threshold of self assembled 3D photonic crystals from ZnO colloidal spheres was found to be lower than the random arrays of identical spheres [114]. Moreover, the fabrication of self-assembly of SiO_2/ZnO core–shell photonic crystals with a high fill factor and enhanced refractive index contrast has been realized [115]. Interestingly, the typical green emission of ZnO was found to be suppressed upon infiltration of ZnO nanocrystalline particles within the porous opal. This was ascribed to the inhibition of spontaneous emission owing to the overlapping of the photonic band gap of opal and the defect level recombination spectrum of ZnO [116]. Besides that, in nano ZnO/peacock feather hybrid system, the PL emission of the ZnO was found to get modified by the feather, giving rise to a broad emission response in the visible region as reported by Han and the co-workers [117]. In this case the photonic crystals of naturally available peacock feathers were selected as the template to grow ZnO nanoparticles.

The fabrication of any semiconductor based prototype device depends on the quality of the contacts formed between the metallic electrodes and the semiconductors. It is expected that investigation on ZnO nanostructure based Schottky nanojunctions would make an important contribution to the rapid development in miniaturized devices. In this regard, the development of rectifying

Schottky contacts fabricated using *M*/ZnO nanostructure (*M* ~ Au, Ag etc) systems have been explored [118, 119]. The effect of various surface and defect states of ZnO nanostructures on the carrier transport property of the Schottky diodes has also been studied [120, 121]. Along with that, the wide band gap and the adsorbate dependent electrical conductance of ZnO nanostructures were the key features which make the system suitable for detecting ultra-violet (UV) light. ZnO nanowire based Schottky diodes have been found to be promising for UV photodetection which possessed very fast recovery time [122, 123]. Also, the UV responsivity of ZnO nanorods in metal-semiconductor-metal (MSM) configuration was found to be stronger as compared to the ZnO thin film based configuration [124]. In addition, high UV photocurrent efficiency with large responsivity of MSM based photodetector made out of colloidal ZnO nanoparticles has been worked out [125]. Meanwhile, it was realized that the presence of the native defects or trap states within the band gap of ZnO leads to the trapping of charge carriers and results in the slowing down of photocurrent decay giving rise to persistence photocurrent (PPC) [124]. The evolution of PPC in a system is extremely useful for the application in bistable optical switching and radiation detectors etc [126, 127].

Reports on the field emission characteristics of elongated ZnO nanostructures are also available in the literature [128-130]. The exceptionally high field emission observed in ZnO nanowires, grown on carbon cloth (a textile-like material) has been correlated to the intrinsic geometry of the nanowires and that of the carbon cloths [128]. Aspect ratio dependent field emission of ZnO nanorods was also studied [129]. It was shown that an optimum density and aspect ratio of ZnO nanorod arrays are exceptionally beneficial to induce high throughput field emission response. A comprehensive study of various nanostructures suggests that the shape geometry, density and substrate nature are the vital factors for field emission enhancement.

Owing to the high sensitivity to the chemical environment, ZnO nanostructures have been widely used for sensing purposes. The oxygen vacancies present on the surface of the nanostructure could influence the electronic properties and are believed to be the origin of the sensing mechanism of ZnO. Depending on the species, the adsorption of gas molecules on these defects results in the decrease or increase in conductivity [131]. Fabrication of single nanowire based O_2, and NO_2, sensors has been demonstrated [132]. Previously, ZnO nanobelt assisted sensing of H_2, NO_2 and hydrocarbons at different operating temperatures has also been reported [133]. Recently, keen interest is being shown on the use of ZnO nanostructures to fabricate nanostructured solar cells [131, 134]. Investigation on hybrid polymer/ZnO solar cells, dye-sensitized solar cells suggests that the nanorod structures are capable of furthering performance of the solar cells and other flexible nanoelectronics in near future.

1.4 Objectives of the present study

The thesis highlights the synthesis, characterization and optoelectronic/photonic application of ZnO nanostructures with a special emphasis on the elongated nanostructures. The ZnO nanostructures have been synthesized using various chemical and physico-chemical routes. In addition, the doping of the nanostructures with Eu^{3+} ions has been worked out. The morphological features of the as-synthesized nanostructures have been carried out using scanning electron microscopy (SEM) and low/high resolution transmission electron microscopy (TEM). Whereas, X-ray diffraction (XRD) and energy dispersive X-ray spectroscopy (EDX) had been used to reveal the structural and elemental detection of the nanostructures. The spectroscopic properties have been investigated using UV-Visible spectroscopy and photoluminescence spectroscopy (PL). Followed by these characterizations, low and high energetic ion irradiation with different ions and fluence was employed to modify the optoelectronic properties of the nanostructures. The ion irradiated samples were also characterized by the above mentioned characterization tools. Apart from these,

theoretical investigation on the observed consequences of the unirradiated and ion irradiated nanostructures has been carried out using simple mathematical analysis.

In the light of the discussion of the previous section, it can be understood that the efficiency of a ZnO nanostructure based device would largely depend on the nature and quality of the *M*/ZnO junction (*M* ~ Metal). In this regard, the transport properties of the substrate assisted ZnO nanorods have been studied using *M*/ZnO configuration (*M* ~ Ag, Pt etc). Additionally, Fowler-Nordheim tunneling characteristics of $Al/Al_2O_3/ZnO$ metal-insulator-semiconductor nanojunctions have been shown apart from other transport mechanisms. Moreover, UV photodetection of ZnO nanostructures supported on aluminum and glass substrates have been demonstrated. Finally, photonic band gap tuning response of natural peacock feather system was explained by growing ZnO nanospheres on the feathers.

References:

[1] Goddard, III, W. A. (Editor) et al. (Ed.). *Handbook of Nanoscience, Engineering, and Technology*, 2nd ed., CRC Press, Florida, 2007.

[2] Drexler, K.E. *Engines of Creation*, Anchor Press, New York, 1986.

[3] Nejo, H. (Ed.). *Nanostructures-Fabrication and Analysis*, Springer-Verlag, Berlin Heidelberg, 2007.

[4] Cao, G. *Nanostructures & nanomaterials: Synthesis, properties & applications*, Imperial College Press, London, 2004.

[5] Liao,H., et al. Biomedical applications of plasmon resonant metal nanoparticles, *Nanomedicine* 1 (2), 201-208 , 2006.

[6] Gao, J., et al. Multifunctional Magnetic Nanoparticles: Design,Synthesis, and Biomedical Applications, *Acc. Chem. Res.* 42 (8),1097-1107, 2009.

[7] Wang, Y. & Herron, N. Nanometer-Sized Semiconductor Clusters: Materials Synthesis, Quantum Size Effects, and Photophysical Properties, *J. Phys. Chem.* 95, 525-532, 1991.

[8] Brus, L. E. Electron-electron and electron-hole interactions in small semiconductor crystallites: The size dependence of the lowest excited electronic state, *J. Chem. Phys.* 80 (9), 4403-4409, 1984.

[9] Nirmal, M., & Brus, L. Luminescence photophysics in semiconductor nanocrystals, *Acc. Chem. Res.* 32, 407-414, 1999.

[10] Gaponenko, S. V. *Optical Properties of Semiconductor Nanocrystals*, United Kingdom, 1998.

[11] Yoffe, A.D. Low-dimensional systems: quantum size effects and electronic properties of semiconductor microcrystallites (zero-dimensional systems) and some quasi-two-dimensional systems, *Adv. Phys.* 42 (2), 173-262, 1993.

[12] Efros, Al. L., & Efros, A. L. Interband absorption of light in a semiconductor sphere, *Sov. Phys. Semicond.* 16, 772-775, 1982.

[13] Wan, Z., et al. Facile synthesis of monodisperse CdS nanocrystals via microreaction, *Nanoscale Res. Lett.* 5, 130-137, 2010.

[14] Fan, H., et al. Surfactant-assisted synthesis of water-soluble and biocompatible semiconductor quantum dot micelles, *Nano Lett.* 5 (4), 645-648, 2005.

[15] Shenkar, R. et al. Ploymer-mediated nanoparticles: Structural control and applications, *Adv. Mater.* 17 (6) 657-669, 2005.

[16] Rogach, A. L. et al. Synthesis and characterization of a size series of extremely small thiol-stabilized CdSe nanocrystals, *J. Phys. Chem. B* 103 (16), 3065-3069, 1999.

[17] Murray C. B., et al. Synthesis and characterization of nearly monodisperse CdE (E=S, Se, Te) semiconductor nanocrystallites, *J. Am.Chem. Soc.* 115, 8706-8715, 1993.

[18] Micic, O. I. & Nozik, A.J. Synthesis and characterization of binary and ternary III-V quantum dots, *J, Lumin.* 70, 95-107, 1996.

[19] Hirasawa, M., et al. Synthesis of GaAs nanoparticles by digital radio frequency sputtering, *Appl. Phys. Lett.* 67 (23), 3483-3485, 1995.

[20] Pal, U., et al. Synthesis of GaAs nanoparticles embedded in SiO_2 matrix by radio frequency co-sputtering technique, *Scripta Mat.* 44, 1841-1846, 2001.

[21] Zhang, J., & Gao, L., Synthesis and characterization of nanocrystalline tin oxide by sol-gel method, *J. Sol. Stat. Chem.* 177,1425-1430, 2004.

[22] Liu, H., et al. Synthesis and characterization of titania prepared by using a photoassisted sol-gel method, *Langmuir* 19 (7), 3001-3005, 2003.

[23] Yang, H., et al. Sol-gel synthesis of TiO_2 nanoparticles and photocatalytic degradation of methyl orange in aqueous TiO_2 suspensions, *J. Alloy. and Compd.* 413, 302-306, 2006.

[24] Meulenkamp, E. A. Synthesis and growth of ZnO nanoparticles, *J. Phys. Chem. B* 102, 5566-5572, 1998.

[25] Lambert, K., et al. PbTe|CdTe Core|Shell Particles by Cation Exchange, a HR-TEM study, *Chem. Mater.* 21 (5), 778-780, 2009.

[26] Yue, G. H., et al. Hydrothermal synthesis of single-crystal ZnS nanowires, *Appl. Phys. A* 84, 409-412, 2006.

[27] Wang, X., et al. Large-scale synthesis of six-nanometer-wide ZnO nanobelts, *J. Phys. Chem. B* 108, 8773-8777, 2004.

[28] Gudiksen, M. S. & Lieber, C. M. Diameter-Selective Synthesis of Semiconductor Nanowires, *J. Am. Chem. Soc. 122,* 8801-8802, 2000.

[29] Duan, X. & Lieber, C. M. General Synthesis of Compound Semiconductor Nanowires, *Adv. Mater.* 12, 298-302, 2000.

[30] Huang, M. H., et al. Catalytic growth of zinc oxide nanowires by vapor transport, *Adv. Mater.* 13, 113-116, 2001.

[31] Rao, C. N. R., et al. Surfactant-assisted synthesis of semiconductor nanotubes and nanowires, *Appl. Phys. Lett.* 78, 1853-1855, 2001.

[32] Zhang, J., et al. Shape evolution of one-dimensional single-crystalline ZnO nanostructures in a microemulsion system, *Crystal Growth & Design,* 4 (2), 309-313, 2004.

[33] Manna, L., et al. Synthesis of soluble and processable rod-, arrow-, teardrop-, and tetrapod-shaped CdSe nanocrystals, *J. Am. Chem. Soc.* 122, 12700-12706, 2000.

[34] Holmes, J. D., et al. Control of thickness and orientation of solution-grown silicon nanowires, *Science* 287, 1471-1473, 2000.

[35] Hanrath, T., & Korgel, B. A. Nucleation and growth of germanium nanowires seeded by organic monolayer-coated gold nanocrystals, *J. Am. Chem. Soc.* 124, 1424-1429, 2002.

[36] Martensson, T., et al. Fabrication of individually seeded nanowire arrays by vapour-liquid-solid growth, *Nanotechnology* 14, 1255-1258, 2003.

[37] Jensen, L. E., et al. Role of surface diffusion in chemical beam epitaxy of InAs nanowires, *Nano Lett.* 4, 1961-1964, 2004.

[38] Hochbaum, A. I., et al. Controlled Growth of Si Nanowire Arrays for Device Integration, *Nano Lett.* 5, 457-460, 2005.

[39] Y. Wu, R. Fang, P. Yang, Block-by-Block Growth of Single-Crystalline Si/SiGe Superlattice Nanowires, *Nano Lett.* 2, 83-86, 2002.

[40] Challa, K. K., et al. Effect of CdS film thickness on the photoexcited carrier lifetime of TiO_2/CdS core-shell nanowires, *Appl. Phys. Lett.* 99, 153111 (1-3), 2011.

[41] Lee, J.-C. et al. Growth of CdS nanorod-coated TiO_2 nanowires on conductive glass for photovoltaic applications, *Cryst. Growth Des.* 9 (10), 4519-4523, 2009.

[42] Lakowicz, J. R., et al. Luminescence Spectral Properties of CdS Nanoparticles, *J. Phys. Chem. B* 103, 7613-7620, 1999.

[43] Artemyev, M. V., et al. Electroluminescence in thin solid films of closely packed CdS nanocrystals, *J. Appl. Phys.* 81 (10), 6975-6977, 1997.

[44] Wageha, S. et al. Growth and optical properties of colloidal ZnS nanoparticles, *J. Cryst. Grow.* 255, 332-337, 2003.

[45] Kong, Y. C. et al. Ultraviolet-emitting ZnO nanowires synthesized by a physical vapor deposition approach, *Appl. Phys. Lett.* 78 (4), 407-409, 2001.

[46] Fang, X., et al. ZnO and ZnS nanostructures: Ultraviolet-light emitters, lasers, and sensors, *Crit. Rev. Sol. Stat. Mat. Sci.* 34, 190-223, 2009.

[47] Jiang, Y., et al. Homoepitaxial growth and lasing properties of ZnS nanowire and nanoribbon arrays, *Adv. Mater.* 18, 1527-1532, 2006.

[48] Chan, Y., et al. Blue semiconductor nanocrystal laser, *Appl. Phys. Lett.* 86, 073102 (1-3), 2005.

[49] Bhargava, R. N., et al. Optical properties of Manganese-doped nanocrystals of ZnS, *Phys. Rev. Lett.* 72 (3), 416-419, 1994.

[50] Liu, S.-M., et al. Surface states induced photoluminescence from Mn^{2+} doped CdS nanoparticles, *Sol. Stat. Commn.* 115, 615-618, 2000.

[51] Yang, H., Syntheses and applications of Mn-doped II-VI semiconductor nanocrystals, *J. Nanosci. Nanotech.* 5 (9), 1364-1375, 2005.

[52] Khosravi, A. A. et al. Green luminescence from copper doped zinc sulphide quantum particles, *Appl. Phys. Lett.* 67 (18), 2702-2704, 1995.

[53] Qu, S. C., et al. Photoluminescence properties of Eu^{3+}-doped ZnS nanocrystals prepared in a water/methanol solution, *Appl. Phys. Lett.* 80 (19), 3605-3607, 2002.

[54] Hu, H., & Zhang, W. Synthesis and properties of transition metals and rare-earth metals doped ZnS nanoparticles, *Opt. Mat.* 28 (5), 536-550, 2006.

[55] Schmidt, T., et al. Activation of 1.54 μm Er^{3+} fluorescence in concentrated II-VI semiconductor cluster environments, *Chem. Mater.* 10, 65-71, 1998.

[56] Jie, J. et al. One-dimensional II-VI nanostructures: Synthesis, properties and optoelectronic applications, *Nano Today* 5, 313-336, 2010.

[57] Liu, C. et al. Synthesis of high quality *n*-type CdSe nanobelts and their applications in nanodevices, *J. Phys. Chem. C* 113, 14478-14481, 2009.

[58] Meng, Q. F., et al. Ohmic contacts and photoconductivity of individual ZnTe nanowires, *Appl. Phys. Lett.* 94, 043111 (1-3), 2009.

[59] Zhang, X., et al. Surface induced negative photoconductivity in p-type ZnSe : Bi nanowires and their nano-optoelectronic applications, *J. Mater. Chem.* 21, 6736-6741, 2011.

[60] Park, W. I., et al. Schottky nanocontacts on ZnO nanorod arrays, *Appl. Phys. Lett.* 82 (24), 4358-4360, 2003.

[61] Liu, X., et al. Synthesis and electronic transport studies of CdO nanoneedles, *Appl. Phys. Lett.* 82 (12), 1950-1952, 2003.

[62] Salfi, J., et al. Electrical properties of Ohmic contacts to ZnSe nanowires and their application to nanowire-based photodetection, *Appl. Phys. Lett.* 89, 261112 (1-3), 2006.

[63] Sze, S. M. & Ng, K. K. *Physics of semiconductor devices*, Wiley-India, Delhi, 2010.

[64] Jie, J. S., et al. Single-crystal CdSe nanoribbon field-effect transistors and photoelectric applications, *Appl. Phys. Lett.* 89, 133118 (1-3), 2006.

[65] Chen, Z.-G., et al. Silicon-induced oriented ZnS nanobelts for hydrogen sensitivity, *Nanotechnology* 19, 055710 (1-5), 2008.

[66] Liu, Y. G., et al. Room-temperature oxygen sensitivity of ZnS nanobelts, *Appl. Phys. Lett.* 90, 042109 (1-3), 2007.

[67] Guo, Z. et al. Highly porous CdO nanowires: preparation based on hydroxy- and carbonate-containing cadmium compound precursor nanowires, gas sensing and optical properties, *Nanotechnology* 19, 245611 (1-8), 2008.

[68] Nazzal, A. Y., et al. Photoactivated CdSe nanocrystals as nanosensors for gases, *Nano Lett.* 3 (6), 819-822, 2003.

[69] Wan, Q., et al. Fabrication and ethanol sensing characteristics of ZnO nanowire gas sensors, *Appl. Phys. Lett.* 84 (18), 3654-3656, 2004.

[70] Wang, Z. L., Zinc oxide nanostructures: growth, properties and applications, *J. Phys.: Condens. Matter* 16, R829–R858, 2004.

[71] Mohanta, D. *Synthesis of semiconductor quantum dots on polymer matrix and application in nonlinear optics/electronics,* Ph. D. Thesis, Tezpur University, India, 2003.

[72] Das, U. *Development of binary semiconductor elongated nanopatterns by energetic ion irradiation/photon illumination for optoelectronics/photonics applications,* Ph. D. Thesis, Tezpur University, India, 2010.

[73] Das, U., & Mohanta, D. Evolution of ZnO nanoparticles and nanorods: aspect ratio dependent optoelectronic properties, *Eur. Phys. J. Appl. Phys.* 53, 10602 (p1-p5), 2011.

[74] Ge, M.Y., et al. Nanostructured ZnO: From monodisperse nanoparticles to nanorods, *J. Cryst. Grow.* 305, 162-166, 2007.

[75] Wang, Z. L. Nanostructures of zinc oxide, *Mater. Today* 7, 26-33, 2004.

[76] Yi, G.-C., et al. ZnO nanorods: synthesis, characterization and applications, *Semicond. Sci. Technol.* 20, S22-S34, 2005.

[77] Pan, Z. W., et al. Nanobelts of semiconducting oxides, *Science* 291, 1947-1949, 2001.

[78] Kong, X. Y. & Wang, Z. L. Spontaneous polarization-induced nanohelixes, nanosprings, and nanorings of piezoelectric nanobelts, *Nano Lett.* 3 (12), 1625-1631, 2003.

[79] Kong, X. Y. & Wang, Z. L. Polar-surface dominated ZnO nanobelts and the electrostatic energy induced nanohelixes, nanosprings, and nanospirals, *Appl. Phys. Lett.* 84 (6), 975-977, 2004.

[80] Wang, Z. L., et al. Induced growth of asymmetric nanocantilever arrays on polar surfaces, *Phys. Rev. Lett.* 91 (18), 185502 (1-4), 2003.

[81] Xu, C., et al. Fabrication and photoluminescence of zinc silicate/silica modulated ZnO nanowires, *Nanotechnology* 16, 2808-2812, 2005.

[82] Krishnan, D., & Pradeep, T. Precursor-controlled synthesis of hierarchical ZnO nanostructures, using oligoaniline-coated Au nanoparticle seeds, *J. Cryst. Grow.* 311, 3889-3897, 2009.

[83] Baruah, S. & Dutta, J. Hydrothermal growth of ZnO nanostructures, *Sci. Technol. Adv. Mater.* 10, 013001 (1-18), 2009.

[84] Lao, J. Y., et. al. Hierarchical ZnO nanostructures, *Nano Lett.* 2 (11), 1287-1291, 2002.

[85] Kittel, C. *Introduction to solid state physics*, Wiley-India, Delhi, 2008.

[86] Tam, K. H., et al. Defects in ZnO nanorods prepared by a hydrothermal method, *J. Phys. Chem. B* 110, 20865-20871, 2006.

[87] Vanheusden, K., et al. Mechanisms behind green photoluminescence in ZnO phosphor powders, *J. Appl. Phys.* 79 (10), 7983-7990, 1996.

[88] Ye, J. D., et al. Correlation between green luminescence and morphology evolution of ZnO films, *Appl. Phys. A* 81, 759-762, 2005.

[89] Zhao, Q. X., et al. Deep-level emissions influenced by O and Zn implantations in ZnO, *Appl. Phys. Lett.* 87, 211912 (1-3), 2005.

[90] Lin, B. et al. Green luminescent center in undoped zinc oxide films deposited on silicon substrates, *Appl. Phys. Lett.* 79 (7), 943-945, 2001.

[91] Cheng, B., et al. Synthesis of variable-aspect-ratio, single-crystalline ZnO nanostructures, *Inorg. Chem.* 45, 1208-1214, 2006.

[92] Das, U., & Mohanta, D. Evolution of ZnO nanoparticles and nanorods: aspect ratio dependent optoelectronic properties, *Eur. Phys. J. Appl. Phys.* 53, 10602 (1-5), 2011.

[93] Ge, M.Y., et al. Nanostructured ZnO: From monodisperse nanoparticles to nanorods, *J. Cryst. Grow.* 305, 162-166, 2007.

[94] Liu, X., et al. Growth mechanism and properties of ZnO nanorods synthesized by plasma-enhanced chemical vapor deposition, *J. Appl. Phys.* 95, 3141-3147, 2004.

[95] Hsu, J. W. P., et al. Luminescent properties of solution-grown ZnO nanorods, *Appl. Phys. Lett.* 88, 252103 (1-3), 2006.

[96] Mishra, Y. K. et al. Controlled growth of gold nanoparticles induced by ion irradiation: An in situ x-ray diffraction study, *Appl. Phys. Lett.* 90, 073110 (1-3), 2007.

[97] Giulian, R. et al. Shape transformation of Sn nanocrystals induced by swift heavy-ion irradiation and the necessity of a molten ion track, *Phys. Rev. B* 82, 113410 (1-4), 2010.

[98] Lian, J. et al. Simultaneous formation of surface ripples and metallic nanodots induced by phase decomposition and focused ion beam patterning, *Appl. Phys. Lett.* 88, 093112 (1-3), 2006.

[99] Kucheyev, S. O., et al. Ion-beam-produced structural defects in ZnO, *Phys. Rev. B* 67, 094115 (1-11), 2003.

[100] Chattopadhyay, S., et al. Interplay of defects in 1.2 MeV Ar irradiated ZnO, *J. Appl. Phys.* 107, 113516 (1-8), 2010.

[101] Bayan, S., et al. Development of Tb-doped ZnO nanorods: Effect of nitrogen ion irradiation on luminescence and structural evolution, *Phys. Stat. Sol. A.* 207 (8), 1859-1863, 2010.

[102] Wang, Y. S., et al. Optical properties of ZnO nanocrystals doped with Cd, Mg, Mn, and Fe ions, *J. Phys. Chem. B*, 110 (43), 21412-21415, 2006.

[103] Bhargava, R. N., et al. Quantum confined atoms of doped ZnO nanocrystals, *Phys. Stat. Sol. B* 229 (2), 897-901, 2002.

[104] Peres, M. et. al. Optical studies of ZnO nanocrystals doped with Eu^{3+} ions, *Appl. Phys. A* 88, 129-133, 2007.

[105] Park, S.-H., et al. Structural Properties of Nitrogen-Ion Implanted ZnO Nanorods, *J. Kor. Phys. Soc.* 50 (5), 1557-1560, 2007.

[106] Sun, X. W., et al. Ultraviolet emission from a ZnO rod homojunction light-emitting diode, *Appl. Phys. Lett.* 95, 133124(1-3), 2009.

[107] Fang, X., et al. Phosphorus-doped p-type ZnO nanorods and ZnO nanorod p-n homojunction LED fabricated by hydrothermal method, *J. Phys. Chem. C* 113 (50), 21208-21212, 2009.

[108] Huang, M. H., et al. Room-temperature ultraviolet nanowire nanolasers, *Science* 292, 1897-1899, 2001.

[109] Li, Y. B. et al. ZnO nanobelts grown on Si substrate, *Appl. Phys. Lett.* 81 (1), 144-146, 2002.

[110] Bao, J., et al. Broadband ZnO Single-Nanowire Light-Emitting Diode, *Nano Lett.* 6 (8), 1719-1722, 2006.

[111] Park, W. I., & Yi, G.-C. Electroluminescence in n-ZnO nanorod arrays vertically grown on p-GaN, *Adv. Mater.* 16, 87-90, 2004.

[112] Hsu, N. E., et al. Origin of defect emission identified by polarized luminescence from aligned ZnO nanorods, *J. Appl. Phys.* 96 (8), 4671-4673, 2004.

[113] Guida, G., et. al. An introduction to photonic band gap (PBG) materials, *Prog. Electromagn. Res.* 41, 1-20, 2003.

[114] Seelig, E. W., et al. Self-assembled 3D photonic crystals from ZnO colloidal spheres, *Mat. Chem. Phys.* 80 (1), 257-263, 2003.

[115] Ma, X., et al. Fabrication of silica/zinc oxide core-shell colloidal photonic crystals, *Appl. Phys. B* 88, 245-248, 2007.

[116] S.M. Abrarov, Sh.U. Yuldashev, S.B. Lee, T.W. Kang, Suppression of the green photoluminescence band in ZnO embedded into porous opal by spray pyrolysis, *J. Luminesc.* 109 (2004) 25–29.

[117] Han, J. et al. Embedment of ZnO nanoparticles in the natural photonic crystals within peacock feathers, *Nanotechnology* 19, 365602 (1-6), 2008.

[118] Wen, L. et al. Fabrication and characterization of well-aligned, high density ZnO nanowire arrays and their realizations in Schottky device applications using a two-step approach, *J. Mater. Chem.* 21, 7090-7097, 2011.

[119] Park, W. I. et al. Schottky nanocontacts on ZnO nanorod arrays, *Appl. Phys. Lett.* 82 (24), 4358-4360, 2003.

[120] Das, S. N., et al. Junction properties of Au/ZnO single nanowire Schottky diode, *Appl. Phys. Lett.* 96, 092111(1-3), 2010.

[121] Harnack, O., et al. Rectifying behavior of electrically aligned ZnO nanorods, *Nano Lett.* 3 (8), 1097-1101, 2003.

[122] Li, Y., et al. Bascule nanobridges self-assembled with ZnO nanowires as double Schottky barrier UV switches, *Nanotechnology* 21, 295502 (1-7), 2010.

[123] Hasan, K. ul et al. Single nanowire-based UV photodetectors for fast switching" *Nanoscale Res. Lett.* 6, 348 (1-6), 2011.

[124] Ji, L. W., et al. Ultraviolet photodetectors based on selectively grown ZnO nanorod arrays. *Appl. Phys. Lett.* 94, 203106 (1-3), 2009.

[125] Jin, Y., et al. Solution-processed ultraviolet photodetectors based on colloidal ZnO nanoparticles, *Nano Lett.* 8 (6), 1649-1653, 2008.

[126] Huang, K., & Zhang, Q. Giant persistent photoconductivity of the WO_3 nanowires in vacuum condition, *Nanoscale Res Lett.* 6, 52 (1-5), 2011.

[127] Nayak, J. et al. Persistent photoconductivity in ZnO nanorods deposited on electro-deposited seed layers of ZnO, *J. Phys.: Condens. Matter* 20, 195222 (1-5), 2008.

[128] Banerjee, D., et al. Enhanced field emission of ZnO nanowires, *Adv. Mat.* 16, 2028-2032, 2004.

[129] Qian, X., et al. Effect of aspect ratio on field emission properties of ZnO nanorod arrays, *Nanoscale Res Lett.* 3, 303-307, 2008.

[130] Zhu, Y. W., et al. Efficient field emission from ZnO nanoneedle arrays, *Appl. Phys. Lett.* 83 (1), 144-146, 2003.

[131] Lukas S.-M. & Judith L. M.-D. ZnO-nanostructures, defects, and devices, *Mater. Today* 10 (5), 40-48, 2007.

[132] Fan, Z. et al. ZnO nanowire field-effect transistor and oxygen sensing property, *Appl. Phys. Lett.* 85 (24), 5923-5925, 2004.

[133] Sadek, A. Z. et al. Characterization of ZnO nanobelt-based gas sensor for H_2, NO_2, and hydrocarbon sensing, *IEEE Sensors* J. 7 (6), 919-924, 2007.

[134] Umar, A. et al. Rapid synthesis and dye-sensitized solar cell applications of hexagonal-shaped ZnO nanorods, *Electrochimica Acta* 54, 5358-5362, 2009.

Chapter 2

Fabrication of ZnO nanostructures and their structural evolution

A breathtaking number of articles on the fabrication of nanostructured materials have been published in the past few years. However, from the application point of view the large scale production and stability of the nanomaterials are the key factors that decide the superiority of a synthesis method. A quality synthesis method should be supported by an appreciable growth mechanism with controllable kinetic and thermodynamic foundation. The knowledge of the growth mechanism is an important aspect to achieve nanomaterials having variation in morphology and size. The present chapter focuses on the different fabrication strategies adopted to fabricate undoped and doped ZnO nanostructures, along with their structural and morphological evolutions.

2.1 Fabrication principle and microstructural characterization

Spherical and elongated ZnO nanostructures of different structural organization have been synthesized using different physicochemical methods with bottom up approach using chemical reagents of analytical grade. The morphological features of the as synthesized nanostructures were studied through low and high resolution transmission electron microscope (TEM: JEOL JSM-100 CX and HRTEM: JEM-2100 and FEI, Tecnai S-twin) working at variable accelerating voltage of electrons (80 kV for TEM and 60-200 kV for HRTEM), Scanning electron microscopy (SEM, JEOL JSM 6390 LV). Whereas, the structural analysis were carried out using a Miniflex X-ray diffractometer (XRD, Rigaku D/max-2000) employing Cu K_α line (λ = 1.54 Å). The elemental analyses were obtained from the Energy dispersive X-ray spectroscopy (EDS) attached to the SEM.

2.1.1 Solid state mixing

The method of solid state mixing involves the reaction among the reagents in absence of any solvent. In such methods, often the interaction among the reactant materials takes place in solid state but in a molten phase. ZnO nanostructures were synthesized using an inexpensive solid state grinding method in presence of

cetyltrimethylammonium bromide (CTAB, $(C_{16}H_{33})N(CH_3)_3Br$) – a cationic surfactant. CTAB is a salt of centrimonium (cetyltrimethyl) which is a quaternary ammonium cation (Appendix 2) and is widely used for providing buffer solution for DNA extraction and nano-material synthesis [1-3]. The molecular structure of CTAB is shown in Figure 2.1. CTAB assisted grinding with variable concentration has led to the formation of ZnO nanostructures with desired morphology which are discussed as below.

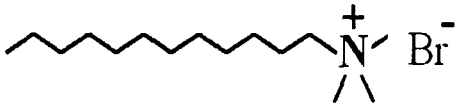

Figure 2.1: The structure of CTAB.

(a) *Fabrication of ZnO nanoparticles*: In a single step solid state process, a mixture of zinc acetate dihydrate (ZAD), CTAB, and sodium hydroxide (NaOH) flakes with a molar ratio of 1:0.3:2 were ground together in an agate mortar for ~ 45 min at room temperature (300 K). The unidirectional soft grinding was accompanied by abrupt decomposition of the reactants followed by heat release while the reaction was in progress. For the sake of purification, the product was then mixed with deionised water and was subjected to ultrasonication bath for 1 h. The sonicated mixture was then washed repeatedly with deionised water and ethanol to remove any undesired species. Finally it was dried in air (at ~ 70 ^{0}C) for 2 h to yield a powder product which was preserved in sealed sample bottles for further experiments.

The visible evidence of the formation of the nanoparticles can be observed in the TEM and HRTEM micrographs as shown in Figure 2.2(a,b). As evident from Figure 2.2(a), the nanoparticles are uniformly distributed in isolation from each other without clustering. The size distribution of the nanoparticles was extracted from the corresponding TEM image and is depicted in the inset. The average size of the nanoparticles was found to be ~ 12 nm. The enlarged view of an isolated nanoparticle can be obtained from the HRTEM image, shown in Figure 2.2(b). The lattice fringes due to the crystalline planes of ZnO are clearly visible in the

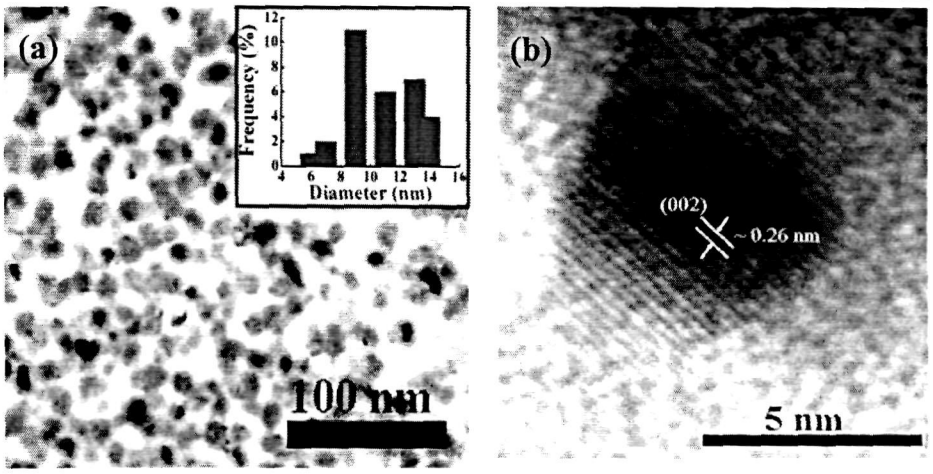

Figure 2.2: (a) TEM image of the ZnO nanoparticles, and (b) HRTEM image of an isolated ZnO nanoparticle.

HRTEM image. As estimated the lattice spacing of ~ 0.26 nm corresponded to the interplanar separation between constructive (002) planes of ZnO [4].

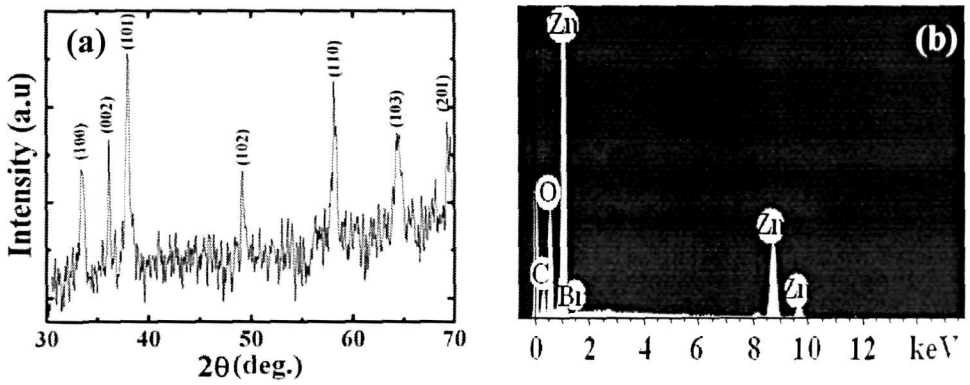

Figure 2.3: (a) XRD pattern, and (b) EDS spectrum of the ZnO nanoparticles.

The structural information of the ZnO nanoparticles can be obtained from the XRD pattern as shown in Figure 2.3(a). The diffraction peaks corresponding to several crystalline planes reveal the formation of hexagonal wurtzite phase of ZnO in accordance with the JCPDS 36-1451 [4]. No extra peak related to other byproducts or $Zn(OH)_2$ was detected. The lattice parameter (a and c) of the hexagonal lattice structure of ZnO was calculated using the formula

$$\frac{1}{d^2} = \frac{4}{3}\left(\frac{h^2 + hk + k^2}{a^2}\right) + \frac{l^2}{c^2} \qquad (1.1)$$

where, d is the interplaner distance and (hkl) being the miller indices. The lattice parameters were found to be a = 3.17 Å and c = 4.98 Å, with c/a ratio ~ 1.57. It can be noted that the lattice parameters of the ZnO nanoparticles vary from the standard values of a = 3.25 Å and c = 5.21 Å (form JCPDS 36-1451), while the c/a ratio of the nanoparticles deviates from that of the ideal value of 1.63 for a hexagonal unit cell [5]. Such deviation of the lattice parameters and the c/a ratio of the unit cell, indicates the presence of various point defects within the crystal of the ZnO nanoparticles [6]. In the XRD pattern, the presence of various crystal planes at different orientations reveals the polycrystalline nature of the nanoparticles. The polycrystalline solids are composed of large number of crystallites (or small single crystals) of different size and orientation and the average crystallite size can be determined using the Debye-Scherrer formula [7, 8]. According to the Debye-Scherrer, the average crystallite size (D) can be given by

$$D = \frac{0.9\lambda}{\beta Cos\theta} \tag{1.2}$$

where λ is the x-ray wavelength, β is full width at half maximum of the most prominent peak and θ being the Bragg angle. Considering the most prominent (101) peak, the average crystallite size of the ZnO nanoparticles was found to be ~ 11 nm. The elemental constitution was ensured from the EDS spectra (Figure 2.3(b)). The presence of Zn and O was detected along with a small trace of Br. A weak signal corresponding to Br might have arisen from the CTAB compound used during the synthesis of the nanoparticles.

(b) *Fabrication of ZnO nanorods*: In Chapter 1, it was mentioned that the reactant concentration has a pronounced effect on the morphology of the nanostructures. In this regard, rod like structure of ZnO was obtained using the same solid state approach but with a different precursor ratio (ZAD, CTAB and NaOH in molar ratio of 1:0.5:3) [9].

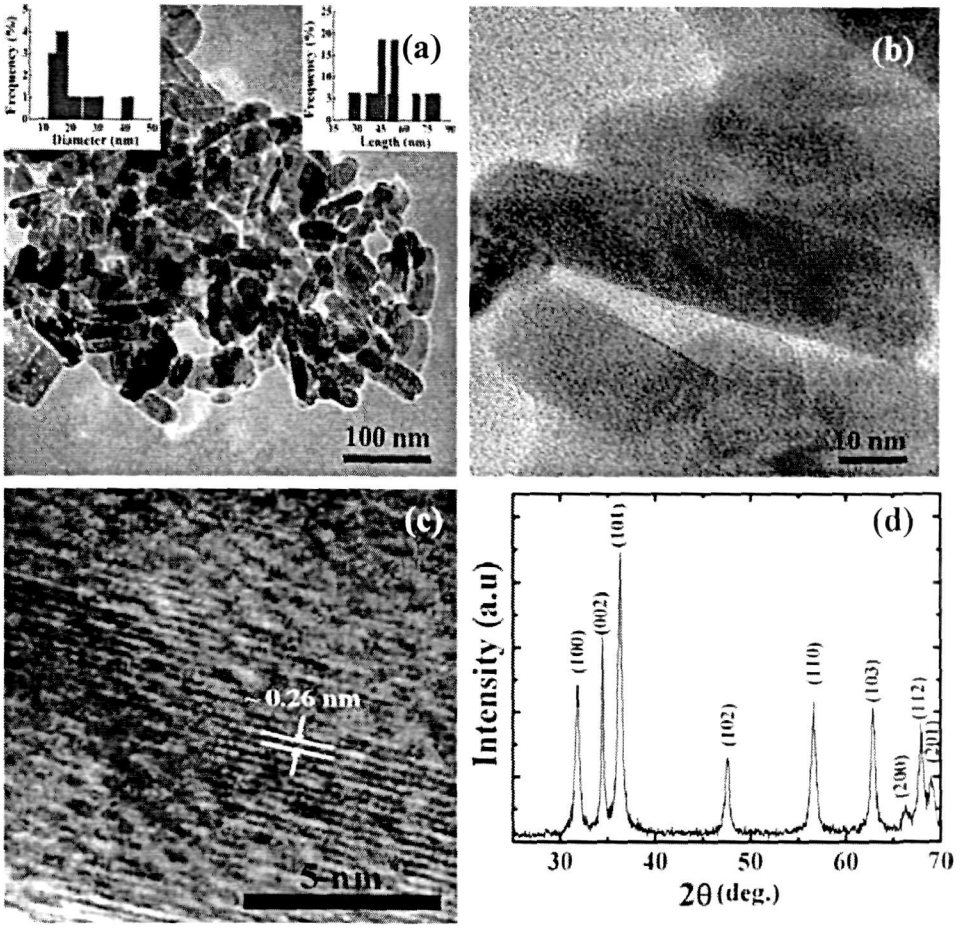

Figure 2.4: (a,b) Assembly of nanorods, (c) higher magnified image of a nanorod, and (d) XRD pattern of the nanorods. Insets of (a) depict the dimension distribution of the nanorods.

The HRTEM image as shown in Figure 2.4(a,b), reveal the formation of fully developed ZnO nanorods. The distribution of length and diameter of the nanorods found from the TEM image was plotted as shown in the inset of Figure 2.4(a). The average length of the nanorods was estimated to be ~ 50 nm, with a standard deviation of ~ 15 nm. While, the average diameter was found to be ~ 21 nm. The lattice spacing of an individual nanorod (Figure 2.4(c)) is found to be ~ 0.26 nm and corresponds to the interplanar separation between the (002) planes of ZnO. The formation of hexagonal wurtzite structure of ZnO with preferred orientation along (101) plane was confirmed from the XRD pattern of the nanorods (Figure

2.4(d)). The lattice parameters related to the ZnO unit cells were found to be a = 3.25 Å and c = 5.21 Å, with c/a ratio ~ 1.6, which is close to the ideal value (1.63). Again, using the Debye-Scherrer formula, the average crystallite size (D) of the nanorods was found to be ~ 13.26 nm.

The observed oblate or rod like structures of ZnO with the increase in CTAB-to-ZAD ratio is consistent with the earlier report [10]. It is expected that the decomposition of ZAD and NaOH under constant grinding will result in the formation of $Zn(OH)_2$ as given below

$$Zn^{2+} + 2\ OH^- \leftrightarrow Zn(OH)_2 \qquad (1.3)$$

As the grinding process is in progress, temperature rises and a fraction of $Zn(OH)_2$ dissociates to give rise to ZnO nuclei, while the remaining parts yield $[Zn(OH)_4]^{2-}$ ions as per following equations [4].

$$Zn(OH)_2 \rightarrow Zn^{2+} + 2\ OH^- \qquad (1.4)$$

$$Zn^{2+} + 2\ OH^- \leftrightarrow ZnO + H_2O \qquad (1.5)$$

$$Zn(OH)_2 + 2\ OH^- \leftrightarrow [Zn(OH)_4]^{2-} \qquad (1.6)$$

Again, owing to the Coulomb attractive force, the CTA^+ ions formed from the decomposition of CTAB, would get attached to the $[Zn(OH)_4]^{2-}$ ions to form complex agents which would act as the growth units. The adsorption of the complex agents on the circumference of the ZnO nuclei opens up the active sites for particle growth along [0001] direction [4, 11]. It is evident that in the presence of sufficient number of growth units, the unidirectional grinding would result in the evolution of rod like structures of ZnO, as demonstrated schematically in Figure 2.5(a). As shown in the magnified view of the TEM image of the nanorods (Figure 2.4(b)), it can be observed that the extreme end of the nanorods resembles a *hemispherical* shape. It is known that a crystal plane having higher growth rate disappears quickly [4]. In the present case, since the growth of the nanorods takes place along [0001] direction, the (001) plane disappears and leads to the formation of the *hemispherical* shape at the extreme end. On the other hand, the lower concentration of CTAB will result in the formation of smaller number of growth units. In such a situation the unidirectional growth process along [0001]

direction is restricted and hence results in the evolution of spherical shaped nanostructures.

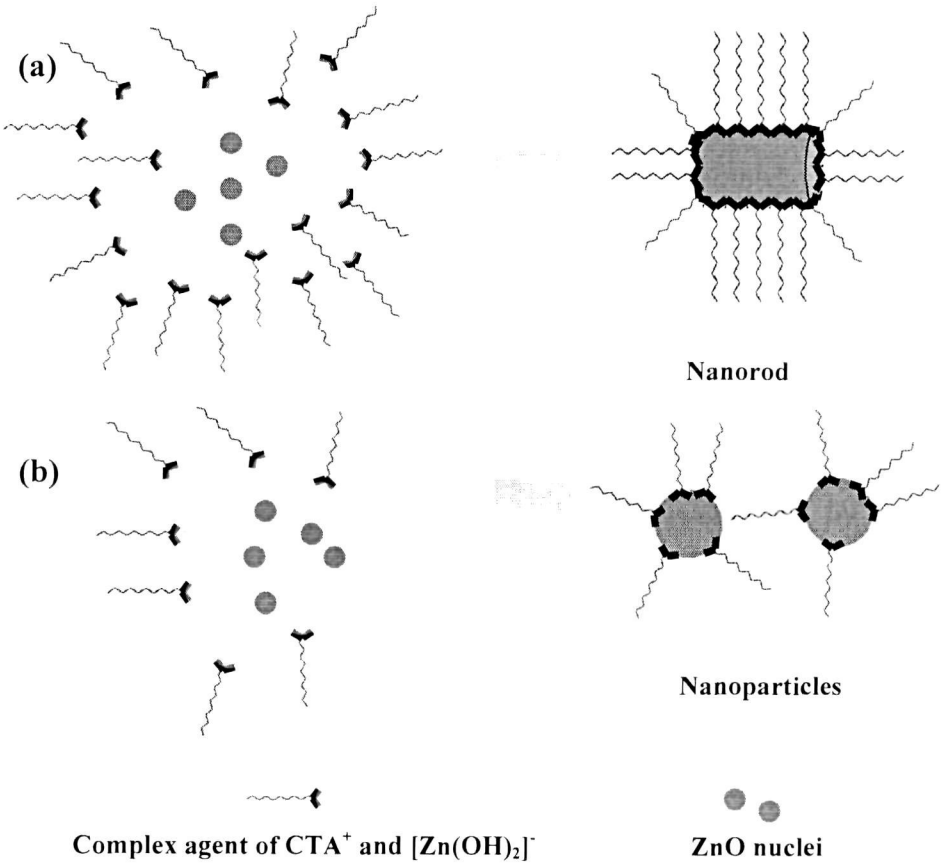

Figure 2.5: Surfactant mediated growth mechanism of (a) nanorod, and (b) nanoparticle systems.

2.1.2 Microemulsion route

Synthesis of nanomaterials using microemulsion routes is a popular technique among chemical physicists and material scientists [12, 13]. Microemulsions are thermodynamically stable isotropic dispersions of aqueous mixture comprising of hydrocarbon liquids (oil), water and surfactant. The different shapes of the micelles (spherical, cylindrical etc) act as the templates for nanostructure growth thus facilitating the development of nanoparticles, nanorods etc. In the present study, CTAB assisted ZnO nanorods have been synthesized using the microemulsion route according to the literature [14]. 30 mL *n*-hexane, 0.5 M

CTAB and 10 mL *n*-butanol (co-surfactant) were mixed and stirred (~ 200 rpm) for about ½ h which has resulted in a homogeneous mixture. The mixture was then divided into two equal and identical parts. An aqueous solution of zinc chloride ($ZnCl_2$) was added to one part, while aqueous solution of sodium hydroxide (NaOH) was added to the other part. Thus two separate microemulsions were obtained where the aqueous phase was encapsulated within the reverse micelles formed by the surfactant and co-surfactant in hexane. One microemulsion contained Zn^{2+} ions, whereas the other contained OH^- ions. Finally, upon mixing the two precursors steadily, continuous stirring was allowed for 8 h. As the two microemulsions were mixed, the growth of ZnO took place in the aqueous phase encapsulated within the reverse cylindrical micelles (as discussed in Chapter 1). The obtained product was subjected to centrifugation, ultrasonication and annealing in air (~ 80 °C) sequentially to yield the elongated ZnO nanostructures in the form of powder.

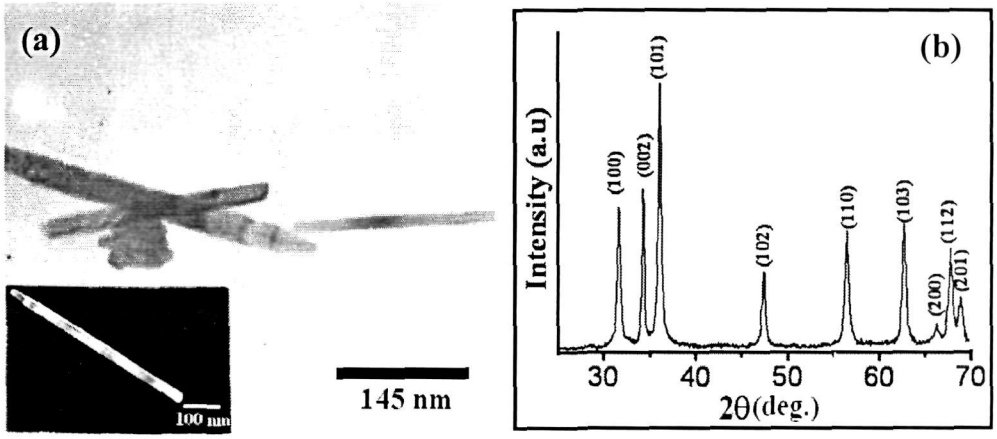

Figure 2.6: (a) TEM image, and (b) XRD pattern of the ZnO nanorods.

Figure 2.6(a) shows the TEM image of the elongated nanostructures of ZnO with figure inset depicting an isolated nanorod. The nanoscale rods resembling polished stick like structures having diameter and lengths within 20–30 nm and 175–200 nm, respectively. Like previous cases, the XRD pattern of these nanosticks (Figure 2.6(b)) corresponds to the hexagonal wurtzite phase of ZnO

with preferred orientation along (101) plane in agreement with the JCPDS data. The lattice parameters were found to be a = 3.25 Å and c = 5.23 Å, (c/a ratio ~ 1.61), while the average crystallite size was estimated to be ~ 16.54 nm.

2.1.3 Thermal annealing process

The fabrication of substrate assisted ZnO nanostructures via thermal annealing of polymer encapsulated hydroxides of zinc has been found to be an effective method to produce quality nanostructures. The role of polymers in the fabrication of nanostructures was illustrated in the Chapter 1. In this context, polyvinyl alcohol (PVA) was used as the host polymer matrix in the thermal annealing process of nanostructure fabrication (Appendix 2). PVA is a well known polymer whose coil like structure forms a cross-linking network template and suitable for providing nucleation sites. The chemical structure of PVA is shown in Figure 2.7. Though PVA is water soluble, it is almost insoluble in cold water. Upon the evaporation of water from any aqueous solution of PVA, a transparent film of PVA with high tensile strength is formed [15]. In the present fabrication technique, the annealing led decomposition of $Zn(OH)_2$ within PVA films facilitates the growth of undoped and europium (Eu^{3+}) doped elongated nanoscale structures of ZnO [16].

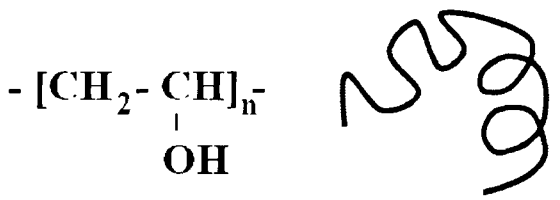

Figure 2.7: Chemical composition and coil like structure of PVA.

(a) *Fabrication of undoped ZnO nanostructures*: The fabrication process can be divided in two sections.

(i) Preparation of the substrates: Metallic aluminum (Al) was chosen as the substrates to support ZnO nanostructures. Commercially available Al substrates of size (~ 0.5 cm x 0.5 cm x 0.5 mm) were repeatedly washed with double distilled water and finally cleaned with ethanol and acetone in an ultrasonicator bath. In order to develop a thin insulating layer of Al_2O_3, the clean Al substrates were

immersed in dilute chromic acid solution at room temperature for several hours (6-8 h). The thin Al_2O_3 layer isolates the ZnO nanostructures from the metallic base, which is an important issue while studying any kind of electrical transport properties.

(ii) Preparation of the ZnO nanostructures: At first, 5% (wt/vol) PVA (degree of polymerization 1700–1800) was dissolved in double distilled water under constant stirring (~ 200 rpm) at a constant temperature of 70 °C for 1.5 h. The development of a transparent and viscous solution has indicated the formation of the active PVA matrix. Next, ZAD was added to the aqueous PVA solution under vigorous stirring, maintaining a weight ratio of ZAD to PVA as 1.5. Subsequently, an aqueous solution of NaOH was injected dropwise to the resulting solution under constant stirring. The dropwise addition of NaOH led to the variation in *p*H value of the mixture from 8.5 to 9 for different instances. The resulting precursor was then spin-casted on the cleaned Al_2O_3/Al substrates and was subjected for annealing in a constant air-flow muffle furnace for 1 h. The zone temperature of the muffle furnace was varied within 400-750 (± 5) °C for different occasions. The ZnO nanostructures in the form of solid films grown on the Al_2O_3/Al substrates were preserved in the desiccator for subsequent experimentation.

Figure 2.8(a) depicts a set of micrographs of the samples grown at 400 °C. The development of 1D ZnO nanostructures distributed over the substrate and forming a clear net-like organization is evident. In addition, the evolution of urchin like structures can be observed at several locations. Each of which is consisting of 1D nanopatterns pointing radially outward but originated from the same base. The urchin like structure of ZnO resembles to *Strongylocentrotus franciscanus* (commonly known as Red sea urchins, picture shown in Figure 2.8(b)) The formation of ZnO was confirmed from the EDS spectra (inset of Figure 2.8(c)) captured at the tip of a nanorod (labeled with the red cursor). The presence of Zn

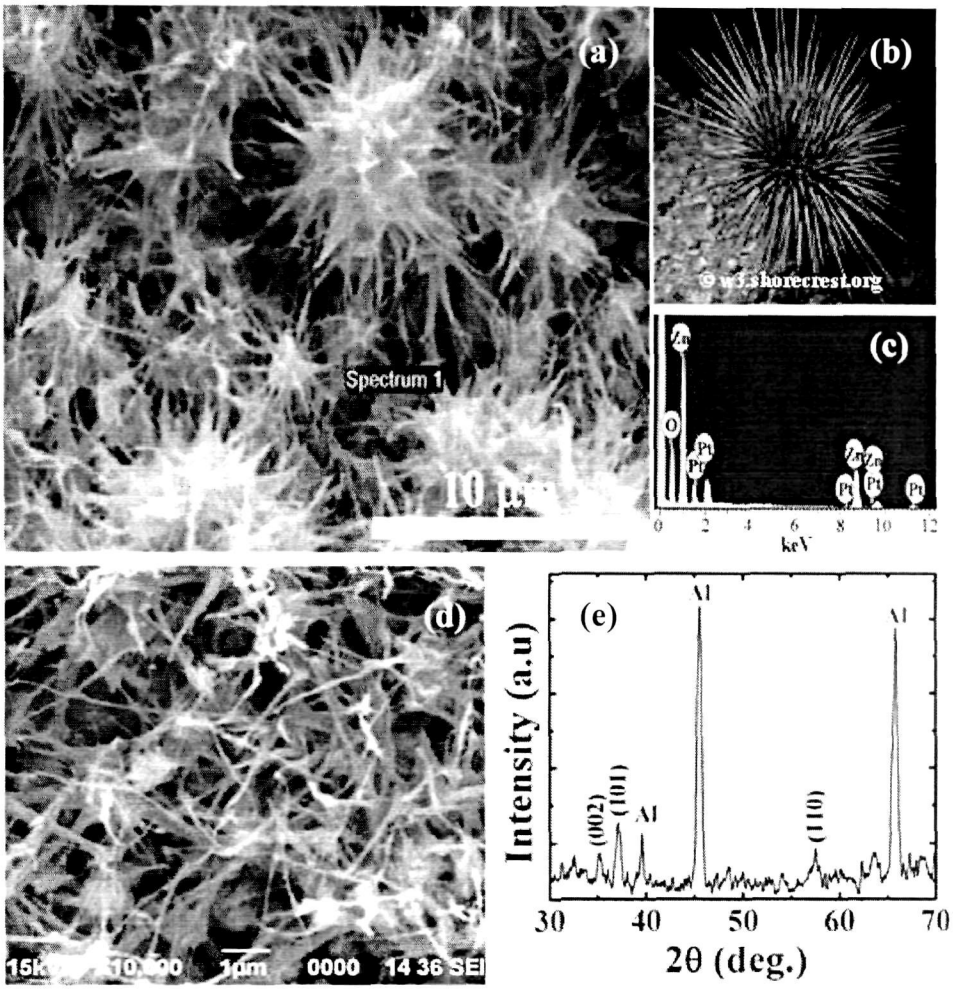

Figure 2.8: (a) SEM image of the nanostructures grown at 400 °C, (b) optical image of a sea urchin, (c) EDS spectra of the nanostructures, (d) SEM image of the samples at higher magnification, and (e) XRD pattern of the ZnO sample.

and O was clearly evident apart from a prominent peak of Pt that arises due to the surface coating of the specimen for imaging purpose. Also, Figure 2.8(d) shows a close look of the ZnO nanostructures with average diameter in the range of 70-90 nm. Note that no trace of the PVA can be found as it decomposes at a temperature of ~ 230 °C. The XRD pattern, as shown in Figure 2.8(e) reveals the hexagonal wurtzite phase of ZnO along with the characteristic planes of metallic Al. The lattice parameters were found to be a = 3.2 Å and c = 5.1 Å, giving rise to the c/a ratio ~ 1.6. On the other hand, using the Debye-Scherrer formula the average

crystallite size was calculated as 9.12 nm. No evidence of $Zn(OH)_2$ or some other byproduct was witnessed in the XRD pattern.

Adopting the same method, ZnO nanorods were fabricated on the Al_2O_3/Al substrates at a higher growth temperature of 750 °C. Figure 2.9(a,b), highlights the formation of ZnO nanorods having average diameter ~ 90 nm and length lies within 2-3 μm.

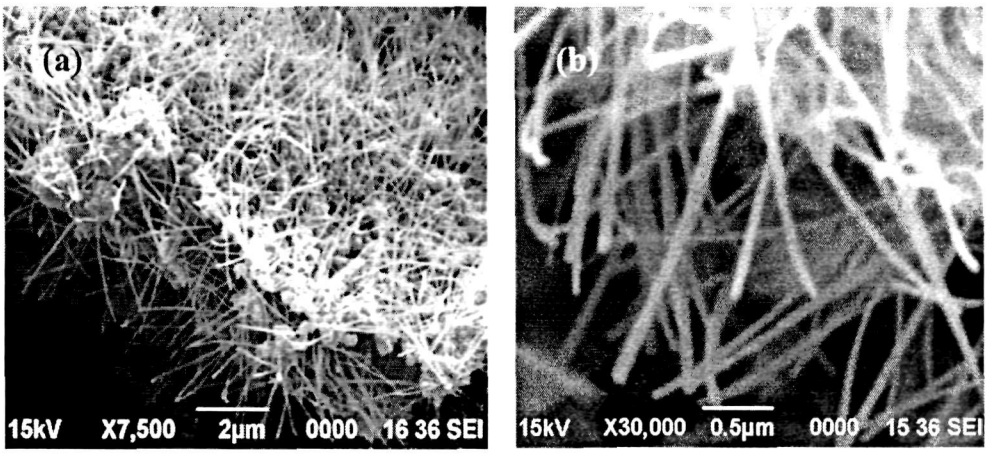

Figure 2.9: SEM image of the randomly oriented ZnO nanorods synthesized at 750 °C on (a) Low and (b) high magnification.

It can be noticed that the urchin like structures are rarely found in this case. As expected upon annealing at a relatively higher temperature (750 °C), the growth process of the nanorods becomes faster than the low temperature case and is accompanied by a rapid amorphisation of the Al-substrate [17]. As a result of amorphisation of the substrate, the base required for supporting urchin like structures is not formed and therefore, the nanorods are distributed randomly but independently over the substrate. As can be seen in the SEM image (Figure 2.9(a)), the surface of the Al substrate has become uneven owing to the annealing led amorphisation. Such unevenness of the substrate was not observed in the previous case.

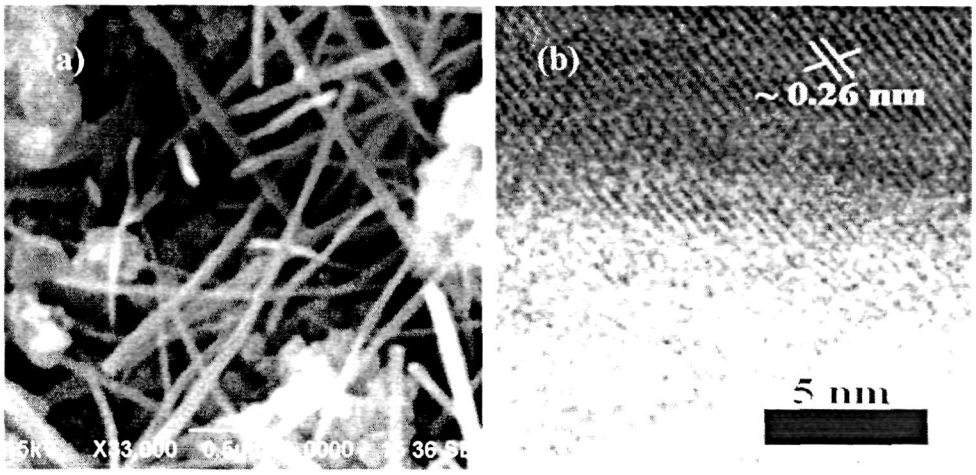

Figure 2.10: (a) SEM and (b) HRTEM image of ZnO nanorods synthesized at 450 °C.

The formation of randomly oriented nanorods (RON) of ZnO was also witnessed when the annealing was performed at ~ 450 °C. Figure 2.10 (a,b) shows the SEM and HRTEM images of ZnO nanorods synthesized at ~ 450 °C. Note that, no signature of urchin like structure was evident in the SEM image of the sample. In the HRTEM image (Figure 2.10(b)), the lattice fringes of the periodically arrayed crystal planes with an inter-planar spacing of ~ 0.26 nm corresponded to the (002) planes of ZnO.

(b) *Fabrication of Eu^{3+} doped ZnO nanostructures*: For the synthesis of the Eu^{3+} doped ZnO nanostructures, europium acetate [$(Eu(CH_3COO_3)_3$] and ZAD were mixed in a weight ratio of 0.04 and were transferred to the aqueous solution of PVA under constant stirring. Aqueous NaOH was added dropwise to the solution until the *p*H of the solution becomes 9. The resulting precursor was then spin casted onto clean Al substrates (1 cm x 2 cm x 300 μm) followed by annealing at 80 °C, 300 °C, and 650 °C for 30 min in a muffle furnace under constant air flow.

The sample annealed at 80 °C (Figure 2.11(a)) shows the development of spherical ZnO nanoparticles embedded in the PVA matrix, without any signature of clustering/agglomeration. As evident from the SEM image (Figure 2.11(a)), the average diameter of the nanoparticles was found to vary within ~ 120-200 nm

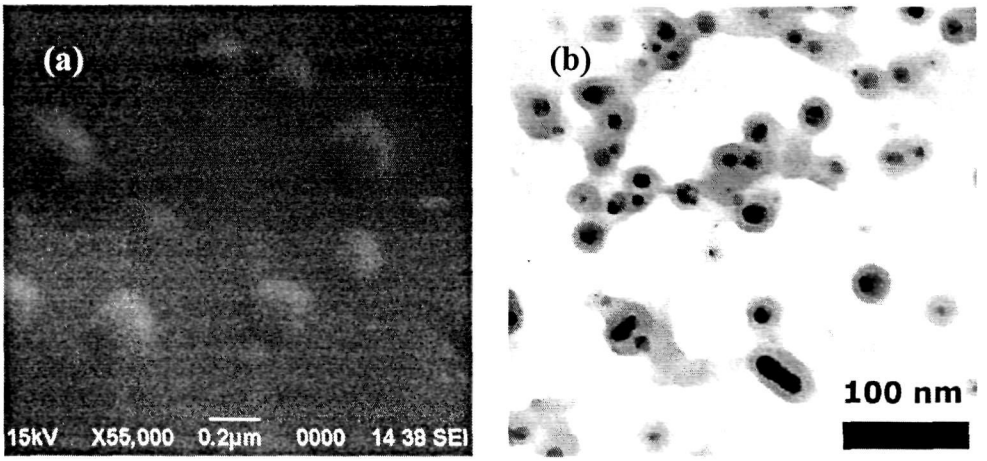

Figure 2.11: (a) SEM and (b) TEM image of the Eu^{3+} doped ZnO nanoparticles embedded in PVA matrix (annealing temperature 80 °C).

range. The PVA encapsulation over the nanoparticles can be clearly observed in the TEM image of the sample (Figure 2.11(b)). The size of the nanoparticles lies in 10-20 nm range. Consequently, the SEM and TEM observations of the sample suggest that the nanoparticles possess a wide range of size distribution.

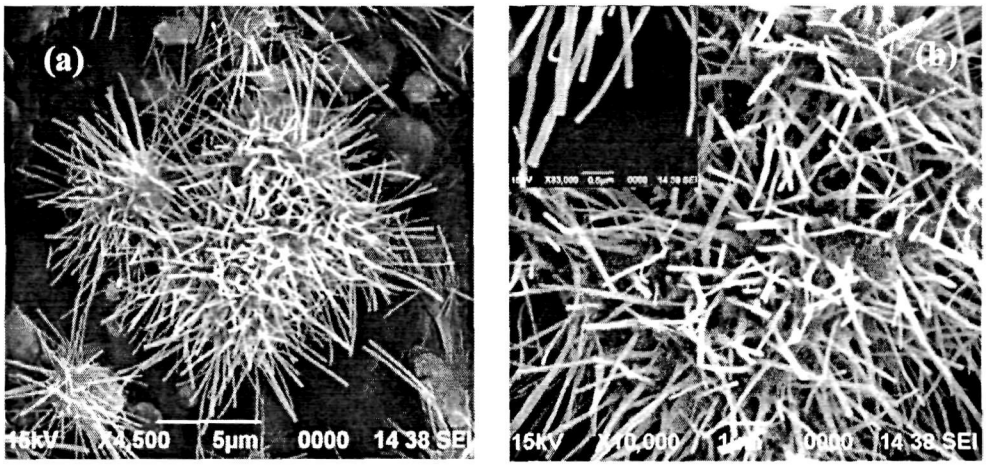

Figure 2.12 (a,b): SEM image of the Eu^{3+} doped ZnO nanorod based urchins (growth temperature 300 °C). Inset of (b) shows an enlarged view at higher magnification.

The sample annealed at a temperature of 300 °C, showed the growth of urchin-like nanostructures which are composed of a large number of independent nanorods, of different orientations but originated from the same base (Figure

2.12(a,b)). The average length and diameter of the nanorods are found to vary within 4-5 μm and 120-200 nm ranges, respectively. The inset of Figure 2.12(b) depicts the close view of the 1D nanostructures. The nanorods though originated from the same base, they are randomly oriented at diverse directions. Hence, the spacing between the nanorods increases as one moves from the core region to the outer region of the urchin like structures. Owing to the higher length compared to the diameter of the nanorods, it can be observed that most of the nanorods are partially bended (Figure 2.12(b)).

As expected, upon annealing the specimen at 650 °C, in addition to the growth of nanorods, more and more Al_2O_3 layer can not be formed which would not favor stable urchin-bases at large. Accordingly the nanorods are fallen randomly on the substrate and can be observed in Figure 2.13(a,b).

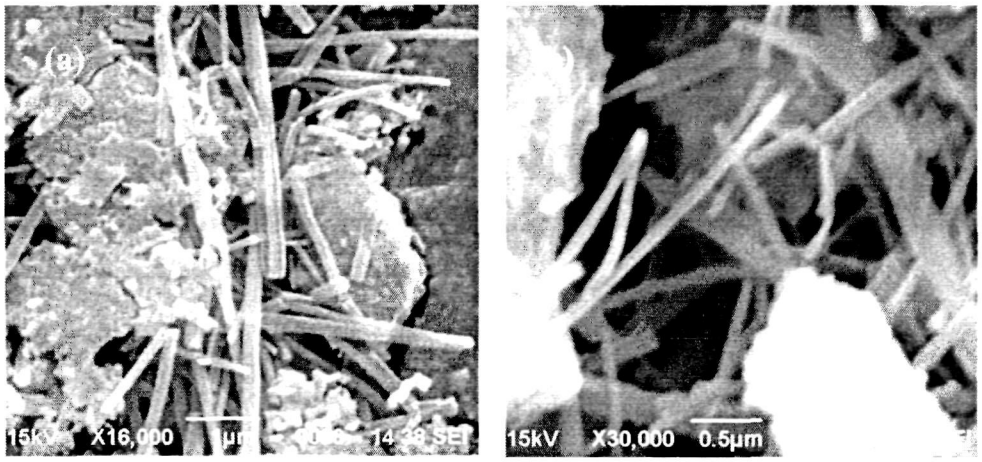

Figure 2.13 (a,b): SEM image of the Eu^{3+} doped ZnO nanorods (growth temperature 650 °C) captured at different locations.

The XRD patterns of the three Eu^{3+} doped ZnO samples are shown in Figure 2.14. The diffraction patterns are characterized by response of the hexagonal wurtzite structure of ZnO with preferred orientation along (101) plane (Figure 2.14(a,b)). No extra peak corresponding to the byproducts (e.g., Eu_2O_3, $Zn(OH)_2$ etc) was detected. A full-width half maxima (FWHM) analysis reveals that there is a decrease in FWHM of the (002) peak from 0.023 to 0.011 rad for the

nanoparticles and urchins, respectively. M. Y. Ge et al. have observed similar results where reflux time dependent growth of ZnO nanoparticles along [0001] direction has resulted in the formation of nanorods [18]. Accordingly, in this present study it can be inferred that upon annealing at 300 °C, the growth of the nanoparticles along the [0001] direction could result in the formation of the nanorods. In the XRD pattern of the urchins, the diffraction peaks due to metallic Al are apparently owing to the decomposition of PVA matrix. In this case a small peak observed at ~ 59° is ascribed to the formation of Al_2O_3. At 650 °C, the Al surface gets oxidized (forming Al_2O_3) and hence the diffraction planes of ZnO are not clearly distinguishable in the XRD pattern of the sample (Figure 2.14(c)). The presence of the amorphized debris is also evident from the SEM images discussed earlier.

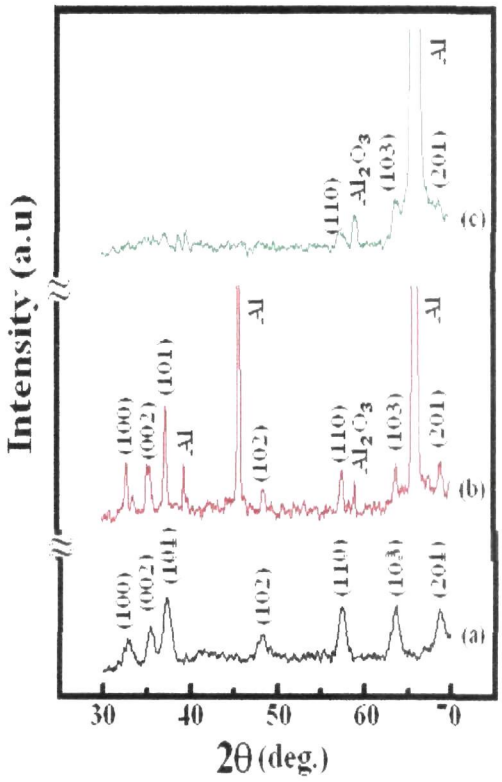

Figure 2.14: XRD patterns the Eu^{3+} doped ZnO samples synthesized at, (a) 80 °C, (b) 300 °C and (c) 650 °C.

The EDS spectra of the sample annealed at 300 °C gives information regarding compositional features as presented in Figure 2.15. The EDS spectrum was captured at a specific site of a single nanorod, labeled by cross. Apparently visible peaks due to

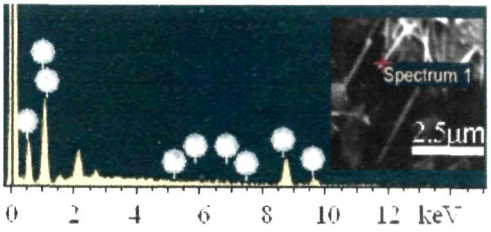

Figure 2.15: EDS spectra of the Eu^{3+} doped ZnO sample synthesized at 300 °C.

Zn, O, and Eu elements were detected in the spectra. Consequently, the presence of Eu^{3+} is ensured in the ZnO host.

(c) *Reaction mechanism in thermal annealing process*: It is very important to acquaint with the guiding principle and reaction mechanism that leads to various nanoscale structures discussed above. The chemical reactions involved during thermal annealing process are given below:

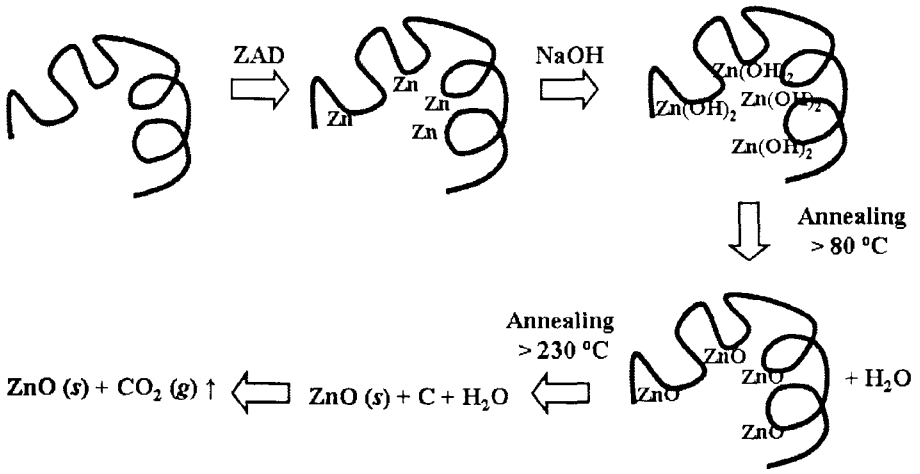

Now, it is evident that for both the undoped and Eu^{3+} doped ZnO nanosystems, the urchin like structures can be formed at moderate temperatures (below or around 400 °C). Above 400 °C, the annealing led amorphisation of the substrate destroys the base of the urchins. In the formation of urchin structures the distribution and arrangement of $Zn(OH)_2$ species in the PVA matrix play important roles. It is expected that the nanoparticles lying close to the surface of the Al-substrate act as seed or nucleation sites [19]. A temperature gradient can also be realized at the interface separating the substrate and the PVA film, due to substantial difference in thermal conductivities. This temperature gradient would enforce seed particle clustering as a result of creation of thermal hot spots. These hot-spots are believed to be the base of the urchins. Above the decomposition temperature of PVA, the unidirectional growth of the ZnO nanoparticles accompanied by transfer of atoms results in the formation of urchin like structures of ZnO [19]. The schematic representation of the whole process is shown in

Figure 2.16. Whereas, the nanorods/wires that grew without the support of the hot spots are located on the substrate.

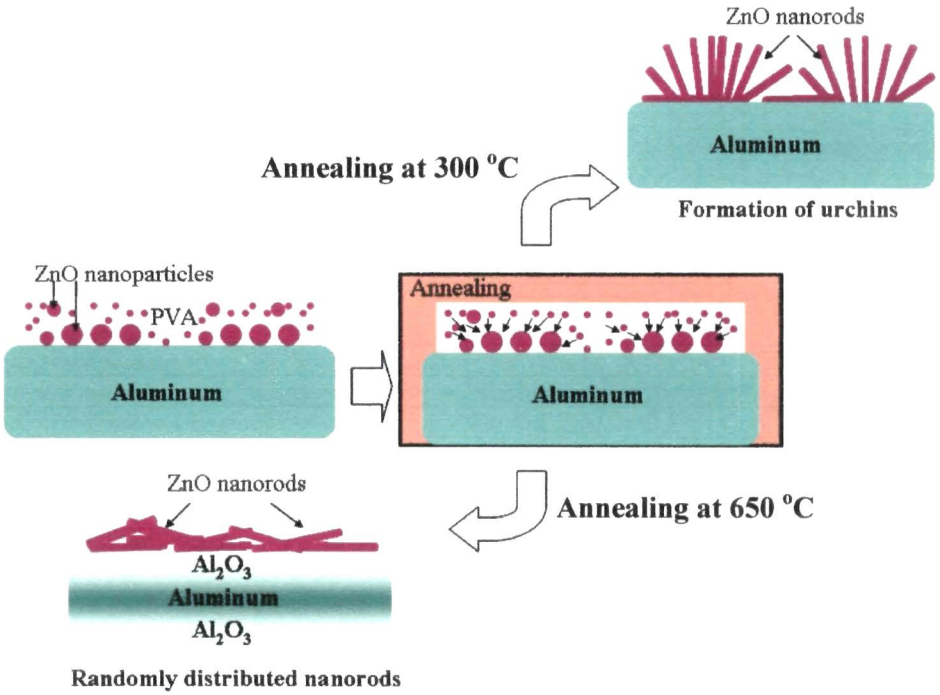

Figure 2.16: Schematic representation of the role of thermal annealing process on ZnO nanopatterns.

2.1.4 Solution phase growth

The fabrication of ZnO nanostructures without using templates and surfactants can be easier and convenient when large scale production is desired. The solution phase growth technique based on seed layer of nanoparicles [20] or thin film [21] of ZnO on a substrate is recognized as an efficient route for growing uniform nanorod arrays. Following similar approach, ZnO nanorod arrays have been fabricated on borosilicate glass using a two step solution growth process. The first step dealt with the formation of a seed layer of ZnO nanoparticles, while directed growth of the nanorods was achieved in the second step.

In the first step, a colloidal solution of ZnO nanoparticles was synthesized by the slow addition of 0.03 M NaOH solution in methanol to 0.01 M of ZAD in methanol kept at a constant temperature of 55 °C. The mixture was then subjected

to vigorous stirring for 1 h. Next, the resulting precursor was spin casted on clean laboratory glass slides (7.5 cm x 2.5 cm x 0.13 cm). Before proceeding to the second step, the nanoparticle seeded substrates were heated at 80 °C for 1 h. In the second step, equimolar zinc nitrate hexahydrate (ZNH) [$Zn(NO_3)_2.6H_2O$], and hexamethylenetetramine (HMT) [$(CH_2)_6N_4$] were mixed together in 75 mL of deionized water. In order to facilitate the growth process the nanoparticle seeded glass substrates were immersed in the aqueous solution and kept under constant stirring for varying time durations (4 to 6 h) at ~ 60 °C. Upon completion of the growth, the samples were taken out, rinsed in deionized water and finally, dried in hot air oven.

Note that the ZnO nanoparticles act as the nucleation sites for the growth of the nanorods. The Zn^{2+} ions were supplied from the decomposition of ZNH. Whereas HMT, being a highly water soluble and non-ionic tetradentate cyclic tertiary amine (Appendix 2), degrades to give rise OH^- ions in the aqueous solution [21, 22].

$$(CH_2)_6N_4 + 6H_2O \rightarrow 6HCHO + 4NH_3,$$

$$NH_3 + H_2O \rightarrow NH_4^+ + OH^-,$$

$$Zn_2^+ + 2OH^- \rightarrow ZnO\ (s) + H_2O.$$

Besides the above mentioned well accepted role of HMT, some reports show that HMT acts as a buffer or a polymer surfactant in the synthesis process [23-25]. It was also reported that HMT acts as a kinetic buffer in yielding ZnO nanostructures [23]. Again in the oxide formation, the $Zn(OH)_2$ becomes thermodynamically unstable and the $Zn(OH)_2$ formed on the substrate on dehydration get reduced to ZnO [24]. On the other hand, it was proposed that HMT having a long chain polymer and a nonpolar chelating agent, which will prefer to get attached on to the non polar facets of the zincite crystal, thereby preventing the attachment of Zn^{2+} ions to them leaving only the polar (001) face [25]. The exposed polar face in [0001] direction facilitates the crystal growth along *c*-axis and finally, leading to 1D nanostructure formation.

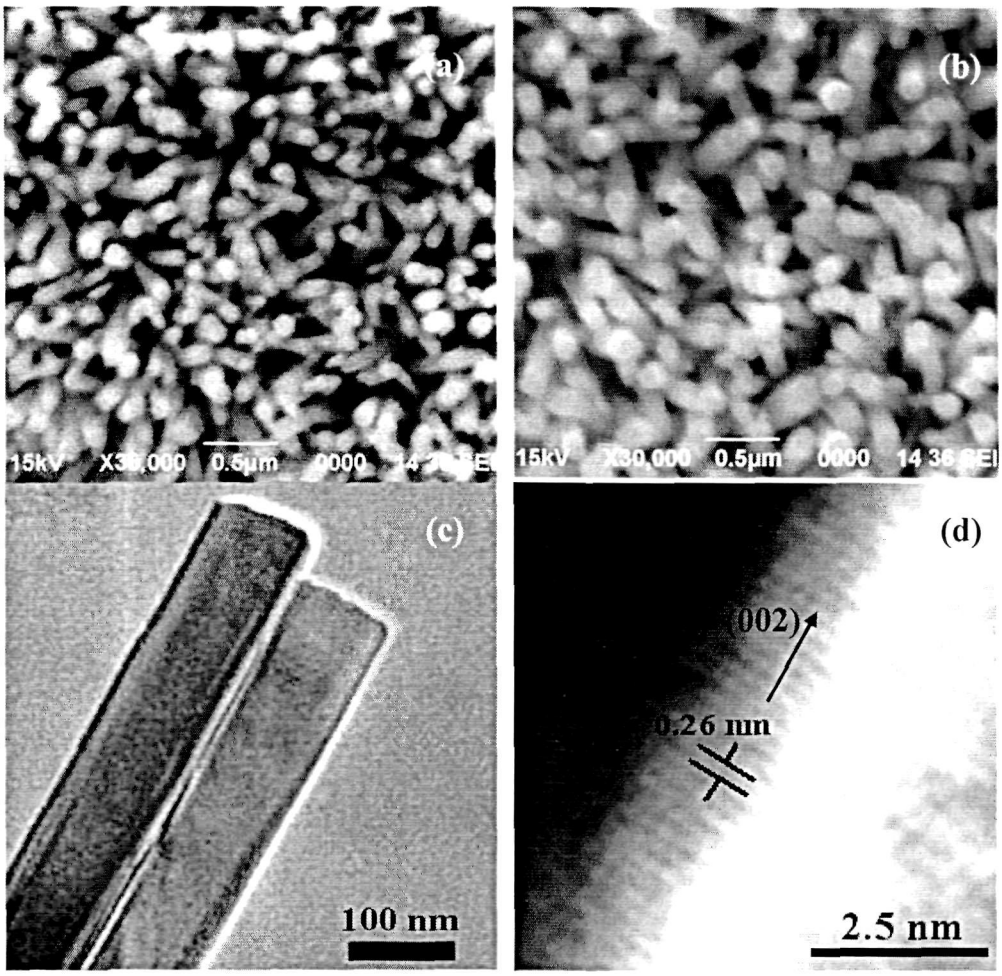

Figure 2.17: SEM image of the ZnO nanorod arrays on glass substrate grown over reaction times of (a) 4 h, and (b) 6 h, HRTEM image at (c) low and (d) high magnification of the nanorods grown after 6 h.

The top view of uniformly grown ZnO nanorods on the glass substrate can be observed in the above micrographs (Figure 2.17 (a, b)). Unlike other nanorods, it can be found that that around 60% of the nanorods are vertically aligned, while others are top-tilted to different degrees. Together, the arrangement gives the impression of a paddy field with top-surface affected by a blow of air-stream. As evident from the SEM image, the nanorods exist in close proximity to each other with tips separated by a distance smaller than the dimension of the rods, the specimen under study signifies a highly compact system. The average diameter of the nanorods synthesized for 4 and 6 h have been found to be ~ 90 and ~ 125 nm;

respectively. Figure 2.17 (c) shows the HRTEM image of the nanorods at low magnification. The nanorods possess a smooth surface as evident from the HRTEM micrograph. Again, the lattice fringes due to the periodically arrayed crystalline planes of ZnO are distinctly visible in the magnified view of the HRTEM image (Figure 2.17 (d)). The crystal planes with an inter-planar spacing of ~ 0.26 nm signifies the (002) growth plane of the ZnO nanorods.

The diffractograms as shown in Figure 2.18 reveal the formation of hexagonal wurtzite phase of ZnO with preferred orientation along (002) plane in consistency with JCPDS 36-1451 [26]. The higher intensity of the (002) peak over the other peaks in both the nanorod samples (grown with different reaction times) suggests that the preferential growth has occurred along the *c*-axis or perpendicular to the plane of the substrate. The other orientation peaks in the XRD pattern have aroused owing to the misalignment suffered by a few nanorods [26]. From the XRD pattern it can be observed that the nanorods fabricated with a reaction time of 6 h, are characterized by higher value of intensity ratio of the (002) and (101) peak ($I_{(002)}$ / $I_{(101)}$), than the nanorods grown in 4 h. It suggests that the preferential growth of the nanorods along the *c*-axis increases as the growth time increases. The lattice parameters were found to be a = 3.25 Å and c = 5.2 Å (c/a ratio ~ 1.6) for the nanorod array grown after 6 h reaction time. Whereas, the average crystallite size of the nanorod array was calculated to be ~ 28 nm.

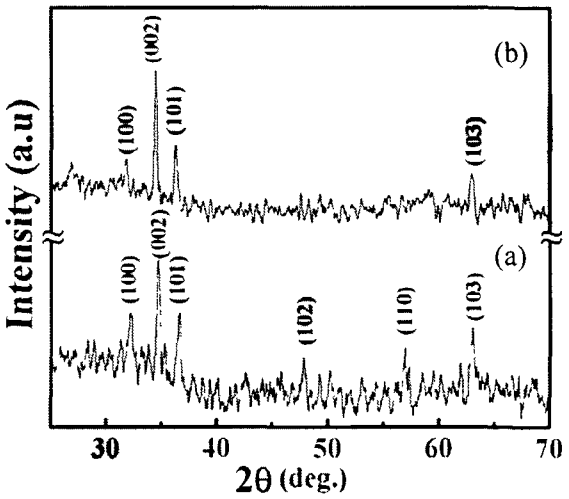

Figure 2.18: XRD pattern of ZnO nanorod array grown after reaction time of (a) 4 h, and (b) 6 h.

2.1.5 Bio-template assisted growth

Apart from the conventional techniques, the fabrication of nanoscale materials using biological templates is quite interesting. This route offers additional benefits such as easier accessibility and environment friendly. In this regard, peacock feathers (Indian Peafowl, *Pavo Cristatus*) were collected from the Manas National Park, Assam (India). A matured feather was used as the base for growing plentiful sub-micron sized nanospheres of ZnO. The peacock feather used in the present study is shown in the adjacent image (Figure 2.19 (a)). It consists of a central stem with an array of barbs on each side and closely spaced barbules on each side of the barb. The schematic view of a peacock tail feather is given in Figure 2.19 (b).

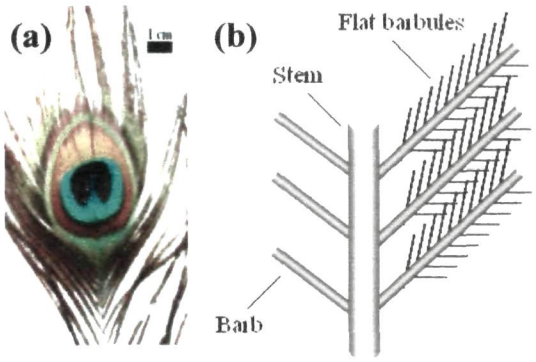

Figure 2.19: (a) Image of the male peacock feather used in the experiment and (b) schematic representation of the peacock feather system.

The ZnO decorated peacock feather was processed using a simple physico-chemical reaction similar to the previous work [27]. 0.005 M ZAD and the peacock feather were put into 20 mL ethanol under continuous stirring environment at a moderate speed (~ 200 rpm) for ½ h. Then, 0.1 M aqueous NaOH in 5 mL ethanol was injected dropwise to the above solution and stirred for another ½ hr at a constant temperature of 70 °C. The resulting precursor was then subjected to ultrasonication for 15-20 minutes to avoid abrupt coalescence of the as-grown structures. It was demonstrated that the carboxyl groups (COO^-) of aspartic ($HOOC\text{-}CH_2\text{-}CH(NH_2)\text{-}COOH$) and glutamic acid ($H_2N\text{-}CO\text{-}(CH_2)_2\text{-}CH(NH_2)\text{-}COOH$) residues in keratin (a type of protein) provide the sites for the Zn^{2+} cations [27]. Consequently $Zn(OH)_2$ is formed in the system upon the introduction of NaOH. Finally, upon annealing the specimen at ~ 80 °C in air for ½ h, submicron sized ZnO structures were developed on the surface of the barbules.

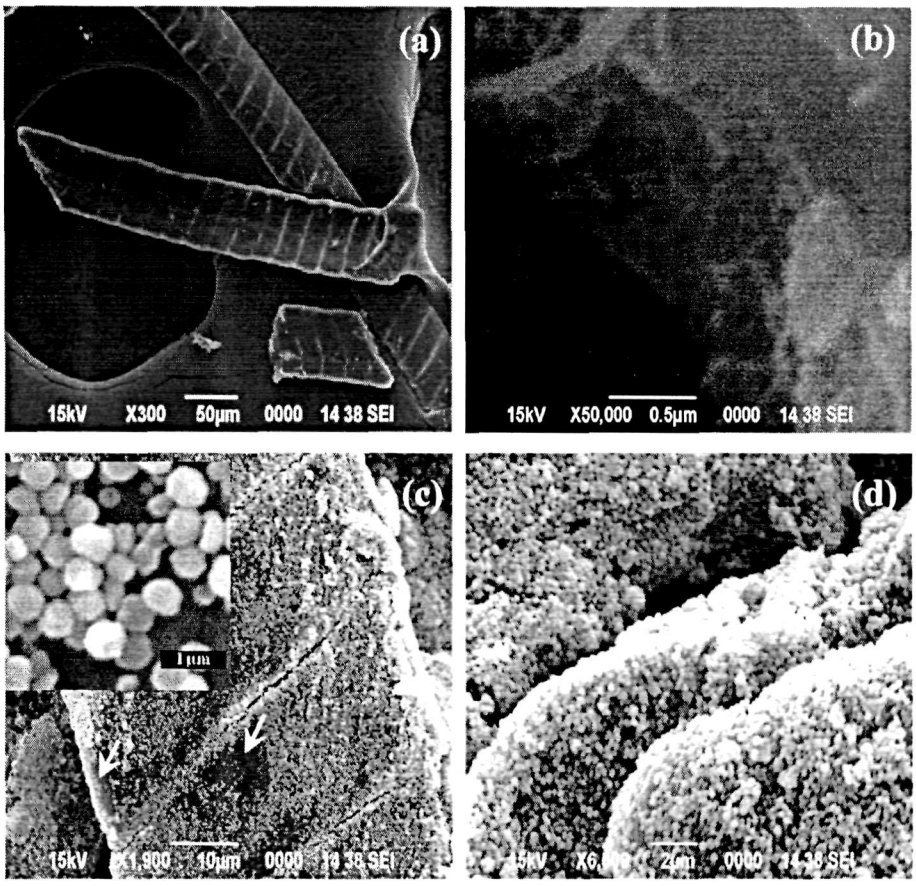

Figure 2.20: Scanning electron micrograph of blue barbules (a,b) before and (c,d) after developing ZnO nanospheres (inset of (c) depicts the hexagonal nanostructures at higher magnification).

Figure 2.20(a) represents the SEM image of the blue barbules of the eye pattern derived from the feather before loading ZnO. As evident from the SEM images, the barbules have a smooth surface. The presence of the melanin rods along with the air gaps can be seen in the next micrograph (Figure 2.20(b)). The homogeneous growth of ZnO nanostructures is clearly visible on the surface of the barbules as shown in Figure 2.20(c,d). It is possible that during the ultrasonication process, some of the nanostructures get detached from the surface of the barbules and thus, a few parts of the barbules are left uncovered (as indicated by the arrows). Figure 2.20(d) depicts a magnified side view of the nanostructures formed on 2-3 different barbules. It can be observed that the ZnO

nanostructures are uniform in size, possessing hexagonal shape with an average diameter varying within 250-270 nm. The inset of Figure 2.20(c) gives a clear impression of the size and shape of the ZnO nanostructures. Thus the barbules of the peacock feather can act as a useful natural template for the fabrication of self organized assembly of nanostructures.

2.2 Concluding remarks

Pure and doped ZnO nanostructures with different structural organization have been synthesized using a few simple and cost effective techniques. The surfactant assisted methods like solid state mixing process and microemulsion route are found to be suitable for synthesizing of spherical as well as elongated nanostructure of ZnO. Furthermore, employing a thermal annealing process, randomly oriented undoped and Eu^{3+} doped ZnO nanorods have been fabricated on metallic Al substrate. In this context, the unidirectional growth of ZnO nanoparticles along [0001] direction leads to the formation of the nanorods. Also, the creation of thermal hotspots on the Al substrate at moderate temperature range (300 - 400 °C) is assigned to the development of urchin like structural organization of ZnO. Whereas annealing at higher temperature destroys the base of the urchin like structures, resulting in the random distribution of the nanorods on the substrate. Finally, nearly vertical ZnO nanorod arrays were also grown adequately on the borosilicate glass substrate using a solution growth technique. The preferential growth of the ZnO nanorods along *c*-axis becomes higher with the increase in reaction time. Apart of these conventional routes, natural peacock feather was used as bio-templates to grow self assembled ZnO nanostructures. Further development and modification of such fabrication techniques may lead to the production of quality ZnO nanostructures which can contribute significantly in modern technological components/devices.

References:

[1] Porebski, S., et. al. Modification of a CTAB DNA extraction protocol for plants containing high polysaccharide and polyphenol components, *Plant Mol. Biol. Rept.* 15 (1), 8-15, 1997.

[2] Nooney, R. I., et. al. Synthesis of nanoscale mesoporous silica spheres with controlled particle size, *Chem. Mater.* 14, 4721-4728, 2002.

[3] Wu, S.-H., & Chen, D.-H., Synthesis of high-concentration Cu nanoparticles in aqueous CTAB solutions, *J. Colloid Interface Sci.* 273, 165–169, 2004.

[4] Zhang, H., et. al. Low temperature synthesis of flowerlike ZnO nanostructures by cetyltrimethylammonium bromide-assisted hydrothermal process, *J. Phys. Chem. B* 108 (13),3955- 3958, 2004.

[5] Kim, J. H., & Lee, J. Y. Hexagonal silicon formation by pulsed laser beam annealing, *Mat. Lett.* 27 (6), 275-279, 1996.

[6] Zhang, F. et. al. Cerium oxide nanoparticles: Size-selective formation and structure analysis, *Appl. Phys. Lett.* 80 (1), 127-129, 2002.

[7] Yin, M., & O'Brien, S. et. al. Synthesis of monodisperse nanocrystals of manganese oxides, *J. Am. Chem. Soc.* 125, 10180-10181, 2003.

[8] Tong, Y. H., et. al. The optical properties of ZnO nanoparticles capped with Polyvinyl Butyral, *J. Sol-Gel Sci. Tech.* 30, 157–161, 2004.

[9] Sun, Z.-P. et. al. Rapid synthesis of ZnO nano-rods by one-step, room-temperature, solid-state reaction and their gas-sensing properties, *Nanotechnology* 17, 2266–2270, 2006.

[10] Das , U., & Mohanta, D. Evolution of ZnO nanoparticles and nanorods: aspect ratio dependent optoelectronic properties, *Eur. Phys. J. Appl. Phys.* 53, 10602 (p1-p5), 2011.

[11] Ge, J. et. al. A rapid hydrothermal route to sisal-like 3D ZnO nanostructures via the assembly of CTA^+ and $Zn(OH)_4^{2-}$:growth mechanism and photoluminescence properties, *Nanotechnology* 17, 1316–1322, 2006.

[12] Holmberg, K. Surfactant-templated nanomaterials synthesis, *J. Colloid Interface Sci.* 274, 355–364, 2004.

[13] Gan, L. M. et. al. Enhanced photoluminescence and characterization of Mn-doped ZnS nanocrystallites synthesized in microemulsion, *Langmuir*, 13, 6427-6431, 1997.

[14] Bhargava, R. N. et. al. Quantum confined atoms of doped ZnO nanocrystals, *Phys. Stat. Sol. B* 229 (2), 897–901, 2002.

[15] Chan, K. S., Senin, H. B., & Naimah. I. Structural and mechanical properties of polyvinyl alcohol (PVA) thin film, AIP Conf. Proc., International Conference on Nanoscience and Nanotechnology-2008, Shah Alam, Selandor, Malaysia,1136, 366-369.

[16] Yong, L. J. et. al. Controlled growth of ZnO nanorods by polymer template and their photoluminescence properties, *Sci. China E-Tech. Sci.*, 52 (4), 888-892, 2009.

[17] Das, S. et. al. Novel method of developing oxide coating on aluminum using microwave heating, *J. Mat. Sci. Lett.* 22, 1635-1637, 2003.

[18] Ge, M.Y. et. al. Nanostructured ZnO: From monodisperse nanoparticles to nanorods, *J. Cryst. Growth* 305, 162-166, 2007.

[19] Bayan, S. & Mohanta, D. Directed growth characteristics and optoelectronic properties of Eu-doped ZnO nanorods and urchins, *J. Appl. Phys.* 108, 023512 (1-6), 2010.

[20] Chander, R. & Raychaudhari, A. K. Growth of aligned arrays of ZnO nanorods by low temperature solution method on Si surface, *J. Mat. Sc.* 41, 3623-3630, 2006.

[21] Schmidt-Mende, L. & MacManus-Driscoll, J. L. ZnO - nanostructures, defects, and devices, *Materialstoday*, 10, 40-48, 2007.

[22] Baruah, S. & Dutta, J. Hydrothermal growth of ZnO Nanostructures, *Sci. Technol. Adv. Mater.* 10, 013001 (1-18), 2009.

[23] Ashfold, M. N.R. et. al. The kinetics of the hydrothermal growth of ZnO nanostructures" *Thin Solid Films* 515, 8679-8683, 2007.

[24] Govender, K. et. al. Understanding the factors that govern the deposition and morphology of thin films of ZnO from aqueous solution, *J. Mater. Chem.* 14, 2575-2591, 2004.

[25] Sugunan, A. et. al. Zinc oxide nanowires in chemical bath on seeded substrates: Role of hexamine, *J Sol-Gel Sci Tech.* 39, 49-56, 2006.

[26] Mamat, M. H. et. al. Controllable growth of vertically aligned aluminum-doped zinc oxide nanorod arrays by sonicated sol–gel immersion method depending on precursor solution volumes, *Jpn. J. Appl. Phys.* 50, 06GH04 (1-6), 2011.

[27] Han, J. et. al. Embedment of ZnO nanoparticles in the natural photonic crystals within peacock feathers, *Nanotechnology* 19, 365602 (1-6), 2008.

Chapter 3

Optical and spectroscopic characterization of ZnO nanoscale systems

The prototype application of ZnO nanostructure based lasers, light emitting diodes (LED) or other photonic devices requires the indepth understanding of the structure-property relationship at large. Both theoretical and experimental attempts have already been made to reveal intrinsic optical properties of ZnO nanostructures for the deployment in photonic and luminescent devices. Nevertheless, owing to the existence of numerous native defect states, it has always been difficult to interpret clearly the luminescence responses of the ZnO based nanostructures. In this chapter, the optical properties of the fabricated ZnO nanostructures are discussed in terms of absorption, excitation and emission characteristics.

3.1 Optical absorption and emission process

Semiconductor materials interact with the electromagnetic radiation within the spectral range of 0.1-1000 μm (0.001-12 eV) [1]. The absorption of photons at the band gap of the semiconductor occurs in the near ultraviolet-visible region (0.4 - 5 μm). It corresponds to the transition of electrons form the valence band to the conduction band edge and is also called as excitation. Figure 3.1 shows the pictorial view of the transition associated with the optical absorption process in semiconductor nanostructures [2]. The fundamental absorption process is strongly affected by whether the band gap is direct or indirect. In a direct semiconductor, the top of the valence band coincides with the bottom of the conduction band and hence characterized by direct transitions of electrons from the valence band to conduction band. In contrast, in indirect semiconductors, the top of the valence band and the bottom of the conduction band doesn't coincide and hence phonon assisted electronic transition can be

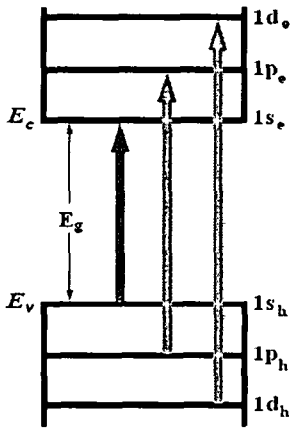

Figure 3.1: Schematic view of optical absorption process in semiconductor nanostructures.

realized. The extent of energy absorption of a semiconductor is determined by the absorption co-efficient of the material. For any direct or indirect semiconductor the absorption co-efficient can be formulated as $\alpha = C\sum n_i n_f P_{if}$, where C is a constant, P_{if} is the probability of the transition from the initial to the final state, n_i and n_f are the densities of electrons in the initial and final states respectively [1]. The band gap (E_g) of the semiconductor material can be related to α as:

$$\alpha h\nu = A(h\nu - E_g)^n$$

where, $h\nu$ is the photon energy, A is a constant and the exponent n is ½ or 2 depending upon the semiconductor type, direct or indirect [1, 3].

When a system gets excited from a lower energy state to a higher energy state by absorbing photons, the system will come back to the original state by emitting the photon as radiation. The complete process that involves the use of photons to excite the system as well as emission of photons is called photoluminescence (PL). In other words, PL corresponds to the light induced light emission characteristics of the material. Such radiative process results in direct recombination of electron-hole pairs (excitons) and is termed as band edge emission [1]. In contrast, the native defects of the crystals create electronic states within the band gap and act as trap centers (sites for trapping of electrons or holes) or recombination centers to contribute in the emission process. Depending upon the nature of these defects, they are classified as donor, acceptor or neutral defects. Such defects of the crystal attract the excitons due to the presence of Coulomb forces and form bound excitons. At this situation the radiative recombination processes results in the emission of photons having energy lower than the free exciton emission (and is known as defect related emission) [1]. The schematic representations of different types of emissions in photoluminescence process are shown in Figure 3.2.

The excitation and band edge emission are depicted in case (1,2), while case (3,4,5) shows the defect related emission. The emission response of a semiconductor is also affected by the non-radiative transitions which could

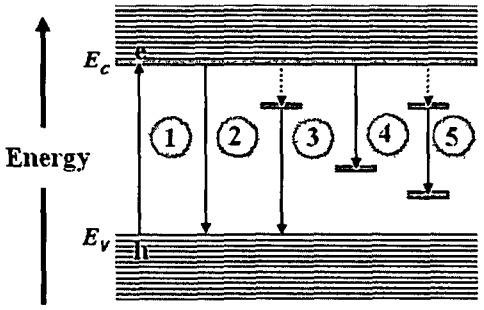

Figure 3.2: Pictorial view of photoluminescence. (1) Excitation of electron from valence band to conduction band edge, (2) band-to-band recombination, (3,4,5) recombination due to native defects. In (2,3,4,5) the solid arrows represent radiative recombination, while dotted arrow signifies non-radiative transition.

obstruct the radiative transitions. The non-radiative processes generally involve the Auger process (three body interaction of carriers) or multiphonon process and are capable of quenching the luminescence of the material [1, 4]. Mediated via the defect states the simultaneous occurrence of both non-radiative and radiative transitions is also possible as depicted in case (3) of Figure 3.2.

In any pure bulk material the band edge emission dominates the emission spectra owing to the presence of less number of native defects. In contrast to that large number of native defect states exists in the nanostructured materials due to the higher surface-to-volume ratio. Hence the defect related emission becomes significant in the emission response of the nanostructures. In general, the dominance of the radiative emission due to the various defects quenches the typical band edge emission [5, 6]. Figure 3.3 represents a simplified illustration of the overall process [7]. The event in case A reveals carrier transitions with regard to band edge emission along with a weak emission due to defect states, whereas

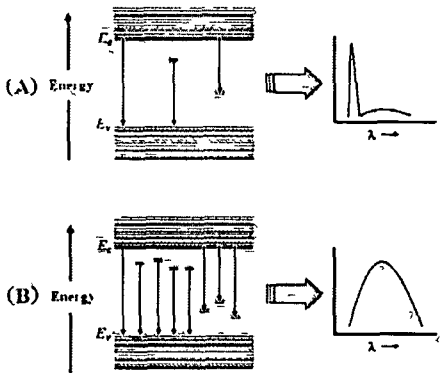

Figure 3.3: Scheme of the luminescence response of ZnO nanostructures with (A) less and (B) large number of defect states within the band gap.

case B depicts a broad emission spectrum owing to the presence of a large number of intermediate states (defects).

3.2 The optical properties of the ZnO nanostructures

The optical properties of the synthesized ZnO nanostructures were investigated using optical absorption spectra (OAS) and photoluminescence (PL) spectra. The absorption spectra were recorded using a computer interfaced UV-Visible spectrophotometer of Shimadzu Corporation, Japan (Model UV2450). Again, the room temperature PL spectra of the samples were revealed by using a Perkinelemer LS 55 spectrophotometer, having Xe line as the excitation source. In this case the data were collected by a computer controlled standard monochromator based photo-detection system.

3.2.1 Pure (or undoped) ZnO nanoscale structures

The optical properties of the quality ZnO nanostructures synthesized using different techniques are discussed below.

(a) *ZnO nanostructures fabricated via solid state mixing*: ZnO nanoparticle and nanorod systems were synthesized by varying the precursor ratio in a solid state grinding process. The UV-Visible absorption spectra of the nanostructures are shown in Figure 3.4 (a,b).

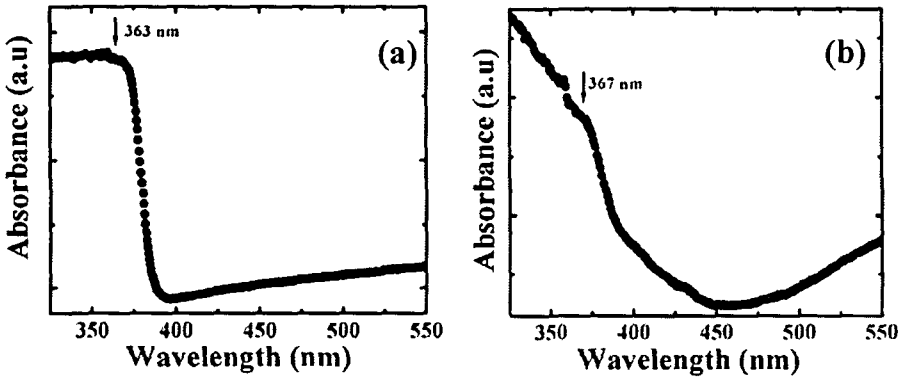

Figure 3.4: UV Visible absorption spectra of the ZnO (a) nanoparticles and, (b) nanorods synthesized using solid state grinding process.

The ZnO nanoparticles show an absorption peak at ~ 363 nm (~ 3.42 eV) which corresponds to the 1s-1s ground state excitonic absorption [8]. Similarly the nanorod system can be characterized by a ground state excitonic absorption at ~ 367 nm (~ 3.38 eV). Near the vicinity of the ground state excitonic absorption, a strong absorption can be observed owing to the free excitons [9]. It can be observed that the ground state excitonic energies of the nanoparticle and nanorod systems are higher than that of the bulk ZnO (~ 3.3 eV) and can be correlated to the quantum confinement effect [10].

Figure 3.5 shows the room temperature PL spectra of the ZnO nanoparticle and nanorod systems under 325 nm excitation (λ_{ex}). The luminescence response of the nanoparticles is found to extend throughout a long range of the visible spectrum, while the nanorods show an intense emission in the violet-blue region. For both the cases, the asymmetrically stretched and broadened emission spectra indicate the involvement of various defect related emission of ZnO. It can be noticed that the typical band edge emission of ZnO is not observed in anyone of the PL spectra. Such an event can be correlated to the presence of large number of defect and surface states within the system [6]. The existence of Zn and O related native defects in ZnO has been validated by both theoretical and experimental studies [11-13].

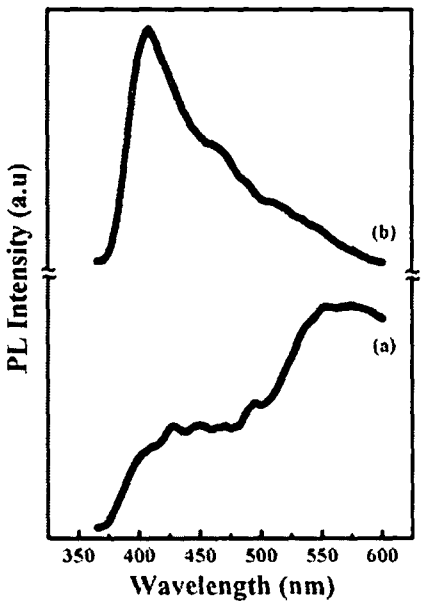

Figure 3.5: Room temperature PL spectra (λ_{ex} = 325 nm) of ZnO (a) nanoparticles and (b) nanorods.

In order to evaluate individual contribution of the native defects, Gaussian curve fitting was performed on the experimentally obtained PL curve. The position and width of the fitted peaks were adjusted in such a way so that the empirical curve

formed by the superposition of these fitted peaks, matched with the experimentally obtained curve.

As can be found from Figure 3.6, the Gaussian fitting of the PL spectra of the nanoparticles reveals the presence of seven major peaks at different positions. As predicted from the literature the peak positions correspond to the respective positions of various Zn and O related defects in ZnO [14-18]. The peaks at ~ 400 and 467 nm correspond to the zinc vacancy related emissions (V_{Zn} and V_{Zn}^- respectively), while peaks at ~ 429 and 450 nm indicate the emission due to Zn interstitials (Zn_i, Zn_i^+ etc) [14-17]. Again, the emission peaks at ~ 493 and 580 nm can be ascribed to the oxygen vacancies (V_O^+, V_O^{++} etc), while the 537 nm peak signifies the oxygen interstitial (O_i) related emission [14, 16]. In the Gaussian fitted PL spectra it is evident that the V_O^{++} defect dominates the other defect related emission. The dominance of V_O^{++} defect indicates the presence of small grains which are greatly depleted [18]. In fact, oxygen vacancies in ZnO occur in three different charge states: the V_O^x state which has captured two electrons and remains neutral relative to the lattice, while the single ionized V_O^+, and the double ionized V_O^{++} states are positively charged with respect to the lattice. V_O^+ can trap a photoexcited electron easily through a non-radiative step to result in neutral V_O^x state. Since V_O^x is unstable at room temperature, a radiative recombination of this center with the photoexcited holes in the valance band yields photons with energy of ~ 2.5 eV [18]. In the present case the emission at ~ 493 nm signifies such an event. In the bulk region, most oxygen vacancies are expected to be in V_O^+ states under flatband conditions. It was earlier reported that due to a small difference between the depletion width and the actual grain size, most of the V_O^+ get converted to

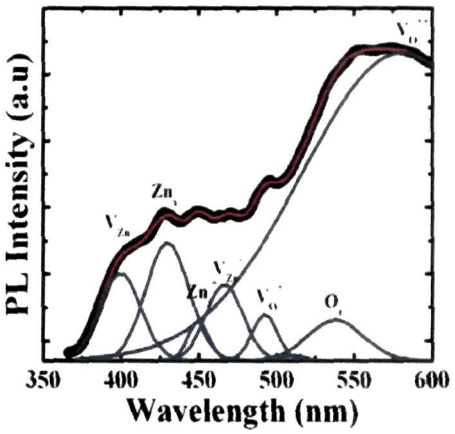

Figure 3.6: Gaussian fitting of the PL spectra of the ZnO nanoparticles.

V_O^{++} states by trapping a hole from the grain surface [18]. Then, a radiative recombination of a photoexcited electron of conduction band with a V_O^{++} center yields photons with energy ~ 2 eV. Thus the dominance of emission at ~ 580 nm corresponds to the formation of large depletion region owing to smaller grain size of the nanoparticles.

On the other hand, the PL spectra of ZnO nanorods upon Gaussian fitting depicts four prominent peaks corresponding to V_{Zn}, Zn_i, V_{Zn}^- and V_O^+ defect related emissions (Figure 3.7). Note that, no signature of V_O^{++} related emission was found in this case owing to the lower surface-to-volume ratio compared to the nanoparticle system [19, 20]. The uni-directional growth of the system has led to the suppression in the depletion width and hence the band bending can be ignored. In such a flat band condition only V_O^+ defects can contribute largely to the emission pattern [18].

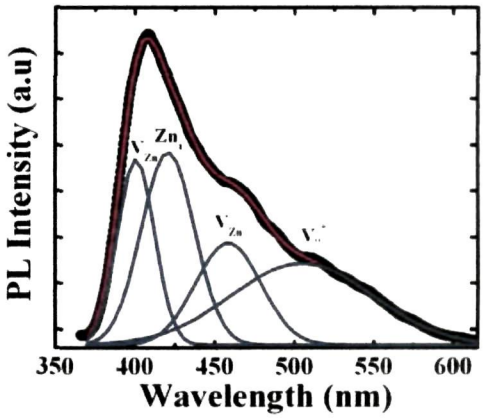

Figure 3.7: Gaussian fitting of the PL spectra of the ZnO nanorods.

(b) *ZnO nanorods fabricated via microemulsion route*: Figure 3.8 (a) shows the

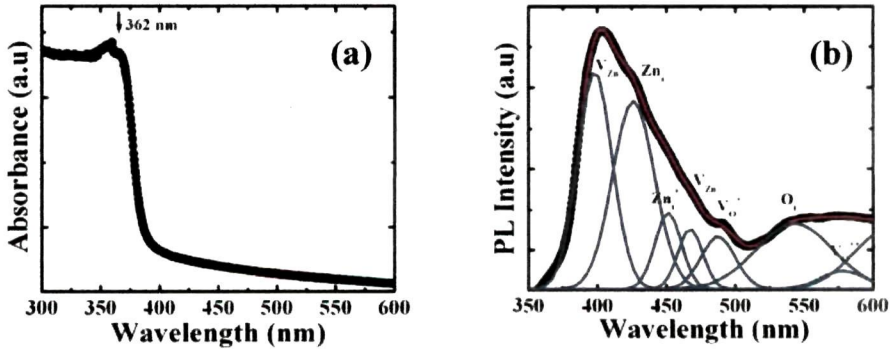

Figure 3.8: (a) UV-Visible absorption spectrum, and (b) PL spectrum (λ_{ex} = 325 nm) of the ZnO nanorods fabricated using the microemulsion route.

UV-Visible absorption spectrum of the ZnO nanorods produced by employing the microemulsion route. The well resolved peak at ~ 362 nm (3.43 eV) corresponds to the ground state 1s-1s excitonic absorption [8]. This higher value of the ground state excitonic absorption peak of the system compared to the bulk value ensures the formation of low dimensional structures with confined geometry.

The room temperature PL spectrum of the nanorods under 325 nm excitation, is shown in Figure 3.8 (b). The asymmetrically stretched PL spectrum depicts the presence of various defect related emission of ZnO. The typical band edge emission of ZnO is found to get suppressed because of the presence of the large number of defect states of different origins. Upon Gaussian fitting the PL spectrum can be de-convoluted into several peaks with V_{Zn} related emission as the most prominent peak, apart from low-intense Zn_i related peak [14]. The V_O^+ and O_i related emissions and weak emissions owing to Zn_i^+ and V_{Zn}^- defects also participate in the evolution of broadened luminescence spectra [15-18]. The V_O^{++} related emission response was also evident in the form of a poorly resolved emission peak.

(c) *ZnO nanostructures fabricated using thermal annealing process*: As discussed in Chapter 2, urchin like structures and randomly oriented nanorods of ZnO were synthesized under annealing temperatures of 400 and 750 °C by adopting the thermal annealing process. The UV-Visible absorption spectra of the two types of nanosystems are shown in Figure 3.9. The ground state 1s-1s excitonic absorption peaks were found to be located at ~ 361 and 364 nm, for the urchins and randomly oriented nanorods of ZnO respectively. In

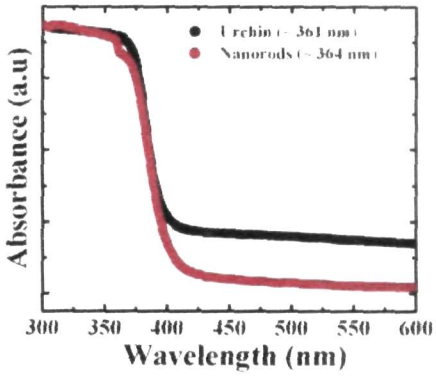

Figure 3.9: UV-Visible absorption spectra of the urchins and randomly oriented nanorods.

both the spectra, the free exciton related strong absorption response can be observed in the vicinity of the ground state excitonic absorption peaks.

The de-convoluted room temperature PL spectrum of the urchin like structures is shown in Figure 3.10 (a). It can be observed that the spectrum is dominated by V_{Zn} defects, along with the emission due to Zn_i and V_{Zn}^- related defects. Additionally, the presence of O_i related emission is also evident at the higher wavelength side of the spectrum. Again, the PL spectrum of the randomly oriented nanorods, is characterized by the presence of three major emission peaks related to Zn_i, Zn_i^+, and V_O^+ defects (Figure 3.10 (b)) [17, 18]. Among these emissions, the radiative response of Zn_i^+ defects was found to dominate the overall spectrum. As predicted, the band edge emission of ZnO is substantially quenched in both the emission spectra due to the dominance of the defect related emission response.

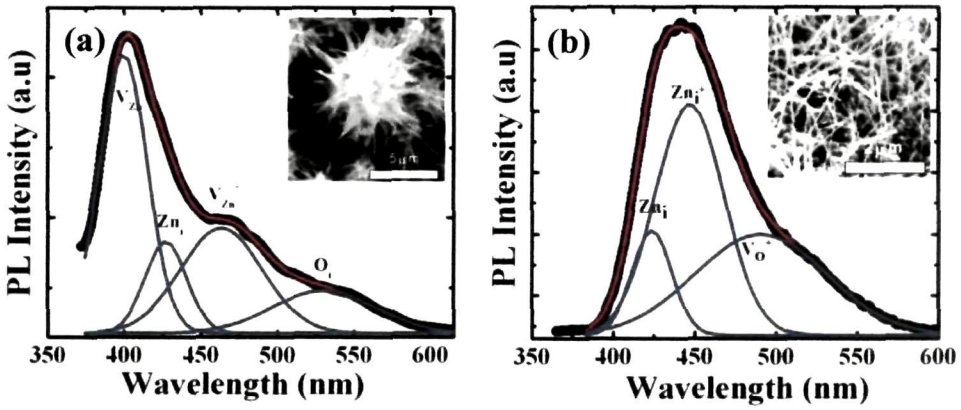

Figure 3.10: PL spectra (λ_{ex} = 325 nm) of (a) urchin like structures, and (b) randomly oriented nanorods of ZnO. Inset being the SEM image of the respective structural organization.

To access out the observed difference of the luminescence pattern of the urchins and nanorods, the origin of the two PL spectra must be linked with the growth dynamics. As evident from the PL spectrum of the urchin like structures, the dominance of V_{Zn} related defects over Zn_i defects and evolution of O_i defects predict a situation where the concentration of O atoms is higher than Zn atoms. Again, the dominance of Zn_i related defects and evolution of V_O^+ defects in the

PL spectrum of the nanorods signify a situation where the concentration of Zn atoms is more abundant than O atoms. It was discussed in Chapter 2, that in thermal annealing process, the unidirectional growth of the nanorods takes place via transferring of atoms from smaller particles to larger particles along [0001] direction of ZnO system. Since the atomic size of O atoms (atomic radius ~ 48 pm) is lower than that of Zn atoms (atomic radius ~ 142 pm), it will require less energy to transfer one O atom from a smaller particle to a larger one. Consequently, it is expected that annealing at 400 °C, would facilitate the transfer of more O atoms than Zn atoms. Thus the sample can be characterized by a PL spectrum which shows the presence of V_{Zn} and O_i defect related emission. On the other hand, for the nanorods synthesized at 750 °C, the Zn_i related defect dominates the PL spectrum owing to the participation of sufficient number of Zn atoms in the growth process [21].

(d) *ZnO nanorod arrays fabricated via solution growth technique*: The solution growth process has been found to be very effective that could yield quality ZnO nanorod arrays. Figure 3.11 depicts a UV Visible absorption spectrum of the as synthesized ZnO nanorods with reaction (growth) time of 6 h. The ground state excitonic absorption peak was found to be located at ~ 356 nm (3.48 eV) for the nanorod arrays. Compared to the bulk counterpart, the higher ground state absorption energy indicates the formation of low dimensional structures.

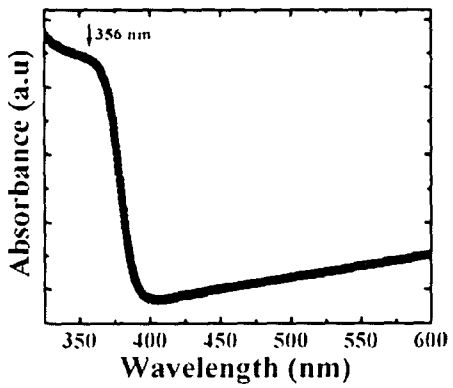

Figure 3.11: UV-Visible absorption spectrum of the ZnO nanorod array.

The PL spectra of the nanorod arrays differ from the others in the sense that strong emission response in the UV region is evident in the former case. The room temperature PL spectrum of the nanorod arrays are shown in Figure 3.12.

The wavelength region of 360 to 430 nm of the PL spectra was examined closely using Gaussian curve fitting so as to extract out individual radiative characteristics. Upon de-convolution three peaks were found to be located at ~ 380, 395 and 407 nm within the above mentioned region. The 380 nm peak corresponds to the band edge emission of ZnO due to the direct recombination of electron-hole (*e-h*) pairs. Whereas the peak at 407 nm corresponds to the V_{Zn} related emission of ZnO [14]. On the other hand, the observed peak at ~ 395 nm is attributed to the emission due to the presence of shallow traps [22].

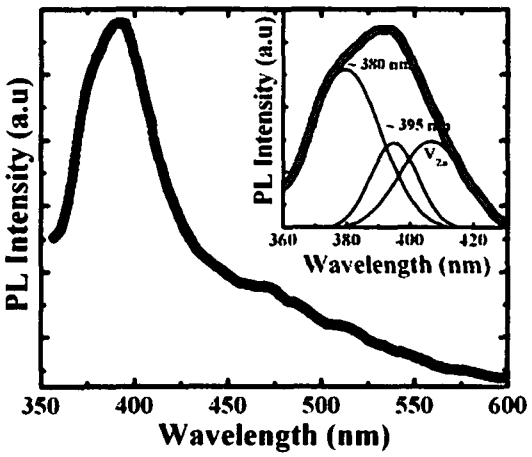

Figure 3.12: PL spectra (λ_{ex} = 325 nm) of the ZnO nanorod arrays. Inset shows the Gaussian fitting of a particular region.

In order to reveal the presence of the trap states within the band gap of ZnO, PLE was performed by considering the, emission wavelength of 600 nm. The PLE spectrum shown in Figure 3.13 depicts a prominent peak centered at ~ 391 nm (3.17 eV). Since the associated energy of the PLE peak is lower than the band edge emission peak (located at ~ 3.26 eV), the PLE peak can not be attributed to the excitation of electrons to the excitonic levels. In fact it is likely that the PLE peak can arise due to the excitation of valence band electrons to some trap levels situated below the excitonic level.

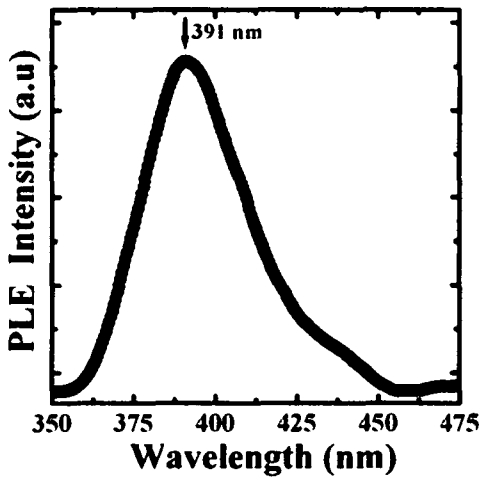

Figure 3.13: The PLE spectra (λ_{em} = 600 nm) of the ZnO nanorod array.

As evident from the PL spectrum, in contrast to the other methods, the nanorods grown via solution growth technique, is characterized by typical band edge emission of ZnO, with minimum defect related emission. This fact can be supported from the crystallographic properties of the various nanorods. In Chapter 2, the crystallographic properties of the nanorods were studied using relevant XRD patterns. The average crystallite size of the nanorods fabricated via solid state grinding, microemulsion, thermal annealing (urchins) and solution growth method were found to be ~ 13.26, 16.53, 9.12 and 28 nm respectively. The average crystallite size of the nanorods fabricated using the solution growth technique is larger than the nanorods produced via other routes. Since the number of defects in the crystals increases as the crystallite size decreases [23], the nanorods grown using the solution growth technique are characterized by week defect related emission as discussed earlier. The nanorods grown using the other synthesis techniques are found to possess smaller crystallite size and hence, associated with higher defect concentrations. This leads to the evolution of strong defect related emission and suppression of the typical band edge emission for the nanorods having lower crystallite size. Yoshikawa *et al.* observed similar results where the band edge and the defect related emission of ZnO nanoparticles were found to vary with the crystallite size of the nanoaprticles [24]. Hence in the present study, it can be assured that the variation observed in the PL spectra of the nanostructures is originated from the synthesis dependent variation in crystallographic properties.

3.2.2 Eu^{3+} doped ZnO nanostructures

The fabrication strategy of Eu^{3+} doped ZnO nanostructured systems, in the form of nanoparticles, urchins and randomly distributed nanorods have been discussed in Chapter 2. The thermal annealing process was employed to fabricate the different nanostructured systems. Figure 3.14 (a,b,c) depicts a set of UV-Visible optical absorption spectra of different nanostructures of Eu^{3+} doped ZnO system.

The specimen containing spherical nanoparticles shows an absorption peak ~ 356 nm (3.48 eV), which is assigned to the 1s-1s ground state excitonic absorption. The ground state excitonic peak exhibits a red shift of ~ 90 meV in case of the specimen annealed at 300 °C (urchin like structures) and 650 °C (randomly distributed nanorods) as compared to the usual nanoparticle system. The observed red shift therefore supports particle growth (here, one directional). No significant shift in the absorption peak of the randomly distributed nanorods was found as compared to the urchin like structures (Figure 3.14 (b,c)). This fact supports the similar dimension of the nanorods present in the two samples.

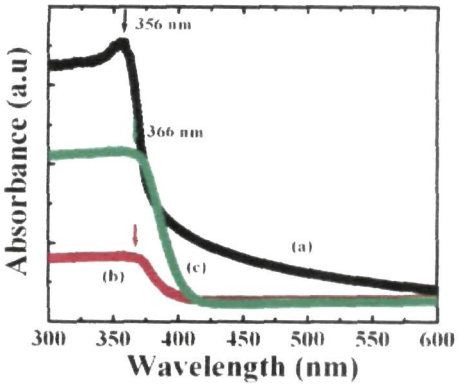

Figure 3.14: UV-Visible absorption spectra of the Eu^{3+} doped ZnO nanostructures, synthesized at (a) 80 °C, (b) 300 °C and (c) 650 °C.

Figure 3.15 (a,b,c) shows the PL spectra of the Eu^{3+} doped ZnO nanostructures (λ_{ex} = 325 nm). Each of the PL spectra is characterized by a number of defect related emission peaks located at approximately same wavelength positions. The impressions at ~ 400 nm and 467 nm corresponded to the emissions related to the zinc vacancy states (V_{Zn}, V_{Zn}^{-}); respectively [14, 15]. Further, the peaks at ~ 429 nm and 452 nm arise due to the respective emissions via zinc interstitial related defects (Zn_i, Zn_i^{+}) [15-17]. On the other hand, the 492 nm and 535 nm peaks are identified as emissions due to the oxygen vacancy (V_o^{+}) and interstitial (O_i)

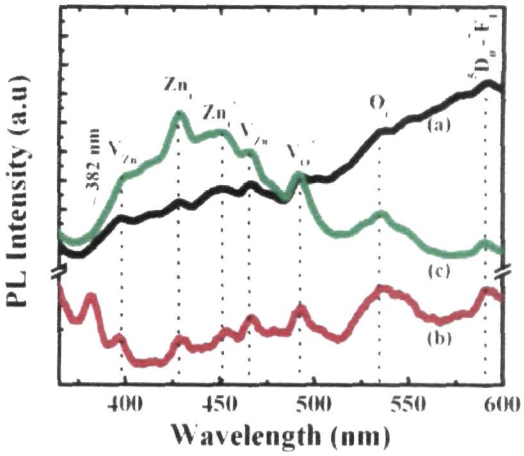

Figure 3.15: PL spectra (λ_{ex} = 325 nm) of the Eu^{3+} doped ZnO nanostructures, synthesized at (a) 80 °C, (b) 300 °C and (c) 650 °C.

defects [14, 18]. Note that the near band edge emission peak of ZnO is found at ~ 382 nm for the urchin like structures. It can be observed that the oxygen (vacancy, interstitial etc) related emissions are dominant in case of the nanoparticle systems than the case of urchins and randomly distributed nanorods. In contrast the zinc related emissions (both vacancies and interstitials) are dominant for the spectra of randomly distributed nanorods (Figure 3.15 (a-c)). The results are consistent to the earlier observations. Apart from these defect related emission peaks, the emission peak at ~ 592 nm is ascribed to the transition related to Eu^{3+} cations ($^5D_0 \rightarrow {}^7F_1$) [25-28].

In order to observe the Eu^{3+} related emissions, the PL spectra corresponding to λ_{ex} = 405 nm is also studied. Characterized by a broad spectrum the oxygen interstitial related emission (centered at ~ 535 nm) is found to be prominent for the specimen containing the nanoparticles (Figure 3.16 (a)). The oxygen vacancy related peak at ~ 492 nm is found to remain intact. In addition, the peak observed at ~ 613 nm, is ascribed to the Eu^{3+} related emission due to $^5D_0 \rightarrow {}^7F_2$ transitions [25-28]. As evident from both the PL spectra (Figure 3.15 and 3.16), the most important aspect of the Eu^{3+} related emission is that it gets quenched with the decrease in defect related emission. So, it can be ascertained that the emission due to $^5D_0 \rightarrow {}^7F_1$ and $^5D_0 \rightarrow {}^7F_2$ transitions take place due to the energy transfer from the host ZnO via the native defect states. The evolution of the Eu^{3+} related transitions via the energy transfer process is in consistent with earlier reports [28-31]. In the present study, upon exciting the systems with energy lower than the band gap of the material, the intensity of the Eu^{3+} related

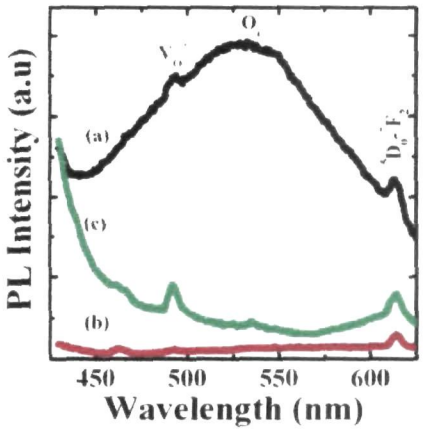

Figure 3.16: PL spectra (λ_{ex} = 405 nm) of the Eu^{3+} doped ZnO nanostructures, synthesized at (a) 80 °C, (b) 300 °C and (c) 650 °C.

emissions increases (Figure 3.16) as the defect related emission (specifically oxygen vacancies and interstitials) gets enhanced.

For a comparative analysis the emission spectra corresponding to λ_{ex} = 325 nm and 405 nm, (for the specimen annealed at 650 °C i.e. randomly distributed nanorods) are presented in Figure 3.17. The Eu^{3+} related emission peak at ~ 613 nm is found to be asymmetrically stretched towards the lower-end wavelength side which might have arisen due to the presence of an inherent peak at ~ 591 nm related to the $^5D_0 \rightarrow {}^7F_1$ transitions (Figure 3.17). It is evident that in the energy transfer mechanism, the oxygen vacancies and interstitials capture the photo-excited electrons and transfer some of them to the $^5D_3$ level of Eu^{3+} cations. This is followed by a non-radiative transition from the $^5D_3$ level to the $^5D_0$ level and later resulting in the $^5D_0 \rightarrow {}^7F_1$ and $^5D_0 \rightarrow {}^7F_2$ transitions. The schematic representation of the energy transfer mechanism is shown in Figure 3.18.

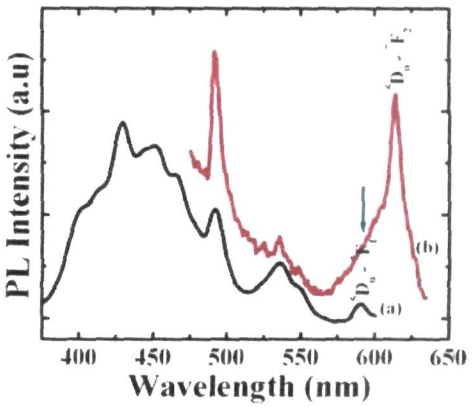

Figure 3.17: PL spectra of the ZnO nanorods synthesized at 650 °C having λ_{ex} = (a) 325 nm and (b) 405 nm.

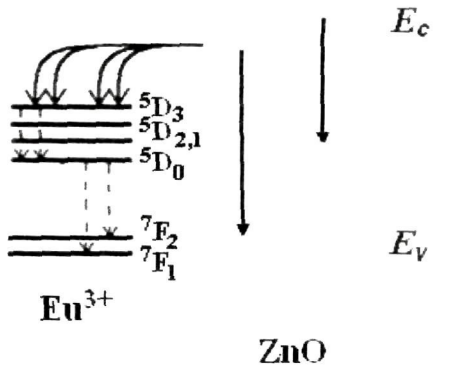

Figure 3.18: Energy transfer mechanism of Eu^{3+} doped ZnO nanostructures.

3.3 Concluding remarks

The optical properties of pure and doped ZnO nanostructures have been explored by analyzing UV-Visible absorption and photoluminescence spectra. The formation of low dimensional, nanoscale structures can be assured from the

quantum confinement effect witnessed in the respective absorption spectra. The PL spectra of the nanostructures were characterized by various native defect states of ZnO, with an occasional presence of the characteristic band edge emission. The variation in the PL spectra of different nanostructures is assigned to the dissimilar crystallographic properties. On the other hand, the Eu^{3+} incorporated ZnO nanostructures show the characteristic red emission due to intra *4f* transitions ($^5D_0 \rightarrow {}^7F_1$ and $^5D_0 \rightarrow {}^7F_2$) related to the Eu^{3+} cations along with the defect related emission of ZnO. An energy transfer mechanism via the native defects of ZnO (especially oxygen interstitials and vacancies) was found to be responsible for the observed Eu^{3+} related transitions. The basic understanding of such emission responses of various ZnO nanostructures would be beneficial for selective to control the luminescence features. In addition, the tunabilty of the various defect related emission of ZnO may form the basis of various light emitting and photonic devices including passive and active elements.

References:

[1] Perkowitz, S. *Optical Characterization of Semiconductors*, Academic Press, Great Britain, 1993.

[2] Gaponenko, S. V. *Optical Properties of Semiconductor Nanocrystals*, United Kingdom, 1998.

[3] Labuayai, S. et al. Synthesis and optical properties of nanocrystalline ZnO powders prepared by a direct thermal decomposition route, *Appl. Phys. A* 94, 755–761, 2009.

[4] Nirmal, M. & Brus, L. Luminescence photophysics in semiconductor nanocrystals, *Acc. Chem. Res.* 32, 407-414, 1999.

[5] Chen, H. S. et al. White-light emission from organics-capped ZnSe quantum dots and application in white-light-emitting diodes, *Appl. Phys. Lett.* 86, 131905 (1-3), 2005.

[6] Gu, Z. et al. Aligned ZnO nanorod arrays grown directly on zinc foils and zinc spheres by a low-temperature oxidization method, *ACS Nano* 3 (2), 273-278, 2009.

[7] Yang, M. et al. Fabrication of two-dimensional ZnO nanostructures from nanoparticles, *J. Phys. Chem. C* 111, 17213-17220, 2007.

[8] Chakraborty, R. et al. Fabrication of ZnO nanorods for optoelectronic device applications, *Indian J. Phys.* 83 (4) 553-558, 2009.

[9] Sturge, M. D. Optical absorption of Gallium Arsenide between 0.6 and 2.75 eV, *Phys. Rev.* 127, 768-773, 1962.

[10] Gu, Y. et al. Quantum confinement in ZnO nanorods, *Appl. Phys. Lett.* 85 (17), 3833-3835, 2004.

[11] McCluskey, M. D. & Jokela, S. J. Defects in ZnO, *J. Appl. Phys.* 106, 071101(1-13), 2009.

[12] Kim, Y.-S. & Park, C. H. Rich variety of defects in ZnO via an attractive interaction between O vacancies and Zn interstitials: Origin of *n*-type doping, *Phys. Rev. Lett.* 102, 086403 (1-4), 2009.

[13] Zhao, Q. X. et al. Deep-level emissions influenced by O and Zn implantations in ZnO, *Appl. Phys. Lett.* 87, 211912 (1-3), 2005.

[14] Lin, B. et al. Green luminescent center in undoped zinc oxide films deposited on silicon substrates, *Appl. Phys. Lett.* 79, 943-945, 2001.

[15] Lima, S. A. M. et al. Luminescent properties and lattice defects correlation on zinc oxide, *Int. J. Inorg. Mater.* 3, 749-754, 2001.

[16] Zhang, L.-L. et al. The synthesis of one-dimensional controllable ZnO microrods, *Chinese Phys.* 14 (3), 586-591, 2005.

[17] Tam, K. H. et al. Defects in ZnO nanorods prepared by a hydrothermal method, *J. Phys. Chem. B* 110, 20865-20871, 2006.

[18] Ye, J. D. et al. Correlation between green luminescence and morphology evolution of ZnO films, *Appl. Phys. A* 81, 759-762, 2005.

[19] Das, U. & Mohanta, D. Evolution of ZnO nanoparticles and nanorods: aspect ratio dependent optoelectronic properties, *Eur. Phys. J. Appl. Phys.* 53, 10602 (p1-p5), 2011.

[20] Cheng, B. et al. Synthesis of Variable-Aspect-Ratio, Single-Crystalline ZnO Nanostructures, *Inorg. Chem.* 45, 1208-1214, 2006.

[21] Bayan, S. & Mohanta, D. Defect mediated optical emission of randomly oriented ZnO nanorods and unusual rectifying behavior of Schottky nanojunctions, *J. Appl. Phys.* 110, 054316 (1-6), 2011.

[22] Wang, Y. S. et al. Nanocrystalline ZnO with Ultraviolet Luminescence, *J. Phys. Chem. B*, 110, 4099-4104, 2006.

[23] Lo, S.-S. et al. Formation and Raman scattering of seed-like ZnO nanostructure, *J. Raman Spectrosc.* 40, 1694–1697, 2009.

[24] Yoshikawa, M. et al. Characterization of ZnO nanoparticles by resonant Raman scattering and cathodoluminescence spectroscopies, *Appl. Phys. Lett.* 92, 113115 (1-3), 2008.

[25] Peres, M. et al. Optical studies of ZnO nanocrystals doped with Eu^{3+} ions, *Appl. Phys. A* 88, 129–133, 2007.

[26] Ashtaputre, S. S. et al. Investigations of white light emitting europium doped zinc oxide nanoparticles, *J. Phys. D: Appl. Phys.* 41, 015301 (1-5), 2008.

[27] Ishizumi, A. & Kanemitsu, Y. Structural and luminescence properties of Eu-doped ZnO nanorods fabricated by a microemulsion method, *Appl. Phys. Lett.* 86, 253106 (1-3), 2005.

[28] Du, Y.-P., Efficient energy transfer in monodisperse Eu-doped ZnO nanocrystals synthesized from metal Acetylacetonates in high-boiling solvents, *J. Phys. Chem. C*, 112, 12234–12241, 2008.

[29] Zhang, Y. et al. Photoluminescence and ZnO→Eu^{3+} energy transfer in Eu^{3+}-doped ZnO nanospheres, *J. Phys. D: Appl. Phys.* 42, 085106 (1-6), 2009.

[30] Bayan, S. & Mohanta, D. Directed growth characteristics and optoelectronic properties of Eu-doped ZnO nanorods and urchins *J. Appl. Phys.* 108, 023512 (1-6), 2010.

[31] Yu, Y. et al. Enhanced emissions of Eu^{3+} by energy transfer from ZnO quantum dots embedded in SiO_2 glass, *Nanotechnology* 19, 055711 (1-5), 2008.

[32] Liu, Y. et al. Optical Spectroscopy of Eu^{3+} Doped ZnO Nanocrystals, *J. Phys. Chem. C*, 112, 686-694, 2008.

Chapter 4

Role of energetic ion irradiation on the luminescence response

When an energetic charged particle is directed onto a crystalline specimen, the projectile can cause several damage or alteration of structural properties. Ions having energy in keV scale generally leads to the formation of point defects in the solid, while ions carrying energy in the MeV range are capable of producing cluster of defects, latent ion tracks and/or phase transformation. Ion irradiation led such modifications result in the alteration of various physical properties of the material. Compared to the other conventional techniques, through ion irradiation the precise tunablity of electrical, optical and magnetic properties can be achieved by varying the ion energy and fluence. The ion irradiation induced modification of the luminescent response of ZnO nanostructures and the analogous theoretical justification are highlighted in the present Chapter.

4.1 Ion irradiation and energy loss process

An energetic ion while traversing through a crystalline solid suffers a series of binary collisions with target atoms and surrounding electrons and loses its energy at each encounter [1]. This results in the transfer of energy from the projectile ion to the target material. The energy transfer mechanism can be conveniently divided into two independent processes, namely nuclear collision and electronic collision [1, 2]. The nuclear collision and electronic collision processes associated with the ion-matter interaction are schematically shown in Figure 4.1 [1].

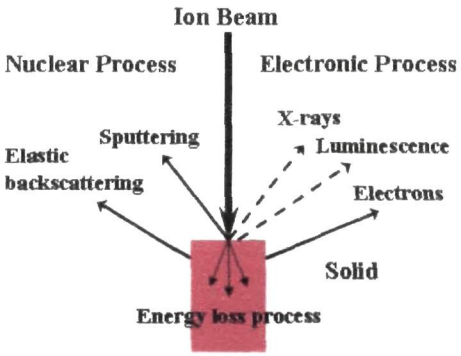

Figure 4.1: Schematic view of different events during ion-matter interaction.

In general, the nuclear collision process corresponds to the collisions between the incident ions and lattice atoms where conservation of energy and momentum is applicable and hence called elastic collisions. During the nuclear collision, the incident ion may scatter back from the surface of the material with the ejection of target atoms (sputtering) or may come into rest after proceeding a few atomic distances beneath the surface. On the other hand, the electronic process is correlated with the interaction of fast ions and electrons of the lattice atoms. This process results in the ionization and excitation of the system leading to emission of X-rays, Auger and secondary electrons [1]. Now the rate of energy loss while traversing a distance x, from the surface can be expressed as the sum of the nuclear and electronic energy loss terms i.e.

$$S = \left(\frac{dE}{dx}\right)_n + \left(\frac{dE}{dx}\right)_e = S_n + S_e$$

where, S_n and S_e represent the nuclear and electronic energy losses [3]. Depending upon the energy of the projectile ion and target materials, the two types of energy losses dominate over each other [1, 3, 4].

For ions carrying energy of the order of a few keV, S_e is dominated by S_n and hence ion led atomic displacements through elastic collisions with the nuclei of the target atoms is expected. In this situation, the recoiling lattice atoms can act as secondary projectiles and are capable of displacing other lattice atoms. This leads to an event known as recoil cascade originating from the initial collisions of the projectile ions and the target atoms. Under such circumstances large number of atomic displacements is predictable and thus results in the formation of plentiful point-defects [5, 6]. The projectile ion after suffering a series of collisions loses its energy and comes into rest at a certain distance from the surface and is known as projected range (R_p). The trajectory of the ion follows a zig zag path as it slows down and experiences frequent collisions

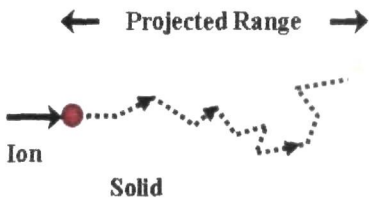

Figure 4.2: The trajectory of the ion during low energy ion irradiation.

(Figure 4.2). This fact accounts for the fact that R_p is always smaller than the path length along the incident direction of the ion [1].

On the other hand, high energy (MeV sacle) ions lose most of the energy through electronic excitations or ionizations of the target atoms and hence in this case, S_e predominates S_n [1, 3, 4]. Due to strong electronic excitation, as the ion passes through the material it leaves an amorphized cylindrical zone known as *latent track*. The possible mechanism of the formation of the latent tracks is explained by two competitive models: *Coulomb explosion* model and the *thermal spike* model. The repulsive electrostatic forces along the cylindrical zone containing the ionized atoms give rise to violent explosions along radial direction until the electronic neutrality is restored. This is known as *Coulomb explosion* which leads to the localized destruction of the lattice [3, 7]. Whereas, the *thermal spike* model reveals that as a result of electronic excitation by the energetic ions, the kinetic energy of the ejected electrons is transmitted to the lattice by electron-phonon interaction. This results in local (lattice) temperature rise well above the melting point of the system. The rise in temperature is followed by the rapid quenching and solidification and thus leads to the formation of amorphous latent tracks [8-10]. The schematic representation of *Coulomb explosion* and *thermal spike* models are shown in Figure 4.3.

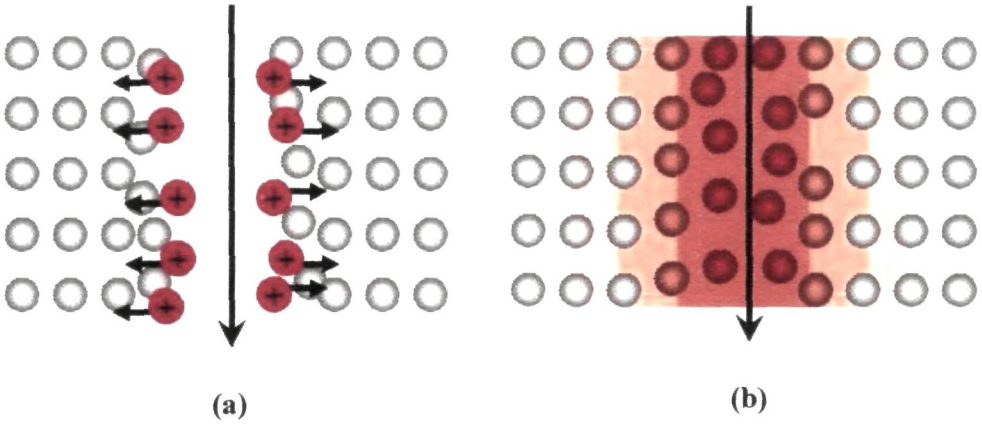

Figure 4.3: Schematic view of (a) *Coulomb explosion* and (b) *thermal spike* model.

Nevertheless, the energy deposition either by S_e or S_n, can result in significant change of the physical properties of the target material [11-13]. It has been previously mentioned that owing to the higher surface-to-volume ratio the nanostructured materials are characterized by plentiful native defects. The irradiation led atomic displacement of the nanostructured materials can result in the creation, annihilation or rearrangement of various point defects [13-16]. Consequently the emission pattern of the nanostructures would be modified largely by the irradiation event. Knowing that, the ZnO nanostructures possess different native defects (like V_{Zn}, Zn_i, V_O and O_i) and owing to enormous energy deposition by irradiation events, their contribution to the luminescence response will be greatly affected.

4.1.1 High energy ion irradiation on ZnO nanostructured system

(a) *ZnO nanoparticles*: The ZnO nanoparticles synthesized using the solid state grinding method (discussed in details in Chapter 2) were subjected to high energy ion irradiation with $S_e > S_n$. Polymers being protecting materials against the agglomeration of nanomaterials, polyvinyl alcohol (PVA) matrix was selected to disperse the nanoparticles [17-19]. The ZnO nanoparticles were dispersed in PVA matrix with approximately 50% volume dispersion in order to avoid agglomeration upon energetic irradiation. For the irradiation experiment, the ZnO nanoparticle-dispersed PVA films (with thickness of ~ 1-2 μm only) were casted on laboratory glass slides (1 x 1 cm^2). Since nitrogen is suitable for surface passivation, it is expected that nitrogen ion irradiation can result in the significant modification of the defect states of ZnO. Again, for uniform energy deposition, the trajectory of the ions should be fairly straight while traversing through the target [1]. In other words, straggling should be as low as possible and the projected range (R_p) of the ions should be greater than the thickness of the films.

Figure 4.4 shows the variation of S_e, S_n and the R_p of nitrogen ion irradiation on ZnO as calculated using SRIM [20]. A moderate value of the ion energy (80-Mev)

was chosen from the plot where both S_e (1.19 x 10^2 eV/Å) and R_p (47.18 μm) bear reasonable magnitudes as shown in Table 4.1. The samples were irradiated in the Material Science chamber under a high vacuum condition (pressure of ~10^{-6} mbar) using 80-MeV N^{4+} ion beams (with a beam current of ~ 1 pnA, particle-nanoampere), available at the 15UD tandem pelletron accelerator of Inter University Accelerator Centre, New Delhi (Appendix 3). The ion beam fluence was measured by integrating the ion charge on the sample ladder, which was insulated from the chamber. The ion fluence was uniformly varied in multiples of 4 viz., 1.25 x 10^{11}, 5 x 10^{11}, 2 x 10^{12} and 8 x 10^{12} ions/cm^2, which were maintained by measuring the duration of irradiation (t) as

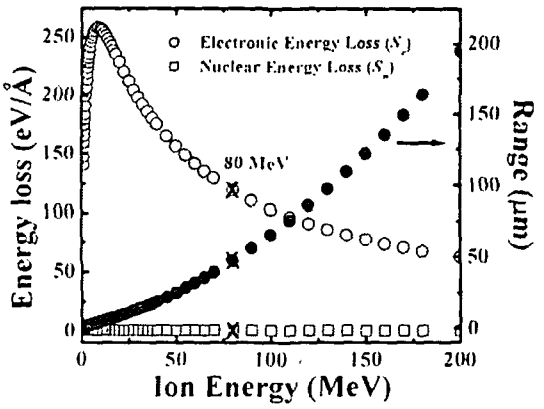

Figure 4.4: Energy dependent variation of energy loss of N^{4+} ion in ZnO.

$$t = \frac{\Phi \times A \times n}{i \times pnA}$$

where 1 pnA corresponds to 6.25 x 10^9 particles/sec.

Table 4.1: The electronic energy loss, (S_e), nuclear energy loss, (S_n), and the stopping range of the 80 MeV N^{4+} ions in PVA and ZnO.

Material	S_e (eV/Å)	S_n (eV/Å)	R_p (μm)
PVA	3.946 x 10	2.201 x 10^{-2}	129.42
ZnO	1.191 x 10^2	6.792 x 10^{-2}	47.18

The PL spectrum of the ZnO nanoparticles was discussed in Chapter 3. Owing to large surface-to-volume ratio, the PL spectrum of the nanoparticles was found to be dominated by the V_O^{++} related defects. The presence of Zn and O related other defects (vacancies, interstitials, anti-sites) were also detected. The PL spectra of

the unirradiated and irradiated nanoparticles (λ_{ex} = 325 nm) are shown in Figure 4.5. The fluence dependent variation of the emission response can be clearly observed in the PL spectra. Upon irradiation with a fluence of 1.25 x 10^{11} ions/cm^2, stronger response of the V_{Zn} related emission was observed [21], while the oxygen vacancy related emission responses (V_O^+, V_O^{++} etc) at the higher wavelength side of the spectrum were drastically reduced [22]. The band edge emission at ~ 385 nm [21], was found to recover upon irradiation. The band-edge emission was found to be intact even in case of irradiation at a higher fluence (5 x 10^{11} ions/cm^2), while comparable emission responses due to the V_{Zn} and Zn_i defects were evident [21]. Moreover, upon irradiation at a fluence of 2 x 10^{12} ions/cm^2, the spectrum became more symmetric with optimum Zn_i and Zn_i^+ related emission [21, 23]. Finally at 8 x 10^{12} ions/cm^2, the spectrum turned into more and more symmetric and peaking at the wavelength position as due to the V_O^+ related defect emissions. At this situation, the signature of the O_i and V_O^{++} defect related emissions were also identified. The evolution of more O_i and V_O^{++} defect is also accountable for the broadening of the emission spectra at this fluence.

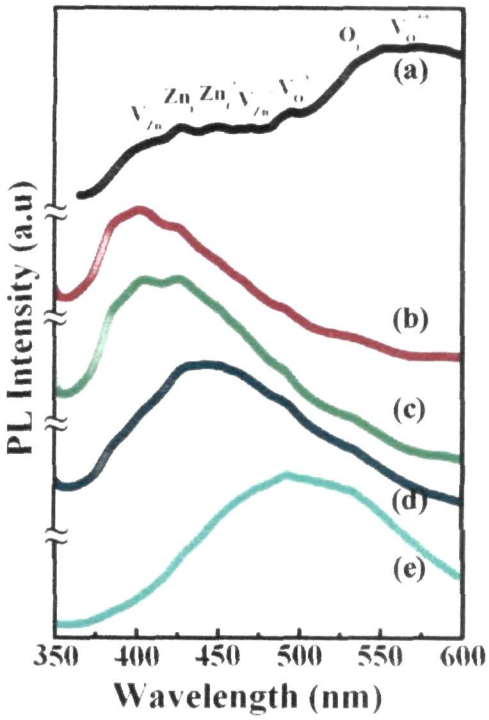

Figure 4.5: Room temperature PL spectra of the (a) unirradiated and 80-MeV N^{4+} ion irradiated nanoparticles with a fluence of (b) 1.25 x 10^{11}, (c) 5 x 10^{11} (d) 2 x 10^{12}, and (e) 8 x 10^{12} ions/cm^2.

It can be observed that with the increase in ion fluence during irradiation, the emission pattern becomes more and more symmetric. Taking the PL maxima into consideration, the variation in asymmetric factor of the emission spectra was

plotted with respect to the ion fluence (Figure 4.6). The asymmetry factor (A_s) is a measure of the tailing of the spectra (Appendix 4). As can be seen in Figure 4.6, the asymmetric factor was found to get reduced (from 3.24 to 1.39) while varying the fluence from 1.25 x 10^{11} to 8 x 10^{12} ions/cm^2. This fact supports the observed improvement in symmetry of the emission spectra with increase in ion fluence. In this case, the lowering of A_s value suggests that the emission is dominated by only one/two types of defects. The modification can be attributed to the fluence dependent creation and annihilation of various defects caused by the significant amount of S_e of the N^{4+} ions in ZnO.

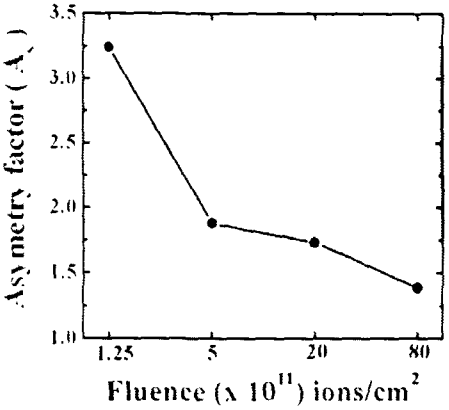

Figure 4.6: Variation in asymmetric factor (A_s) of the emission spectra at different ion fluence.

(a) *ZnO nanorods*: The ZnO nanorods synthesized using microemulsion route (as discussed in Chapter 2), were subjected to 80-MeV N^{4+} ion irradiation. For irradiation purpose, the ZnO nanorod-dispersed PVA films were casted on laboratory glass slides (1 x 1 cm^2) as mentioned in the earlier discussion. In this study the ion fluence was maintained as 1.25 x 10^{11} and 8 x 10^{12} ions/cm^2.

Figure 4.7 shows the room temperature PL spectra of the unirradiated and 80-MeV N^{4+} ion irradiated ZnO nanorods at λ_{ex} = 325 nm. The emission response of the ZnO nanorods, synthesized using the microemulsion route was discussed in the Chapter 3. The typical band edge emission of ZnO was found to get suppressed due to the participation of various defect related emission. The luminescence spectrum was dominated by both neutral and ionized zinc interstitial (Zn_i and Zn_i^+) and zinc vacancy (V_{Zn} and V_{Zn}^-) related defects.

Moreover, oxygen interstitial (O_i) along with single and double ionized oxygen vacancies (V_O^+ and V_O^{++}) were also detected.

The PL spectrum of the irradiated nanorods reveals significant modification as the defect related emission at the higher wavelength side gets improved upon irradiation. At the highest fluence of 8 x 10^{12} ions/cm^2 the PL spectrum became broad compared to the unirradiated one. The central maxima of the emission spectrum of the unirradiated nanorods is situated in the violet region, while the sample irradiated at the highest fluence is located in the blue region of the electromagnetic spectrum. To make a clear assessment of the defect induced modification, Gaussian fitting of the individual PL spectra of the unirradiated and irradiated nanorods was studied (Appendix 5).

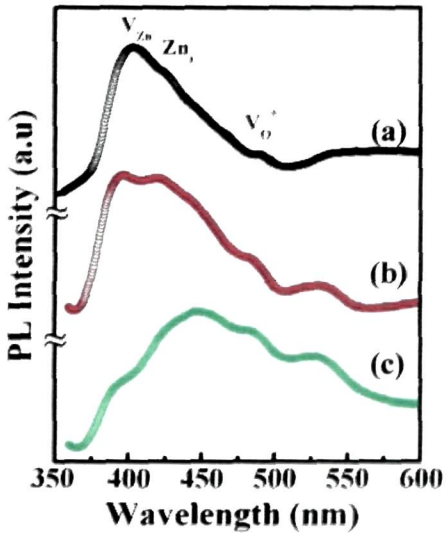

Figure 4.7: The room temperature PL spectra (λ_{ex} = 325 nm) of (a) unirradiated and N^{4+} ion irradiated nanorods at (b) 1.25 x 10^{11} and (c) 8 x 10^{12} ions/cm^2.

The typical band edge emission of ZnO was recovered upon Gaussian fitting of the PL spectra of the N^{4+} ion irradiated nanorods (Figure 4.8(a)). Unlike the PL spectrum of the unirradiated nanorods, the nanorods irradiated with a fluence of 1.25 x 10^{11} ions/cm^2 revealed the dominance of Zn_i related emission over V_{Zn} ones. This was accompanied by the rise in the emission response due to Zn_i^+ defects compared to the unirradiated one. Though the V_O^{++} defect related emission is totally quenched, V_{Zn}^-, V_O^+ and O_i defect related emissions are noticeable. On the other hand upon irradiation with a fluence of 8 x 10^{12} ions/cm^2, there is a significant change in the PL spectrum compared to the unirradiated one. As evident from Figure 4.8(b), the emission due to Zn_i^+ defects shoots up and becomes comparable to the Zn_i related emission. Further, the V_{Zn}^- related

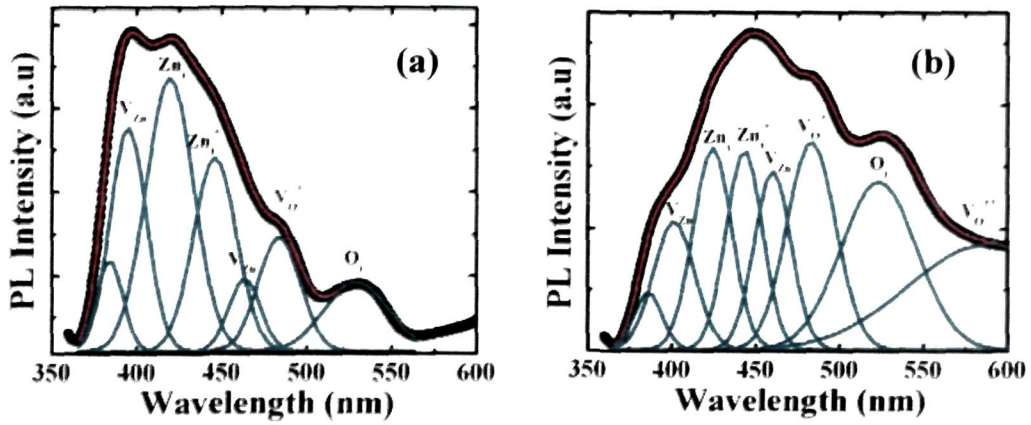

Figure 4.8: Gaussian fitting of the PL spectra of the samples irradiated at a fluence of (a) 1.25 x 10^{11} and, (b) 8 x 10^{12} ions/cm^2.

emission peak turns out to be prominent and becomes higher than the emission due to V_{Zn} defects. It can be seen in the PL spectrum of the nanorods irradiated at the highest fluence, there is a significant development in the V_O^+ and O_i related emissions. The evolution of V_O^{++} related emission peak was also witnessed in the higher wavelength side. The development of the oxygen related emission peaks is responsible for the broadening of the PL spectrum of the nanorods irradiated at the highest fluence.

Figure 4.9 depicts the variation of V_{Zn}/Zn_i, Zn_i^+/Zn_i and V_{Zn}^-/V_{Zn} emission intensity ratio with the ion fluence. In contrast to the unirradiated one, upon irradiation, the V_{Zn}/Zn_i ratio decreases with increase in ion fluence, while V_{Zn}^-/V_{Zn} ratio shows an increasing trend. This suggests that upon irradiation the Zn_i defect concentration increases with respect to V_{Zn} defects, while the newly formed V_{Zn} defects as a result of Zn_i formation gets converted to V_{Zn}^- defects. During the irradiation event, a substantially large amount of S_e (1.19 x 10^2 eV/Å) results in the formation of Zn_i defects and helps in the conversion of V_{Zn} defects to V_{Zn}^- defects. Again, the conversion of Zn_i defects to Zn_i^+ defects is also observable from the increment nature of the intensity ratio of Zn_i^+/Zn_i defects with fluence. Enduring this process at the highest fluence, the Zn_i^+ related emission peak gets improved giving a nearly equal contribution to the emission due to Zn_i defects. Additionally, at this fluence the V_{Zn}^-/V_{Zn} ratio also increases abruptly

owing to the conversion of most of the V_{Zn} to V_{Zn}^{-} defects. The conversion of the neutral to the ionized defects turns out to be effective at the highest fluence owing to the fact that S_e led enormous energy deposition increases as a result of increase in ion bombardments during that fluence. Conversely, the quenching of V_O^{++} defects by O_i has led to the increase in V_O^{+}/O_i ratio (~ 1.8) at a fluence of 1.25 x 10^{11} ions/cm^2 compared to the pristine one (~ 0.9). Whereas, at 8 x 10^{12} ions/cm^2 the V_O^{+}/O_i ratio decreases (~ 1.24) owing to increase in O_i defects as the V_O^{++} defects could reappear at that fluence (Figure 4.8(b)).

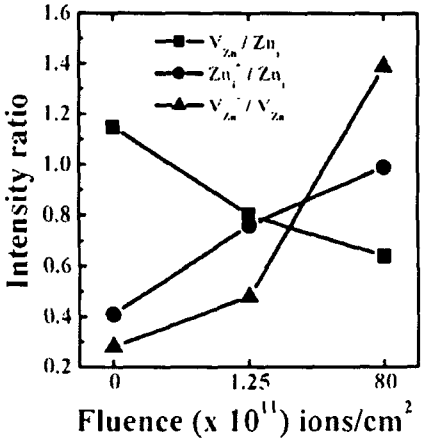

Figure 4.9: Variation of the emission intensity ratio of different kinds of defects.

Therefore the fluence dependent modification of the emission response of the nanoparticle and nanorod systems can be observed as a result of 80-MeV N^{4+} irradiation on the nanostructures. Using nitrogen ion irradiation one can recover not only band edge emission but also improve the defect related tunable and selective emission [24].

4.1.2 Low energy ion irradiation on ZnO nanorod system

To investigate the S_n (> S_e) led modification in the luminescence response of the ZnO nanorods, 80-keV Ar^+ ion irradiation was performed on the nanorods. Similar to the earlier study PVA dispersed nanorods were casted in laboratory glass slides (1 x 1 cm^2) for the irradiation experiment. To avoid the chances of formation of complexes among the projectile ions and with the atoms of the target material, the use of inert gas ions is encouraged. Argon having a moderate mass was considered as a projectile ion for the irradiation experiment. A reasonable value of ion energy was chosen with S_n > S_e. Figure 4.10 shows the energy loss

profile of the ion in ZnO (density 5.6 g/cc) versus ion energy obtained by using the SRIM-2008 software [20].

In the present experiment, 80-keV Ar^+ ion was chosen so that S_n possesses a higher value than S_e. The values of S_e, S_n, and R_p associated with 80-keV Ar^+ ion irradiation on ZnO and PVA have been shown in Table 4.2. The irradiation experiment on the samples was performed using the low energy ion beam facility (LEIBF) available at Inter University Accelerator Centre, New Delhi (Appendix 3). The samples were put in ladder, which was insulated from the chamber and were subjected to irradiation. The beam current was kept ~ 1 μA, while the fluence was varied as 1 x 10^{13} and 1 x 10^{15} ions/cm^2. The ion fluence (Φ) was maintained by measuring the duration of irradiation (t) given by

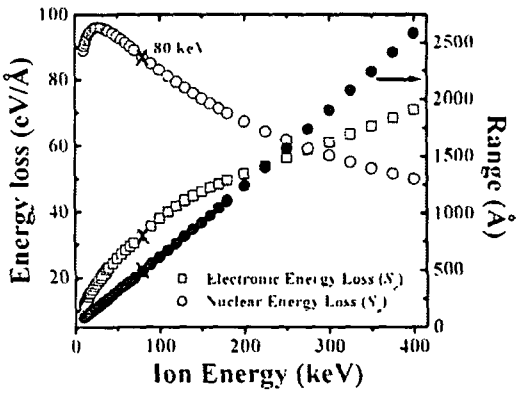

Figure 4.10: Energy dependent variation of energy loss of Ar^+ ion in ZnO.

$$t = \frac{\Phi \times A \times n \times q}{i}$$

where, A is the area of the sample, n is the charge state, i is the beam current and q being the electronic charge.

Table 4.2: Electronic energy loss (S_e), Nuclear energy loss (S_n) and Projected range (R) of the 80 keV Ar^+ ion irradiation.

Material	**Density** (gm/cc)	S_e (eV/Å)	S_n (eV/Å)	R_p (Å)
PVA	1.2	28.33	40.08	1172
ZnO	5.6	32.54	87.07	491

Since the projected range of the ions (491 Å) is very less than the thickness of the films (~ 1 μm), it is expected that upon irradiation the surface of the samples will be affected at large. To extract out the irradiated nanorods, the films were first

dipped in ethanol and then subjected to ultrasonication for 5-10 min. The nanorods those are located on the surface of the film and have experienced the irradiation, will be able to overcome the matrix encapsulation under ultrasonic agitation. Finally, the as-received solution of the nanorods and ethanol were studied independently in the differential mode to extract emission response due to irradiated nanorods.

The room temperature PL spectra of the unirradiated and Ar^+ ion irradiated nanorods are depicted in Figure 4.11. The variation in the luminescence response of the irradiated samples can be distinguished clearly. Upon irradiation, the modification of the emission spectra arises owing to significant variation in the native defect related radiative emissions. In order to distinguish individual contribution of these defects, the overall PL responses were Gaussian fitted and are shown in (Figure 4.12(a,b)).

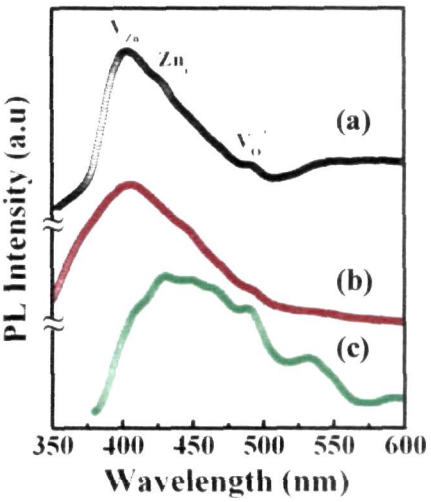

Figure 4.11: Room temperature PL spectra (λ_{ex} = 325 nm) of (a) unirradiated and Ar^+ ion irradiated nanorods at (b) 1 x 10^{13} and (c) 1 x 10^{15} ions/cm^2.

Unlike the unirradiated nanorods, the nanorods irradiated with a fluence of 1 x 10^{13} ions/cm^2 reveal a broad PL spectrum. The broadening is a consequence of the evolution of ZnO related band edge emission peak at ~ 375 nm [21]. The V_{Zn} defect related emission peak still remains prominent, while the Zn_i related peak gets lowered with respect to the former peak. Though the emission due to O_i defects gets substantially quenched, the emission peaks corresponding to Zn_i^+ and V_{Zn}^- still exist. In contrast, in the PL spectrum of nanorods irradiated with the fluence of 1 x 10^{15} ions/cm^2, the band edge emission gets suppressed completely, whereas both Zn_i and Zn_i^+ defect related emissions are enhanced by appreciable amounts. In addition to that the V_{Zn} and V_{Zn}^- related emission peaks get lowered

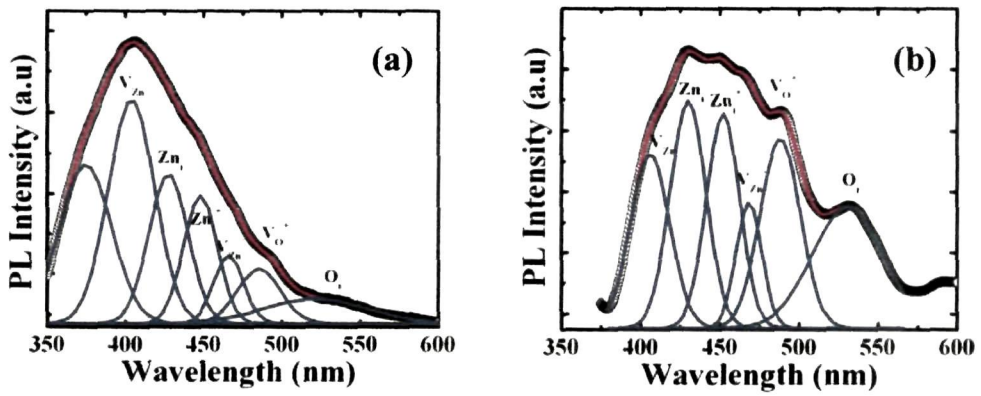

Figure 4.12: Gaussian fitting of the PL spectra of the irradiated samples at (a) 1 x 10^{13} and, (b) 1 x 10^{15} ions/cm^2.

compared to the interstitials (both neutral and ionized). Furthermore, the V_O^+ related emission gets improved and as a result, the intensity of O_i related emission shoots up. It is now evident that there is a fluence dependent variation in the defect related emissions. This variation arises because of the irradiation led creation and annihilation of the point defects in the nanorod systems. To justify the fact creation/annihilation of various defects, the Zn and O related vacancy-to-interstitial emission intensity ratios have been compared for the unirradiated and irradiated nanorods.

From Figure 4.13, it is apparent that in case of the unirradiated ZnO nanorods, the V_{Zn}/Zn_i ratio is just greater than unity (~ 1.14) and therefore, represents a nearly equal contribution to the PL emission by these two types of defects. Conversely, upon irradiation the nanorods with a fluence of 1 x 10^{13} ions/cm^2, a higher value of V_{Zn}/Zn_i ratio (~ 1.5) is found, which corresponds to the increase in V_{Zn} defects or decrease in Zn_i related defects. The increase of V_{Zn} is ascertained and can be assigned to the irradiation led nuclear energy loss which is capable of knocking out Zn atoms form its regular lattice site. The increase of V_{Zn} defects would also lead to the increase of Zn_i defects. On the contrary, it is probable that during the irradiation event, Zn_i defects are formed and latter converted to Zn_i^+ ones. It can be observed in the PL spectra of Figure 4.12(a,b), that there is a variation in the intensity of the Zn_i and Zn_i^+ related emissions of the nanorods before and after

irradiation. This can be clearly observable in Figure 4.13, where the sharp rise of the Zn_i^+/Zn_i ratio, of the nanorods irradiated at 1 x 10^{13} ions/cm^2, compared to the pristine one, gives the hint of the increase of Zn_i^+ defects upon irradiation. Therefore, the decrease in Zn_i defects can be originated from the transformation of Zn_i to Zn_i^+ defects by ion impact. As obtained from SRIM 2008 program [20], though the S_e is smaller than the S_n (Table 4.2), it is capable of ionizing a few atoms and can result in the conversion of some Zn_i defects to Zn_i^+ defects. On the other hand, upon irradiation with the highest fluence (1 x 10^{15} ions/cm^2), the scenario becomes distinctly different owing to the suppression of some V_{Zn} defects as predicted by the lower value of V_{Zn}/Zn_i ratio (<1). Since Zn_i atoms are mobile even at room temperature [25, 26], it is expected that during irradiation, several Zn_i atoms migrate to the V_{Zn} defects, resulting in the reduction of these defects.

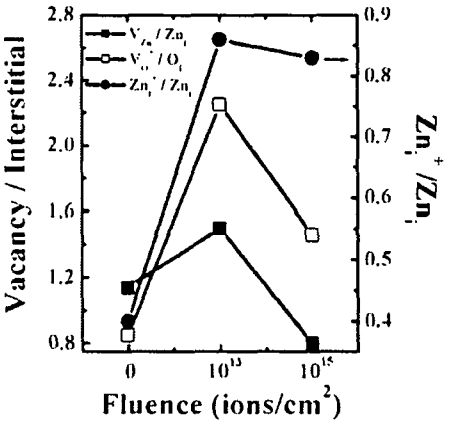

Figure 4.13: The variation of zinc and oxygen vacancy-to-interstitial with ion fluence. Irradiation dependent ionized zinc to neutral zinc interstitial response is also depicted in the plot.

Again, the V_O^+/O_i ratio becomes less than unity for the unirradiated nanorods due to the dominance of O_i defects. Whereas, the ratio acquires quite a large value upon irradiation with a fluence of 1 x 10^{13} ions/cm^2, owing to the fact that O_i defects are being used in the annihilation of V_O^{++} defects during irradiation. In this case the annihilation of V_O^{++} defects is responsible for the evolution of the band-edge emission peak of ZnO. Finally, in case of the irradiation at a fluence of 1 x 10^{15} ions/cm^2, V_O^+ defects are created, and hence more O_i defects were formed. The V_O^+/O_i ratio at this fluence acquires a moderate value due to the simultaneous formation of V_O^+ and O_i defects.

Therefore, it has been observed that upon 80-keV Ar^+ ion irradiation, the nuclear energy loss (S_n) is responsible for the formation of V_{Zn} and V_O^+ defects, along with the annihilation of V_O^{++} defects through O_i atoms. The substantial amount of electronic energy loss (S_e) by the Ar^+ ions also participates in the defect modification process and converts the newly formed Zn_i to Zn_i^+ defects [27].

4.2 Theoretical interpretation of the observed phenomena

It is evident from both low and high energy ion irradiation on ZnO nanostructures that the Zn related defect formation is more favorable in all fluences, while the O related defect formation is mainly observed at higher fluence values. The origin of the defect dynamics with regard to creation and annihilation of vacancies and interstitials owing to energetic ion irradiation can also be explored through suitable theoretical justification.

In an embedded system, both the matrix as well as dispersed nanostructures experiences the impact of ions during irradiation. As per calculation from SRIM 2008 program, the projected range (R_p) of 80-MeV N^{4+} ions is ~ 129.42 μm (Table 4.1). Whereas, the 80-keV Ar^+ ions are capable of traversing upto a distance of ~ 1172 Å (Table 4.2) within the PVA matrix. This suggests that during N^{4+} irradiation all the nanorods along the path of the ion will respond to the incoming ion. On the contrary during Ar^+ ion irradiation, the nanorods located within its range only, would experience the impact of the ions. In order to visualize the events more clearly, it is assumed that the ions after traversing through the matrix encounter only one nanoscale rod to show its effect. The energy deposition process and the outcome during the impact of two different types of irradiation events are discussed:

(a) *80-MeV N^{4+} ion irradiation*: As the energy deposited in the PVA film is small compared to the incident energy (80-MeV) of the projectile ions, the effective

energy realized on the individual nanorods, to a good approximation, will be ~ 80-MeV. It has been mentioned that, the energy deposited by the projectile ions would dissipate to the atomic subsystem (via electron-phonon coupling) following the *thermal spike* model [28]. The energy deposited in the core is maximum and decreases gradually as one moves away from it and hence, the development of several concentric cylindrical zones (each with definite energy values) can be expected (Figure 4.14). Considering the fact that cylindrical regimes are inseparable from each other, three independent cylinders; central, middle and the outer have been considered as shown in Figure 4.14.

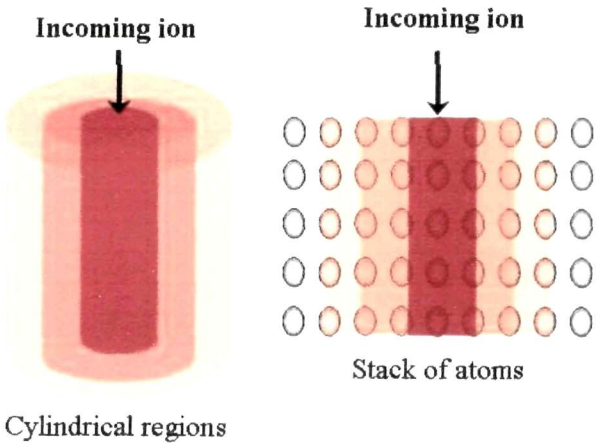

Figure 4.14: Schematic diagram of the cylindrical zones created upon high energy ion irradiation.

Since the nanorods consist of N number of atoms, the volume of a nanorod is equal to the volume of N atoms [29]. If x_i (i=1,2,3....) is the atomic percentage of each element of diameter d_i (i=1,2,3...) present in a nanorod of diameter D and length L, then the number of atoms present in the nanorod will be given by

$$N = \frac{1.5 f D^2 L}{\sum x_i d_i^3} \tag{4.1}$$

where f is the packing fraction and $\sum x_i = 1$.

If δ and l are the diameter and the length of any cylindrical zone, then the number of atoms present in it is given by

$$n = \frac{N\delta^2 l}{D^2 L} \tag{4.2}$$

From the basic understanding point of view the amount of energy deposited during the *thermal spike* event refers to the product of the electronic energy loss (S_e) and the electron-phonon coupling efficiency (g) [30, 31]. So, the total energy deposited along the path of the projectile ion is gS_el and the amount of energy received by each of the atoms in the cylindrical region of diameter δ will be

$$E = \frac{g S_e l}{\frac{N\delta^2 l}{D^2 L}} = \frac{g S_e D^2 L}{N\delta^2} \tag{4.3}$$

Assuming g = 0.4 [31], the variation of the energy received by each atom of the cylindrical regions can be predicted (Figure 4.15).

In Figure 4.15, it can be seen that the energy deposited per atom decreases as the diameter of a cylinder increases from the centre. For Zn and O atoms in ZnO lattice, the displacement energy varies as 18.5 eV and 41.4 eV respectively [32]. The energies equivalent to the displacement energies for the Zn and O atoms are availed by the cylindrical region of diameters (δ) ~ 0.50 nm and 0.34 nm respectively. As shown in equation (4.2), the number of atoms n, present in the cylindrical region is directly proportional to the square of δ. Thus the number of Zn atoms is larger than the number of O atoms so as to acquire the effective displacement energies. Consequently, upon irradiation, the formation of Zn related defects is more favorable than O related defects. At a higher fluence

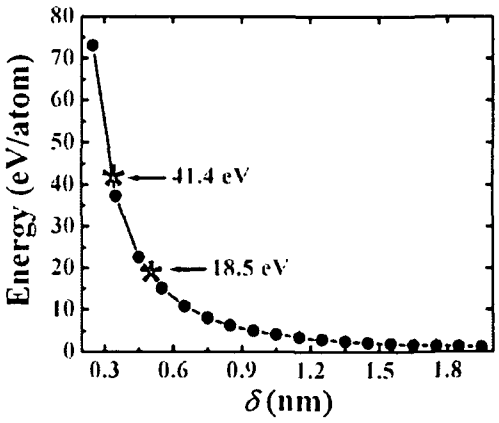

Figure 4.15: Variation of the energy deposited per atom during irradiation and the diameter of the cylindrical zones.

the creation of O related defects is obvious owing to the overlapping of two or more cylindrical regions as a result of increased ion fluence.

(b) *80-keV Ar^+ ion irradiation*: The total energy loss per unit length of the ion in PVA medium is $S = S_e + S_n$. Now, the initial energy of the ion before striking a nanorod surface is $(80 - S.z)$ keV, where z is the distance traversed by the ion from the surface of the PVA film to the nanorod surface (Figure 4.16). Three arbitrary values of z such as 5, 500 and 1000 Å are considered, which correspond to the nanorod positions just at the surface, in the middle and at the extreme end of the matrix but all within the projected range (R_p) of the ions. Consequently, the initial energy of the ion before striking the nanorod will be 79.66, 45.8 and 11.6 keV respectively. Using these three values of the initial energy the correponding S_e, S_n, and projected range (R_p) of the Ar^+ ion within the ZnO/PVA system have been calculated as shown in Table 4.3.

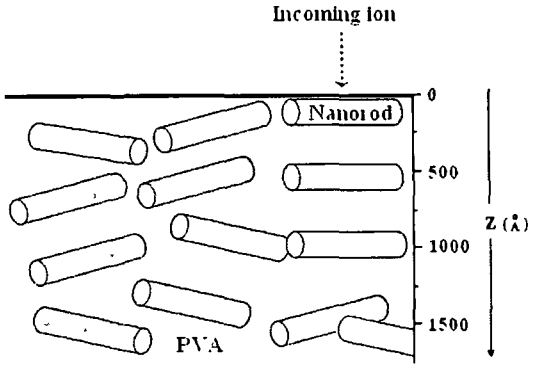

Figure 4.16: Scheme of the ZnO nanorods distributed within the matrix.

Table 4.3: Electronic energy loss (S_e), nuclear energy loss (S_n) and projected range (R) of the ZnO nanorods situated at different positions in the PVA matrix.

z (Å)	$80 - Sz$ (keV)	S_e (eV/Å)	S_n (eV/Å)	R_p (Å)
5	79.66	32.5	87.1	489
500	45.8	24.6	94.1	289
1000	11.6	12.4	90.9	91

It is now obvious that the energy of the ions decrease as it penetrates within the solid i.e. encounter more and more atomic planes from the point of impact and traverses to a distance equal to the projected range of the ion. For the ions having

energy in the keV scale, the deposited energy can be assumed interms of some co-axial conical zones as schematically shown in Figure 4.17. The maximum length of the axis of a cone will be equal to the R_p, whereas the maximum radius will be the distance between the point of impact, and the spot where the deposited energy becomes vanishingly zero. Since the energy deposition is continuous and spreads from the point of impact towards the other parts, the conical regimes are also inseparable from each other. However, for the sake of clarity and demonstration, three independent cones; central, middle and the outer have been considered as shown in Figure 4.17.

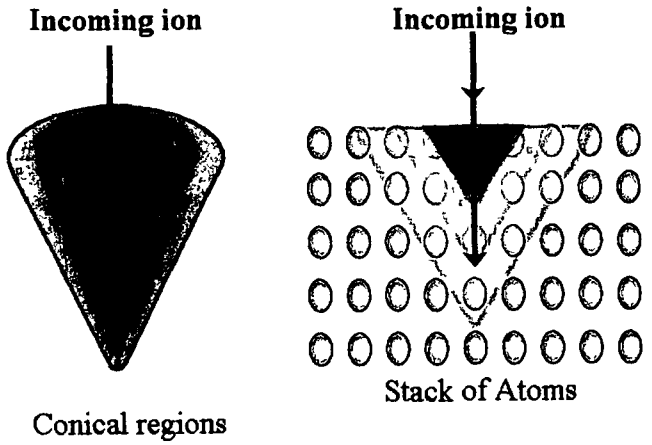

Figure 4.17: Schematic diagram of the conical zones created upon low energy ion irradiation.

Considering the volume of any conical region to be v, then the number of atoms present in a conical zone will be given by,

$$n = \frac{4Nv}{\pi D^2 L} \tag{4.4}$$

where, N is the number of atoms present in the nanorods as given by equation (4.1).

Now, the total energy deposited by an ion within the effective region in the material, will be equal to S_n times the projected range (R_p) of the ion within that

material. Therefore, the energy deposited per atom within a definite conical zone is given by,

$$E = \frac{S_n R_p}{n} = \frac{\pi D^2 L S_n R_p}{4Nv} \tag{4.5}$$

Next, using the various values of S_n and R_p (from Table 4.3), in the above equation, it can be found that the energy deposited per atom decreases as the volume of the cones increases from the centre (Figure 4.18). This trend is maintained in all the nanorods irrespective of their position within the matrix (i.e. whether nanorods are on the surface or in the interior). Upon irradiation, the atoms of any cone that acquire an energy greater than the displacement energies of Zn and O atoms will be able to get displaced from their regular lattice site. The energy equivalent to the displacement energy of Zn in ZnO (18.5 eV) corresponds to the imaginary cones having approximate volumes of 17.5, 11.5 and 3.7 nm^3 for z values of 5, 500 and 1000 Å respectively. Whereas, for O atoms, the volume of the cones corresponding to its displacement energy (41.4 eV) are 7.6, 4.7 and 1.5 nm^3 for z values of 5, 500 and 1000 Å; respectively. As the number of atoms present in a cone is proportional to the volume of the cone (equation (4.4)), in acquiring displacement energy, the number of Zn atoms will be definitely larger than the O atoms. Hence, upon irradiation, the Zn atoms are most affected irrespective of the position of the nanorods within the matrix and thereby resulting variation of Zn related defects.

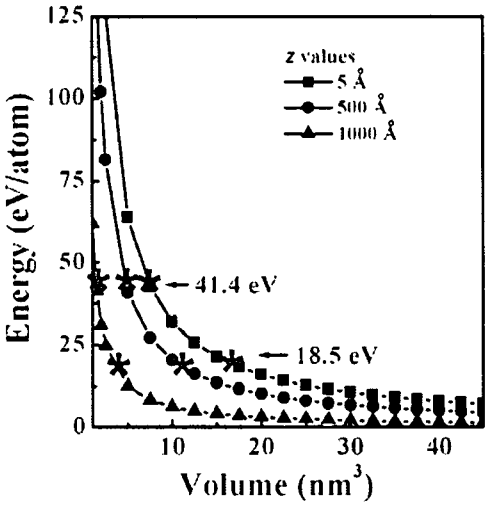

Figure 4.18: Variation of energy deposited per atom during irradiation and the volume of the cones.

Now, the overlapping of two or more energetic conical regions is not considered in the above discussion, which comes out to be an important aspect as the fluence increases. With the increase in ion fluence, the probability of overlapping of the conical zones becomes significant. This is due to the fact that the nanorods experience more and more ion impacts leading to the formation more conical regions. In this situation, the atoms present in the overlapping region of two conical zones posses more energy than the atoms beyond that region. As evident in the present system at a fluence of 1 x 10^{15} ions/cm^2, it is possible that the atoms present in the overlapping region acquire an energy equivalent to the displacement energy of O atoms and create more V_O^+ and O_i defects.

4.3 Concluding remarks

Low and high energy ion beams have been used to modify the luminescence response of ZnO nanostructures. As an important observation the typical band edge emission was found to get evolve steadily upon irradiation. The enormous electronic energy loss (S_e) during 80-MeV N^{4+} ion irradiation on the ZnO nanostructures has been found to be responsible for the symmetric and selective emission response via creation, annihilation and ionization of the defects. On the contrary, the significant nuclear energy loss (S_n) during 80-keV Ar^+ ion irradiation on ZnO nanorods were found to accountable for the creation, annihilation and ionization of various point defects of ZnO. It has been speculated that the energy deposition upon irradiation takes place in some co-axial cylindrical and conical regions for high energy and low energy ions respectively. At a low fluence, the formation of Zn related defects is favorable as compared to oxygen ones owing to the relatively smaller displacement energy of Zn in ZnO system. The overlapping of two or more cylindrical or conical regions at a higher fluence, is accountable for the evolution of more O related defects at that fluence. The diverse but highly controllable emission response, achieved by irradiation of properly chosen ion species, energy and fluence could furnish long-standing demand in ultrafast lasing, display and imaging devices.

References:

[1] Williams, J. S. Materials modification with ion beams, *Rep. Prog. Phys.* 49, 491-587, 1986.

[2] Lindhard, J. & Schad, M. Energy dissipation by ions in the keV region, *Phys. Rev.* 124, 128-130, 1961.

[3] Mehta, G.K. Materials modification with high energy heavy ions, *Nucl. Instr. and Meth. in Phys. Res. Sect. A* 382, 335-342, 1996.

[4] Trautmann, C. Modifications induced by swift heavy ions, *Bull. Mater. Sci.* 22 (3), 679-686, 1999.

[5] Swanson, M. L. et al. Damaged regions in neutron-irradiated and ion-bombarded Ge and Si, *Rad. Effects* 9 (3-4), 249-256, 1971.

[6] Hensel, H. & Urbassek, H. M. Implantation and damage under low-energy Si self-bombardment, *Phys. Rev. B* 57, 4756-4763, 1998.

[7] Fleischer, R. L. et al. Ion explosion spike mechanism for formation of charged-particle tracks in solids, *J. Appl. Phys.* 36, 3645-3652, 1965.

[8] Toulemonde, M. et al. Transient thermal process after a high-energy heavy-ion irradiation of amorphous metals and semiconductors, *Phys. Rev. B* 46(22), 14362-14369, 1992.

[9] Dufour, C. et al. A high-resistivity phase induced by swift heavy-ion irradiation of Bi: a probe for thermal spike damage? *J. Phys.: Condens. Matter* 5, 4573-4584, 1993.

[10] Norman, A. Thermal spike effects in heavy-ion tracks, Rad. Res. Suppl. 7, 33-37, 1967.

[11] Brown, R. A. & Williams, J. S. Crystalline-to-amorphous phase transformation in ion-irradiated GaAs, *Phys. Rev. B* 64(15), 155202 (1-6), 2001.

[12] Meillon, S. et al. Changes in magnetic properties of magnetite Fe,O, ceramics induced by high energy heavy ion irradiation, *Nucl. Instr. and Meth. in Phys. Res. B* 107, 363-367, 1996.

[13] Kucheyev, S. O. et al. Ion-beam-produced structural defects in ZnO, *Phys. Rev. B* 67, 094115 (1-11), 2003.

[14] Pons, D. & Bourgoin, J. C. Irradiation-induced defects in GaAs, *J. Phys. C: Solid State Phys.* 18, 3839-3871, 1985.

[15] Krasheninnikov, A. V. et al. Formation of ion-irradiation-induced atomic-scale defects on walls of carbon nanotubes, *Phys. Rev. B* 63, 245405 (1-6), 2001.

[16] Chattopadhyay, S. et al. Interplay of defects in 1.2 MeV Ar irradiated ZnO, *J. Appl. Phys.* 107, 113516 (1-8), 2010.

[17] Mohanta, D. et al. Optical absorption study of 100-MeV chlorine ion-irradiated hydroxyl-free ZnO semiconductor quantum dots, *J. Appl. Phys.* 92, (12), 7149-7152, 2002.

[18] Mohanta, D. et al. Influence of ion bombardment on the photoluminescence response of embedded CdS nanoparticles, *Central Eur. J. Phys.* 4(2), 187-195, 2006.

[19] Bayan, S. et al. Development of Tb-doped ZnO nanorods: Effect of nitrogen ion irradiation on luminescence and structural evolution, *Phys. Status Solidi A* 207 (8), 1859-1863, 2010.

[20] Zeigler, J.F. et al. *SRIM (2008) – The Stopping and Range of Ions in Matter.* www.srim.org, 2008.

[21] Lin, B. et al. Green luminescent center in undoped zinc oxide films deposited on silicon substrates, *Appl. Phys. Lett.* 79, 943-945, 2001.

[22] Ye, J. D. et al. Correlation between green luminescence and morphology evolution of ZnO films, *Appl. Phys. A* 81, 759-762, 2005.

[23] Tam, K. H. et al. Defects in ZnO nanorods prepared by a hydrothermal method, *J. Phys. Chem. B* 110, 20865-20871, 2006.

[24] Bayan, S. & Mohanta, D. Effect of 80-MeV nitrogen ion irradiation on ZnO nanoparticles: Mechanism of selective defect related radiative emission features, *Nucl. Instr. and Meth. in Phys. Res. B* 269, 374–379, 2011.

[25] Rackauskas, S. et al. Mechanistic investigation of ZnO nanowire growth, *Appl. Phys. Lett.* 95, 183114 (1-3), 2009.

[26] Potzger, K. & Zhou, S. Non-DMS related ferromagnetism in transition metal doped zinc oxide, *Phys. Status Solidi B* 246 (6), 1147–1167, 2009.

[27] Bayan, S. & Mohanta, D. Interplay of native defect-related photoluminescence response of ZnO nanosticks subjected to 80 keV Ar ion irradiation, *Rad. Effects and Defects Sol.* 166 (11), 884–893, 2011.

[28] Dufour, C. et al. Transient thermal process induced by swift heavy ions: Defect annealing and defect creation in Fe and Ni, *Bull. Mater. Sci.* 22 (3), 671-677, 1999.

[29] Qi, W.H. Generalized Surface-Area-Difference model for cohesive energy of nanoparticles with different compositions, *J. Mater. Sci.* 41, 5679-5681, 2006.

[30] Szenes, G. et al. Tracks induced by swift heavy ions in semiconductors, *Phys. Rev. B* 65, 045206 (1-5), 2002.

[31] Szenes, G. et al. Tracks induced in TeO_2 by heavy ions at low velocities, *Nucl. Instr. and Meth. in Phys. Res. B* 166-167, 949-953, 2000.

[32] Look, D. C. et al. Residual native shallow donor in ZnO, *Phys. Rev. Lett.* 82 (12), 2552- 2555, 1999.

Chapter 5

Investigation on nanostructure growth and elongation principle

The fabrication of quality nanostructures with desired shape and size has become feasible owing to the advancement and sophistication achieved in various chemical and physical routes. Over the years, a variety of nanomaterials with a diverse range of size have been examined for various technological applications. However from the theoretical stand-point, there is always a lack of in depth understanding of the nanostructure growth process. A sound knowledge of the kinetics of the growth process is of primary importance to describe and correlate different morphology of nanostructures with definite properties. The present chapter emphasizes on theoretical models highlighting temperature assisted elongation phenomenon and ion irradiation induced controlled growth of ZnO nanostructures.

5.1 Role of surface energy in nanostructure growth

Atoms of a solid surface contain dangling or unsaturated bonds due to the fewer nearest neighbor atoms or coordination number. Owing to the presence of these dangling bonds on the surface, the surface atoms experience an inward pull from the sub-surface atoms. The extra amount of energy possessed by the surface atoms due to the inward pull is described as the surface energy (γ) of the material. Due to the higher surface to volume ratio, the nanostructures possess higher surface atoms compared to the core atoms and higher surface energy. The higher surface energy of the nanostructures makes them thermodynamically unstable and this is the reason why they grow in size in order to reduce the overall surface energy. On attaining sufficient energy the individual nanostructures combine together to reduce the overall surface area and thereby the surface energy. The relevant mechanism of combining individual nanosystems into larger sized structures include (a) sintering, in which individual structures merge together and (b) Ostwald ripening, in which relatively large structures grow at the expense of smaller ones [1, 2]. In general, the sintering process is significant at a higher temperature, but for nanomaterials, due to high surface energy, sintering becomes prominent at moderate temperatures. This process is associated with the solid

state diffusion, evaporation-condensation, viscous flow and dislocation creep [1]. On the other hand, the Ostwald ripening process is considerable in a system that contains nanomaterials of dissimilar size. In this process two or more individual nanostructures become a single system. It is associated with the growth via atomic diffusion from the smaller nanostructures to the larger one until the former ones disappear completely. Figure 5 1 depicts the schematic representation of sintering and Ostwald ripening process. Microscopically, the differential surface energy of the surfaces with different curvature is the driving force for the mass transport during sintering and Ostwald ripening process [2]. The formation of the 1D ZnO nanostructures via thermal annealing process can be understood from the relevant mass transport mechanism appreciable at sufficiently high temperature.

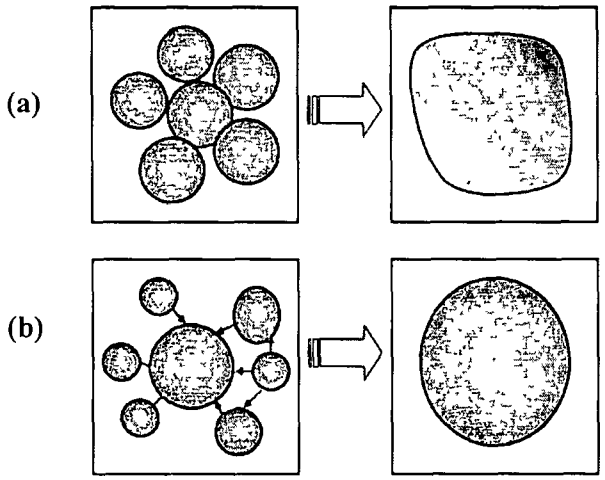

Figure 5.1: Scheme of (a) sintering and (b) Ostwald ripening process.

As discussed in Chapter 2, the 1D ZnO nanostructures were obtained upon annealing the PVA encapsulated $Zn(OH)_2$ species at different temperatures at different instances. During the annealing process (within temperature 60-80 °C) the $Zn(OH)_2$ species gets converted into ZnO The formation of ZnO nanoparticles with a wide range of size distribution was confirmed from the SEM and TEM images as discussed in Chapter 2. Now, since the annealing temperatures were higher than the decomposition temperature of PVA (~ 230 °C),

the ZnO nanoparticles gradually lose support from the matrix. In this situation, the growth phenomena can be described by the Ostwald ripening process.

In the absence of the matrix encapsulation two spherically symmetric free-standing nanoparticles of radii R_1 and R_2 (where $R_2 > R_1$) are considered (shown in Figure 5.2). Now, owing to the difference in size, the chemical potentials (work per atom) of the two nanoparticles will be dissimilar. The chemical potential of the two nanoparticles can be defined using the Young-Laplace equation [1] and are given as

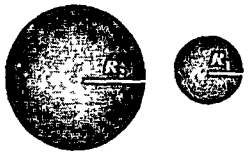

Figure 5.2: Two isolated nanoparticles of different radii ($R_2 > R_1$).

$$\mu_1 = 2\gamma\frac{\Omega}{R_1} \tag{5.1}$$

$$\mu_2 = 2\gamma\frac{\Omega}{R_2} \tag{5.2}$$

where, μ_1 and μ_2 are the chemical potentials of the respective particles. γ and Ω being the surface energy and atomic volume respectively.

Now, the difference in chemical potential between the two particles will be given by [1],

$$\Delta\mu = 2\gamma\Omega\left[\frac{R_2 - R_1}{R_1 R_2}\right] = kT\ln\frac{P_{R_1}}{P_{R_2}}. \tag{5.3}$$

Here, P_{R_1} and P_{R_2} are the vapor pressures of the two particles, alongwith k and T are the Boltzmann constant and the temperature of the surrounding environment. The above equation represents the change in chemical potential while transferring an atom from a particle of radius R_1 to R_2. The chemical potential of a system increases with the temperature and hence with the supply of external heat. Now, if the chemical potential increases, the term in the parenthesis will tend to increase for fixed values of γ and Ω.

Therefore,

$$\left[\frac{R_2 - R_1}{R_1 R_2}\right]_{After\ Heating} > \left[\frac{R_2 - R_1}{R_1 R_2}\right]_{Before\ Heating}$$

$$\Rightarrow (R_2 - R_1)_{After\ Heating} > (R_2 - R_1)_{Before\ Heating} \quad or, \quad (R_1 R_2)_{After\ Heating} < (R_1 R_2)_{Before\ Heating}$$

The above two conditions will be valid only if the numerical value of R_2 tend to increase while R_1 decreases. Now the total number of atoms in a nanoparticle is constant and such a situation can be realized only if mass transport takes place from smaller particle (radius R_1) to the larger one (radius R_2). Owing to the loss of the surrounding matrix above the decomposition temperature, the inter-particle mass transport is highly favorable and facilitating particle growth.

From the crystallographic point of view it can be said that the nanoparticle growth will occur at the unit cell level along preferential directions. However, the surface energy of ZnO is different along different directions of the unit cell [3], and hence the particle growth would not occur in all the directions equally. According to the calculation of Fujimara et al. [3], the surface energy per mole, along different directions varies as $\gamma_{[0001]} < \gamma_{[11\bar{2}0]} < \gamma_{[10\bar{1}0]}$.

Following equation (5.3), upon heat treatment, $\frac{(R_2 - R_1)}{R_1 R_2} = \frac{\Delta\mu}{2\Omega}\frac{1}{\gamma}$

Consequently, $\Delta R_{[0001]} > \Delta R_{[11\bar{2}0]} > \Delta R_{[10\bar{1}0]}$, where $\Delta R = R_2 - R_1$.

In other words, the growth of the nanoparticles along [0001] direction (i.e. along *c*-axis) is energetically favorable owing to minimum surface energy and so the formation of elongated nanostructures is expected (Figure 5.3). Now it is apparent that the plane with higher growth rate will disappear

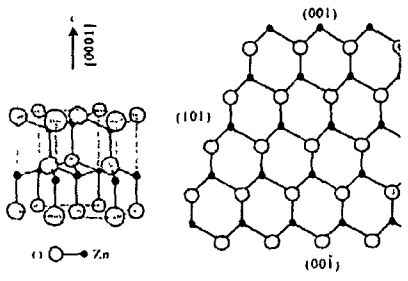

Figure 5.3: Demonstration of ZnO crystal structure and configuration model of the stack of zinc and oxygen atoms.

quicker [4] and as a result of which the growth along the [0001] direction can lead to the vanishing of (002) plane. This fact is also supported by the XRD results of the Eu^{3+} doped ZnO nanoparticles and urchins, where the FWHM of the (002) peak for the urchin system has decreased compared to the nanoparticle system (discussed in Chapter 2). Hence it is confirmed that the one directional growth of the particles along [0001] direction has led to the formation of 1D nanostructures under thermal annealing process.

5.2 Nanostructure growth under energetic ion irradiation

Earlier it was demonstrated that the energetic ion irradiation could play a major role in tailoring size, shape, and distribution of the nanostructures [5-10]. This is due to the fact that the energy deposited during irradiation leads either to particle growth, or splitting of the nanostructures. Ion induced particle melting and growth are generally attributed to the Ostwald ripening process [10]. In contrast, nanoparticle fragmentation into still smaller particles, was considered to be the result of ion hammering effect [11]. The irradiation led growth of PVA dispersed ZnO nanoparticles has also been witnessed upon 80-MeV N^{4+} ion irradiation.

The morphological features of the pristine nanoparticles synthesized using the solid state grinding method, have been discussed in Chapter 2. The average size of the spherical nanopartcles of ZnO was found to be ~ 12 nm. The structural modification of the nanoparticles upon irradiation at different fluences was evident from the TEM images as shown in Figure 5.4. The TEM micrograph in Figure 5.4 (a) basically shows the PVA dispersed ZnO nanoparticles upon irradiation with a fluence of 1.25×10^{11} ions/cm^2. It can be observed that there is no substantial change in the structural organization of the nanoparticles as compared to the unirradiated specimen [12]. However at a moderate fluence of 5×10^{11} ions/cm^2, the host polymer matrix that supports the nanoparticles experiences significant C-C bond breakage leading to the disruption in polymer chains. As revealed by the TEM image shown in Figure 5.4 (b), the nanoparticles

tend to overcome the polymer encapsulation (at ~ 5 x 10^{11} ions/cm^2), which was not observed in case of the sample irradiated at a lower fluence (1.25 x 10^{11} ions/cm^2). At this situation, no structural deformation of the nanopaticles can be observed i.e. the spherical shape is retained by the nanoparticles. Again, irradiation with a fluence of 2 x 10^{12} ions/cm^2, the nanoparticles overcome the matrix encapsulation completely and at occasional instances the particle-coalescence is also noticed (Figure 5.4 (c)). The nanoparticles just recovered from the matrix encapsulation become free-standing and cause coalescence with the neighboring nanoparticles.

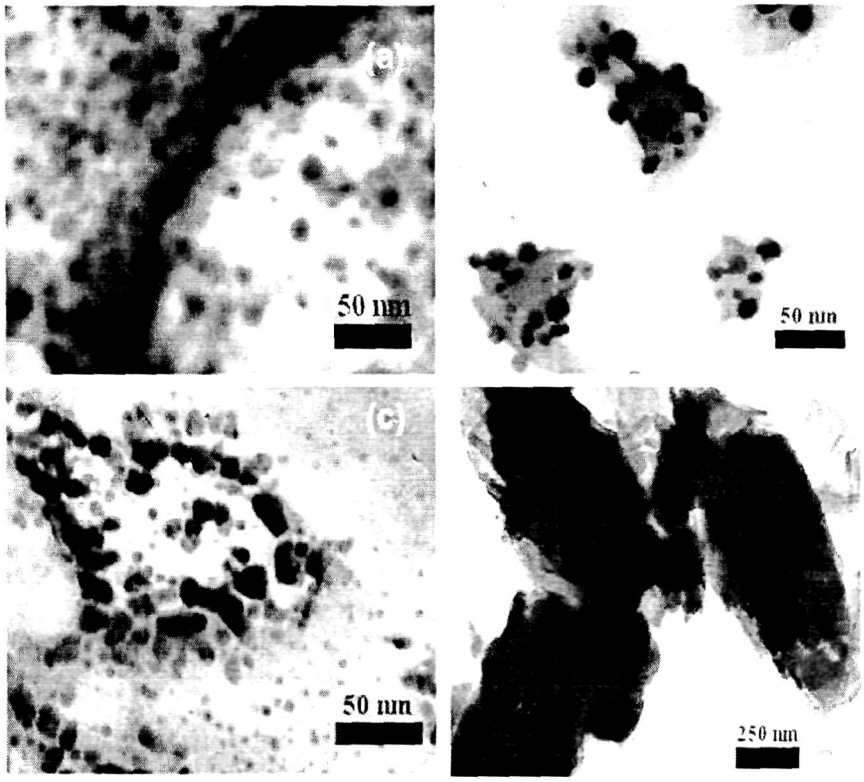

Figure 5.4: TEM image of ZnO nanoparticles after 80-MeV N^{4+} ion irradiation with a fluence of (a) 1.25x10^{11}, (b) 5x10^{11}, (c) 2x10^{12}, and (d) 8x10^{12} ions/cm^2; respectively.

As result of coalescence the nanoparticles lose the spherical shape and turn out to be oblate. The extent of recovery of the nanoparticles from the matrix encapsulation depends on the amount of energy supplied to the specimen. In this context, upon irradiation with the highest fluence of 8 x 10^{12} ions/cm^2, the energy

deposition is maximum and therefore, the matrix would be amorphized completely. In this situation, the rapid mass transport between the particles with interparticle separation relatively smaller than that of their dimension can result in particle coalesce/agglomeration. The TEM micrograph in Figure 5.4 (d) represents the agglomerated view of the nanostructures irradiated at the highest fluence.

The coalescence of the nanoparticles under energetic ion irradiation is a consequence of nanoparticle melting owing to the irradiation led enormous energy deposition and rise in temperature above the melting point. Now, based on the Linderman criterion of melting, Tateno [13] has shown that the melting point of a bulk material can be expressed in terms of its cohesive energy:

$$T_{mB} = \frac{sE_B \eta^2}{3k_B Z} \tag{5.4}$$

where, s is the exponent of the repulsive part of the interaction potential (proportional to r^{-s}) between the constituent atoms separated by a distance r, k_B being the Boltzmann constant, Z as the co-valency of the atoms and E_B is the bulk cohesive energy. The characteristic function η is defined as the ratio of the atomic displacement at T_{mB} to the interatomic separation at equilibrium. The cohesive energy of a material system is the amount of energy required to separate out its constituent neutral atoms and is directly related to the melting temperature of the crystalline material as evident from the above expression.

According to the previous work of Nanda et al [14], the melting point can be correlated with the cohesive energy per coordination number for both the nanoparticles, and the bulk which are given by

$$\begin{aligned} \frac{E_{np}}{N} &= C_1 T_m + C_2 \\ \frac{E_B}{N} &= C_1 T_{mB} + C_2 \end{aligned} \tag{5.5}$$

where T_m and E_{np} are the melting point and the cohesive energy of the nanoparticles, respectively. N being the coordination number per atom and C_1, C_2 are the constants which depend on the crystal structure.

If the spherical nanoparticles of average diameter D embedded in the host matrix possess elements of diameter d_i (i=1,2,3.....) with atomic percentage of x_i (i=1,2,3.....) such that $\sum x_i$ =1, then the total number of atoms that make up each of the nanoparticles, can be represented by [15]:

$$n = \frac{f.D^3}{\sum x_i d_i^{\,3}} \tag{5.6}$$

where f is the packing factor which is the fraction of volume in a crystal that is occupied by the atoms.

Now, according to the LDM [14], the cohesive energy of a nanoparticle represents the difference of the bulk cohesive energy per atom (E_B) and the surface energy of the nanoparticle. The cohesive energy per atom can be expressed as:

$$E_{np} = E_B - \frac{\pi D^2 \gamma_{np}}{n} \tag{5.7}$$

where γ_{np} is the surface energy per unit area of the nanoparticle.

Further, the size dependent cohesive energy per atom of the nanoparticles embedded in a dielectric matrix of surface energy per unit area γ_{mx} [14] can be reformulated as

$$E_{np} = E_B - \frac{\pi D^2}{n}(\gamma_{np} - \gamma_{mx}) \tag{5.8}$$

Now it is assumed that upon irradiation, the energy deposition will be uniform all throughout the specimen. If F is the number of ions incident per unit area (i.e., fluence), then the number of ions received by each of the nanoparticle of diameter D is $F\pi D^2/4$. If S_e and S_n represent the electronic and nuclear energy losses of the projectile ion then upon irradiation with higher energetic ions having $S_e >> S_n$, the maximum energy deposition on the nanoparticle will be caused by S_e.

Considering the thickness of the film as 'z' (as depicted in Figure 5.5), then the energy deposited by one ion while traversing the above mentioned thickness is $gS_e z$, where g is the electron-phonon coupling efficiency [16, 17]. Therefore, upon irradiation with fluence F, the energy deposited per atom of a matrix encapsulated nanoparticle will be given by

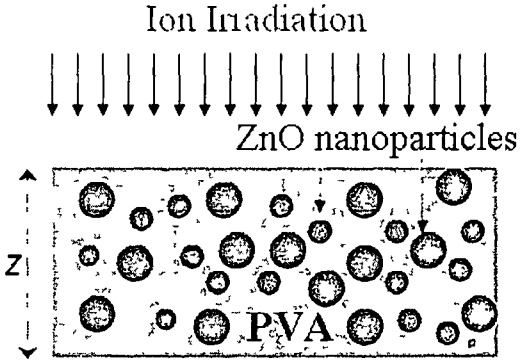

Figure 5.5: Schematic representation of the ZnO nanoparticles embedded PVA matrix subjected to irradiation

$$E_i = \frac{F\pi D^2}{4n} gS_e z \tag{5.9}$$

It is evident that the irradiation process would increase the internal energy of the nanoparticles and therefore the cohesive energy of the particles will be suppressed by the above mentioned energy deposited during irradiation [18]. Thus, during irradiation the cohesive energy of the nanoparticles embedded in a matrix can be written as

$$E_c = E_{np} - E_i$$

$$or,\ E_c = E_B - \frac{\pi D^2}{n}(\gamma_{np} - \gamma_{mx}) - \frac{F\pi D^2}{4n} gS_e z \tag{5.10}$$

In the above equation, the second term on the right hand side is dependent on F and should increase with the ion fluence Owing to the irradiation led enormous energy deposition, the internal energy of the system would increase making the nanoparticles thermodynamically unstable. At a critical fluence, the irradiation energy can be comparable with the cohesive energy of the nanoparticle and therefore the effective cohesive energy (E_c) would be vanishingly small At a higher fluence, the dominance of the irradiation energy over the cohesive energy of the nanoparticles will make the magnitude of $E_c < 0$. It can also be noted that the zero value of the effective cohesive energy represents a situation where the atoms are no longer bound to each other. The negative effective cohesive energy

signifies that the atoms can dislodge and fly out of the nanoparticle surface. Nevertheless, under these circumstances, if the particles are closely spaced (i.e. the interparticle separation is comparable or, smaller than the particle dimension), then the mass transport would result in particle growth.

It is known that the ions while traversing through the insulator matrix create ion tracks having radius of several nanometers [19]. If sufficient number of tracks were created between any two adjacent nanoparticles, then the medium separating the particles (i.e. interparticle spacing) will be lost. At this situation, the diffusion led mass transport among the adjacent nanoparticles, followed by the rapid solidification would result in particle growth [20, 21]. This is analogous to the process of coalescence of the nearby islands during the growth of thin films [22].

It is quite apparently clear that the growth of the nanoparticles under irradiation is accompanied by the decrease of cohesive energy and the interparticle spacing. In order to visualize this event more clearly, two nanoparticles of diameter D and separated by a distance R from each other (Figure 5.6) are considered. As the ion proceeds along a certain direction (say, z-direction), the uniformly dispersed nanoparticles will pass through the molten phase along that direction giving rise to regular oblate ellipsoids (Figure 2A and 2B). Upon melting, in order to minimize the surface energy the molten species get condensed and acquire a spherical shape. Now, the three sides of a regular oblate

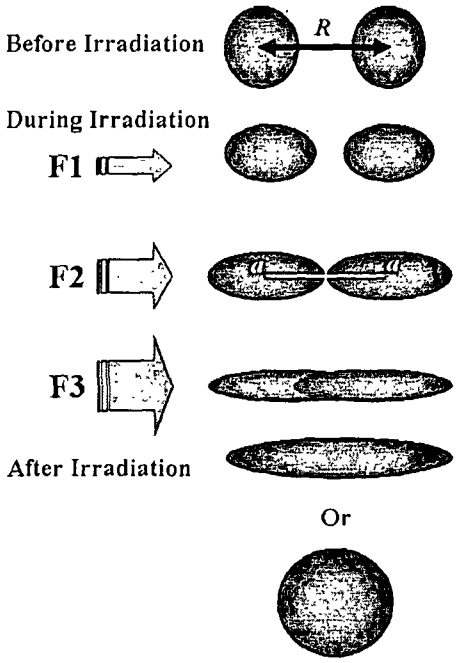

Figure 5.6: Different stages of nanoparticle growth, under energetic ion irradiation. (Fluence $F_3 > F_2 > F_1$).

are a, b and c such that $a > b = c$. As the mass is conserved during the irradiation process, it can be written as

$$\frac{4}{3}\pi\left[\frac{D}{2}\right]^3 \rho = \frac{4}{3}\pi a b^2 \rho' \qquad (5.11)$$
$$or, \quad a = \frac{1}{8}\left(\frac{D^3}{b^2}\right)\frac{\rho}{\rho'}$$

where ρ and ρ' ($< \rho$) are the densities of the system before and during irradiation. For complete melting, the two oblates will be in the closest proximity if the sum of the two equatorial radii of the two oblates (along the z-direction) is equal to R. Such a situation can facilitate the exchange of atoms between the two molten species with great ease. In general, upon coalescence, two or more particles can grow into an independent particle of larger size (Figure 5.6).

Accordingly, $2a = \frac{1}{4}\left(\frac{D^3}{b^2}\right)\frac{\rho}{\rho'} \geq R$ will be neglected as the growth condition of the nanoparticles subjected to ion irradiation. In other words, the equatorial diameters of the oblates should be at least equal, or larger than the interparticle separation of the two nanoparticles under investigation.

Now the structural modification upon 80-MeV N^{4+} irradiation on the ZnO nanoparticles embedded in the PVA matrix was analyzed in light of the current discussion. The values of the various physical parameters related to ZnO and PVA are listed in Table 5.1. The E_B for ZnO was considered to be 3.76 eV/atom [23], while the thickness of the film was considered to be 1 μm.

Table 5.1: Different physical parameters of the materials.

Material	**Melting point (K)**	**Density (g/cc)**	**Thermal conductivity (W/m.K)**	**Surface energy (J/m^2)**	**S_e for 80-MeV N^{4+} irradiation** (eV/Å)
ZnO	2248	5.6	1.16 [24]	1.95 [25]	1.191×10^2
PVA	503	1.2-1.3	0.2 [18]	0.037 [26]	3.946 x 10

Figure 5.7 depicts a comparison between the irradiation energy (E_i) deposition and the cohesive energy for different sized nanoparticles of ZnO in the matrix. It can be seen that with the increase of ion fluence (from 1 x 10^{11} to 2 x 10^{12} ions/cm^2), the energy deposited per atom increases rapidly. In the Figure 5.7, the

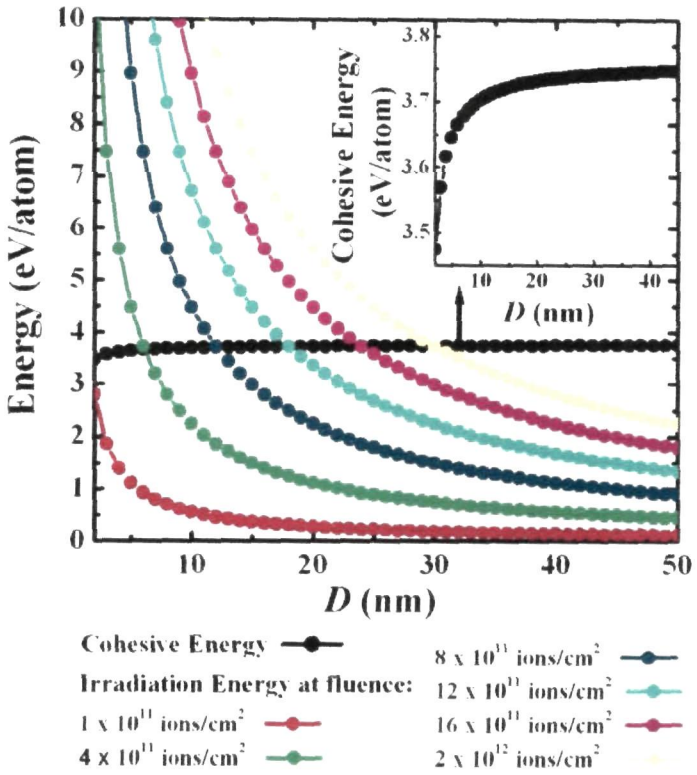

Figure 5.7: Variation of cohesive energy and irradiation energy with particle size for ZnO nanoparticles embedded in PVA. Inset being the magnified version of the cohesive energy vs. size (pointed by arrow).

horizontal line at ~ 3.75 eV/atom (also highlighted in the Figure inset) represents the size dependent cohesive energy of the ZnO nanoparticles embedded in PVA matrix. The irradiation energy (for ion fluence of 1 x 10^{11} ions/cm^2) is completely dominated by the respective cohesive energy. Conversely, at the fluence of 4 x 10^{11} ions/cm^2, the irradiation energy deposited on the particles having size below a critical size of 6 nm (the intersection point) dominates the cohesive energy. The intersection point of the cohesive energy and the irradiation energy represent the critical size for a particular fluence.

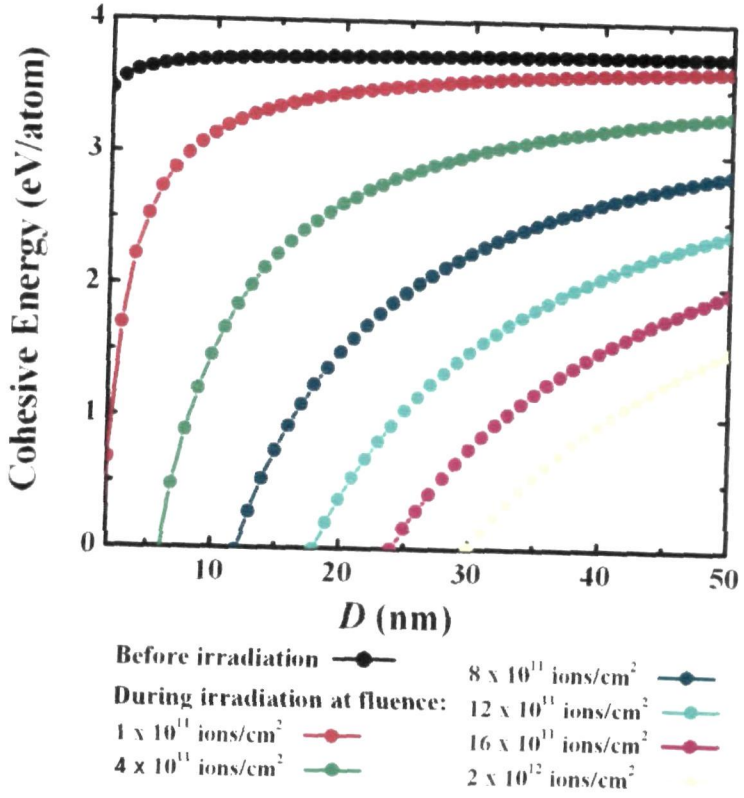

Figure 5.8: Size dependent effective cohesive energy response during irradiation of the ZnO nanoparticles embedded in PVA.

The curves related to the effective cohesive energy (E_c) as a function of nanoparticle size, is shown in Figure 5.8. During irradiation, the E_c value decreases by substantial amount. For a finite size of the nanoparticles, gradually E_c becomes zero with the increase in fluence. Upon irradiation with a fluence of 4 x 10^{11} ions/cm^2, E_c vanishes for the particles having size below the critical value. This trend is maintained for the higher values of fluence. A vanishing E_c represents no interactive force between the atoms that make up a nanoparticle. In this situation initiation of coalescence process between two identical nanoparticles takes place (with sizes larger than the interparticle spacing) due to interparticle diffusion led mass transport.

In the present study the ZnO nanoparticles having average size ~ 12 nm were found to recover from the matrix encapsulation at a fluence of 5 x 10^{11} ions/cm^2,

while the nanoparticles in coalesced form was observed at 2 x 10^{12} ions/cm^2. These two facts indicate that the nanoparticles attain the condition of zero cohesive energy (E_c ~ 0, initiation of the coalescence process) at a particular fluence which lies within the two above mentioned ion fluence values. Now, as evident from the Figure 5.8, the E_c for ~ 12 nm particles becomes zero at a fluence of 8 x 10^{11} ions/cm^2 which is in the above mentioned range. Therefore it can be understood that the initiation of the coalescence process takes place at a fluence of 8 x 10^{11} ions/cm^2. This proves a sound correlation among the theoretical assessment and the experimental consequences observed upon 80-MeV N^{4+} ion irradiation.

However the matrix plays a vital role in the particle coalescence process. The growth process would occur through the coalescence of particles within the matrix medium which becomes amorphized as a result of creation of ion tracks. Hence the melting followed by coalescence would certainly depend on the nature of the host matrix. It is obvious that the matrix with a lower thermal conductivity would dissipate heat at a slower rate from the point of ion impact to the surroundings. In the present system of ZnO encapsulated in PVA matrix, the nanoparticle growth was observed above a fluence of 8 x 10^{11} ions/cm^2. On the other hand, the growth of metallic nanoparticles (e.g., Ag, Au etc.) in a-SiO_2 was found to occur at a higher fluence of 10^{13} ions/cm^2 [10]. Such discrepancy can be assigned to the difference in thermal conductivity of the two systems. The thermal conductivities of the metallic system (~ 318 W/m-K for Au) and matrix (~ 1.3 W/m-K for a-SiO_2) are higher than ZnO and PVA. The higher thermal conductivity results in faster heat dissipation and so the growth of the nanoparticle occurs at a comparatively higher fluence. Thus it is evident that the fluence required for particle growth is decided by the nanoparticle size, type and the nature of the surrounding matrix.

5.3 Concluding remarks

Theoretical aspects of growth and elongation of ZnO nanostructures have been investigated. It was found that during the annealing, the annealing temperature triggers the Ostwald ripening process in a system containing particles of various sizes. Moreover, the growth of the nanoparticles along [0001] direction (i.e. along *c*-axis) is energetically favorable owing to the minimum surface energy. The unidirectional growth of the ZnO nanostructures along the *c*-axis was believed to be the main cause behind the formation of elongated nanopatterns during thermal treatment. Under energetic ion irradiation, the observed particle growth was shown to the suppression of effective cohesive energy of the nanoparticles. The particle growth was found to occur through interparticle mass transport during irradiation. The nature of the dispersing media (matrix) and the nanomaterial type would also take decisive role in determining the critical the fluence at which coalesce of particles can be achieved.

References:

[1] Cao, G. *Nanostructures & nanomaterials: Synthesis, properties & applications*, Imperial College Press, London, 2004.

[2] Rathake, L. & Voorhees, *P. W. Growth and Coarsening: Ripening in Material Processing*, Springer, New York, 2002.

[3] Fujimara, N., et. al. Control of preferred orientation for ZnO_x films: control of self-texture, *J. Crystal Growth* 130, 269-279, 1993.

[4] Zhang, H., et. al. Low temperature synthesis of flowerlike ZnO nanostructures by cetyltrimethylammonium bromide-assisted hydrothermal process, *J. Phys. Chem. B* 108 (13), 3955- 3958, 2004.

[5] Penninkhof, J. J. et. al. Anisotropic deformation of metallo-dielectric core-shell colloids under MeV ion irradiation, *Nucl. Instr. and Meth. in Phys. Res. B* 242, 523-529, 2006.

[6] Ridgway, M. C., et. al. Changes in metal nanoparticle shape and size induced by swift heavy-ion irradiation, *Nucl. Instr. and Meth. in Phys. Res. B* 267, 931-935, 2009.

[7] Singh, F. et. al. Shape deformation of embedded metal nanoparticles by swift heavy ion irradiation, *Nucl. Instr. and Meth. in Phys. Res. B* 267, 936-940, 2009.

[8] Awazu, K., et. al. Mechanism of elongation of gold or silver nanoparticles in silica by irradiation with swift heavy ions, *Nucl. Instr. and Meth. in Phys. Res. B* 267, 941-943, 2009.

[9] Mohanta, D., et. al. SHI induced grain growth and grain fragmentation effects in polymer embedded CdS quantum dot systems, *Mater. Letters*, 58(29), 3694-3699, 2004.

[10] Mishra, Y. K., et. al. Controlled growth of gold nanoparticles induced by ion irradiation: An in situ x-ray diffraction study, *Appl. Phys. Lett.* 90, 073110 (1-3), 2007.

[11] Berthelot, A., et. al. Nanometric size effect on irradiation of tin oxide powder, *Nucl. Instr. and Meth. in Phys. Res. B* 146, 437-442, 1998.

[12] Bayan, S. & Mohanta, D. Effect of 80-MeV nitrogen ion irradiation on ZnO nanoparticles: Mechanism of selective defect related radiative emission features, *Nucl. Instr. and Meth. in Phys. Res. B* 269, 374–379, 2011.

[13] Tateno, J. An empirical relation on melting temperature of some ionic crystals, *Solid State Commun.* 10, 61-62, 1972.

[14] Nanda, K. K. et. al., Liquid-drop model for the size-dependent melting of low-dimensional systems, *Phys. Rev. A* 66, 013208 (1-8), 2002.

[15] Qi, W.H. Generalized Surface-Area-Difference model for cohesive energy of nanoparticles with different compositions, *J. Mater. Sci.* 41, 5679-5681, 2006.

[16] Szenes, G. et al. Tracks induced by swift heavy ions in semiconductors, *Phys. Rev. B* 65, 045206 (1-5), 2002.

[17] Szenes, G. et al. Tracks induced in TeO_2 by heavy ions at low velocities, *Nucl. Instr. and Meth. in Phys. Res. B* 166-167, 949-953, 2000.

[18] Bayan, S. & Mohanta, D. Role of cohesive energy on the interparticle coalescence behavior of dispersed nanoparticles subjected to energetic ion irradiation, *J. Mater. Res.* 25 (5), 814-820, 2010

[19] Fleischer, R.L., et. al. (eds.). *Nuclear Tracks in Solids*, University of California Press, Berkeley, 1975.

[20] Joseph, B., et. al. Effect of 100 MeV Au irradiation on embedded Au nanoclusters in silica glass, *Nucl. Instr. and Meth. in Phys. Res. B* 256, 659-664, 2007.

[21] Srivastava, S.K. et. al. Swift heavy ion induced formation of nanocolumns of C clusters in a Si based polymer, *Nanotechnology* 17, 2518-2522, 2006.

[22] Venables, J.A. et. al., Nucleation and growth of thin films, *Rep. Prog. Phys.* 47, 399-459, 1984.

[23] Uddin, J. & Scuseria, G. E. Theoretical study of ZnO phases using a screened hybrid density functional, *Phys. Rev. B.* 74, 245115 (1-7), 2006.

[24] Olorunyolemi, T. et. al. Thermal conductivity of zinc oxide: From green to sintered state, *J. Am. Ceram. Soc.* 85 (5), 1249-53, 2002.

[25] Adach, S. *Properties of Group-IV, III-V and II-VI semiconductors*, John Wiley & Sons, Chichester, 2005.

[26] Tezuka, Y. & Araki, A. Temperature-modulated environmental responses on the surface of poly(vinyl alcohol)-polystyrene graft copolymers, *Langmuir* 10, 1865-1870, 1994.

Chapter 6

Transport properties of ZnO nanorod based junctions

The superiority of an optoelectronic device depends on the quality and reliability of a given metal-semiconductor junction. For technological applications, a network of metal strips are developed on semiconductors to form interconnects which could allow charge transfer from one point to another. These interconnections appear as Ohmic contacts to provide low resistance paths for carrier transport. Alternatively it can form Schottky contacts to afford non-linear current-voltage (*I-V*) responses. With the advancement of fabrication strategies it has been possible to obtain efficient metal-semiconductor junctions based on nanoscale systems. Furthermore, the fabrication of a metal-insulator-semiconductor structure by inclusion of an insulating layer between the metal and semiconductor has its own technological importance. However, from the practical application point of view, the achievement of a reliable and reproducible nanoscale metal-semiconductor junction still requires a lot of attention. The present chapter highlights the transport characteristics of ZnO nanostructure based various metal-semiconductor and metal-insulator-semiconductor junctions.

6.1 Metal-Semiconductor Schottky junctions

A metal-semiconductor (MS) junction can exhibit rectifying nature with non-linear *I-V* characteristics similar to a *pn* junction diode. Such a rectifying device is called Schottky junction [1,2]. The Schottky junctions have been proven to be advantageous over conventional *pn* junction diodes owing to their faster switching response and lower turn-on voltages [2]. In principle, when a metal is brought into intimate, at thermal equilibrium the Fermi level of the two materials must coincide or align If a metal is brought in contact with an *n*-type semiconductor, owing to large value of metal

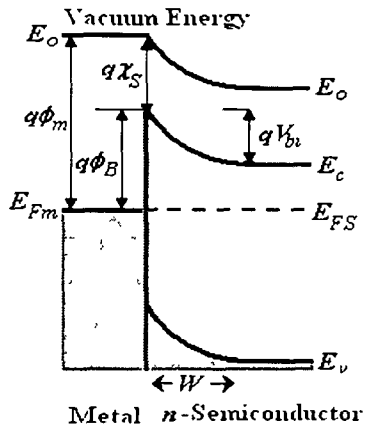

Figure 6.1: Schematic representation of a Schottky contact.

work function (ϕ_m), electrons move out from the semiconductor side to the metal side and ensure the alignment of the Fermi levels. As the electrons leave the semiconductor side, ionized donor atoms are left behind and a dipole region is created in the same way as for the *pn* junction diodes. According to the Schottky-Mott model, the barrier height (ϕ_B) of an ideal Schottky contact can be expressed as the difference of the metal work function (ϕ_m) and the semiconductor electron affinity (χ_s) i.e., $\phi_B = \phi_m - \chi_s$ [3]. Figure 6.1 shows the formation of a Schottky contact under such a condition. Finally, the electron movement from the semiconductor side is hindered by the built-in potential (V_{bi}) developed at the junction and results in the formation of a depletion region of width W.

Now, under the application of forward bias, the forward diode current can be expressed in accordance with the well known thermionic model and is given by [1]

$$I = I_s \left[\exp\left(\frac{qV_a}{\eta kT}\right) - 1\right] \tag{6.1}$$

where, q is the fundamental electronic charge, V_a is the applied voltage, k being the Boltzmann constant and T is the working temperature. The dimensionless quantity η is called the ideality factor which determines the quality of the electrical contact for establishing a rectifying junction. The reverse saturation current, I_s, is given by [1]

$$I_s = AA^*T^2 \exp\left(-\frac{q\phi_B}{kT}\right) \tag{6.2}$$

where, A is the effective area of the metal-semiconductor contact, A^* is the Richardson constant and ϕ_B being the Schottky barrier height. For $V > 3kT/q$, the forward diode current can be written as [4],

$$I = I_s \exp\left(\frac{qV_a}{\eta kT}\right) \tag{6.3}$$

The electron affinity of ZnO is ~ 4.35 eV [3], and hence metals having work function greater than this value would be able to form Schottky junctions with ZnO. The development of rectifying Schottky contacts fabricated using M/ZnO (M = Au, Ag, Pt, Pd, etc.) systems have previously been reported by various

groups [5-8]. Further, the thermal stability of the contacts has been a major concern and it was reported that Ag/ZnO Schottky contacts are more stable over Au/ZnO counterparts [5].

6.1.1 Effect of annealing temperature on the transport property of Ag/ZnO Schottky junctions

The ZnO nanorods grown on Al_2O_3/Al substrate using the thermal annealing process under different annealing environments (discussed in Chapter 2), were used to fabricate the Ag/ZnO Schottky junctions. In this regard, metallic contacts were fabricated by depositing two separate thin Ag-layers (~70 nm) on the top-surfaces of the nanorod-grown Al_2O_3/Al substrates via thermal evaporation process using a vacuum coating unit (Hind High Vacuum, chamber pressure ~10^{-6} mbar) for the said purpose. In order to avoid chances of short circuit along the vertical direction, the contacts were made horizontally on the top-surface of the specimens. The current vs. voltage (*I-V*) characteristics were studied at room temperature (298 K) by using a computer interfaced Keithley 2400 sourcemeter® via a two probe method. Figure 6.2 shows the schematic representation of the Ag/ZnO junction on Al_2O_3/Al substrate alongwith the two probe-lids. The *I-V* characteristics were recorded independently for the Ag/ZnO junctions of different specimens each comprising a number of randomly distributed nanorods. Note that though the samples were fabricated with same precursor (having pH value of 9.0), the growth process was carried out at different annealing temperatures of 450, 550, 650 and 750 °C. The corresponding Ag/ZnO junctions were named as *S1*, *S2*, *S3* and *S4*; respectively.

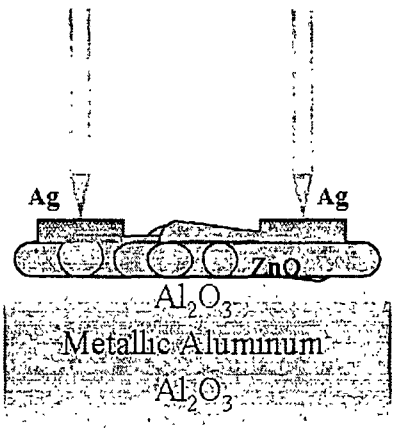

Figure 6.2: Schematic view of the Ag/ZnO junction on Al_2O_3/Al substrate.

Figure 6.3 shows the *I-V* characteristic curve of Ag/ZnO junction made out of the nanorods synthesized at an annealing temperature of 450 °C (*S1*). Under a forward bias, the turn-on voltage of the sample was found to be ~ 3.2 V, while reverse breakdown occurred at ~ -9.1 V. The nonlinear and rectifying nature of the curve ensures the formation of a Schottky contact between the randomly distributed ZnO nanorods and metallic Ag. The inset of Figure 6.3 depicts the corresponding semi-logarithmic *I-V* curve. Referring to the equation (6.3), the η and ϕ_B were calculated from the linear fit of the semi-logarithmic *I-V* curve. The η and ϕ_B related to the Schottky junction were estimated as 18.4 and 0.77 eV. The observed high value of ideality factor depicts the non-ideal behavior of the Ag/ZnO junction. The non-ideal behavior of the junction can be attributed to the atomic scale non-uniformity of the Schottky contacts arising due to the presence of some intermediate states/surface states and defects [9] or, because of the surface damage during the formation of the Ag layers on the nanorods [10].

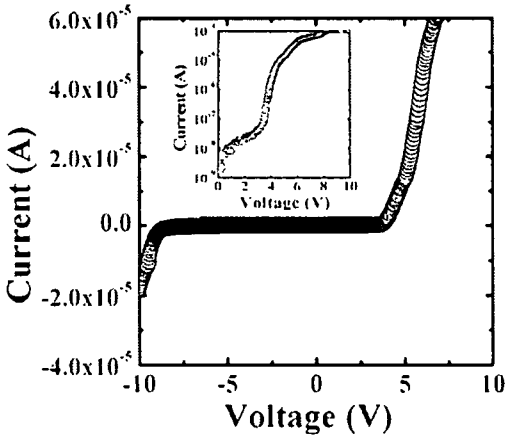

Figure 6.3: *I-V* characteristic curve of Ag/ZnO junction made out of the nanorods synthesized at 450 °C (*S1*). Inset of the figure depicts the corresponding semi-logarithmic curve.

Conversely, the Ag/ZnO junctions fabricated out of the nanorods prepared at annealing temperatures of 550 and 650 °C (*S2* and *S3*), show very large current flow under reverse bias (Figure 6.4). Though the rectifying nature of the two Schottky junctions is noticeable (inset (i)), the current under reverse bias is fairly dominant. The semi-logarithmic *I-V* curves (inset (ii)), meant for *S2* and *S3* samples were characterized by very high values of η i.e., 35.4 and 33.2, and ϕ_B of 0.64 and 0.63 eV; respectively. Among the two Ag/ZnO junctions, *S2* is governed by higher current beyond a given bias voltage both in forward and reverse modes.

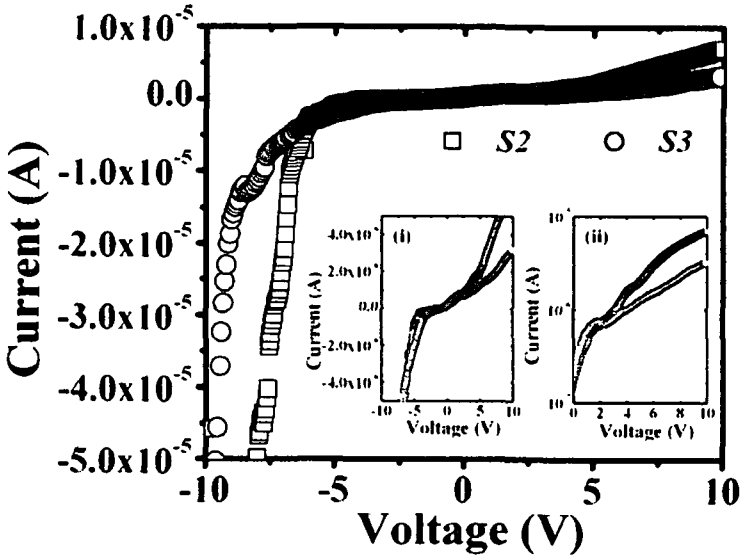

Figure 6.4: *I-V* characteristic curve of Ag/ZnO junction made out of the nanorods synthesized at 550 and 650 °C (*S2* and *S3*). Inset (i) shows the magnified version of the *I-V* curve, while inset (ii) represents the semi-logarithmic *I-V* curve for these samples.

In contrast, as depicted in Figure 6.5, the Ag/ZnO junction obtained from the nanorods fabricated at 750 °C (*S4*), reveals a good rectifying response. The present *I-V* characteristics curve exhibit lower turn on voltage in the forward biasing mode and less leakage current under reverse biasing. Using the semi-logarithmic *I-V* curve (shown in the inset), the η was calculated to be 12.2, while ϕ_B has assumed a value of 0.78 eV.

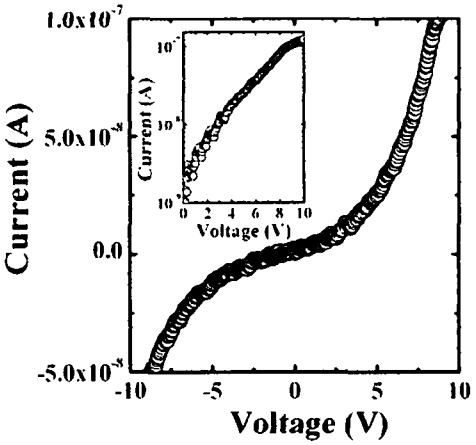

Figure 6.5: *I-V* characteristic curve of Ag/ZnO junction made out of the nanorods synthesized at 750 °C (*S4*). Inset being the corresponding semi-logarithmic curve.

It can be noticed that for all the Ag/ZnO junctions, the values of η were found to be very high (>> 1). Earlier, Allen and Durbin also observed the high values of η in ZnO based Schottky junctions [8]. The high values of η was attributed to the

significant electron tunneling as a result of formation of a layer of positively ionized oxygen vacancies with thickness comparable to a few atomic dimensions at the interface separating the metal probe and the host ZnO. Similarly, for Au/ZnO systems, the observed values of η between 20.5 and 38 were assigned to the existence of an interfacial insulating layer or the surface states at the junction [11]. In order to investigate the presence of various defects in the ZnO system, the PL spectra of the nanorods were studied Figure 6.6 shows the room temperature PL spectra of the nanorods fabricated at different annealing temperatures considering an excitation wavelength (λ_{ex}) of 325 nm. The sample dependent various native defect of ZnO were found to be the major contributor of the PL emission response. The various peak positions describing different kinds of zinc and oxygen related defects have been discussed in earlier reports [12-16].

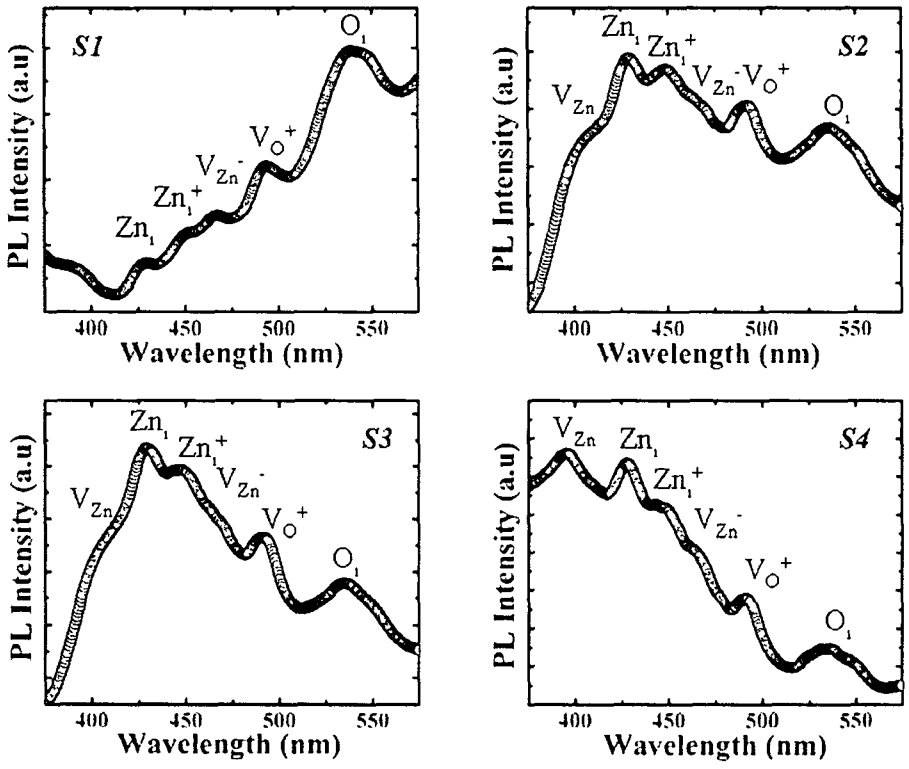

Figure 6.6: Room temperature PL spectra of the nanorods fabricated at different annealing temperatures (λ_{ex} = 325 nm)

The PL spectra of the nanorods of *S1* is dominated by the oxygen interstitial (O_i) defects (~ 535 nm) [13], along with the presence of singly ionized oxygen vacancy (V_O^+) emission peak at ~ 490 nm [14]. Additionally, signature of poorly resolved peaks due to neutral and singly ionized Zn interstitials (Zn_i at ~ 430 nm and Zn_i^+ at ~ 450 nm) [12, 15] and ionized zinc vacancy (V_{Zn}^- at ~ 465 nm) were also detected [13, 16]. In contrast, in the PL spectra of the nanorods of *S2* and *S3*, the Zn interstitials (Zn_i and Zn_i^+) related emission responses were found to be substantially improved. In these two samples, the V_O^+ related emission at ~ 490 nm is profoundly strengthened, along with the development of neutral zinc vacancy related emission peak (V_{Zn}), located at ~ 400 nm [12] and that of the ionized vacancy (V_{Zn}^-) at ~ 465 nm. Finally, in the emission spectra of the nanorods of *S4*, the V_{Zn} related emission intensity gets enhanced and became comparable with the Zn_i related emission. The annealing temperature dependent evolution of different defects in thermal annealing process has already been discussed in Chapter 3. Therefore, the PL study ensures the presence of various defect/surface states of zinc and oxygen, within the band-gap of ZnO. Accordingly, mechanisms such as image force barrier lowering (IFBL), generation-recombination of carriers in the space charge regions, tunneling current etc. can be realized to a great extent [6, 8, 17]. All these key factors are accountable for the non-ideal behavior of the Ag/ZnO Schottky junctions under investigation.

In ZnO system, V_O^+ and Zn_i defects act as donors, whereas V_{Zn}, O_i and O_{Zn} behave as acceptors [12]. Now, it is probable that the presence of these donors and acceptors in different concentration would alter the Fermi level position within the band gap [12]. The variation of η and ϕ_B of the four different specimens is shown in Figure 6.7 (a). The decrement of η with the increase of barrier height and vice-versa is in consistent to earlier reports [5, 6, 9]. Now, Figure 6.7 (b) depicts the variation of ϕ_B with the ratio of acceptor type defect to donor type defect i.e. zinc vacancy-to-interstitial (V_{Zn}/Zn_i) and oxygen interstitial-to-vacancy

(O_i/V_O^+) of the four different samples. It can be observed that the O_i/V_O^+ ratio is significantly higher for the nanorods of *S1* owing to the dominance of O_i defects

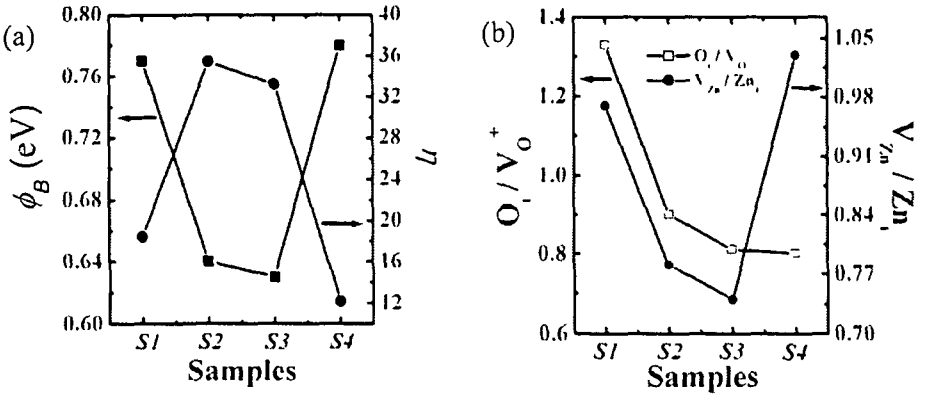

Figure 6.7: (a) Variation of η and ϕ_B and (b) variation of the ratio of acceptor-to-donor type defect emission response for the four different specimens.

over the defects of other kinds. The Ag/ZnO junction made of these nanorods possesses a moderate value of Schottky barrier height and typically shows a typical *I-V* curve of a Schottky junction with less leakage current. Whereas, in Ag/ZnO junction made out of the nanorods grown at 550 and 650 °C (i.e. *S2* and *S3*), large reverse current was found as a result of large electron flow from the metal to semiconductor under reverse bias. It can be noticed in the PL spectra (Figure 6.6) that Zn_i related defect emission gets improved in the nanorod systems of *S2* and *S3* and that is why V_{Zn}/Zn_i ratio is lower in these cases (Figure 6.7 (b)). Now, the presence of Zn_i-donors will increase the *n*-type conductivity of the ZnO samples [17] and making thereby the Fermi level position in *S2* and *S3* closer to the conduction band as compared to *S1*. This means that, the Fermi level in the corresponding Ag/ZnO junctions lies just below the conduction band as depicted in Figure 6.8 (i). Consequently, the depletion region of the metal-semiconductor contact becomes narrow in *S2* and *S3* systems. As a result, under reverse bias when the semiconductor Fermi level shifts downward well below the equilibrium position, the electrons experience a no barrier situation and tunnel from the metal to the semiconductor side (Figure 6.8 (ii)). Accordingly, a very high reverse current is predicted in *S2* and *S3*. Moreover, the free electrons donated by the V_O^+ and Zn_i defect states increase the surface charge density and results in high IFBL

effect [6]. Apparently, there is a reduction in the effective Schottky barrier height (0.64 and 0.63 eV for *S2* and *S3* respectively), along with a decrease in the barrier

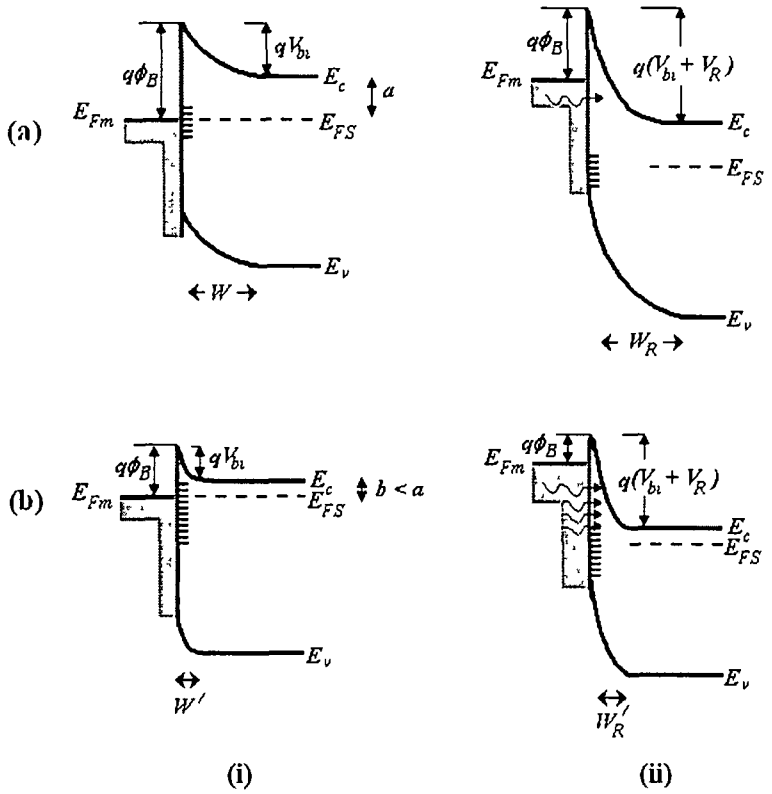

Figure 6.8: Energy band diagram of the Ag/ZnO junctions with samples (a) *S1*, (b) *S2* and *S3*; for (i) equilibrium and (ii) reverse biasing cases. Here, *a* and *b* represent the difference between the semiconductor Fermi level (E_{FS}) and the conduction band (E_C) of *S1* and *S2* respectively. Again, *W* and *W'* denote the width of the depletion region of the two junctions such that $W' < W$. Upon application of a reverse bias V_R, significant electron tunneling occurs from the metal side to the semiconductor in *S2*.

width. Hence the presence of adequate Zn_i-donor states results in the decrease in barrier width owing to the Fermi level re-adjustment and large IFBL effect. Accordingly, a large reverse current flows across the two Ag/ZnO junctions (*S2* and *S3*).

As evident from the Figure 6 7 (b), the ratio of the acceptor-to-donor defect concentration (for O_i/V_O^+ as well as V_{Zn}/Zn_i) has a decreasing trend while moving from sample *S1* to *S2*. Interestingly, though the O_i/V_O^+ ratio of *S4* follows the same tendency, the V_{Zn}/Zn_i ratio exhibited a reverse trend. Owing to the

prominence of V_{Zn} related emission in the nanorods of *S4*, the V_{Zn}/Zn_i ratio, in this case is larger than for the nanorods of *S2* and *S3* specimen. In view of the fact that the V_{Zn} defects are compensating acceptors [18], the dominance of the V_{Zn} acceptors would result in the lowering of *n*-type conductivity of the nanorods of *S4* than that of *S2* and *S3*. Hence, the Fermi level position of the nanorods of *S4* will be comparatively lower than the nanorods of *S2* and *S3*. Moreover, the evolution of more compensating V_{Zn} acceptors will cause fall of surface charge density, thus leading to a weak IFBL effect. This accounts for the higher ϕ_B for *S4* (0.78 eV) as compared to *S2* and *S3* (Table 6.1). Accordingly, there is a sufficient enhancement in the barrier width in *S4* system where the free tunneling of electrons is substantially hindered under reverse bias condition resulting a very small leakage current.

Table 6.1: Various physical parameters of the samples synthesized under different annealing environment.

Sample	ϕ_B (eV)	η	V_{Zn}/Zn_i	O_i/V_O^+
S1	0.77	18.4	0.97	1.33
S2	0.64	35.4	0.78	0.90
S3	0.63	33.2	0.74	0.81
S4	0.78	12.2	1.03	0.80

It has been seen that the defects have pronounced effect on the transport property of the four kinds of Ag/ZnO junctions. In order to distinguish the nature of carrier transport mechanism of the Ag/ZnO junctions, the *I-V* characteristics were also plotted in the *log-log* scale (Figure 6.9). The *log-log I-V* characteristic curve of *S1* is presented in Figure 6.9 (a). Basically, it depicts four independent regions highlighting the nature of carrier transport for different voltage regime under forward bias. The nature of current transport in the region I ($V < 1.2$ V) is found to vary linearly with the bias voltage as per the conventional Ohms law ($I \propto V$). Therefore the tunneling assisted current transport mechanism is favored within the regime I. The region II (1.2 V < V < 4.6 V) is characterized by an exponential growth of the current with the applied voltage following the relation $I \propto \exp(\alpha V)$,

α being a system dependent parameter. The ideality factor (η) of the sample was calculated within this region and here the carrier transport is assigned to the

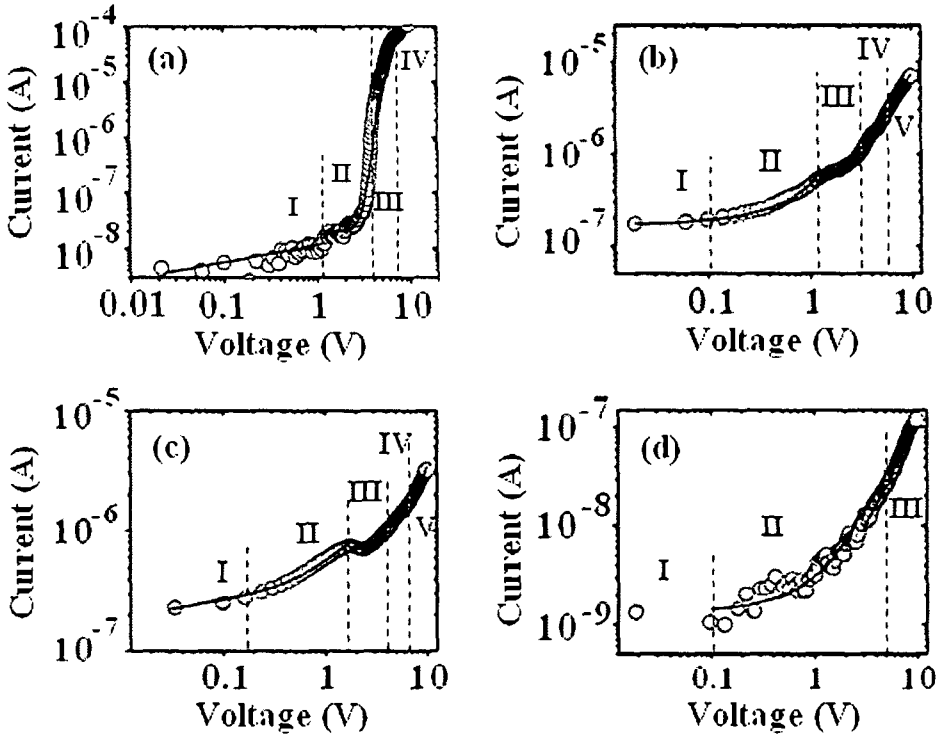

Figure 6.9: *I-V* characteristics of the four samples in *log-log* scale (a) *S1*, (b) *S2*, (c) *S3* and (d) *S4*.

recombination tunneling mechanism where an electron experiences a series of tunneling via local recombination sites [19-22]. In the present situation, the recombination centers are provided by the various native defects of ZnO, facilitating thereby an effective recombination tunneling phenomena. The region III (4.6 V < V < 6.2 V) is characterized by a steep exponential growth of current with the bias voltage and is also attributed to the multiple recombination tunneling events. Finally, beyond 6.2 V (region IV), the current transport follows a power law ($I \propto V^2$), which is recognized as the contribution owing to the space charge limited current (SCLC) conduction process [21, 22].

The *log-log I-V* characteristics of *S2* (Figure 6.9 (b)) has invariably exhibited five different regions. The transport mechanism within region I (V < 0.1 V) is dominated by a tunneling current, whereas, the current transport in region II (0.1

V < *V* 1.3 < V), III (1.3 V < *V* < 4.3 V) and IV (4.3 V < *V* < 6.4 V) are dominated by the recombination tunneling mechanism to different extents. Beyond *V* > 6.4 V (region V), the transport mechanism is governed by SCLC phenomena. Similarly, five independent regions corresponding to direct tunneling, recombination tunneling and SCLC mechanisms are also observed in the *log-log I-V* plot of *S3* (Figure 6.9 (c)). On the other hand the *log-log I-V* response of *S4* (Figure 6.9 (d)) is characterized by only three regions. For instance the tunneling current is evident in the region I (*V* < 0.1 V), whereas the current conduction through the recombination tunneling process is dominant within region II (0.1 V < *V* < 2.3 V). Finally, the SCLC mechanism becomes predominant over other mechanisms for biasing voltage beyond 2.3 V (region III). The dominance and extent of different characteristic regions in different samples are the outcome of annealing temperature led variation and distribution of the different native defects within the band gap of the ZnO nanorods.

6.1.2 Modification in transport properties of Ag/ZnO junction by energetic ion irradiation

As discussed in Chapter 4, energetic ion irradiation is capable of tuning (through creation and annihilation) various native defects in the ZnO nanorod system. In this context, ion irradiation can be very effective for controlling the transport properties of the Metal/ZnO junction. Having this objective in mind, the transport properties were investigated in Ag/ZnO junctions which make use of unirradiated and 80-MeV oxygen ion (O^{6+}) irradiated randomly oriented ZnO nanorods. The ZnO nanorods on Al_2O_3/Al substrates were fabricated through a thermal annealing process with precursor pH value of 8.5 and annealing temperature of 750 (± 5) °C as discussed in Chapter 2. The ZnO nanorods grown on Al_2O_3/Al substrates were irradiated in the Material Science chamber under a high vacuum (pressure ~10^{-7} mbar) condition and using 80-MeV O^{6+} ion beams (at a low beam current of ~ 0.6 pnA, particle-nanoampere), available at the 15UD tandem pelletron accelerator of Inter University Accelerator Centre, New Delhi. In order to facilitate defect-related modification without inducing agglomeration of the

nanorods, the fluence values were kept as low as 3 x 10^{10}, 6 x 10^{10}, and 9 x 10^{10} ions/cm^2. Next the metallic contacts of Ag were fabricated on the top-surfaces of the unirradiated and irradiated nanorods by means of thermal evaporation process as discussed in the earlier section.

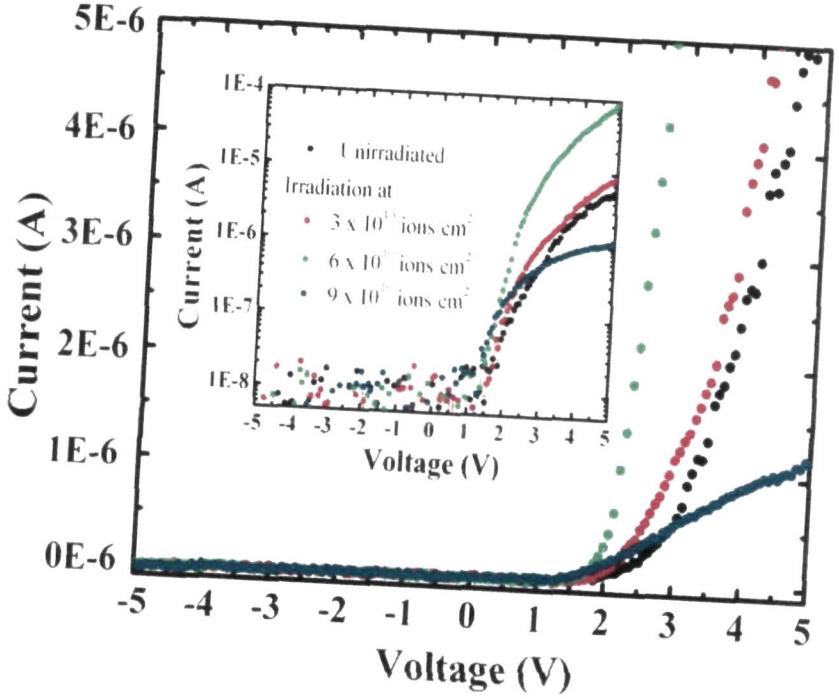

Figure 6.10: Room temperature *I-V* curves of the Ag/ZnO junctions before and after irradiation at different fluences. Inset being the corresponding semi-logarithmic *I-V* curves.

As shown in Figure 6.10, the room temperature *I-V* curves of the Ag/ZnO junctions before and after irradiation exhibit excellent rectifying nature with very low values of leakage currents. Ideally a non-linear *I-V* response could ensure the formation of Schottky contact between the Ag metallic contacts and the ZnO nanorods. The η and ϕ_B of the Ag/ZnO junctions were calculated using the semi-logarithmic *I-V* curve, depicted in the inset of Figure 6.10. As to the unirradiated nanorod system, the η of the corresponding Ag/ZnO junction was found to be as high as 17.7, while ϕ_B beared a value of 0.78 eV. In the pretext of earlier section, the presence of a large number of surface/defect states within the band gap of ZnO is largely responsible for the non-ideal character of the Schottky junction.

Upon 80 MeV O^{6+} ion irradiation of the nanorods (with fluences of 3 x 10^{10} and 6 x 10^{10} ions/cm^2), the current under forward bias in the respective Ag/ZnO junctions was found to be substantially improved exhibiting steep slopes (Figure 6.10). The Schottky barrier height, ϕ_B, of these Schottky junctions also show adequate enhancement with respective values of 0.95 and 0.9 eV for nanorod systems subjected to irradiation. The corresponding values of η were estimated to be 6.9 and 7.3, which are comparatively smaller than the case for unirradiated system (η = 17.7). Finally, for the nanorod system irradiated at the highest fluence (9 x 10^{10} ions/cm^2), a lower forward current was witnessed, which maintains a higher value of ϕ_B (0.87 eV) and a moderate value of η (8.0), compared to the unirradiated system.

The different native defects of ZnO nanorod systems that were responsible for the non-ideal characteristics of the Ag/ZnO junction can be identified through the analysis of the PL spectra. Figure 6.11 depicts the room temperature PL spectra of the virgin and irradiated samples considering an excitation wavelength, λ_{ex} = 325 nm. The PL spectra show the radiative emission response via various native defect states of ZnO such as, zinc/oxygen vacancies, interstitials and antisites. The PL emission intensities of the nanorods irradiated with a fluence of 3 x 10^{10} and 6 x 10^{10} ions/cm^2 were found to be improved as compared to the unirradiated one. Such an increase in the emission intensity can be assigned to the dominance of

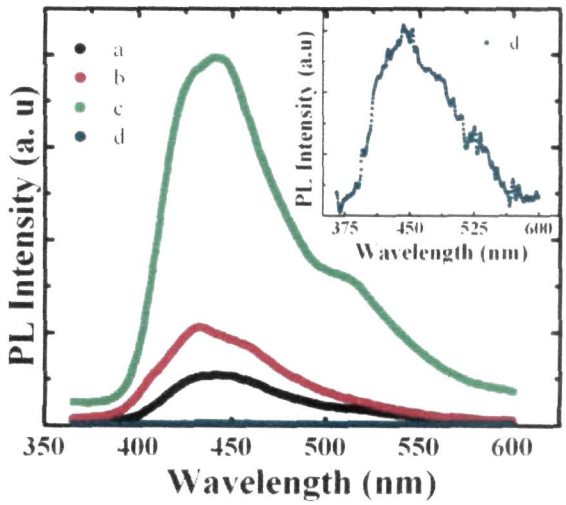

Figure 6.11: Room temperature PL spectra of the nanorods a) before, and after irradiation with a fluence of (b) 3 x 10^{10} ions/cm^2, (c) 6 x 10^{10} ions/cm^2, and (d) 9 x 10^{10} ions/cm^2. Inset being the magnified version of the PL spectra of the nanorods irradiated at 9 x 10^{10} ions/cm^2.

creation over annihilation of native defects as a result of the bombardment of energetic ions [23, 24]. The irradiation induced increase of defect concentration of the nanorods was chiefly responsible for the observed enhancement in the current conduction in the *I-V* response of the two Ag/ZnO nanojunctions under study. Moreover, upon irradiation at the highest fluence (9 x 10^{10} ions/cm^2), the luminescence intensity of the nanorods gets suppressed. The luminescence quenching can be attributed to the collective annihilation of the various defect states owing to adequate migration of interstitials and fast structural ordering in view of significant electronic energy loses of projectile ions [25]. In gist, the noticeable lowering of forward current in the Ag/ZnO junction made out of these nanorods is solely attributed to the suppression of native defect concentration as compared to the unirradiated one.

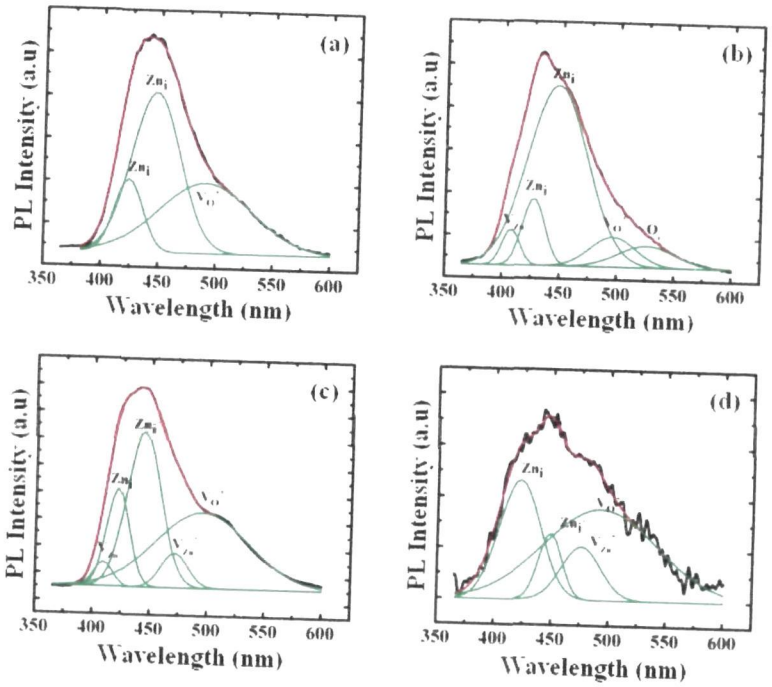

Figure 6.12: Gaussian fittings of the PL spectra. a) Before irradiation, and after irradiation with a fluence of (b) 3 x 10^{10} ions/cm^2, (c) 6 x 10^{10} ions/cm^2, and (d) 9 x 10^{10} ions/cm^2.

To make a comprehensible assessment of the independent contribution of the native defects, generalized Gaussian fitting was used to extract different peak maxima associated with different types of defect (Figure 6.12). The PL spectrum

of the unirradiated nanorods (Figure 6.12(a)), shows three major peaks corresponding to neutral zinc interstitial (Zn_i at ~ 423 nm), singly ionized zinc interstitial (Zn_i^+ at ~ 446 nm), and singly ionized oxygen vacancy (V_O^+ at ~ 491 nm) related emissions. Among these three defects related emissions, the Zn_i^+ related emission was dominating one in the overall spectrum. Upon irradiation with a fluence of 3 x 10^{10} ions/cm^2 (Figure 6.12(b)), emission peaks related to the neutral zinc vacancy (V_{Zn} ~ 407 nm) as well as oxygen interstitials (O_i at ~ 526 nm) have evolved [12, 13]. Although the emission peaks related to Zn_i and Zn_i^+ defects remain intact, the V_O^+ related response gets suppressed. This fact could be accounted for annealing out of considerable amount of V_O^+ defects than other types of defects when the sample was subjected to oxygen irradiation (equivalent of annealing in air) [26]. Secondly, irradiation with a fluence of 6 x 10^{10} ions/cm^2 (Figure 6.12(c)) has resulted in the decrease of the neutral V_{Zn} related emission but leads to the appearance of an emission peak due to singly ionized zinc vacancy (V_{Zn}^-) defects at ~ 472 nm. Finally, at the highest fluence of 9 x 10^{10} ions/cm^2, the V_{Zn} related emission gets completely quenched, while V_{Zn}^- related response remained unaltered, as found in Figure 6.12(d). Therefore, it suggests that the V_{Zn} defects created at a fluence of 3 x 10^{10} ions/cm^2, were partly converted to V_{Zn}^- defects when a higher value of fluence (6 x 10^{10} ions/cm^2) was considered. At 9 x 10^{10} ions/cm^2, all the V_{Zn} defects get transformed into V_{Zn}^- defects as a result of which V_{Zn} related emission is drastically quenched. It can also be noticed that the Zn_i related emission increases over Zn_i^+ related emission, as one moves from a low to a high fluence value. It was known earlier that during irradiation, the electronic energy loss (S_e) is generally used in ionizing the target material along the path of the ions [25]. In the present study, the considerable magnitude of S_e (1.62 x 10^2 eV/Å) of the oxygen ions in host ZnO is capable of ionizing Zn_i and the neutral V_{Zn} defects. Consequently, there will be a conversion of V_{Zn}-to-V_{Zn}^- defects and Zn_i^+-to-Zn_i defects along the trajectory of the ions. The probability of such conversions increases as more ions have impact with the target material. At the highest fluence, the V_{Zn} defects get converted to V_{Zn}^- defects, and

at the same time the Zn_i^+ defects were transformed to Zn_i defects via manifestation of electron transfer process.

The carrier transport mechanism of the Ag/ZnO junctions were analyzed from the characteristic *I-V* curves in the *log-log* scale (Figure 6.13). The Ag/ZnO Schottky contacts that use pristine nanorods, have exhibited two distinct regions of current conduction as shown in Figure 6.13(a). The current in region-I ($V < 3.1$ V) shows

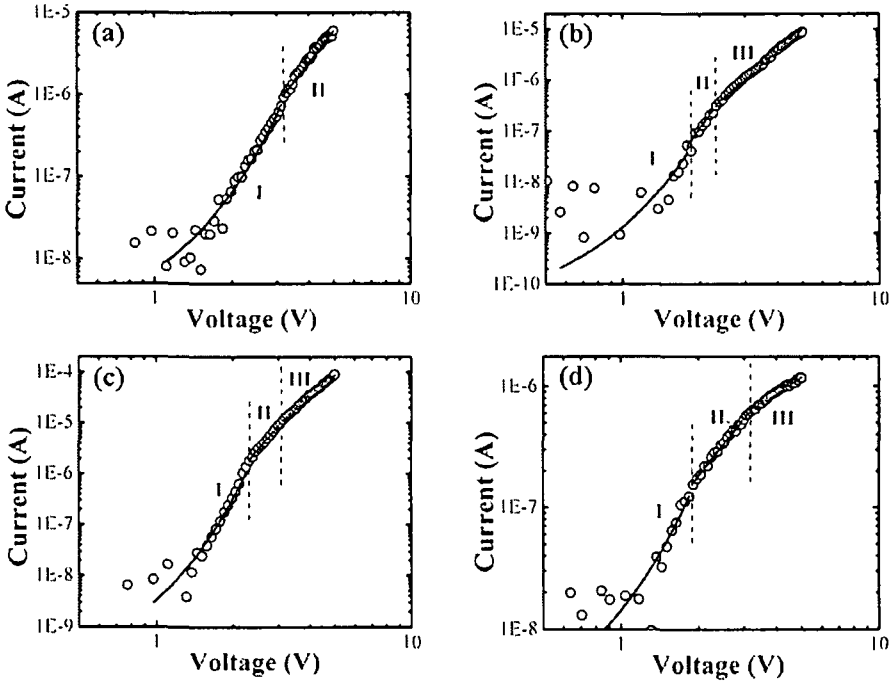

Figure 6.13: The *log-log* plot of the *I-V* characteristics of the Ag/ZnO junction using pristine and irradiated nanorods. Here, Ag/ZnO junction comprises (a) pristine nanorods, and ion irradiated nanorods at fluence (b) 3 x 10^{10} ions/cm^2, (c) 6 x 10^{10} ions/cm^2, and (d) 9 x 10^{10} ions/cm^2.

an exponential increase with respect to the applied voltage following a relation $I \propto \exp(\alpha V)$, α being a system dependent parameter. The η value of the system was calculated within this region where the conduction mechanism is dominated by the recombination tunneling. Beyond 3.2 V (region-II), the current conduction follows a power law obeying the relation: $I \propto V^m$, where $m = 4$ and the effective current transport mechanism is assigned to the space charge limited conduction

(SCLC). The current is dominated by the drift component of the injected carriers i.e. due to the movement of charge carriers on the application of electric field. In the present case, as $m > 2$, the SCLC is said to be in the mobility region where the carrier velocity depends on the electric field with an exponential distribution of the traps within the band gap of ZnO [27, 28]. For this reason, it is also termed as trap charge-limited current (TCLC) [27].

Table 6.2: The parameters associated with various transport mechanism for different ZnO nanorod systems used in making Ag/ZnO junctions.

Fluence (ions/cm^2)	ϕ_B (eV)	η	**Recombination tunneling**	**SCLC / TCLC**	
			Region I	**Region II**	**Region III**
0 (Unirradiated)	0.78	17.7	1.1 V – 3.1 V	> 3.2 V ($m \sim 4$)	-
3×10^{10}	0.95	6.9	0.6 V – 1.8 V	1.8 V – 2.2 V ($m \sim 7$)	> 2.2 V ($m \sim 4$)
6×10^{10}	0.9	7.3	0.9 V – 2.2 V	2.3 V – 3.1 V ($m \sim 6$)	> 3.1 V ($m \sim 4.3$)
9×10^{10}	0.87	8.0	0.7 V – 1.8 V	1.8 V – 3.2 V ($m \sim 2.7$)	> 3.2 V ($m \sim 1.4$)

For the junctions comprising of the irradiated ZnO nanorods, the injected current exhibited three separate regions in the *log-log* scale of *I-V* plots (Figure 6.13 (b-d)). Table 6.2 shows the typical ranges responsible for the transport mechanism. In all the Ag/ZnO junctions under study, the current conduction is predominantly governed by the recombination tunneling mechanism which is characterized by an exponential increase in current (region-I). The current in region-II is described by a power law indicating the dominance of TCLC mechanism similar to the unirradiated one but with a different value of m (>2). Apart from these two conventional regimes, an additional zone (region-III) has evolved for the Schottky junctions based on irradiated nanorods (Figure 6.13 (b-d); Table 6.2). Governed by the SCLC mechanism, the current conduction in this new region still obeys the power law but possesses lower values of m. Moreover, dominated by TCLC

transport mechanism, the Schottky junctions that use the ZnO nanorods irradiated with fluences of 3 x 10^{10} ions/ cm^2, and 6 x 10^{10} ions/ cm^2, have exhibited higher values of m ($\geq$ 4) (Figure 6.13 (b,c) Table 6.2). At the highest fluence (9 x 10^{10} ions/cm^2), in the region III, m acquires a marginal value of 1.4. At this time, the SCLC is in ballistic regime i.e. the critical dimension where the carrier transit is comparable or smaller than the mean free path [1]. In this situation, the carrier velocity is independent of the field and scattering process, but depends on the injection velocity of the source [1, 29]. The appearance of the new region (III) for the Schottky contacts made of the irradiated nanorods is attributed to the irradiation induced modification in the charge carrier distribution due to the reorganization of the different defects of ZnO.

6.2 Metal-insulator-semiconductor junction

The existence of a thin insulator layer (of the order of few atomic dimensions) between a metal and semiconductor forms a typical metal-insulator-semiconductor (MIS) junction. The current conduction in MIS junction differs from that of the MS junction, in the sense that, the former is accompanied by unlike potential barriers at the metal-insulator and insulator-semiconductor interfaces. These interfacial potential barriers have considerable effect on the electron transport mechanism from semiconductor-to-metal or vice-versa [30]. The transport mechanism, in the MIS junction, is mostly expressed in the light of the following models: Direct tunneling, Thermionic emission, Poole-Frenkel

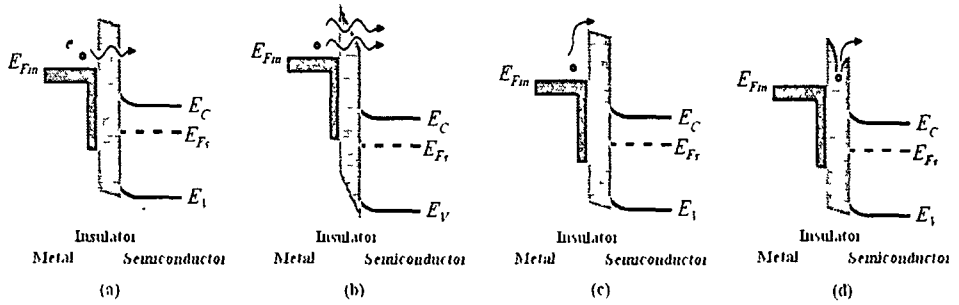

Figure 6.14: Different conduction processes occurring in a typical MIS junction.

emission, and Fowler-Nordheim tunneling. Figure 6.14 depicts a series of various conduction processes in a typical MIS junction [1, 31-33]. The tunneling current is a quantum mechanical phenomenon where the electron can tunnel through a potential barrier. Such an event is called direct tunneling (DT) of electrons. In the MIS junction DT takes place across the trapezoidal shaped barrier under biasing condition (Figure 6.14 (a)). Further, Fowler-Nordheim tunneling (FN) is unusual mechanism where carriers tunnel through only a partial width (i.e. through the triangular segment) of the barrier as depicted in Figure 6.14 (b) [1, 34]. Thermionic emission (TM) over the metal-insulator barrier or the insulator-semiconductor barrier is also responsible for carrier transport in MIS junction. Finally Poole-Frenkel emission (PF) in MIS junction occurs owing to the emission of trapped electrons into the conduction band (Figure 6.14 (d)) [1].

The urchin like structure and the randomly distributed nanorods of ZnO fabricated using a thermal annealing process at 400 and 650 °C were used for the fabrication of MIS junctions. The two samples were named as *S1* and *S2* and their structural and morphological features were described in Chapter 2. Metallic contacts of Ag (~ 60 nm layer) were deposited on the ZnO nanostructure grown Al_2O_3/Al substrate using a thermal evaporation method. As shown in the schematic of Figure 6.15 the intentionally grown Al_2O_3 layers act as interfacial layer separating the ZnO nanostructures and metallic Al-base. Two vertical terminals were made out of the Ag-contacts upon the nanostructure systems (terminals *a* and *b*), while another terminal was taken directly from the metallic-Al substrate (terminal *c*). In this way the Al/Al_2O_3/ZnO MIS configuration was achieved with terminals *a* and *c*, while Ag/ZnO MS configuration was realized with terminals *a* and *b*

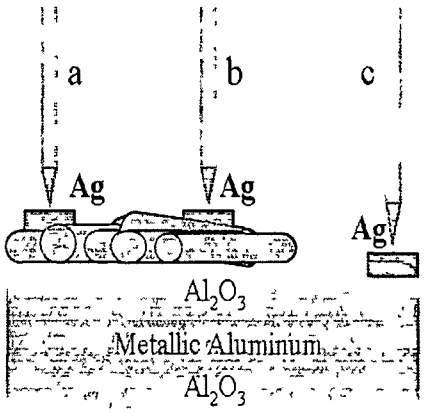

Figure 6.15: Schematic view of the Ag/ZnO and Al/Al_2O_3/ZnO junctions.

The representative *I-V* curves of the Ag/ZnO MS (terminal *a* and *b*) and $Al/Al_2O_3/ZnO$ MIS junctions (terminal *a* and *c*) are illustrated in Figure 6.16. The *I-V* characteristics of the Ag/ZnO junctions prepared out of the nanorod samples *S1* and *S2* have exhibited a nonlinear rectifying response. The Schottky contact

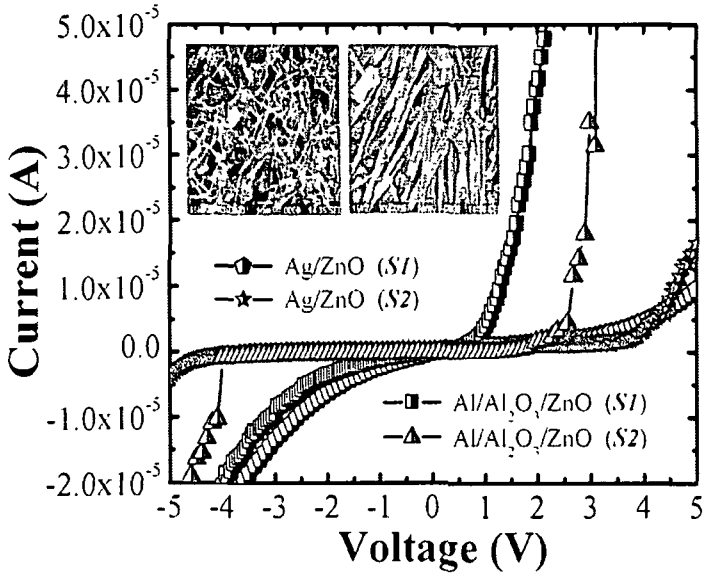

Figure 6.16: *I-V* characteristic curves of the Ag/ZnO MS and $Al/Al_2O_3/ZnO$ MIS nanojunctions.

formed between metallic-Ag and the ZnO nanostructures is thus established. In contrast to that, the *I-V* patterns of the $Al/Al_2O_3/ZnO$ junctions witness higher current conduction. Both the MIS junctions formed out of the samples *S1* and *S2*, are characterized by a sharp rise in current, beyond a critical voltage. The critical voltages were found to be ~ 0.9 V for *S1* and ~ 1.2 V for *S2*. The difference of the current conduction in MS and MIS junctions is believed to have occurred because of the interplay of different transport mechanisms in the two types of junctions.

The nature of current transport mechanism responsible for the current conduction in the Ag/ZnO Schottky junction has already been discussed in the earlier section. The Ag/ZnO Schottky junctions were found to be dominated by direct tunneling current, recombination tunneling and space charge limited conduction (SCLC) at different regions of the applied voltage. So as to find the dominant transport

mechanism in the Al/Al_2O_3/ZnO MIS junctions, the corresponding *I-V* responses were fitted in the thermionic emission model using the equation [1]:

$$I \propto A^* T^2 \exp\left(-\frac{q\phi_B}{kT} + \sqrt{\frac{q^5 V}{4\pi\varepsilon_d}}\right) \qquad (6.4)$$

where, A^*, ϕ_B, k, T, ε_d and q denote the Richardson's constant, barrier height, Boltzmann constant, working temperature, dielectric permittivity and fundamental electronic charge respectively. As shown in the plot of *log (I)* and $V^{1/2}$ (Figure 6.17), under forward biasing, the linear fits, within the region upto ~ 1 V reveal that the current conduction in this region follow the thermionic emission model. In the present situation, the thermionic emission is reasonable as a number of thermally excited electrons are able to overcome the barrier and take part in the current conduction process. The dominance of thermionic emission current is also found under reverse bias condition (upto the biasing voltages of ~ 1.3 V and 4 V) in case of MIS junctions produced from nanorod samples of *S1* and *S2*.

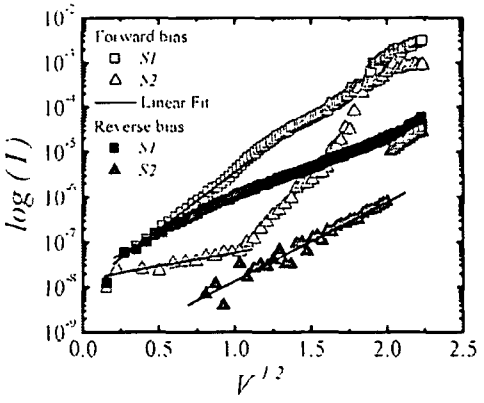

Figure 6.17: Variation of *log(I)* with $V^{1/2}$ of two Al/Al_2O_3/ZnO junctions. The unfilled (open) and filled (solid) labels represent forward and reverse biasing.

A significant electron tunneling through any insulator layer is the prime event that is applicable to any MIS junction where the energy barrier for tunneling varies with the applied voltage. The occurrence of tunneling current, in the Al/Al_2O_3/ZnO MIS junction has been realized in the *log-log* plot of the *I-V* curves (Figure 6.18). Under forward bias condition, the linear fit within a region upto ~ 0.6 V for the junction with *S1* and ~ 1.1 V for that with *S2*, corresponded to the conventional Ohmic feature ($I \propto V$). Likewise, upon reverse biasing, the Ohmic conduction due to the electron flow from Al to ZnO through the barrier was

evident upto ~ 2.2 V and 4 V for the respective junctions that use *S1* and *S2* nanorod systems. Therefore, it can be suggested that the dominance of direct tunneling of electrons through the insulating Al_2O_3 layer is highly favorable when the applied voltage is less than the height of the trapezoidal barrier [1, 35]. Should the applied voltage exceeds the barrier height, the barrier gradually transforms into triangular shape. This accounts for significant electron tunneling through the partial width of the barrier [1, 35]. The situation where tunneling through the triangular barrier predominates, is recognized as FN tunneling. The FN tunneling related current conduction follows the equation [1]:

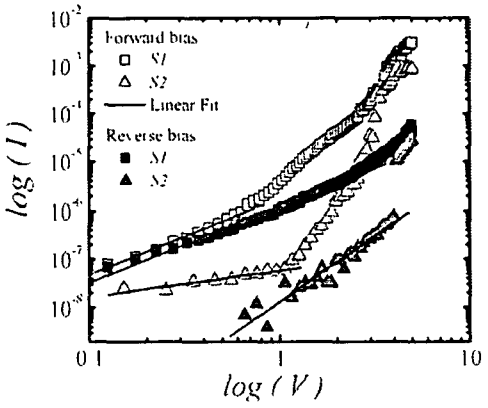

Figure 6.18: Variation *log(I)* vs. *log(V)* of two $Al/Al_2O_3/ZnO$ junctions. The unfilled (open) and filled (solid) labels represent forward and reverse biasing; respectively.

$$I \propto V^2 \exp\left(-\frac{4t\sqrt{2m_e\phi^3}}{3\hbar qV}\right) \qquad (6.5)$$

here, t, m_e are the barrier width and the effective mass of electron; respectively.

The plots depicts FN tunneling across two MIS junctions are shown in Figure 6.19, while the schematic of the figure inset represents the ongoing event. The plot of *log* (I/V^2) as a function of V^{-1} possesses a linear trend above 0.8 V and 1.2 V for the two junctions made out of samples of *S1* and *S2*; respectively. The linear responses observed above these

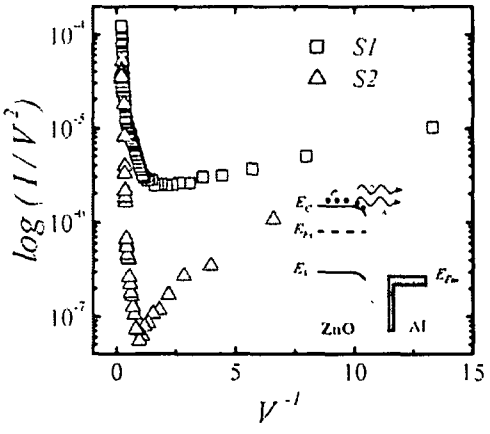

Figure 6.19: Variation of *log* (I/V^2) vs. V^{-1} under forward bias of two $Al/Al_2O_3/ZnO$ junctions. Inset shows the corresponding schemes of FN tunneling.

voltages reveal the dominance of the FN tunneling of electrons through the insulating Al_2O_3 layer. Now, the two voltages beyond which the MIS junctions exhibit FN tunneling were investigated in the characteristic *I-V* plots (Figure 6.16). It was found that above the two voltage regions the current grows significantly with the applied voltage. Therefore, the rapid current growth observed in the *I-V* plots of two junctions, is a consequence of FN tunneling of electrons from the ZnO nanorods to the Al-substrate mediated through the thin Al_2O_3 interfacial layer. In the lower voltage region and below the critical voltage, the current conduction was found to be dominated by TE and DT events of electrons. Earlier, Beebe *et al.* have demonstrated the transition of DT tunneling to FN tunneling above a transition voltage in case of metal-molecular nanojunctions and ascribed to the transformation of the trapezoidal barrier to a triangular one [35]. Again, Cheo and the co-workers have also observed the transition of DT tunneling to FN tunneling while considering field effect transistor action of ZnO nanowires [36]. A similar situation can also be recognized in the present case also, where a changeover from both the DT tunneling and TM to the FN tunneling is assured. Thus, both TM and DT tunneling were observable with a small barrier height and width of the interfacial Al_2O_3 layer, while transition to the FN tunneling beyond a critical voltage accounts for the slanted barrier width. In contrast, an analogous trend was also observed in the reverse bias mode, where the FN tunneling of electrons takes place from the metallic Al to ZnO nanorods through the interfacial Al_2O_3 layer (Figure 6.20). Under a reverse bias mode, the critical voltage above which the FN tunneling occurs was found to be ~ 2.4 V and 4.1 V for the junctions with *S1* and *S2* samples respectively.

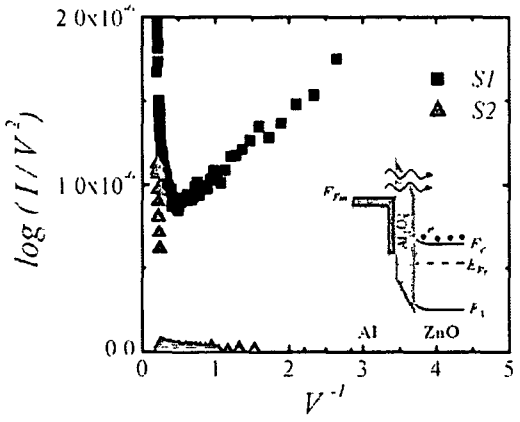

Figure 6.20: The variation of *log* (I/V^2) vs. V^{-1} under reverse bias. Inset being the corresponding scheme of the FN tunneling.

It can be noticed in Figure 6.19 that the critical voltage above which FN tunneling dominates the *I-V* response is different for two Al/Al_2O_3/ZnO MIS junctions made out of samples *S1* and *S2*. The mean critical voltage was determined by considering 10 different *I-V* scans at different contact positions of the samples (referring to Figure 6.15, terminals *a* and *c; b* and *c*) and was found to be ~ 1.2 V and ~ 1.6 V for the two individual junctions. The variation in the critical voltages of the two types of junctions suggests the non-identical thickness of the Al_2O_3 layer in the two samples *S1* and *S2*. The width of the barrier is expected to be less in the MIS junction with *S1* due to which the critical voltage acquires a lower value (~1.2 V) as compared to that of *S2* (~1.6 V). It is now ascertained that the formation of Al_2O_3 layer over the metallic-Al, is depended on the annealing temperature. As *S2* was prepared at a comparatively higher temperature than *S1*, it is speculated that, the insulating layer formed is thicker in *S2* than in *S1*. Figure 6.21 represents the schematic view of the two junctions with different thicknesses of the insulating layer. Consequently, above the critical voltages, electron tunneling occurs in larger amount across the MIS junction with *S1* as the width of the triangular region of this junction becomes smaller than that of *S2*

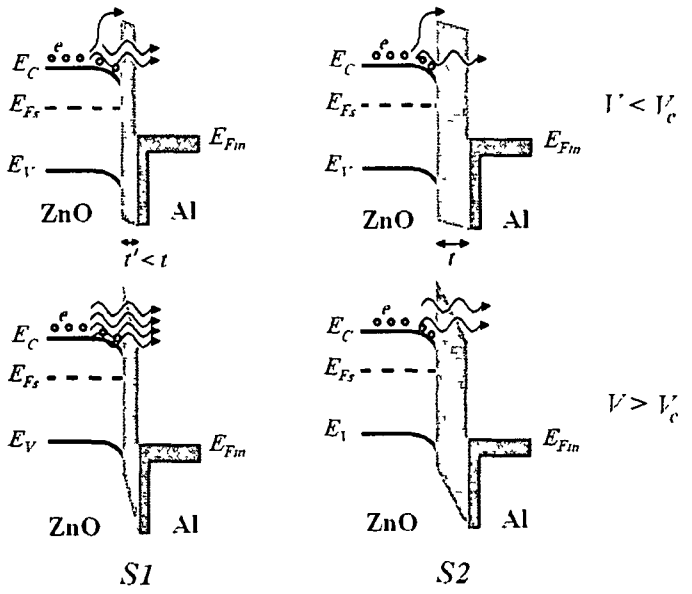

Figure 6.21: Schematic view of the electron transport across the MIS junctions with different thicknesses of the insulating layer under forward bias.

6.3 Concluding remarks

The salient current transport features of ZnO nanostructure based various metal-semiconductor (MS) and metal-insulator-semiconductor (MIS) junctions have been investigated. The MS Ag/ZnO junction exhibited rectifying nature with higher ideality factor due to the presence of various native defects of ZnO. The annealing temperature led dominance of the donor or acceptor type defects has foremost effect on the current transport properties of the junction and hence, alters the ideality factor and barrier height of the Schottky junctions. The current transport mechanism in the Ag/ZnO junction was found to be dominated by direct tunneling, recombination tunneling and space charge limited conduction. Again, energetic ion irradiation was found to play crucial role in controlling nanostructure defects and hence altering the transport properties of Ag/ZnO Schottky junctions. The ion fluence dependent variation in the ideality factor and barrier height can be assigned to the competition among the donor and acceptor type of defects of ZnO. In contrast, significant Fowler-Nordheim (FN) tunneling across $Al/Al_2O_3/ZnO$ MIS junction have also been demonstrated. The current transport was found to be dominated by thermionic and direct tunneling events through the insulating Al_2O_3 layer. Above a critical voltage (< 5 V), the $Al/Al_2O_3/ZnO$ junctions exhibited sharp rise in current due to the dominance of the FN tunneling of electrons through the Al_2O_3 insulating layer, over other transport processes. The fundamental investigations of such current transport mechanism in metal-semiconductor and metal-insulator-semiconductor junctions are useful for direct electrical probing and essential for the development of prototype devices that can work at low operating voltage but with high throughout and figure of merit.

References:

[1] Sze, S. M. & Ng, K. K. *Physics of semiconductor devices*, Wiley-India, Delhi, 2010.

[2] Mishra, U. K. & Singh, J. *Semiconductor device physics and design*, Springer, Netherlands, 2008.

[3] Gu, Q. L., et. al. Au/*n*-ZnO rectifying contact fabricated with hydrogen peroxide pretreatment, *J. Appl. Phys.* 103, 093706 (1-8), 2008.

[4] Cheung, s. K. & Cheung, N. W. Extraction of Schottky diode parameters from forward current-voltage characteristics, *Appl. Phys. Lett.* 49 (2), 85-87, 1986.

[5] Kim, H., et. al. Silver Schottky contacts to *a*-plane bulk ZnO, *J. Appl. Phys.* 108, 074514 (1-5), 2010.

[6] Lee, S., et. al. Impact of defect distribution on transport properties for Au/ZnO Schottky contacts formed with H_2O_2-treated unintentionally doped *n*-type ZnO epilayers, *Appl. Phys. Lett.* 96, 142102 (1-3), 2010.

[7] Allen, M. W., et. al. Oxidized noble metal Schottky contacts to *n*-type ZnO, *Appl. Phys. Lett.* 94, 103508 (1-3), 2009.

[8] Allen, M. W., & Durbin, S. M., Influence of oxygen vacancies on Schottky contacts to ZnO, *Appl. Phys. Lett.* 92, 122110 (1-3), 2008.

[9] Das, S. N., et. al. Junction properties of Au/ZnO single nanowire Schottky diode, *Appl. Phys. Lett.* 96, 092111 (1-3), 2010.

[10] Motayed, A., et. al. Fabrication of GaN-based nanoscale device structures utilizing focused ion beam induced Pt deposition, *J. Appl. Phys.* 100, 024306 (1-8), 2006.

[11] Harnack, O., et. al. Rectifying Behavior of Electrically Aligned ZnO Nanorods, *Nano Lett.* 3, 1097-1101, 2003.

[12] Lin, B. et al. Green luminescent center in undoped zinc oxide films deposited on silicon substrates, *Appl. Phys. Lett.* 79, 943-945, 2001.

[13] Lima, S. A. M. et al. Luminescent properties and lattice defects correlation on zinc oxide, *Int. J. Inorg. Mater.* 3, 749-754, 2001.

[14] Ye, J. D. et al. Correlation between green luminescence and morphology evolution of ZnO films, *Appl. Phys. A* 81, 759-762, 2005.

[15] Zhang, L.-L. et al. The synthesis of one-dimensional controllable ZnO microrods, *Chinese Phys.* 14 (3), 586-591, 2005.

[16] Tam, K. H. et al. Defects in ZnO nanorods prepared by a hydrothermal method, *J. Phys. Chem. B* 110, 20865-20871, 2006.

[17] Bayan, S., & Mohanta, D., Defect mediated optical emission of randomly oriented ZnO nanorods and unusual rectifying behavior of Schottky nanojunctions, *J. Appl. Phys.* 110, 054316 (1-6), 2011.

[18] Look, D,C., et. al. Electrical and optical properties of defects and impurities, *Physica B* 340–342, 32–38, 2003.

[19] Klason, P., et. al. Electrical characteristics and stability of gold and palladium Schottky contacts on ZnO nanorods, *Nanotechnology*, 19, 475202 (1-5), 2008.

[20] Bindal, A., et. al. Observation of recombination centre assisted tunneling current in Al(Cu)-penetrated PtSi Schottky barrier diodes, *J. Appl. Phys.* 68, 6259-6262, 1990.

[21] Kishwar, S., et. al. A comparative study of the electrodeposition and the aqueous chemical growth techniques for the utilization of ZnO nanorods on p-GaN for white light emitting diodes, *Superlattices and Microstructures* 49, 32–42, 2011.

[22] Ghosh, R. & Basak, D. Electrical and ultraviolet photoresponse properties of quasialigned ZnO nanowires/*p*-Si heterojunction, *Appl. Phys. Lett.* 90, 243106 (1-3), 2007.

[23] Bayan, S. & Mohanta, D. Effect of 80-MeV nitrogen ion irradiation on ZnO nanoparticles: Mechanism of selective defect related radiative emission features, *Nucl. Instr. and Meth. in Phys. Res. B* 269, 374-379, 2011.

[24] Bayan, S. & Mohanta, D. Unusual rectifying response of nanojunctions using randomly oriented nanorods (RON) of ZnO irradiated with 80-MeV oxygen ions, *J. Electron. Mater.* 41(7), 1955-1961, 2012.

[25] Fleischer, R. L. et al. Ion explosion spike mechanism for formation of charged-particle tracks in solids, *J. Appl. Phys.* 36, 3645-3652, 1965.

[26]. Tinchev, S.S. Properties of YBCO weak links prepared by local oxygen-ion induced modification, *Physica C* 256, 191-198, 1996.

[27] Son, D.I., et. al. Electrical bistabilities and memory mechanisms of organic bistable devices based on colloidal ZnO quantum dot-polymethylmethacrylate polymer nanocomposites, *Appl. Phys. Lett.* 97, 013304 (1-3), 2010.

[28] Yen, T.F., et. al. Effect of post-deposition processing on ZnO thin films and devices, *J. Electron. Mater.* 39, 568-572, 2010.

[29] Catalfamo, F., et. al. Effects of high-energy electron irradiation on ZnO/Si MSM photodetectors, *J. Electron. Mater.* 40, 433-439, 2011.

[30] Zhou, S. X., et. al. *I-V* Characteristics of Metal-Oxide-ZnSe Nanowire Structure, *J. Phys. Chem. C* 112, 18644-18650, 2008.

[31] Dahlke, W. E. & Sze, S. M. Tunneling in metal-oxide-silicon structures, *Solid. St. Electron.* 10, 865-873, 1967.

[32] Jacques, E., et. al. Electrical behavior of MIS devices based on Si nanoclusters embedded in SiO_xN_y and SiO_2 films, *Nanoscale Res. Lett.* 6, 70 (1-6), 2011.

[33] Son, D.I., et. al. Carrier transport in flexible organic bistable devices of ZnO nanoparticles embedded in an insulating poly(methyl methacrylate) polymer layer, *Nanotechnology*, 20, 195203 (1-6), 2009.

[34] Hu, Y. et. al. Monodisperse ZnO nanodots: Synthesis, charaterization, and optoelectronic properties, *J. Phys. Chem. C* 111, 9757-9760, 2007.

[35] Beebe, J. M., et. al. Transition from Direct Tunneling to Field Emission in Metal-Molecule-Metal Junctions, *Phys. Rev. Lett.* 97, 026801 (1-4), 2006.

[36] Choe, M. et. al. Electrical properties of ZnO nanowire field effect transistors with varying high-*k* Al_2O_3 dielectric thickness, *J. Appl. Phys.* 107, 034504 (1-4), 2010.

Chapter 7

Ultraviolet photodetection characteristics of ZnO nanostructures

With the swift advancement of modern civilization, environment related several aspects have become a point of threat to humanity. Ultraviolet (UV) photodetection has gained an immense attention over the recent years. The UV photodetectors find applications not only in environment and solar UV monitoring but also in various technological aspects. As far as UV detection is concerned, extensive research is being perused to develop enduring and cost effective UV photodetectors based on semiconductor materials. ZnO being a wide band gap semiconductor is suitable for UV detection. Again, the high surface-to-volume ratio of nanoscale materials makes the system more promising for UV detection application. The current Chapter focuses on the UV detection aspect of the ZnO nanostructures and the on going mechanism.

7.1 Photoconductivity in ZnO

A photodetector is a device that can provide an electrical response as a measure of incident electromagnetic radiation. There are several varieties of photodetectors, such as photoconductors, photodiodes, phototransistors, charge-coupled devices (CCD) etc. Generally, the photodetection in a photodetector involves the formation of electron-hole pairs upon the absorption light having energy greater than the band gap of the material [1]. However, the photoconductivity in ZnO (typically within 300-400 nm range) is explained in terms of two different mechanisms: first one is the bulk related process and the second as the surface related process [2-8]. The bulk related process deals with the fact that ZnO can adsorb O_2 from the ambient atmosphere in the grain boundaries and form O_2^- ions by capturing electron(s).

$$O_2 + e^- \rightarrow O_2^- \qquad (7.1)$$

This process leads to the formation of a barrier which lowers the conductivity of the material. Upon UV illumination (energy greater than the band gap of ZnO) electron-hole (*e-h*) pairs are generated.

$$h\nu \rightarrow e^- + h^+ \qquad (7.2)$$

The O_2^- species captures the hole and gets desorbed as neutral O_2.

$$O_2^- + h^+ \rightarrow O_2 \qquad (7.3)$$

This results in the reduction of the barrier height and increase in the effective conductivity [3, 4]. Since this process is associated with the events occurring across the grain boundaries and/or the core of the material, it can be assigned as a *core* process. On the other hand, the surface related process corresponds to the adsorption and desorption of O_2 at the surface of ZnO and is, prominent in nanoscale systems owing to high surface-to-volume ratio. The adsorbed O_2 species on the surface of ZnO captures an electron and becomes O_2^- as per in equation (7.1). Consequently, a depletion region is formed near the surface which would lower the conductivity. Upon UV illumination, the photogenerated hole compensates the O_2^- species through the surface *e-h* recombination. Thus desorption of neutral O_2 leads to the reduction of the width of the depletion region, while the photoexcited unpaired electron increases the photoconductivity of the material. Figure 7.1 demonstrates the situation in the absence and presence of the UV light. Although both the UV detection mechanisms are related with the variation in conductivity upon adsorption and desorption of O_2, the surface related process is slow compared to the *core* process [3, 4].

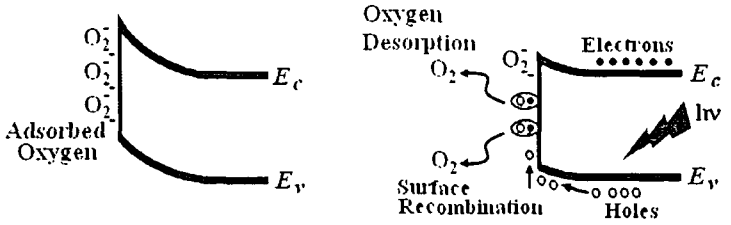

Figure 7.1: Schematic representation of UV sensing mechanism in ZnO system.

The urchin like structures of ZnO on Al_2O_3/Al substrate and ZnO nanorod arrays on glass substrate were tested for the UV detection. The structural and optical properties of the two types of nanostructures have been explored in the earlier Chapters. The current vs. voltage responses of the photodetectors were recorded using Keithley® 2400 Sourcemeter via two probe method. The photoconductivity

measurement were performed under a continuous illumination of a UV lamp (λ = 365 nm) at room temperature.

7.1.1 UV photodetection of ZnO Urchins system

In order to fabricate the UV-sensing device, metallic contacts in the form of two Ag-layers (thickness ~ 70 nm) were deposited on the urchin like structures grown on the Al_2O_3/Al substrate by using a thermal evaporation technique as discussed in Chapter 6. Figure 7.2 depicts a schematic view of the nanostructures with Ag-metallic contacts used for UV detection. The semilogarithmic *I-V* characteristics under forward bias condition for the urchin like structures of ZnO (recorded in dark and in presence of UV illumination) are shown in Figure 7.3. Basically, the inset of the figure reveals the *I-V* response in the dark. The non-linear rectifying trend of the typical *I-V* response originates from the Ag/ZnO Schottky junction formed between metallic Ag and the ZnO nanostructure. It can be observed that upon UV illumination, the current gets substantially enhanced as compared to the dark current. At a given bias voltage of 3V, the current under UV illumination is found to be ~ 11 times higher than the current in absence of UV light. The liberation of O_2 from the ZnO nanostructures via the *core* and surface related process has led to the increment in current during UV illumination.

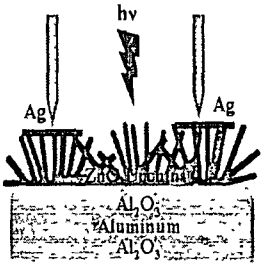

Figure 7.2: Schematic arrangement of the ZnO urchins used in UV detection.

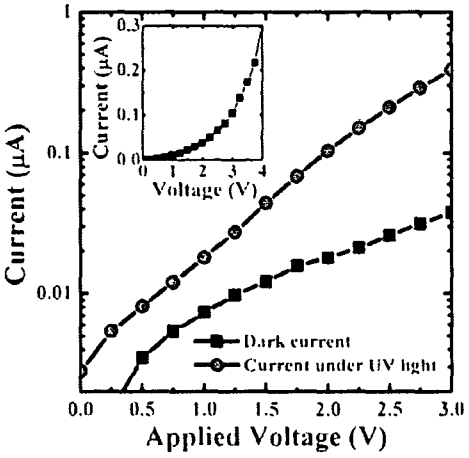

Figure 7.3: *I-V* characteristic curve (in semi-logarithmic scale) of the ZnO urchins in dark and in presence of UV light. Inset being the typical *I-V* response in dark.

Now the quality of a photodetector is evaluated in terms of the responsivity ($\mathcal{R}$). The responsivity of a photodetector is the ratio of the obtained photocurrent (I_{ph}) to the incident optical power (P_{in}) and is given by [1, 9-11],

$$\mathcal{R} = \frac{I_{ph}}{P_{in}} = G\frac{\eta q}{h\nu} \qquad (4)$$

where, G is the photoconductive gain, $h\nu$ is the incident photon energy, and q being the electronic charge. The basic metric on which the photocurrent depends is the quantum efficiency (η) which is defined as the number of carriers produced per photon. Ideally η is unity, while the non-ideality arises due to the current loss in mechanisms like recombination, unwanted scattering etc [1]. In the present case, assuming η as unity for convenience, $\mathcal{R}$ was determined as ~ 1.4 A / W at 3 V. The obtained value of $\mathcal{R}$ is a moderate one compared to the reported values for ZnO nanostructures or thin films [10-12].

The rise and decay current of the photodetector was recorded after every 15 s, for turning on/off conditions of the UV light at a constant forward biasing of 7.5 V as shown in Figure 7.4. The current under UV illumination increases rapidly with time and also falls quickly upon terminating the UV light. Under UV light (90-330 s), the current gets enhanced compared to the dark value (< 90 s). The photocurrent initially shows small fluctuation, but afterward becomes almost steady. In contrast to this region, the current upon UV termination (beyond 330 s) decreases in magnitude. The observed fast growth and decay responses suggest that the photoconductivity mechanism in the urchins is

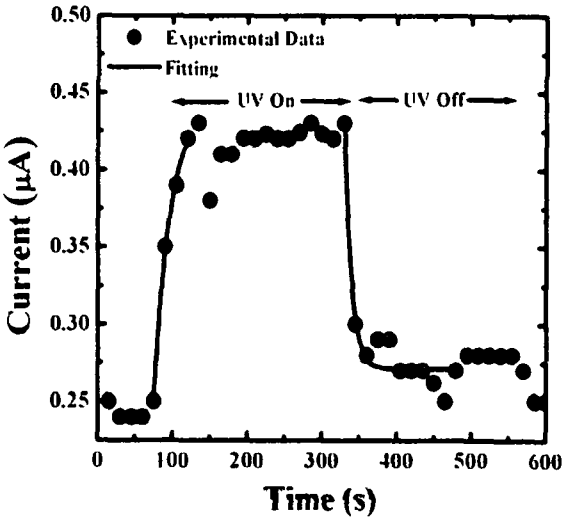

Figure 7.4: The photocurrent growth and decay under ON/OFF conditions of the UV light (at 7.5V).

dominated by the *core* process [3, 4]. The growth and decay part of the experimental data were fitted with exponential equation of the type: $y = y_o + A_1\exp(x/\tau_1)$ and $y = y_o + A_2\exp(-x/\tau_2)$, where τ_1 and τ_2 are the growth and decay constants [8, 13] and were found to be ~ 21 s and 9.6 s respectively with respect to the recording time interval. Upon termination of UV light the current value drops down to the initial dark current due to the rapid band-to-band recombination of *e-h* pairs.

7.1.2 ZnO nanorod array based UV photodetectors

The ZnO nanorod arrays grown over the borosilicate glass substrate (using a solution growth process) were also investigated for the purpose of UV detection. The photodetector was designed by making two Pt-contacts (thickness ~ 30 nm) on the nanorod films by using a sputtering unit. The forward biased *I-V* response of the ZnO arrayed system in presence and in absence of the UV illumination (λ=365 nm) is shown in Figure 7.5. The inset of the Figure shows the schematic representation of the nanorod array with Pt-contacts and probe-lids. In presence of UV illumination, the current conduction is found to be significantly higher than the dark current.

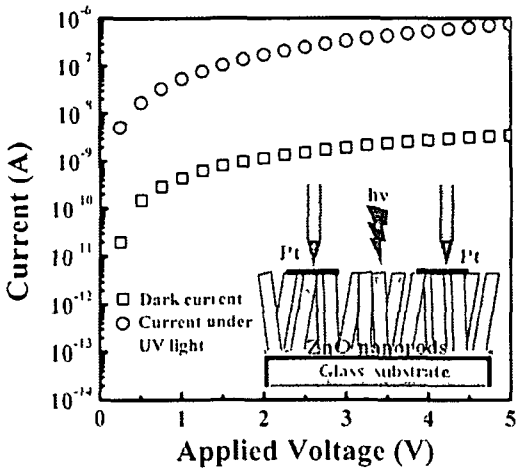

Figure 7.5: *I-V* characteristics of the nanorod specimen in dark and under UV illumination.

The rise and decay of current of the ZnO nanorod arrays after every 15 s, for turning on/off conditions of the UV light at constant forward biasing of 5 V is shown in Figure 7.6. It can be observed that unlike the previous UV detection system, the photocurrent in this case increases slowly with time during UV illumination and also decreases slowly upon terminating the UV light. The

photoresponse curve resembles the saw tooth pattern. The growth and decay constants, τ_1 and τ_2 are found to be ~ 102 s and 70 s respectively. Compared to the urchins, the observed slow rise and decay of photocurrent of the nanorod arrays suggest that the photoconduction mechanism is dominated by the surface related process.

In the photoresponse curve it can be noticed that upon turning off the UV light the photocurrent didn't decay completely. Consequently, a persistent photoconductivity (PPC) was maintained in the nanorod array based photodetection system [9]. The presence of various defects or trap states within the band gap of ZnO help trapping of charge carriers and slows down the decay of photocurrent [4, 14]. The trapping of charge carriers at the defects or trap states are often correlated with the origin of persistent photoconductivity (PPC) in ZnO nanostructures [9]. To reaffirm the observation further, the photoresponse of a sample was recorded for 2nd time after keeping it in the ambient environment for 15 min. The inset of Figure 7.6 shows a comparative view of the photoresponse recorded for the 1st time (Case 1) and 2nd time (Case 2). The photoresponse curve in Case 2 has a close resemblance with that of Case 1. It is also notable that the initial dark current in the transient photoresponse curve in Case 2 is higher (~ 18 times) compared to that of Case 1. This can be attributed to the fact that most of the electrons which were responsible for PPC in Case 1, remain in excited state even upto 15 min (900 s) of duration since the UV light was terminated. Previously, the PPC in WO_3 nanowires was found to last for a time duration over 10^3 s [15].

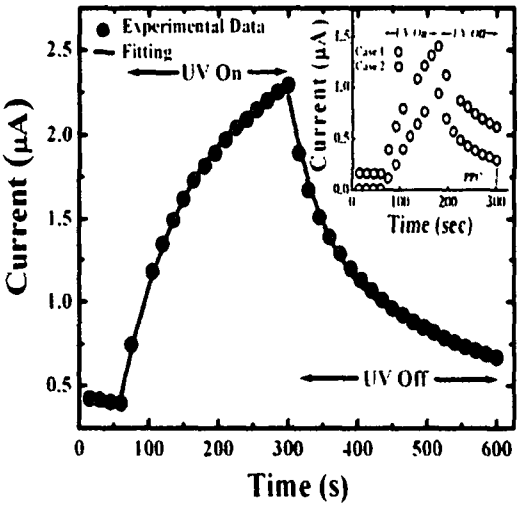

Figure 7.6: Rise and decay in photocurrent of the ZnO nanorod array for on/off conditions of the UV light (at 5 V).

The existence of PPC has been witnessed several times in various materials [16-18]. However the origin of PPC had always been a subject of controversy. Earlier, the evolution of PPC was related to the presence of point defects, traps states [9] or to the electron-hole separation associated with the surface of the oxide materials [19]. Lany and Zunger have argued that PPC in *n*-ZnO system is caused by oxygen vacancy V_O, originating from a metastable shallow donor state [20]. Further, suggesting the PPC as a surface phenomenon, it was experimentally demonstrated that the oxygen vacancies act as the rich source of PPC [19, 21]. In contrast, Yadav and the co-workers have reported that the evolution of PPC is due to the presence of deeply trapped electrons located at the recombination centers [22].

In the present system under investigation, the existence of the trap states within the band gap of ZnO can be an efficient source of the observed PPC. As discussed in Chapter 3, the presence of the trap states in the ZnO nanorod arrays was ensured from the spectroscopic analysis. Here, the proposed mechanism for the evolution of PPC in the ZnO nanorod array based photodetetctor, is summarized in schematic diagram in Figure 7.7. Upon UV illumination a major fraction of electrons are excited to the conduction band, while some electrons get entrapped in the trap centers which lie just below the conduction band as shown in Figure 7.7 (a). When an equilibrium is established between the charge carriers residing in the conduction band and the shallow trap states, the thermal transition from the

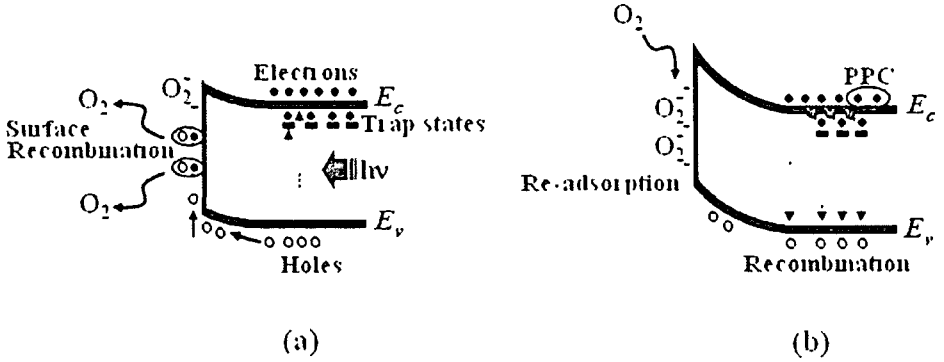

Figure 7.7: Schematic representation of UV detection process and origin of PPC. (a) depicts the situation during UV illumination, while (b) represents the situation right after UV termination.

traps to the conduction band (or vice versa) is allowed [4, 22]. When UV light is terminated (Figure 7.7 (b)), electrons both from the conduction band and the trap centers recombine with the hole-counterparts left in the valence band. Under these circumstances the recombination process gets slower as a part of conduction band electrons has to come across the trap states before they recombine with the valence band holes. This fact is also evident from the PL spectra of the nanorod arrays as discussed in Chapter 3. In the PL spectra both the band edge (band-to-band direct recombination of *e-h* pair) and trap assisted emissions were observed upon exciting the system with a wavelength of 325 nm. Simultaneously, the O_2 species which were earlier desorbed from the surface of the nanorods during UV illumination get re-adsorbed upon UV termination, leading to the development of a built-in potential near the surface (Figure 7.7 (b)). Consequently, the separation of charge carriers is achieved as a fraction of holes accumulate near the surface of the nanorods and electrons in the interior [19]. Therefore, the electrons residing at the conduction band or at the trap centers do not find enough number of holes to encounter in the valence band. The excess number of electrons present in conduction band and the trap states even after switching off the UV light give rise to the PPC effect.

Figure 7.8 shows the transient photoresponse of the ZnO nanorod array based photodetector with UV light on/off conditions, for three periodic cycles and each of 240 s time duration. During UV illumination the current in the photoresponse curve, is found to get increased with every cycle and consequently the PPC

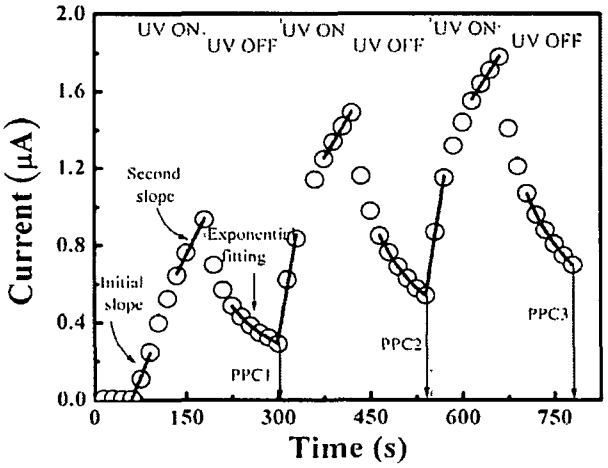

Figure 7.8: The photoconductive response of the nanorod arrays for periodic cycles of illumination and termination of the UV light (at 5V).

too. Previously, it was demonstrated that the shape of a photoresponse curve depends on the number of trap states suggesting two different slopes [3, 4]. The initial slope corresponds to the fast-rise signifying the *core* process. While mediated by surface related mechanism, the second slope represents a slow response owing to the establishment of equilibrium between the charge carriers in the conduction band and the trapping states [3, 4].

Table 7.1: Different parameters related to the photoresponse of the nanorod system.

Cycles	Initial slope x 10^{-3}	Difference in slopes x 10^{-3}	Ratio of PPC-to-dark current	τ_2 (s)
1st	7.9	1.5	32.9	72.8
2nd	18.2	12.9	61.3	75.6
3rd	20.3	15.3	79.1	79.0

In the photoresponse curve, linear fitting was adopted on the initial and end-parts of each cycle under UV illumination. It can be noted that the slope of the initial part has an increasing trend as one moves from the 1st cycle to the succeeding cycles (Table 7.1). While in the 2nd part of the photoresponse curve no significant increment has been observed. A similar trend was realized in the transient photoresponse curve in Case 2. Consequently, the difference between the slopes of the two parts (i.e. initial and the 2nd part of the photoresponse curve), acquires the lowest value in the 1st cycle and increases for the next two cycles. Now, the difference in slopes physically represents the contribution that arise due to the fraction of charge carrier concentration available in the conduction band, while the remaining charge carriers are at the trapping sites [3, 4]. This signifies that the electron concentration at the conduction band increases in every cycle of the turning ON conditions. The substantial increase of electron concentration in the conduction band is associated with the enhanced contribution of the *core* process in every cycle. Again, the improved *core* process can be assigned to the enhancement in the quantum efficiency of the photogenerated charge carriers, in each cycle. It is expected that, for a longer period of UV illumination, more and

more photogenerated holes combine with O_2^- available in the grain boundaries of the polycrystalline ZnO nanorod system. This leads to the release of more and more captured electrons, thus resulting in increase of the quantum efficiency. Also, it can be observed that the rate of increase of the initial slope decreases as one moves from 2nd cycle to the 3rd one. In fact, this situation corresponds to the saturative nature of the photocurrent contributed from the *core* process, appreciable for longer duration of UV illumination.

When the UV light is turned off, the photocurrent decayed slowly. The decay constant (τ_2) was estimated through the exponential fitting of the decay part with values 72.8, 75.6 and 79 s, at the completion of 1st, 2nd and 3rd cycles; respectively (Table 7.1). As the electron concentration in the conduction band increases after every cycle, the recovery process becomes slow owing to the finite surface recombination centers in the nanorods. This accounts for the observed incremental trend of τ_2 and PPC after every cycle. Note that the PPC at the end of 2nd and 3rd cycle were found to be 1.89 and 2.45 times higher than the PPC observed at the end of 1st cycle. Additionally, the PPC to initial dark current ratio was predicted to be 32.9, 61.3 and 79.1 at the end of 1st, 2nd and 3rd cycles respectively (Table 7.1).

To study the surface effect on the observed PPC, the ZnO nanorods were annealed at 120 °C for 3 h. Figure 7.9 represents the transient response of the annealed nanorod arrays. Annealing at a lower temperature would lead to the desorption of some O_2 species rather than changing the structural arrangement of the nanorods. The dark current in the annealed sample is found to be slightly higher than the pristine sample as a result of the lowered band-bending owing to

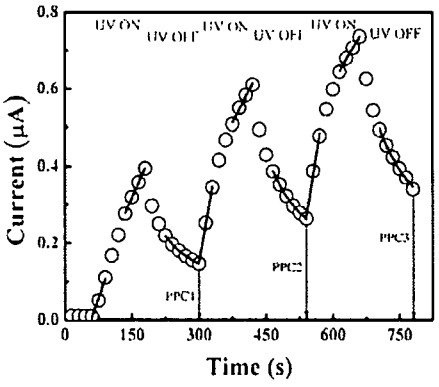

Figure 7.9: Photoconductive response of the nanorod arrays annealed at 120 °C for periodic cycles of illumination and termination of the UV light (at 5V).

less adsorbed O_2 species after annealing. Due to the smearing out of surface adsorbed O_2 molecules from the nanorods, the photocurrent of the annealed sample is expcted to be lower than the pristine sample. In spite of the low photocurrent, the photoresponse curve of the annealed sample shows similar trend with regard to the slopes of the initial and end-parts, as discussed above. The quantum efficiency led increase in the contribution of the *core* process in every cycle is also maintained. Ensuring a similar type of PPC as observed in the pristine one, the PPC at the end of 2^{nd} and 3^{rd} cycles in this case was found to be 1.85 and 2.41 times of the value obtained in the 1^{st} cycle. In contrast, the PPC-to-initial dark current ratio at the end of 1^{st}, $2^{nd}$and 3^{rd} cycles for the annealed samples bear values of 14.7, 26.4 and 34, respectively (Table 7.2). The lower value of PPC to dark current ratio for the annealed samples is a result of less number of adsorbed O_2 species on the nanorod system. If less O_2 species were adsorbed on the surface, the development of built-in potential will become lower. Hence, the event of hole accumulation near the surface of the nanorods will be hindered. Consequently more holes will be available in the interior of the nanorods facilitating more *e-h* recombination. This leads to the decrement in number of conduction band electrons which were earlier responsible for PPC. The comprehensive scenario of lower PPC in the annealed sample signifies the surface dependent nature of PPC in the nanorods.

Table 7.2: Different parameters related to the photoresponse of the nanorod array after annealing.

Cycles	Initial slope x 10^{-3}	Difference in slopes x 10^{-3}	Ratio of PPC-to-dark current	τ_2 (s)
1^{st}	3.6	0.9	14.7	65.0
2^{nd}	6.6	4.3	26.4	69.8
3^{rd}	7.2	5.2	34.0	80.7

The extent of chemisorbed oxygen species on the crystallite boundaries largely depend on the orientation and the crystallite size of the materials [3, 23]. Since the photoresponse of ZnO is largely affected by the content of chemisorbed oxygen

species, the orientations and crystallite size are the important factors as far as the photoconduction in ZnO is concerned. The crystallographic properties of the urchins and the nanorod arrays were discussed using XRD patterns in Chapter 2. The XRD pattern of the urchin like structures was characterized by the presence of different prominent orientations. On the other hand, the (001) orientation was found to be most prominent in the XRD pattern of the nanorod arrays. Again, the crystallite size the two types of the nanostructures were determined using the Debye-Scherrer formula, and were found to be ~ 9 nm and 28 nm for the urchins and the nanorod arrays respectively. Now it is evident that for smaller crystallite size the chemisorbed oxygen is expected to be more owing to the large number of grain boundaries [3, 23]. Therefore, in the photoresponse curve the contribution of the *core* process will be profound for the material with smaller crystallite size. Since the crystallite size of the urchins is smaller than the nanorod arrays, the photoresponse of the urchins is dominated by the core process exhibiting thereby a faster growth and decay of photocurrent, compared to the nanorod arrays. This observation is consistent with the earlier report of fast photoresponse for the ZnO thin films with mixed orientations and smaller grain size [23]. The nanorod arrays having higher crystallite size possess less chemisorbed O_2 species due to the less grain boundary region. Consequently, the contribution of the *core* process in the photoconductivity of the nanorod arrays is marginal and so the photoresponse curve is characterized by a slow rise and decay in photocurrent.

7.2 Concluding remarks

UV photodetection properties of urchins and nanorod arrays of ZnO were investigated. The urchin based photodetection system showed fast rise and decay of photocurrent under UV illumination. The *core* process i.e. desorption of chemisorbed oxygen from the grain boundaries and liberation of electrons under UV illumination, is mainly responsible for the fast photoresponse of the urchins. In contrast to that the nanorod array based photodetection system is characterized by a slow rise and decay of current under illumination, thereby maintaining a

persistence photoconductivity (PPC). The presence of trap states within the band gap of ZnO is believed to be the source of the PPC in the nanorod array. Also, the lowering of PPC upon annealing the nanorod arrays at 120 °C reveals the surface dependent nature of the PPC. The variation in the crystallite size of the two types of nanostructures is assigned to the observed diverse photoresponse. Further development and processing of quality urchins like structures could lead to the exhibition of faster photoresponse for practical UV sensing and switching applications. In contrast, the ZnO nanorod arrays that exhibit PPC are impressive for the deployment in bistable optical switching devices, practical radiation detectors or dosimetric applications.

References:

[1] Sze, S. M. & Ng, K. K. *Physics of semiconductor devices*, Wiley-India, Delhi, 2010.

[2] Soci, C. et. al. Nanowire Photodetectors, *J. Nanosci. Nanotech.* 10, 1-20, 2010.

[3] Sharma, P. et. al. Analysis of ultraviolet photoconductivity in ZnO films prepared by unbalanced magnetron sputtering, *J. Appl. Phys.* 93, 3963- 3970, 2003.

[4] Kumar, S. et. al. Mechanism of ultraviolet photoconductivity in zinc oxide nanoneedles, *J. Phys.: Condens. Matter* 19, 472202 (1-10), 2007.

[5] Ji, L. W., et. al. Ultraviolet photodetectors based on selectively grown ZnO nanorod arrays, *Appl. Phys. Lett.* 94, 203106 (1-3), 2009.

[6] Jin, W., et. al. Solution-processed ultraviolet photodetectors based on colloidal ZnO nanoparticles, *Nano Lett.* 8 (6), 1649-1653, 2008.

[7] Soci, C., et. al. ZnO nanowire UV photodetectors with high internal gain, *Nano Lett.* 7 (4), 1003-1009, 2007.

[8] Li, Y., et. al. Fabrication of ZnO nanorod array-based photodetector with high sensitivity to ultraviolet, *Physica B* 404, 4282–4285, 2009.

[9] Su, Y. K., et. al. Ultraviolet ZnO nanorod photosensors, *Langmuir* 26(1), 603–606, 2010.

[10] Ali, G. M., et. al. Ultraviolet ZnO photodetectors with high gain, *J. Elect. Sci. Tech.* 8 (1), 55-59, 2010.
[11] Luo, L. et. al. Fabrication and characterization of ZnO nanowires based UV photodiodes, *Sensors and Actuators A* 127, 201–206, 2006.

[12] Jiang, D., et. al. Ultraviolet Schottky detector based on epitaxial ZnO thin film, *Solid-State Elect.* 52, 679-682, 2008.

[13] Ghosh, T. & Basak, D. Highly efficient ultraviolet photodetection in nanocolumnar RF sputtered ZnO films: a comparison between sputtered, sol–gel and aqueous chemically grown nanostructures, *Nanotechnology* 21, 375202 (1-6), 2010.

[14] Bera, A & Basak, D. Role of defects in the anomalous photoconductivity in ZnO nanowires, *Appl. Phys. Lett.* 94, 163119 (1-3), 2009.

[15] Huang, K. & Zhang, Q. Giant persistent photoconductivity of the WO_3 nanowires in vacuum condition, *Nanoscale Res Lett* 6, 52, 2011.

[16] Qiu, C. H. & Pankove, J. I. Deep levels and persistent photoconductivity in GaN thin films, *Appl. Phys. Lett.* 70 (15), 1983-1985, 1997.

[17] Zardas, G.E., et. al. Room temperature persistent photoconductivity in GaP:S, *Solid State Commn.* 105 (2), 77-79, 1998.

[18] McKnight, S. W. & El-Rayess, M. K. Wavelength dependence of persistent photoconductivity in indium-doped $Pb_{1-x}Sn_xTe$, *Semicond. Sci. Technol.* 5, S155-S158, 1990.

[19] Prades, J. D., et. al. The effects of electron–hole separation on the photoconductivity of individual metal oxide nanowires, *Nanotechnology* 19, 465501 (1-7), 2008.

[20] Lany, S. & Zunger, A. Anion vacancies as a source of persistent photoconductivity in II-VI and chalcopyrite semiconductors, *Phys. Rev. B* 72, 035215 (1-13), 2005.

[21] Studenikin, S. A., et. al. Carrier mobility and density contributions to photoconductivity transients in polycrystalline ZnO films, *J. Appl. Phys.* 87 (5), 2413-2421, 2000.

[22] Yadav, H. K., et. al. Persistent photoconductivity due to trapping of induced charges in Sn/ZnO thin film based UV photodetector, *Appl. Phys. Lett.* 96, 223507 (1-3), 2010.

[23] Zhang, D. H. Fast photoresponse and the related change of crystallite barriers for ZnO films deposited by RF sputtering, *J. Phys. D Appl. Phys.* 28, 1273-1277, 1995.

Chapter 8

ZnO nanostructures for tuning natural photonic band gap material

The photonic crystals and photonic band gap materials are quite fascinating for precise modulation and propagation of electromagnetic waves. It has been established that the infiltration or embedment of luminescent materials in the photonic crystals is useful for solid-state lasers that require low threshold currents but high gains. In contrast to these artificial structures, the existence of natural photonic crystals has been discovered in different biological systems. The presence of such natural photonic crystals causes the iridescence of various colourful creatures from birds to butterflies. Nevertheless, the cost effectiveness and perfection of such natural photonic structures are accountable for their superiority over the artificial ones. Consequently, the infiltration or embedment of luminescent material in the natural photonic crystals may be useful for achieving novel optical properties. The present chapter is focused on the tuning of photonic band gap of the inbuilt photonic structures of the peacock feather due to nanoscale ZnO embedment.

8.1 Photonic crystals

The photonic crystals/materials are alternate periodic dielectric structures that offer precise control over the propagation of electromagnetic waves of selective wavelength ranges in the same manner as the periodic potential does for migration of electrons in electronic crystals [1, 2]. These materials are characterized by photonic band gaps (PBG) or stop-bands: ranges of wavelength in which light can not propagate through the crystal. Using the proper correlation between Schrödinger's and Helmholtz's equations, E. Yablonovitch proposed that artificial periodic structures can be built to tune the propagation of light by interplay of optical frequency and permittivity [1, 3, 4]. The concept of strong localization of photons in disordered dielectric superlattices was also forwarded by S. John [5]. The geometrical arrangement and the refractive index contrast determine the wavelength range of the stop-bands for which light propagation is forbidden through the material. The stop-bands are size dependent. Upon reducing the size of the elementary cell of the periodic lattice, the wavelength range gets shifted to

a lower value [1]. Depending upon the geometrical and structural arrangement, the photonic crystals are classified as one, two and three dimensional (1, 2 and 3D) and are schematically represented in Figure 1. In general, the photonic crystals are fabricated using microlithography (top-down) or self-assembly (bottom-up) routes [6]. It is relatively easier to achieve 1D or 2D photonic crystals than the 3D one. The fabrication of 3D is quite challenging while maintaining long-range order of the 3D lattices [6-8].

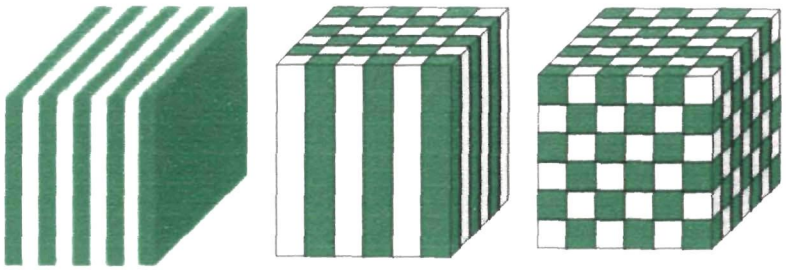

Figure 8.1: Schematic representation of (a) 1D, (b) 2D and (c) 3D photonic crystals.

The artificial photonic crystals mainly include the close-packed patterns assembled by colloidal polymers or silica spheres, while the fabrication of other patterns require highly expensive equipment and sophisticated processes [6, 9, 10]. In contrast the natural systems such as *Ophiocoma Wendtii, Morpho Rhetenor* butterflies, peacock feather etc. also possess remarkable photonic structures, better than artificially fabricated photonic crystals. Many of the natural photonic crystals are composed of periodic arrays of 1D multilayers, 2D deep concavities or 3D cuticle of different sizes and shapes [11, 12]. In these systems, the structural colour results from the interaction of light with the featured structure having same order of size as that of the light wavelength.

8.1.1 Natural photonic crystals in peacock feather

The male peacock tail is very attractive owing to the bright and iridescent colour combination at regular sites. The central region of the eye-pattern of a male peacock feather (Indian Peafowl, *Pavo Cristatus*) generally appears dark blue. As

one moves away from the central-core, cyan, brown and green colours can be observed in the outward directions of feathers. The schematic representation of the basic structure of the peacock tail feather in the eye region is shown in Figure 8.2. The colours of the barbules are well distinguished from the front faces of the tail feather as the barbules completely cover the barbs.

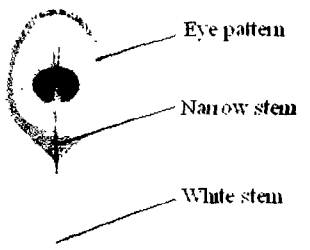

Figure 8.2: A scheme of the eye pattern of a matured peacock tail feather.

The studies on the submicron structure of the barbules reveal that a barbule consists of a medullar core enclosed by a cortex layer [12]. The cortex of differently coloured barbules contains 2D photonic-crystal structure composed of melanin rods connected by keratin. Note that the arrangement of the melanin rods is analogous to the conventional crystal lattice structures. Figure 8.3 shows the schematic view of the square and rectangular lattices of the different coloured barbules. The microstructure in the blue and green barbules, is characterized by a nearly square lattice, while the brown barbule corresponds a rectangular lattice [12, 13]. The lattice constants (rod spacing) for the blue, and green barbules are ~ 140, and 150 nm, respectively, while that of the brown barbule varies as ~ 150 and 185 nm along the directions parallel and perpendicular to the cortex surface. On the other hand, the number of periods (melanin rod stacks) for the blue and green barbules roughly varies within

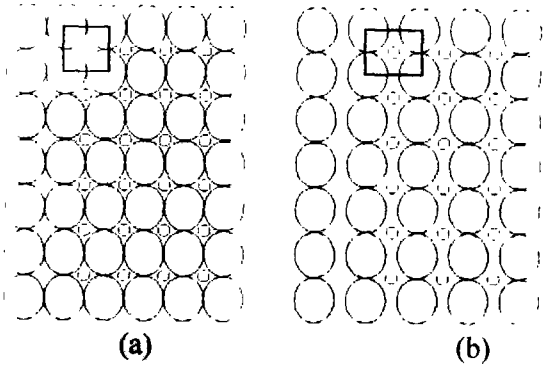

Figure 8.3: Schematic view of the lattice pattern of the different coloured barbules, (a) square and (b) rectangular. The small open circles represent the air holes, while the larger ones signify transverse view of the melanin rods of the two dimensional photonic crystals. The light gray portion stands for the keratin matrix.

~ 9–12, and ~ 4 in case of the brown barbule [12]. Infact, the variation in lattice constant and the periodicity along the direction normal to the cortex surface would result in the variation of the PBG of different types of barbules. The apparently diverse PBG is accountable for distinctly different colour display in different coloured barbules.

The PBG features of the different barbules of the male peacock feather were studied by reflection spectroscopy. In principle, a reflectance spectrum reveals variation of light reflected from the material as a function of wavelength. A material can absorb light having energy equal to the energy difference between two quantum mechanical states of the molecules. For a solid material, the energy which is not absorbed is reflected and can be detected in the reflectance spectrum. The prominent peak in the reflectance spectra exhibited by the photonic crystals corresponds to the characteristic stop-band in which electromagnetic radiation is totally reflected back. Figure 8.4 depicts the reflectance spectra of blue, cyan and brown barbules. As depicted in Figure 8.4 (a), the reflectance spectrum of the blue barbules shows a prominent peak at ~ 470 nm which clearly indicate the presence of a distinct PBG. In this case, the PBG is the characteristic property of the periodically arranged melanin rod-air gap alternate structure of the photonic crystal. The prominent reflectance peak in the blue region confirms the optically active blue colour of the barbules under visible light. Similarly, as shown in Figure 8.4 (b), the reflectance peak at ~ 490 nm validates the cyan colour impression of the cyan barbules. In contrast, two peak maxima were observed for the brown barbules. The reflectance peak was

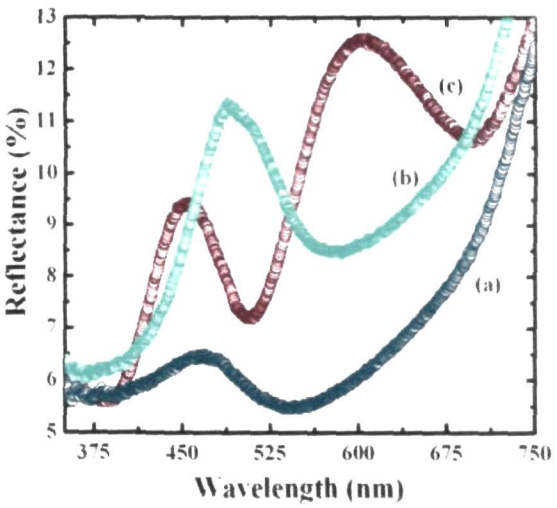

Figure 8.4: Reflectance spectra of (a) blue, (b) cyan and (c) brown barbules.

found at ~ 600 nm, along with an extra peak in the blue region (at ~ 450 nm) as shown in Figure 8.4 (c). The event of Fabry-Perot interference between the two surfaces of a material with finite thickness is assigned to the production of the additional colour. The effect of Fabry-Perot interference is expected to be stronger in the brown barbules owing to the existence of rectangular lattices alongwith reduced periodicity [13].

8.1.2 Tuning of the photonic band gap upon ZnO loading

The growth of the ZnO nanospheres on the peacock feather has been discussed in Chapter 2. Figure 8.5 (a, b) represents the reflectance spectra of the blue barbules before and after ZnO embedment. It can be observed in Figure 8.5(b) that upon ZnO loading the reflectance peak becomes broad and gets red-shifted to ~ 545 nm. It is expected that, the deposition of the ZnO nanospheres (of size of the order of visible wavelength) results in an appreciable change of the effective refractive index of the system and hence, a modification in the PBG is ensured. The reflectance peak after ZnO embedment is not sharp and can be attributed to non-uniform covering of the ZnO nanostructures on the barbules (as revealed from the SEM images depicted in Chapter 2). For instance, in some parts of the barbules, there could be unfilled space left where no ZnO nanostructures exist or in some areas there might be stacks of overlapped nanostructures. The uneven distribution of nanoscale ZnO over the barbules has affected the symmetry of the reflectance peak considerably.

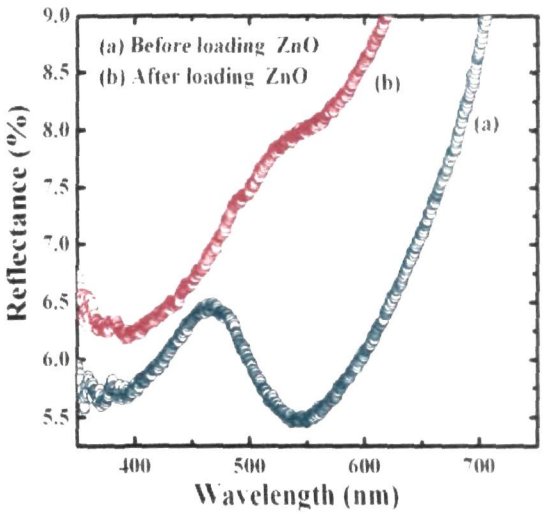

Figure 8.5: Reflectance spectra of the blue barbules, (a) before and (a) after ZnO embedment.

Now the attachment of the ZnO nanospheres to the surface of the blue barbules would lead to a change in the refractive index of the overall system and can be estimated using the fundamental equation $\lambda = 2Dn_e$ [14]. Here D is the lattice constant of the photonic crystals, and n_e as the effective refractive index of the system. If λ_1, λ_2 signify the wavelength maxima corresponding to reflection, and n_{e1}, n_{e2} be the effective refractive indices before and after embedding ZnO on the barbules, then n_{e2} can be expressed as,

$$n_{e2} = \frac{\lambda_2}{\lambda_1} n_{e1} . \tag{8.1}$$

Since the internal structure of the melanin rods remain unaffected, D does not change upon ZnO loading.

Again, the effective refractive index of the system before embedding ZnO, can be expressed as $n_{e1} = \sum_{i=1}^{3} f_i n_i$. Here n_1, n_2, n_3 are the refractive indices and f_1, f_2, f_3 are filling factors of the melanin rods, air gaps and the keratin layer respectively, with the satisfying condition: $f_1 + f_2 + f_3 = 1$ [15]. Now, it can be expressed as

$$n_{e1} = n_3 - f_1(n_3 - n_1) - f_2(n_3 - n_2) . \tag{8.2}$$

The filling factor can be considered as $f = \pi(r/D)^2$, while the other structural parameters are taken as $r_{rod} = 60$ nm, $r_{air} = 37.5$ nm, with n_1, n_2, and n_3 being 1.54, 1, and 2 respectively and D as 140 nm for the blue barbules [12]. As a result, the effective refractive indices i.e., n_{e1}, and n_{e2}, before and after ZnO embedment are found to be 1.68 and 1.95.

In order to justify the fact that the loading of the ZnO assemblies are mainly responsible for the observed red-shift, the reflectance spectra of the cyan barbules were also studied with and without ZnO loading (Figure 8.6). The characteristic reflectance peak of the ZnO embedded cyan

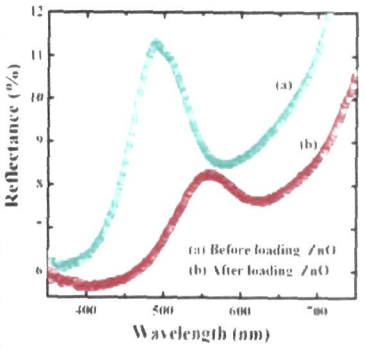

Figure 8.6: Reflectance spectra of the cyan barbules, (a) before and (a) after ZnO embedment.

barbules is also found to be red-shifted ($\Delta\lambda$ = 70 nm). In this case the effective refractive index of the system becomes ~ 1.91 (Table 8.1).

Finally, the reflectance spectra of the brown barbules before and after embedding ZnO were recorded and are depicted in Figure 8.7(a, b). The effective refractive index of the brown barbules was 1.64, which was found to change with ZnO loading. Upon embedding the system with ZnO, the reflectance spectra also experiences a notable red-shift of $\Delta\lambda$ = 90 nm w.r.t. the aforesaid 600 nm peak and the effective refractive index becomes 1.89. It can be noticed that the reflectance peak of the barbules before embedding ZnO located in the blue region (Figure 8.7(a)), gets suppressed upon ZnO loading. It can be argued that upon loading the ZnO nanostructures on the surface of the patterned barbules, the Fabry-Perot interference effect becomes no longer valid thereby suppressing peak at ~ 450 nm.

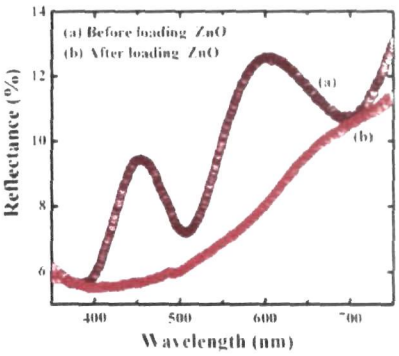

Figure 8.7: Reflectance spectra of the brown barbules, (a) before and (a) after ZnO embedment.

Table 8.1: Various physical parameters related to the barbules.

Barbules	**Lattice Constant** D (nm)	**Before embedding ZnO**		**After embedding ZnO**	
		Reflectance peak centre (nm)	Refractive index (n_{e1})	Reflectance peak centre (nm)	Refractive index (n_{e2})
Blue	140	470	1.68	545	1.95
Cyan	145	490	1.67	560	1.91
Brown	$D_{\parallel}$ ~150, $D\perp$~185	450, 600	1.64	690	1.89

Essentially, the loading of the ZnO nanospheres on the different coloured barbules results in the modification of the PBG of the photonic crystals present in the barbules. The scheme presented in Figure 8.8, is basically an illustration of the underlying mechanism on modification of PBG. To clarify further, it must be

noted that, electron transport is regulated by the electronic band gap (EBG) that arises due to periodic potentials of the constituent atoms that make up the solid. Similarly, the stop-band or photonic band gap is the characteristics of the photon propagating within a medium of periodic structures. In the peacock feather, the stop-bands arise owing to the typical structural organization of the melanin rods,

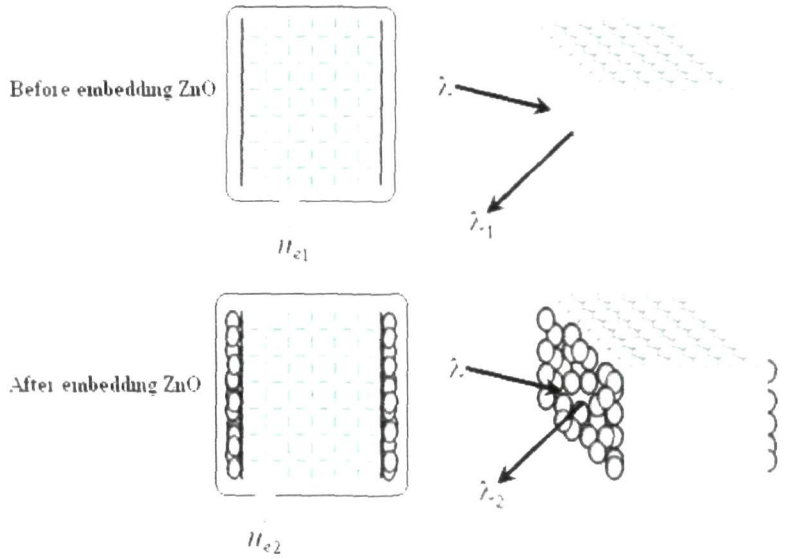

Figure 8.8: Schematic representation of the mechanism behind the modification of PBG.

air gaps and keratin layers. If ZnO is infiltrated within the air gaps then there is a chance of overlapping of EBG of ZnO and PBG of barbules. Consequently, there will be a substantial change in the PL spectra of the peacock feather system i.e. either band edge or defect related emission will be suppressed depending on the range of PBG [16-19]. But in the present study, ZnO intrusion into the air gaps is very unlikely owing to the larger dimension of the ZnO nanospheres. However, the effective refractive index would change as a result of ZnO surface-layer [20].

Figure 8.9 represents the room temperature photoluminescence (PL) spectra (λ_{ex}= 325 nm) of the blue barbules before and after loading ZnO nanospheres. The barbules show emission spectrum having a maximum in the ultra-violet region (~ 388) nm before loaded with ZnO nanostructures (Figure 8.9(a)). The effect of ZnO loading is clearly visible in the PL spectra shown in Figure 8.9(b). Along

with the emission response related to the barbules peaking at ~ 388 nm, several other peaks due to the defect related emission of ZnO were also observed. The emission peaks at ~ 426 and 449 nm correspond to the emissions via neutral and ionized zinc interstitials (Zn_i and Zn_i^+) [21-23]. Further, the emission peaks at ~ 463 and 490 nm arise due to the zinc vacancy (V_{Zn}^-) and oxygen vacancy (V_o^+) related defects respectively [22, 24]. To verify the luminescence response, the PL spectra of bare ZnO system (synthesized using the same protocol but without feathers), was also studied at the same excitation wavelength (Figure 8.9(c)). As for the bare ZnO system, the peak observed at ~ 405 nm corresponds to the zinc vacancy states (V_{Zn}) [23]. The V_{Zn} related peak was not found in the PL spectra of the ZnO embedded feather system because of the superimposition of V_{Zn} peak (~ 405 nm) with the emission peak of the barbules (at ~ 388 nm). Due to the presence of large number of defect states of ZnO, the band edge emissions in both the cases were not observed. The PL spectra of the bare ZnO and ZnO embedded feather systems suggest that the defect related emission response of ZnO is not quenched by the photonic crystals. It is now apparent that the ZnO nanostructures are present on the surface of the barbules independently and hence, the chance of incorporation of ZnO nanostructures within the photonic crystals is less probable. In such a condition, the overlapping of the PBG of the photonic crystals and the EBG of the ZnO nanostructures is not encountered.

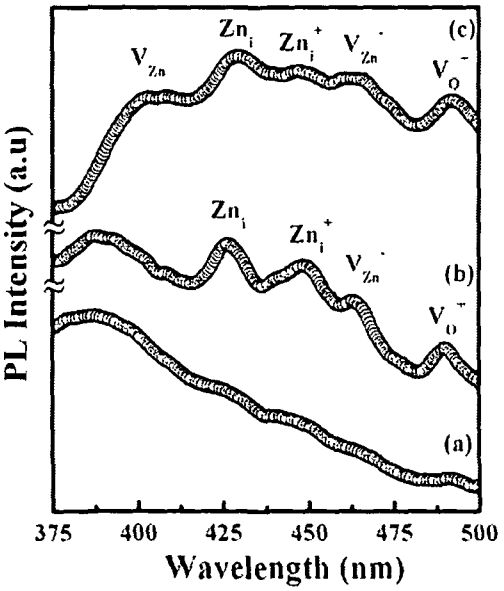

Figure 8.9: Room temperature PL spectra (λ_{ex}= 325 nm) of the blue barbules (a) before, (b) after loading ZnO nanospheres and (c) bare ZnO system.

8.3 Concluding remarks

Decorating the surface of the natural peacock feathers with uniformly distributed nanostructures without destroying the internal structure of the feathers has a unique advantage for altering the photonic band gap with high selectivity. The PBG modification of the different coloured barbules was accounted for the change in the effective refractive index of the system after ZnO loading. The resemblance of the emission pattern of the bare ZnO and ZnO decorated peacock feather specimen suggests that the nanostructures are situated on the surface of the barbules only. The tunability of the PBG and emission pattern of such artificially decorated natural systems could find immense potential in nanoscopy, nanophotonics and other such hybrid elements/devices.

References:

[1] Guida, G., et. al. An introduction to photonic band gap (PBG) materials, *Prog. Electromagn. Res.* 41, 1-20, 2003.

[2] Maka, T., et. al. Three dimensional photonic crystals in the visible regime, *Prog. Electromagn. Res.* 41, 307-335, 2003.

[3] Yablonovitch, E. Photonic band-gap structures, *J. Opt. Soc. Am. B* 10 (2), 283-295, 1993.

[4] Yablonovitch, E. Inhibited spontaneous emission in solid-state physics and electronics, *Phys. Rev. Lett.* 58 (20), 2059-2062, 1987.

[5] John, S. Strong Localization of Photons in Certain Disordered Dielectric Superlattices, *Phys. Rev. Lett.* 58 (23), 2486–2489, 1987.

[6] Waterhouse, G. I. N., et. al. Physical and Optical Properties of Inverse Opal CeO2 Photonic Crystals, *Chem. Mater.* 20, 1183-1190, 2008.

[7] Yablonovitch, E., et. al. Photonic band structure: The face-centered-cubic case employing nonspherical atoms, *Phys. Rev. Lett.* 67, 2295-2298, 1991.

[8] Qi, M. et. al. A three-dimensional optical photonic crystal with designed point defects, *Nature* 429, 538-542, 2004.

[9] Shkunov, M.N., et. al. Tunable, gap-state lasing in switchable directions for opal photonic crystals, *Adv. Funct. Mater*, 12, 21-26, 2002.

[10] Zhou, Z. & Zhao, X. S. Flow-controlled vertical deposition method for the fabrication of photonic crystals, *Langmuir* 20, 1524-1526, 2004.

[11] Vukusic, P. & Sambles, J. R. Photonic structures in biology, *Nature*, 424, 852- 855, 2003.

[12] Zi, J., et. al. Coloration strategies in peacock feathers, *Proc. Natl. Acad. Sci.* 100 (22), 12576-12578, 2003.

[13] Li, Y., et. al. Structural origin of the brown color of barbules in male peacock tail feathers, *Phys. Rev. E* 72, 010902 (1-4), 2005.

[14] Abrarov, S.M., et. al. Dominant ultraviolet-blue photoluminescence of ZnO embedded into synthetic opal, *J. Luminesc.* 114, 118-124, 2005.

[15] Pradhan, R.D., et. al. Impurity modes in the optical stop bands of doped colloidal crystals, *Phys. Rev. B* 54, 13721-13726, 1996.

[16] Abrarov, S.M., et., al. Suppression of the green photoluminescence band in ZnO embedded into porous opal by spray pyrolysis, *J. Luminesc.* 109, 25-29, 2004.

[17] Abrarov, S.M., et. al. Deep level emission of ZnO nanoparticles deposited inside UV opal, *Opt. Commun.* 259, 378-384, 2006.

[18] Han, J., et. al. Novel Photonic Crystals: Incorporation of Nano-CdS into the Natural Photonic Crystals within Peacock Feathers, *Langmuir* 25, 3207-3211, 2009.

[19] Han, J., et. al. Embedment of ZnO nanoparticles in the natural photonic crystals within peacock feathers, *Nanotechnology* 19, 365602 (1-6), 2008.

[20] Bayan, S., Peacock feather supported self assembled ZnO nanostructures for tuning photonic properties, *Eur. Phys. J. D* 61, 463-468, 2011.

[21] Zhang, L.-L., et al. The synthesis of one-dimensional controllable ZnO microrods, *Chinese Phys.* 14 (3), 586-591, 2005.

[22] Lima, S. A. M., et al. Luminescent properties and lattice defects correlation on zinc oxide, *Int. J. Inorg. Mater.* 3, 749-754, 2001.

[23] Lin, B., et al. Green luminescent center in undoped zinc oxide films deposited on silicon substrates, *Appl. Phys. Lett.* 79, 943-945, 2001.

[24] Ye, J. D., et al. Correlation between green luminescence and morphology evolution of ZnO films, *Appl. Phys. A* 81, 759-762, 2005.

Chapter 9

Conclusions and future directions

With the progressive advancement of various fabrication routes, it has become feasible to obtain quality nanostructures of different shape, size and assembly. The development in imaging techniques has extended significant contributions to obtain visual information about these nanoscale structures. Among various types of semiconductor nanostructures, ZnO system is a potential candidate for future optical, electrical, optoelectronic and spintronic device applications. In the present investigation, various optoelectronic and photonic properties of ZnO nanostructured systems are discussed. An effort was made to correlate the structural organization and microstructural features with the optoelectronic and photonic properties of the ZnO nanostructures.

Spherical as well as elongated ZnO nanostructures have been synthesized by adopting different chemical and physico-chemical routes. In addition to the undoped nanostructures, both spherical and elongated Eu^{3+} doped ZnO nanostructures were also synthesized. The visible evidence and morphological features of the nanostructures were investigated via SEM, TEM/HRTEM. On the other hand, XRD was used to explore the structural properties of the nanostructures. Apart from that, the structural evolution of the nanostructures has been discussed in the light of the underlying growth mechanism. As evident from the PL spectra, the undoped nanostructures exhibited intense emission in the violet-blue region of the electromagnetic spectrum. The presence of various native defect related emission was also witnessed in the PL spectra of the nanostructures. The presence of the band edge and defect related emission was found to vary with the average crystallite size of the nanostructures. In contrast to that the Eu^{3+} doped ZnO nanostructures were characterized by well resolved emission peak in the red region associated with the intra *4f* transition of Eu^{3+} cations.

The luminescence response of the nanostructures was modified using high and low energy ion irradiation. In this regard, the PL spectra of the ZnO nanostructures were studied after irradiation with 80-MeV N^{4+} and 80-keV Ar^{+}

ions. To be specific, ion fluence dependent variation in the emission response was observed. The luminescence spectra of the nanostructures were found to get modified owing to the irradiation induced creation, annihilation and ionization of the defects. The enormous electronic energy loss (S_e) during 80-MeV N^{4+} ion irradiation on the ZnO nanostructures is accountable for the symmetric and selective emission response. In contrast, upon 80-keV Ar^{+} ion irradiation, the significant amount of nuclear energy loss (S_n) was responsible for the modified of emission response mediated via redistribution and reorganization of point defects in ZnO. The observed ion fluence dependent variation in various defects was supported by relevant theoretical modeling based upon energy deposition schemes during both low and high energy ion irradiations. On the other hand, the energetic ion irradiation led structural evolution of ZnO nanosystem was discussed in the light of *Liquid drop model.* It was revealed that the suppression of the effective cohesive energy of the nanoparticles during irradiation is the origin of the observed pattern. During irradiation when the nanoparticles lose the support of the surrounding matrix, the growth process occurred as a result of interparticle mass transport among the adjacent nanoparticles.

Direct electrical probing of single nanostructure is difficult due to the interference of charge imbalance on the surface. However, through junctions (both rectifying and non-rectifying), one can explore the transport process in nanostructures. In an attempt to probe the carrier transport properties of the nanorods, the current conduction mechanism in nanorod-based metal-semiconductor (MS), Ag/ZnO and metal-insulator-semiconductor (MIS), $Al/Al_2O_3/ZnO$ junctions were studied. The current conduction was found to be influenced by various acceptor and donor type of native defects of ZnO. The conduction mechanisms like direct tunneling, recombination tunneling and space charge limited conduction contribute to the overall transport process in Ag/ZnO Schottky junctions. Furthermore, Ag/ZnO nano-junctions were fabricated using 80-MeV oxygen ion (O^{6+}) irradiated ZnO nanorods. The improved rectifying properties of the junctions are assigned to the

irradiation led creation and annihilation of various donor and acceptor type defects within ZnO nanorods that make up the junction.

Fabrication of high throughput field emitters having low turn-on voltage and longer life is a recent technological need. Fowler-Nordheim (FN) carrier tunneling event is central to any field emission device. In the present study, significant FN tunneling of electrons was witnessed at low voltage regime (< 5 V), across $Al/Al_2O_3/ZnO$ junction apart from the usual thermionic and direct tunneling. Owing to the presence of FN tunneling process, the MIS junctions were characterized by higher current conduction than the MS junctions. The critical voltage above which the FN tunneling becomes dominant was found to be dependent largely on the thickness of the Al_2O_3 layer of the junction.

The ZnO nanostructure based metal/semiconductor junctions were tested for UV light sensing. In this regard, the urchin like structures of ZnO exhibited faster photoresponse than the nanorod arrays. The observed unalike photoresponse characteristic was assigned to the dissimilar crystallite size of the two types of the nanostructures. Besides that, owing to the presence of the trap states within the band gap of ZnO, substantial amount of persistence photoconductivity was found in the photoresponse characteristic of the urchin like structures.

The photonic band gap (PBG) materials confer the ability to control the propagation of electromagnetic waves in a similar way as the periodic potential does for electrons in electronic crystals. In this context, the photonic properties of hybrid photonic crystals comprising of ZnO nanostructures and natural peacock feather were also explored. As evident from the reflectance spectra, the PBG of the photonic crystals of the feather was found to alter upon ZnO loading. The observed modification in PBG of different colored barbules of the feather was correlated with the change in the effective refractive index of the system upon ZnO loading. In this case, the infiltration of ZnO within the photonic crystals is discarded owing to the larger size of the nanostructures than the airgaps within the

photonic crystals. Moreover, the similarity observed in the emission pattern of bare ZnO and ZnO loaded peacock feather system has ensured that the nanostructures are actually located on the surface of the barbules only.

During this investigation, efforts were made to minimize the time-gap between synthesis and characterization of the ZnO nanostructures to obtain more and more accurate results. The adopted fabrication techniques may be modified to obtain more and more homogenous nanostructures. Furthermore, improvement of the characterization methods is required for indepth understanding of the defect dynamics in the nanostructures. This can be an important issue for improving the performance of a nanostructure based practical device. However, the present investigation can lead to the development of various photonic and optoelectronic devices. The following works are recommended as the one of the most prospective research in the future:

(a) Development of luminescent devices: The evolution of sharp and intense band edge emission is attractive for UV light emitting diode (LED). The size and structure dependency of the band edge emission can be a vital issue for making prototype LED or electroluminescent devices. The present study of doping was restricted to Eu^{3+} cation only. The introduction of other rare earth ions could lead to multicolor luminescence patterns. Integration of such systems will be useful for achieving white LED. On the other hand, controlled ion irradiation with suitable ion species and energy will be attractive for tuning the emission response of the nanostructures across the visible region of the electromagnetic spectrum.

(b) Improvement of metal/semiconductor nano-junctions: In the current study, the nanorod based metal/semiconductor junctions were studied with Ag/ZnO and $Al/Al_2O_3/ZnO$ junctions. The elimination of surface or defect states from the nanorods could improve the rectifying characteristics of the Schottky junctions. Again, control over the insulator thickness of the metal/insulator/semiconductor junction might be beneficial for achieving low voltage field emission devices.

(c) Fabrication of practical UV detectors: The aspect of UV light detection was studied in both urchin and nanorod arrays of ZnO. From the photodetector application point of view, the systems require further modification in order to give faster photoresponse with higher efficiency. The presence of persistence photoconductivity in ZnO nanostructures is generally attractive for radiation detectors or dosimetric applications. The sustainability of such persistence photoconductivity for longer time is the chief criteria for practical applications. In this context, ion implantation may be an alternative pathway to create intermediate states within the band gap to achieve long time persistency of photocurrent.

(d) Development of hybrid photonic crystals: The fabrication of biological template based hybrid photonic crystals will be quite fascinating for the application in modern photonic and plasmonic devices. The present study was limited with the synthesis of peacock feather based hybrid photonic structures. This may be extended to other natural systems like butterfly wings, parrot feather etc. In this context the infiltration of nanocrystals within the natural photonic structures will be an interesting and exciting study for photonic band gap engineering and light wave modulation. The photonic band gap tuning aspect can also be investigated upon depositing nanostructure layer of varying size and thickness over the natural photonic crystals.

Appendix

Appendix 1

Physical properties of zinc oxide (ZnO)

Molar mass	81.408 g/mol
Density	5.6 g/cc
Solubility in water	0.16 mg/100 mL (at 300 K)
Melting point	2248 K
Crystal structure	Cubic (Zinc blende) Hexagonal (Wurtzite)
Lattice parameters (at 300 K)	a = 3.249 Å and c = 5.206 Å (Wurtzite)
Refractive index	2.029
Bulk modulus, B (GPa)	162.3
Young's modulus, E (GPa)	111.2
Band gap (at 300 K)	3.37 eV
Bohr excitonic radius (at 300 K)	60 meV
Dielectric constant	8.5

Appendix 2

Physical properties of the host materials

Cetyltrimethylammonium bromide (CTAB)	
Molecular formula	$C_{19}H_{42}BrN$
Molar mass	364.45 g/mol
Density	390 kg/m^3
Melting point	Decomposes at ~ 510 K
Appearance	White powder
Solubility in water	0.019 g/100mL (at ~ 300 K)
pH value of water solution	5-7
Polyvinyl Alcohol (PVA)	
Molecular formula	$(C_2H_4O)_x$
Molar mass	44 g/mol of repeat unit
Density	1.19-1.31 g/cm^3
Melting point	Decomposes at ~ 503 K
Appearance	White crystalline powder
pH value of water solution	5-7
Hexamethylenetetramine (HMT)	
Molecular formula	$C_6H_{12}N_4$
Molar mass	140.186 g/mol
Density	1.33 g/cm^3 (at ~ 300 K)
Melting point	Sublimes at ~ 553 K
Appearance	White powder
Solubility in water	85.3 g/100mL (at ~ 300 K)

Appendix 3

Ion irradiation experiment

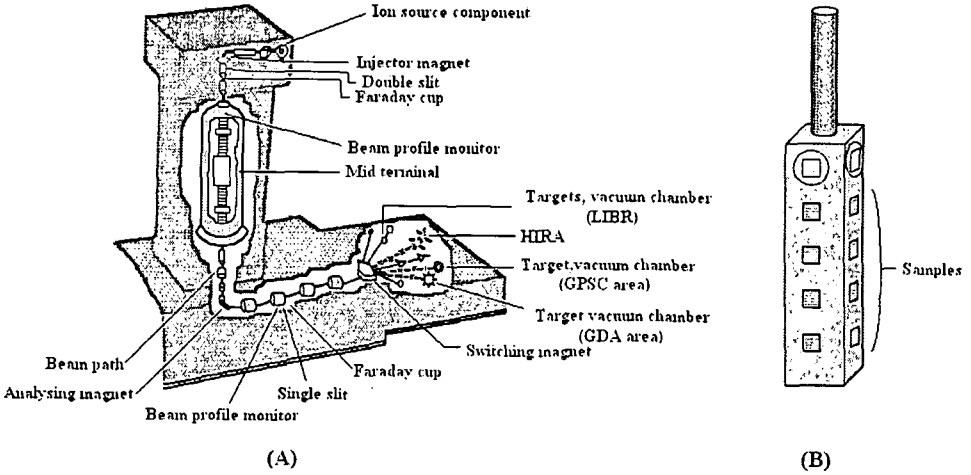

Schematic diagram in (A) represents the ion irradiation chamber and ion trajectory at Inter University Accelerator Center, New Delhi (A). The scheme in (B) shows the ladder used to mount the samples in the vacuum chamber.

The 15UD Pelletron available at Inter University Accelerator Center (IUAC), New Delhi, offers the facility in performing experiments with high energy ions beams. The schematic representation of the 15UD Pelletron is demonstrated in the above figure (A). In the present study, the irradiation experiments were performed in the material science chamber by mounting the samples in a ladder (schematic shown in B). The ladder can be controlled to rotate and move up/down. Irradiation can be done in 16-20 samples attached to the ladder at a time without releasing the vacuum.

The Low Energy Ion Beam Facility (LEIBF) at IUAC, provides ion beams having energy in the range of a few keV to an MeV for performing experiments in atomic, molecular and material sciences. The LEIBF comprises of an Electron Cyclotron Resonance (ECR) ion source installed on a high voltage deck. The attached electronic devices of the ECR source are controlled through optical fiber

communication. The existing system includes high voltage platform, accelerating system and the beam lines with chief components like electrostatic quadruple triplet lens, double slit, Faraday cups, UHV scattering chamber etc. The samples were attached to a ladder and were irradiated in the vacuum chamber.

Appendix 4

Asymmetry factor determination

The asymmetry factor is a measure of how much a peak deviates from being symmetric. It is defined as the ratio between the distance from the peak midpoint to the trailing edge and the distance from the leading edge to the midpoint, with all measurements made at 10% of the maximum peak height.

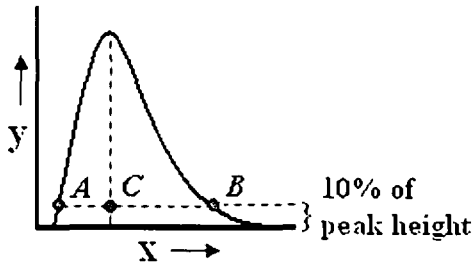

Here the asymmetry factor (A_s) = $\frac{BC}{CA}$

where,

BC = distance from the peak midpoint to the trailing edge (measured at 10% of peak height) and

CA = distance from the leading edge to the midpoint (measured at 10% of peak height).

Appendix 5

Multiple peak fitting in PL spectrum

Very often, the PL spectra of the ZnO nanostructures are found to be broadened and asymmetrically stretched. This can be attributed to the fact that, a PL spectrum is actually composed of multiple peaks (both band edge and defect related emission peaks), which may overlap with each other with intervening full width regions. In order to extract out individual peaks, multiple peak fitting of Gaussian type was performed on the experimental data using Origin software. Out of broad and asymmetric PL spectra of ZnO, the extraction of independent emission peaks using multiple Gaussian peak fitting tool can also be found in the literature [1-5]. The use of Origin software for multiple peak fitting in a PL spectra can be seen in other instances [6, 7].

During multiple fitting process, the number of peaks, and their probable positions are supplied by the user. The peak positions are chosen in such a way that, they adequately fit the band edge emission and emission from various native defect states of ZnO. The position of various native defects within the band gap of ZnO has been discussed in page number 18 (see *Chapter 1*) of the thesis.

In fact, the software itself estimates the overall half-width through integration, and then divides by the number of peaks to arrive at the half-width estimate. The fitting operation is controlled by a non-linear curve fitting tool available in the software. While doing so, it solves a system of equations designed to minimize the aggregated point-by-point differences between the data and the selected fitting function via iteration. Origin uses the well-known Levenberg-Marquardt algorithm to perform the iterative computation. Upon completion of the fitting process, the fitting parameters, as well as related statistics and Results Log, are displayed in the graph window. The best fitting will be obtained only when appropriate number of peaks are considered. In this situation, the empirical curve

(red label) formed by the composition of the fitted peaks is well-matched with the experimental curve (black label) as shown in the example. Although in the present study, the available algorithm of the software has been employed for multiple peak fitting operation, attempts will be made to use self-developed algorithm for this purpose in future investigations.

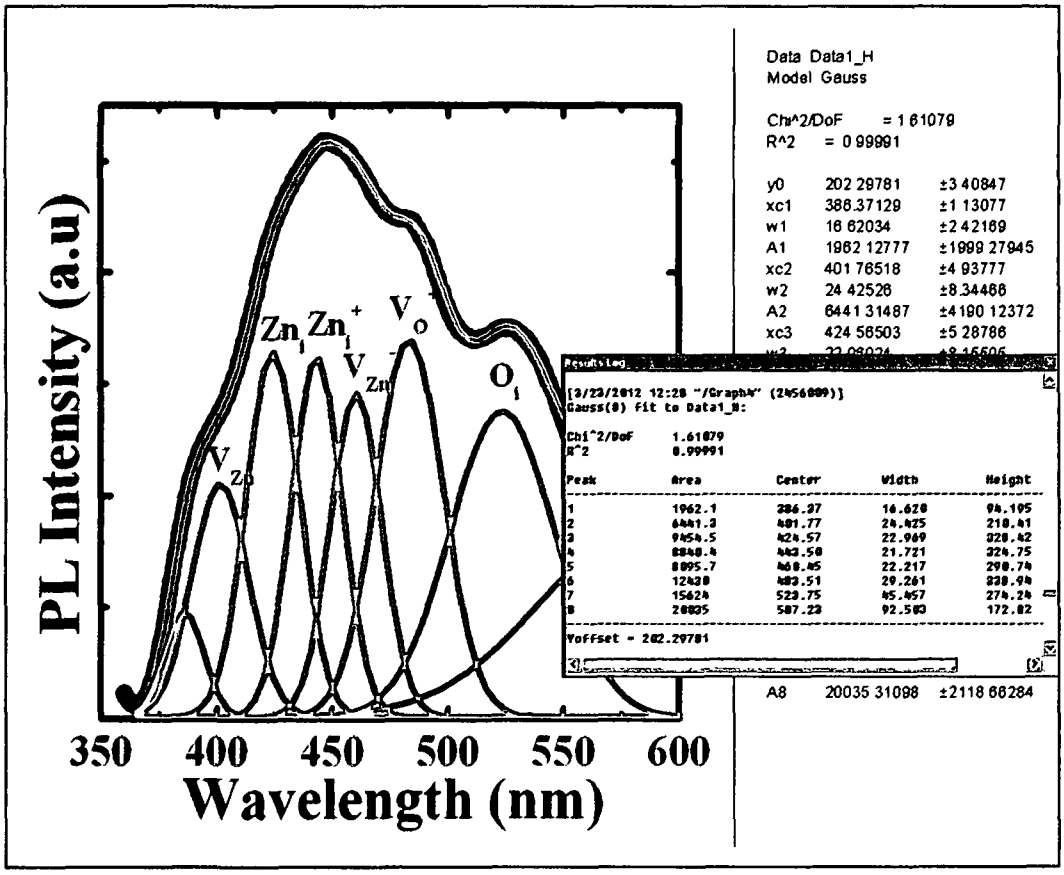

Figure: Multiple Gaussian peak fitting in a PL spectra of ZnO nanorods.

References

[1] Gong, Y., et. al. Origin of defect-related green emission from ZnO nanoparticles: effect of surface modification, *Nanoscale Res Lett* 2, 297-302, 2007.

[2] Wang, Y. S., et. al. Nanocrystalline ZnO with ultraviolet luminescence, *J. Phys. Chem. B*, 110, 4099-4104, 2006.

[3] Omari, M., et. al. Temperature-dependent studies of defect-assisted light emission and excitation processes in crystalline ZnO nanowire phosphors, *J. Appl. Phys.* 108, 024315 (1-5), 2010.

[4] Vempati, S., et. al. One-step synthesis of ZnO nanosheets: a blue-white fluorophore, *Nano. Res. Lett.* 7, 470 (1-10), 2012.

[5] Chattopadhyay, S., et. al. Disorder driven optical processes in nanocrystalline ZnO, *J. Luminescence* 132, 6-11, 2012.

[6] Lopez-Cabana, Z., et. al. Semiconducting properties of layered cadmium sulphide-based hybrid nanocomposites, *Nanoscale Res. Lett.* 6, 523 (1-8), 2011.

[7] Li, L., et. al. Three-photon induced ultraviolet emissions from polymers, *J. Phys. D: Appl. Phys.* 35, 451-453, 2002.

Publications

1. Bayan, S. & Mohanta, D. ZnO-nanorod based UV-photodetection and the role of persistent photoconductivity, *Philosophical Magazine* (In press, 2012 DOI:10.1080/14786435.2012.698761).

2. Bayan, S. & Mohanta, D. Unusual rectifying response of nanojunctions using randomly oriented nanorods (RON) of ZnO irradiated with 80-MeV oxygen ions, *J. Electron. Mater.* 41(7),1955-1961, 2012.

3. Bayan, S. & Mohanta, D. Interplay of native defect-related photoluminescence response of ZnO nanosticks subjected to 80 keV Ar ion irradiation, *Radiation Effects & Defects in Solids*, 166 (11), 884-893, 2011.

4. Bayan, S. & Mohanta, D. Defect mediated optical emission of randomly oriented ZnO nanorods and unusual rectifying behavior of Schottky nanojunctions, *J. Appl. Phys.* 110, 054316 (1-6), 2011.

5. Bayan, S. & Mohanta, D. Effect of 80-MeV nitrogen ion irradiation on ZnO nanoparticles: Mechanism of selective defect related radiative emission features, *Nuclear Instruments and Methods in Physics Research B* 269, 374-379, 2011.

6. Bayan, S. et al. Peacock feather supported self assembled ZnO nanostructures for tuning photonic properties, *Eur. Phys. J. D* 61, 463-468, 2011.

7. Bayan, S. & Mohanta, D. Directed growth characteristics and optoelectronic properties of Eu-doped ZnO nanorods and urchins, *J. Appl. Phys.* 108, 023512 (1-6), 2010.

8. Bayan, S. et al. Development of Tb-doped ZnO nanorods: Effect of nitrogen ion irradiation on luminescence and structural evolution, *Phys. Status Solidi A* 207 (8), 1859-1863, 2010.

9. Bayan, S. & Mohanta, D. Role of cohesive energy on the interparticle coalescence behavior of dispersed nanoparticles subjected to energetic ion irradiation, *J. Mater. Res.* 25 (5), 814-820, 2010.

Addenda

Philosophical Magazine
2012, 1–11, iFirst

Taylor & Francis
Taylor & Francis Group

ZnO nanorod-based UV photodetection and the role of persistent photoconductivity

S Bayan and D Mohanta*

Nanoscience and Soft Matter Laboratory, Department of Physics, Tezpur University PO Napaam, Tezpur-784 028, Assam, India

(*Received 18 April 2012, final version received 8 May 2012*)

We report on the substantial persistent photoconductivity (PPC) response exhibited by the zinc oxide (ZnO) nanorod-based ultraviolet (UV) photodetection system An increase in photocurrent and, hence, rise in PPC was observed for larger UV exposure times at regular intervals Triggered by quantum efficiency, the increment in sustained conduction band electrons is proposed as the main reason behind the increased photocurrent response In contrast, the trap centers located below the conduction band are expected to slow down the recombination rate, which accounts for the rise in PPC The lowering of PPC upon annealing suggests the surface dependent nature of the PPC The growth and decay mechanism of PPC has a direct relevance while assessing figure of merit of prototype nanostructure-based optical sensor and UV photodetectors

Keywords: ZnO, UV photodetector, nanorod, photoluminescence

1. Introduction

Nanoscale oxide semiconductors, either in free-standing powder form or matrix-encapsulated form, have received ever increasing demand in recent years for possible application in optoelectronic and photonic components [1,2] Owing to restricted motion of carriers and recombination along specific direction, one-dimensional (1D) nanostructures have immense potential in a number of functional devices, e g light-emitting diodes (LEDs), field effect transistors (FETs), optical modulators, gas-sensors, etc [3–5] Amongst others, the 1D nanostructured zinc oxide (ZnO) system is a technologically-proven candidate which can play a key role in nano-photonic, nano-optic and nano-optoelectronic elements [5–7] The wide band gap (~3 37 eV at 300 K) and the adsorbate-dependent electrical conductance of 1D ZnO nanostructures are the key factors which could make them useful for sensing ultra-violet (UV) light [8–10] The fabrication of ZnO nanowires with very high internal photoconductive gain [11] and fast response time [11,12] has already been reported Also, the responsivity of ZnO nanorods in metal–semiconductor–metal configuration under UV light illumination has been reported to be much stronger as compared to the ZnO thin film-based configuration [13] On the other hand, the rapid advancement of

*Corresponding author Email best@tezu ernet in

ISSN 1478–6435 print/ISSN 1478–6443 online

http //dx doi org/10 1080/14786435 2012 698761
http //www tandfonline com

fabrication and processing technology has helped in the manufacture of bascule nanobridges out of ZnO nanowires that are capable of displaying high sensitivity and fast response towards UV light detection [14].

It is known that the presence of Zn- and O-related native defects (vacancies, interstitials, antisites, etc.) plays a leading role in determining selective optoelectronic properties. The synthesis parameter dependent dominance of band edge or defect-related emission enables the possibility of deploying the material in lasers and sensors [15]. The presence of various defects or trap states within the band gap of ZnO helps trapping of charge carriers and slowing down the decay of photocurrent [9,10]. The trapping of charge carriers at the defects or trap states is often correlated with the origin of persistent photoconductivity (PPC) in ZnO nanostructures [8]. Earlier, the defect-mediated build-up and decay of PPC at room temperature was predicted in S- doped bulk GaP system [16]. Additionally, Qiu and Pankove have observed the PPC in GaN thin films and ascribed it to the existence of metastable states above the valence band edge of GaN [17]. The exhibition of PPC by individual ZnO nanowires has recently been demonstrated and was assigned to the effect of electron–hole separation near the surface [18]. The PPC property is extremely useful as far as application of bistable optical switch and radiation detectors is concerned [19]. Previously, very high PPC response was reported in highly porous ZnO thin films [20] and, recently, in ZnO nanowire systems [21]. Nevertheless, there is plentiful scope with regard to the exploration of simultaneous evolution of trap states and PPC response of symmetric and asymmetric nanoscale systems.

The present study deals with the controlled photoresponse behavior of ZnO nanorod arrays synthesized via a seed-assisted solution growth technique. As an important aspect, noticeable PPC was witnessed in periodic cycles of the photoresponse activity. The presence of trap states (within the band gap of ZnO) and the occurrence of PPC are discussed, taking into account optical and electrical characteristics.

2. Experimental details

ZnO nanoscale rods were fabricated via a two-step reaction process [22]. In the first step, a seed layer of ZnO nanoparticles was grown over a borosilicate glass substrate (size: $75 \times 25 \times 1.35$ mm). In this step, a solution of ZnO nanoparticles was synthesized from a mixture of zinc acetate dihydrate (ZAD) ($Zn(CH_3COO)_2.2H_2O$, Merck, 99%) and sodium hydroxide (NaOH) prepared with a molar ratio of 3:1 in 20 mL methanol. The mixture was subjected to vigorous stirring for 1 h at a constant temperature of 55°C. Later, a thin layer of the precursor was spin-cast on the laboratory slides. Before proceeding to the second step, the nanoparticle-seeded glass substrates were subjected to mild heating at 80°C for 1 h.

In order to facilitate nanorod growth in the second step, the nanoparticle-seeded glass substrates were immersed in an equimolar solution of zinc nitrate hexahydrate (ZNH) ($Zn(NO_3)_2.6H_2O$, Merck, 99%) and hexamethylenetetramine (HMT) [$(CH_2)_6N_4$, Otto, 99%] in 150 mL of deionized water, under a constant stirring at 60°C for 6 h. Upon completion of the growth, the samples were taken out, washed with deionized water and, finally, dried in a hot air oven.

Scanning electron microscopy (SEM) was used for the morphological analysis whereas an X-ray diffraction (XRD) study was carried out to reveal crystallographic information. The optical properties were explored by using UV–visible absorption spectroscopy, photoluminescence emission (PL) and photoluminescence excitation (PLE) spectroscopy. As for current transport phenomena, two Pt contacts (thickness ~30 nm) were made on the nanorod films using a sputtering unit. The current vs. voltage response was recorded using a Keithley® 2400 sourcemeter via a two-probe method. The room temperature photoconductivity measurement was performed upon illuminating the nanojunction with the help of a UV lamp ($\lambda \sim 365$ nm).

3. Results and discussion

Figure 1a depicts the top view of uniformly grown ZnO nanorods supported on the borosilicate glass substrate. The average diameter and length of the unclustered nanorods were found to be ~125 nm and ~1.2 μm, respectively. Over 60% of the nanorods were found to be vertically aligned, while others were top-tilted to different degrees. Together, the arrangement gives the impression of a paddy field with top surface affected by a blow of airstream. As is evident from the SEM image, the nanorods exist in close proximity to each other with tips separated by a distance smaller than the dimension of the rods Thus, the specimen under study signifies a highly compact system. As shown in the XRD pattern (Figure 1b), the ZnO nanorods exhibit characteristic hexagonal wurtzite crystal structure with preferred orientation along (002) plane and is consistent with JCPDS 36-1451 [23]. The dominance of the (002) peak over the other peaks indicates that preferential growth has occurred along the *c*-axis or perpendicular to the plane of the substrate [23].

The room temperature UV–visible absorption spectra are shown in Figure 2a. The spectrum is characterized by a strong absorption feature below 330 nm and an

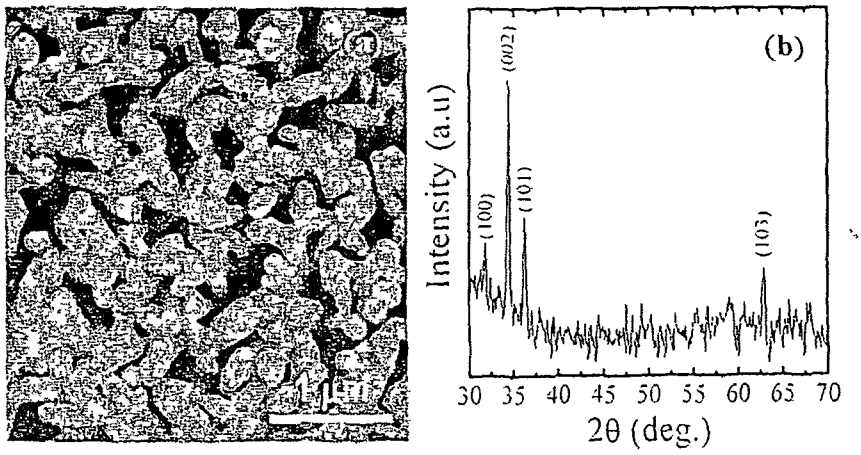

Figure 1. (a) SEM image of the top-view of the ZnO nanorods developed on glass substrate; (b) XRD pattern of the nanorod system.

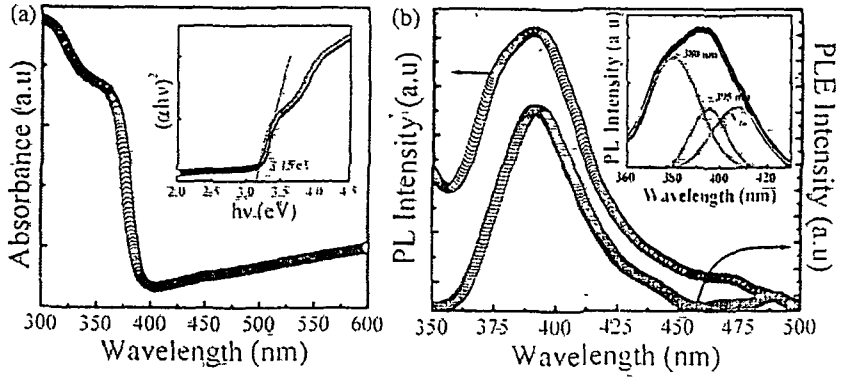

Figure 2. (a) Room temperature UV–visible absorption spectra; inset. plot of $(\alpha h\nu)^2$ vs. $h\nu$. (b) PL ($\lambda_{ex} = 325$ nm) and PLE ($\lambda_{em} = 600$ nm) measurements of the ZnO nanorods; inset: Gaussian fitting of the PL spectra.

absorption edge at ~360 nm. From the absorption data, the direct band gap of the material can be found using the popular relation given by,

$$\alpha h\nu \propto (h\nu - E_g)^{1/2}, \tag{1}$$

where α is the optical absorption coefficient, $h\nu$ is the photon energy and E_g is the band gap [24]. The inset of Figure 2a represents the plot $(\alpha h\nu)^2$ vs. photon energy $(h\nu)$ where the extrapolated section of the linear region gives the band gap of the system under study. The band gap of the nanorod system is found to be 3.15 eV, which is lower than the bulk value of 3.37 eV. Previously, such a low value of the band gap for ZnO nanostructured systems was observed by Labuayai et al. [24]. It was demonstrated that the apparent band gap obtained in such a situation is due to the transition from the valence band to some donor states, rather than valence band to the conduction band [25]. Consequently, in the present study, the obtained value of 3.15 eV can be assigned to the associated transition up to some trap states below the conduction band.

To confirm the presence of trap states below the conduction band, we performed room temperature PL and PLE measurements, the results of which are presented in Figure 2b. The asymmetrically stretched PL spectra (at $\lambda_{ex} = 325$ nm) exhibits a prominent peak at ~392 nm and a notable feature at the shoulder at ~375 nm. The wavelength region of 350 nm to 450 nm of the PL spectra was examined closely using Gaussian fit to extract individual emission characteristics. Upon Gaussian fitting (shown in the inset), three peaks were found at ~378, 395 and 406 nm within the above-mentioned region. The 378 nm peak corresponds to the band edge emission of ZnO due to the direct recombination of electron–hole (*e-h*) pairs, whereas the peak at 406 nm corresponds to the zinc vacancy (V_{Zn}) related emission of ZnO [26,27]. On the other hand, the peak observed at 395 nm is attributed to emission due to the presence of shallow traps [26]. In order to reveal the presence of various defects or trap states within the band gap, PLE was performed by considering the emission wavelength, $\lambda_{em} = 600$ nm. The PLE spectrum depicts a prominent peak centered at

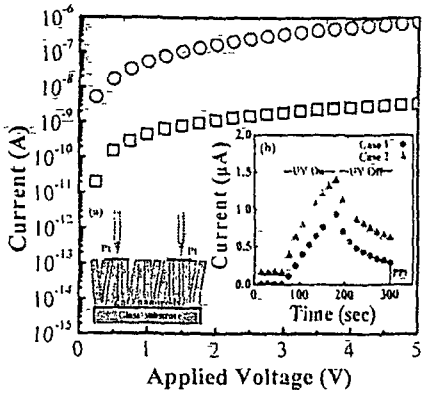

Figure 3. *I–V* characteristics of the nanorod specimen in dark (label '□') and under UV illumination (label '○'). Inset (a) is a schematic representation of the ZnO nanorods with Pt contacts. Inset (b) depicts photocurrent growth and decay under ON/OFF conditions of the UV light (at ~5 V). Case 1(solid circle) represent the photoresponse recorded for the 1st time, while Case 2 (solid triangle) signifies the photoresponse measured for the 2nd time.

~391 nm (3.17 eV). Since the associated energy of the PLE peak is lower than the exciton PL peak (3.28 eV), it cannot be attributed to the excitation of electrons to excitonic levels. Thus, the PLE peak arises as a result of excitation of valence band electrons to some trap levels situated below the excitonic level. Accordingly, the results of PLE and PL studies are in close agreement with the ensuing results of the UV–visible analysis on the presence of trap states.

The current–voltage (*I-V*) characteristic curves of the ZnO nanorod array both in dark and in presence of UV illumination ($\lambda \sim 365$ nm) are depicted in Figure 3. The inset-(a) in Figure 3 shows a schematic representation of the ZnO nanorod array with Pt metallic contacts. It can be observed that under forward bias condition and upon the UV illumination, the current becomes substantially enhanced compared to the dark current. Again, the response curve of current rise and decay of the ZnO nanorod arrays for turning on/off conditions of the UV light at a constant forward biasing of 5 V has been shown in the inset-(b) of Figure 3 (referred to as Case 1). Under UV illumination, the photocurrent increases slowly with time and also falls slowly upon terminating the UV light. In fact, the photoconductivity in ZnO can be explained in terms of two distinctly different mechanisms: first a bulk-related process and second a surface-related process. In so far as the bulk process is concerned, ZnO can adsorb O_2 from the ambient atmosphere in the grain boundaries and form O_2^- ions by capturing electron(s) [28]. This would lead to the development of a depletion region with appreciable band-bending, thus forming a barrier among the crystallite boundaries which lowers the conductivity. Upon UV illumination, the barrier height decreases and the conductivity increases, in accordance with earlier work [28]. Since this process is associated with the collective events occurring across the crystallite boundaries and/or the core of the material, we can designate it as a core process. In contrast, the surface-related process corresponds to the adsorption and desorption of O_2 at the surface of ZnO and is, hence, prominent in nanostructures owing to their higher surface-to-volume ratio. The adsorbed O_2 species on the surface of ZnO

becomes O_2^- and form a depletion region. Upon UV illumination, the photo-generated hole attacks the negatively charged oxygen ion through surface electron–hole recombination. The photoexcited unpaired electron results in the increase of the photoconductivity of the sample. The desorption of O_2 leads to the reduction of the depletion width and the conductivity increases as compared to the dark current. Although both processes result in variation in conductivity due to the adsorption and desorption of O_2, the surface-related process is slow compared to the core process [10,28].

It can be observed in the photoresponse curve that upon turning off the UV light the photocurrent did not decay completely Thus, a PPC was maintained in the nanorod-based junction. To confirm the observation further, the photoresponse of the sample (which was illuminated earlier for 360 s) was recorded for a second time (referred to as Case 2 in the inset-(b) of Figure 3) after keeping it in the ambient environment for about 15 min. The photoresponse of the second measurement has a close resemblance with the first one. It can also be noted that the initial base line of the transient photoresponse curve, i.e. current before turning on the UV light, has a higher sensitivity for Case 2 than that of Case 1. This is due to the fact that the carriers responsible for PPC remain in the excited state even if the UV light was switched off after 15 min (900 s) of exposure. Earlier, the observation of PPC in WO_3 nanowires was found to last for a duration over 10^3 s [19]. To find out the recovery time of the PPC in the sample, the decay of photocurrent upon UV termination was noticed. Figure 4 shows the variation of time dependent photo-to-dark current ratio (I/I_o) after illuminating the specimen for 240 s. The photo-to-dark current ratio decreases exponentially with time and approaches the initial dark current value exhibiting recovery nature of PPC. The recovery time was determined using interpolation of the experimental data (up to $I/I_o = 1$) and was found to be ~800 s for the above-mentioned illumination time.

The origin of the PPC has always been an issue of controversy and has been related to the presence of point defects, traps states [8] or to the electron–hole separation related to the surface properties of the oxide systems [18]. Using first-principle electronic structure calculations, Lany and Zunger came up with the argument that the PPC in *n*-ZnO is caused by oxygen vacancies (V_O), originating

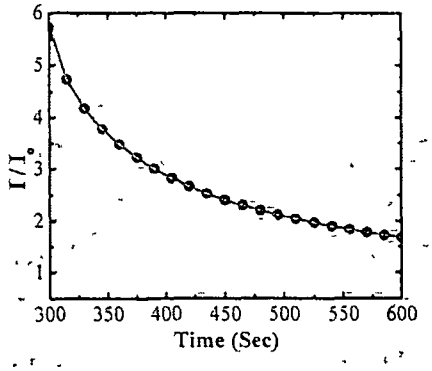

Figure 4. Photo-to-dark current ratio (I/I_o) after continuous UV illumination for 240 s.

from the metastable shallow donor states [29]. Ensuring the PPC as a surface phenomenon, the presence of surface states in the form of oxygen vacancies has been experimentally verified, which act as the chief source of PPC [18,30]. On the other hand, Yadav et al. have argued that the presence of deeply trapped electrons at the recombination centers is the main reason behind the evolution of PPC [31]. In the present case, the existence of the trap states within the band gap of ZnO can be an effective source of the observed PPC. The presence of the trap states was evident from the spectroscopic analysis as discussed above.

The schematic diagram of Figure 5 summarizes the complete process of the observed PPC in the present system. Under UV illumination, a major part of the electrons are excited to the conduction band, while some become entrapped in the trap centers just below the conduction band. While maintaining thermal equilibrium, the transition from the shallow trap states to the conduction band (or vice versa) is adequately favored [31]. Figure 5a demonstrates the situation during UV illumination. However, Figure 5b shows that, upon UV light termination, electrons both from the conduction band and the trap centers recombine with the hole counterparts in the valence band. Essentially, the recombination process becomes slower as a part of the conduction band electrons come across the trap states before compensating the valence band holes. This event can be correlated with the PL spectra, where both the band edge (band-to-band direct recombination of *e-h* pair) and trap assisted emissions were observed. On the other hand, the O_2 species which were desorbed earlier during UV illumination become re-adsorbed on the surface of the nanorods upon UV termination, leading to the development of a built-in potential near the surface (Figure 5b). Consequently, the separation of charge carriers prevails as a fraction of holes accumulate near the surface of the nanorods, which are then unable to take part in the recombination process [18]. As a result, the electrons which were at the conduction band or entrapped at the trap centers would not find sufficient number of holes for successive recombination. It is now clear that a number of electrons were available in the conduction band and the trap states even after switching off the UV light. The excess number of electrons apparently gives rise to the PPC effect.

Figure 6 shows the transient photoresponse of the ZnO nanorod array with UV light on/off conditions for three periodic cycles of duration 240 s. It can be seen that the photocurrent increases with every cycle and hence the PPC. Earlier, it was

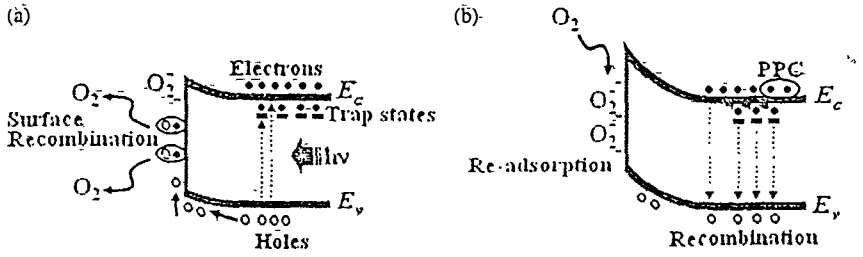

Figure 5. Schematic representation of UV detection process (a) during UV illumination and (b) right after UV termination.

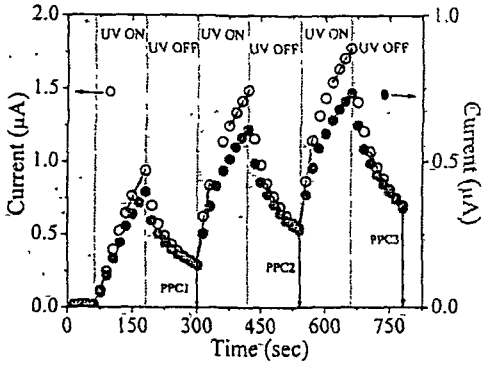

Figure 6. A comparative view of the photoconductive response (at 5 V) of the ZnO nanorod array before annealing (symbol 'o') and after annealing (symbol '•') at 120°C for periodic cycles of illumination and termination of the UV light.

Table 1. Different parameters related to photoresponse of the nanorod array before and after annealing.

Original sample					Annealed sample			
Cycle	Initial slope $\times 10^{-3}$	Difference in slopes $\times 10^{-3}$	Ratio of PPC-to-dark current	τ_d (s)	Initial slope $\times 10^{-3}$	Difference in slopes $\times 10^{-3}$	Ratio of PPC-to-dark current	τ_d (s)
1st	7.9	1.5	32.9	72.8	3.6	0.9	14.7	65.0
2nd	18.2	12.9	61.3	75.6	6.6	4.3	26.4	69.8
3rd	20.3	15.3	79.1	79.0	7.2	5.2	34.0	80.7

demonstrated that the shape of the photoresponse curve would depend on the number of trap states characterized by two different slopes [10,28]. The initial slope represents to the fast rise and is a signature of the core process. Mediated by surface-related process, the second slope corresponds to a slow response while establishing carrier equilibrium between the conduction band and the trapping states [10,28]. In the present context, the photoresponse curve was fitted independently for different trends in the initial part and the end part of the curve for different cycles of UV illumination. Note that the slope of the initial part has an increasing trend as one moves from the first cycle to the succeeding cycles (Table 1), whilst no significant increment was observed in the second part of the photoresponse curve. A similar trend was maintained in the transient photoconductive response in Case 2. Accordingly, the difference between the two slopes (the initial and second parts of the photoresponse) is the lowest in the first cycle and increases for the next two cycles. The difference in slopes could represent the contribution that arise due to the fraction of charge carrier density available in the conduction band, while the

remaining charge carriers are at the trapping sites [10]. This suggests that the electron density of the conduction band increases in every cycle of the turn-on conditions. The increase in electron density in the conduction band can be correlated with the increase in the slope of the initial part of the photoconductive response curve, i.e. increase in the contribution of the core process in every cycle. The augmented core process can be assigned to the enhancement in the actual quantum efficiency of the photo-generated charge carriers, in every cycle. For longer duration of UV illumination, more and more photo-generated holes combine with O_2^- at the particle-boundaries and surfaces of the polycrystalline ZnO, and release captured electrons thus leading to the enhanced quantum efficiency. It can be noticed that the rate of increase of the slope of the initial part becomes low as one moves from second cycle to the third one. This situation, in fact, corresponds to the saturative nature of photocurrent arising from the core process, particularly for longer duration of UV illumination.

When the UV light was switched off, the observed photocurrent decays initially with fast decay characteristics and is then followed by a slow decay mechanism, consistent with earlier results [10]. Yet again, the fast decay corresponds to the core related process which involves rapid band-to-band recombination of *e-h* pairs [10,18]. Under UV illumination, the increment in the fast component was observed in each cycle and was assigned to the enhancement in quantum efficiency. The faster decay of the photocurrent was witnessed in the photoresponse curve when UV light was switched off [10]. In our case, within 15 s of termination of the UV light, the current drops by 25.4%, 22.1% and 20.8% from the respective inititial photocurrent magnitudes, for three successive cycles. Upon exponential fitting, the decay constant (τ_d) was estimated to be 72.8, 75.6 and 79 s at the completion of 1st, 2nd and 3rd cycles, respectively (Table 1). The incremental trend of τ_d after every cycle can be correlated with the photocurrent enhancement due to the core process. In the present case, the increase in electron density in the conduction band after every cycle would slow down the recovery process owing to finite surface recombination centers of the nanorods. This fact accounts for the respective decay duration, and PPC, after every cycle. Note that at the end of 2nd and 3rd cycles, the respective PPC was found to be enhanced by a factor of 1.89 and 2.45 with regard to the 1st cycle. Additionally, the ratio of the PPC with respect to the initial dark current was found to be 32.9, 61.3 and 79.1 at the end of 1st, 2nd and 3rd cycles; respectively (Table 1).

With the aim of investigating the surface-related effects on the observed PPC, the ZnO nanorods were annealed at 120°C for 3 h. The right *y*-axis of Figure 4 represents the transient response of the annealed nanorods. It is expected that the annealing at a lower temperature would not change the structural arrangement of the nanorods substantially, but could lead to the desorption of O_2 species. The dark current of the annealed sample is slightly higher than the non-annealed sample due to the lower band bending and owing to less adsorbed O_2 species due to annealing. The observed photocurrent of the annealed sample is lower than the pristine sample as a result of smearing out of surface adsorbed O_2 molecules from the nanorods. In spite of the low photocurrent, the photoresponse curves show similar characteristics with regard to the slopes of the initial and end-parts as discussed above. The core process increases with the number of cycles due to the enhancement of quantum efficiency in every cycle and that is why similar pattern of PPC was still maintained. Ensuring a

similar nature of PPC as observed in the pristine one, the PPC in this case was found to be 1.85 and 2.41 times the value corresponding to the 1st cycle at the end of 2nd and 3rd cycles. In contrast to that, the PPC to initial dark current ratio for the annealed samples were estimated as 14.7, 26.4 and 34 at the end of 1st, 2nd and 3rd cycles; respectively. The availability of less number of adsorbed O_2 species on the nanorods is responsible for lowering the PPC-to-dark current ratio for the annealed samples. The development of built-in potential will be lower if less amount of O_2 species are adsorbed on the surface and the events of hole accumulation near the surface of the nanorods will be hindered drastically. Eventually, more holes will be available for *e-h* recombination leading to the decrement of number of conduction band electrons which were responsible for PPC. The overall picture of PPC of the annealed sample signifies the surface dependent nature of PPC of the nanorods under study.

It is now clear that the photocurrent enhancement under UV illumination in periodic cycles is a consequence of increase of conduction band electrons in view of the enhanced quantum efficiency. The presence of excess electrons in the conduction band due to the trap-state led slowing down of *e-h* recombination process was expected to be responsible for the enhancement of PPC in every cycle.

4. Conclusion

The UV photoconductive response of characteristic ZnO nanorod arrays grown over glass substrate has been demonstrated. The transient photoresponse under UV light was characterized by an apparent increment of the photocurrent that demonstrated the existence of a relevant PPC response. The increase in photocurrent can be correlated with the enhancement in the quantum efficiency accompanied by the core process, whereas the presence of trap states within the band gap of ZnO was the chief reason behind the observation of adequate PPC. The shallow trap states, which were detected by spectroscopic tools, have slowed down the *e-h* recombination resulting in the increase of carrier concentration in the conduction band. The surface dependent behavior of the PPC was revealed from the lower PPC-to-dark current ratio of the annealed nanorods. The ZnO nanorod arrays exhibiting significant PPC would find scope for making radiation detector, image storage and other such nanoscale optical and optoelectronic elements.

Acknowledgements

One of the authors (SB) acknowledges UGC, New Delhi for the financial support received under the Rajiv Gandhi National fellowship (RGNF) scheme.

References

[1] M.D. Frogley, J.F. Dynes, M. Beck, J. Faist and C.C. Phillips, Nat. Mater. 5 (2006) p.175
[2] J.G. Lu, P. Chang and Z. Fan, Mater. Sci. Eng. R 52 (2006) p.49.
[3] A. Kolmakov and M. Moskovits, Annu. Rev. Mater. Res. 34 (2004) p.151.
[4] M. Law, J. Goldberger and P. Yang, Annu. Rev. Mater. Res. 34 (2004) p.83.

[5] G.-C. Yi, C. Wang and W.I. Park, Semicond. Sci. Tech. 20 (2005) p.S22.
[6] M. Willander, O. Nur, N. Bano and K. Sultana, New J. Phys. 11 (2009) p.125020.
[7] B. Weintraub, Z. Zhou, Y. Libe and Y. Deng, Nanoscale 2 (2010) p.1573.
[8] Y.K. Su, S.M. Peng, L.W. Ji, C.Z. Wu, W.B. Cheng and C.H. Liu, Langmuir 26 (2010) p.603.
[9] A. Bera and D. Basak, Appl. Phys. Lett. 94 (2009) p.163119.
[10] S. Kumar, G.-.H. Kim, K. Sreenivas and R.P. Tandon, J. Phys.: Condens. Matter 19 (2007) p.472202.
[11] C. Soci, A. Zhang, B. Xiang, S.A. Dayeh, D.P.R. Aplin, J. Park, X.Y. Bao, Y.H. Lo and D. Wang, Nano Lett. 7 (2007) p.1003.
[12] K. ul Hasan, N.H. Alvi, J. Lu, O. Nur and M. Willander, Nanoscale Res. Lett. 6 (2011) p.348.
[13] L.W. Ji, S.M. Peng, Y.K. Su, S.J. Young, C.Z. Wu and W.B. Cheng, Appl. Phys. Lett. 94 (2009) p.203106.
[14] Y. Li, A. Paulsen, I. Yamada, Y. Koide and J.-.J. Delaunay, Nanotechnology 21 (2010) p.295502.
[15] U. Das and D. Mohanta, Eur. Phys. J. Appl. Phys. 53 (2011) p.10602.
[16] G.E. Zardas, D.E. Theodorou, P.C. Euthymiou, C.L. Symeonides, F. Riesz and B. Szentpall, Solid State Comm. 105 (1998) p.77.
[17] C.H. Qiu and J.I. Pankove, Appl. Phys. Lett. 70 (1997) p.1983.
[18] J.D. Prades, F.H. Ramirez, R.J. Diaz, M. Manzanares, T. Andreu, A. Cirera, A.R. Rodriguez and J.R. Morante, Nanotechnology 19 (2008) p.465501.
[19] K. Huang and Q. Zhang, Nanoscale Res. Lett. 6 (2011) p.52.
[20] J. Reemts and A. Kittel, J. Appl. Phys. 101 (2007) p.013709.
[21] J. Bao, I. Shalish, Z. Su, R. Gurwitz, F. Capasso, X. Wang and Z. Ren, Nanoscale Res. Lett. 6 (2011) p.404.
[22] R. Chander and A.K. Raychaudhari, J. Mater. Sci. 41 (2006) p.3623.
[23] M.H. Mamat, Z. Khusaimi, M.M. Zahidi, S. Abu Bakar, Y.M. Siran, S.A.M. Rejab, A.J. Asis, S. Tahiruddin, S. Abdullah and M.R. Mahmood, Jpn. J. Appl. Phys. 50 (2011) p.06GH04.
[24] S. Labuayai, V. Promarak and S. Maensiri, Appl. Phys. A 94 (2009) p.755.
[25] V. Srikant and D.R. Clarke, J. Appl. Phys. 83 (1998) p.5447.
[26] Y.S. Wang, P.J. Thomas and P.O. Brien, J. Phys. Chem. B 110 (2006) p.4099.
[27] B. Lin, Z. Fu and Y. Jia, Appl. Phys. Lett. 79 (2001) p.943.
[28] P. Sharma, K. Sreenivas and K.V. Rao, J. Appl. Phys. 93 (2003) p.3963.
[29] S. Lany and A. Zunger, Phys. Rev. B 72 (2005) p.035215.
[30] S.A. Studenikin, N. Golego and M. Cocivera, J. Appl. Phys. 87 (2000) p.2413.
[31] H.K. Yadav, K. Sreenivas and V. Gupta, Appl. Phys. Lett. 96 (2010) p.223507.

[5] G.-C. Yi, C. Wang and W.I. Park, Semicond. Sci. Tech. 20 (2005) p.S22.
[6] M. Willander, O. Nur, N. Bano and K. Sultana, New J. Phys. 11 (2009) p.125020.
[7] B. Weintraub, Z. Zhou, Y. Libe and Y. Deng, Nanoscale 2 (2010) p.1573.
[8] Y.K. Su, S.M. Peng, L.W. Ji, C.Z. Wu, W.B. Cheng and C.H. Liu, Langmuir 26 (2010) p.603.
[9] A. Bera and D. Basak, Appl. Phys. Lett. 94 (2009) p.163119.
[10] S. Kumar, G.-.H. Kim, K. Sreenivas and R.P. Tandon, J. Phys.: Condens. Matter 19 (2007) p.472202.
[11] C. Soci, A. Zhang, B. Xiang, S.A. Dayeh, D.P.R. Aplin, J. Park, X.Y. Bao, Y.H. Lo and D. Wang, Nano Lett. 7 (2007) p.1003.
[12] K. ul Hasan, N.H. Alvi, J. Lu, O. Nur and M. Willander, Nanoscale Res. Lett. 6 (2011) p.348.
[13] L.W. Ji, S.M. Peng, Y.K. Su, S.J. Young, C.Z. Wu and W.B. Cheng, Appl. Phys. Lett. 94 (2009) p.203106.
[14] Y. Li, A. Paulsen, I. Yamada, Y. Koide and J.-J. Delaunay, Nanotechnology 21 (2010) p.295502.
[15] U. Das and D. Mohanta, Eur. Phys. J. Appl. Phys. 53 (2011) p.10602.
[16] G.E. Zardas, D.E. Theodorou, P.C. Euthymiou, C.L. Symeonides, F. Riesz and B. Szentpall, Solid State Comm. 105 (1998) p.77.
[17] C.H. Qiu and J.I. Pankove, Appl. Phys. Lett. 70 (1997) p.1983.
[18] J.D. Prades, F.H. Ramirez, R.J. Diaz, M. Manzanares, T. Andreu, A. Cirera, A.R. Rodriguez and J.R. Morante, Nanotechnology 19 (2008) p.465501.
[19] K. Huang and Q. Zhang, Nanoscale Res. Lett. 6 (2011) p.52.
[20] J. Reemts and A. Kittel, J. Appl. Phys. 101 (2007) p.013709.
[21] J. Bao, I. Shalish, Z. Su, R. Gurwitz, F. Capasso, X. Wang and Z. Ren, Nanoscale Res. Lett. 6 (2011) p.404.
[22] R. Chander and A.K. Raychaudhari, J. Mater. Sci. 41 (2006) p.3623.
[23] M.H. Mamat, Z. Khusaimi, M.M. Zahidi, S. Abu Bakar, Y.M. Siran, S.A.M. Rejab, A.J. Asis, S. Tahiruddin, S. Abdullah and M.R. Mahmood, Jpn. J. Appl. Phys. 50 (2011) p.06GH04.
[24] S. Labuayai, V. Promarak and S. Maensiri, Appl. Phys. A 94 (2009) p.755.
[25] V. Srikant and D.R. Clarke, J. Appl. Phys. 83 (1998) p.5447.
[26] Y.S. Wang, P.J. Thomas and P.O. Brien, J. Phys. Chem. B 110 (2006) p.4099.
[27] B. Lin, Z. Fu and Y. Jia, Appl. Phys. Lett. 79 (2001) p.943.
[28] P. Sharma, K. Sreenivas and K.V. Rao, J. Appl. Phys. 93 (2003) p.3963.
[29] S. Lany and A. Zunger, Phys. Rev. B 72 (2005) p.035215.
[30] S.A. Studenikin, N. Golego and M. Cocivera, J. Appl. Phys. 87 (2000) p.2413.
[31] H.K. Yadav, K. Sreenivas and V. Gupta, Appl. Phys. Lett. 96 (2010) p.223507.

Journal of ELECTRONIC MATERIALS, Vol 41, No 7, 2012
DOI: 10.1007/s11664-012-1995-8

Unusual Rectifying Response of Nanojunctions Using Randomly Oriented Nanorods (RON) of ZnO Irradiated with 80-MeV Oxygen Ions

SAYAN BAYAN[1] and DAMBARUDHAR MOHANTA[1,2]

1.—Nanoscience and Soft Matter Laboratory, Department of Physics, Tezpur University, PO Napaam, Tezpur 784 028, Assam, India. 2.—e-mail: best@tezu.ernet.in

The present work highlights the improved Schottky behavior of Ag/ZnO nanojunctions which make use of unirradiated and 80-MeV oxygen ion (O^{6+}) irradiated randomly oriented ZnO nanorods. While leakage current is apparently low, the rectifying nature of the nanojunctions was clearly evident from room-temperature current–voltage (I–V) measurements. In case of use of irradiated nanorods, the Schottky barrier height (ϕ_B) of the Ag/ZnO nanojunctions was found to be enhanced from 0.78 eV to 0.95 eV along with decrease of the ideality factor (η) from 17.7 to 6.9. This is ascribed to reorganization and modification of the native defect states via creation and annihilation events as revealed by photoluminescence spectroscopy. The fluence-dependent variation of ϕ_B and η was assigned to competition among donor and acceptor types of defects. The current transport mechanism of the Schottky contacts was found to be dominated by trap-assisted recombination tunneling and space charge-limited conduction in the mobility and ballistic regime.

Key words: ZnO, ion irradiation, nanorods, photoluminescence, Schottky contact

INTRODUCTION

One-dimensional (1D) semiconductor nanostructures exhibit unusual properties that can be utilized for potential applications in electronic and optoelectronic devices.[1,2] Previously, various 1D structure-based functional devices such as light-emitting diodes (LED), gas sensors, and field-effect transistors (FET) have been reported.[2–4] Amongst many other 1D nanostructured systems, zinc oxide (ZnO) has immense potential in a wide variety of applications, including nanophotonic, nanooptic, and optoelectronic components.[4–6] Owing to difficulty in electrical probing, most of the 1D structures are generally characterized via optical spectroscopy and diffraction methods. In spite of rapid growth and development of synthesis techniques and fabrication strategies, formation of reliable and reproducible nanoscale metal/semiconductor contacts still requires careful consideration. Specifically, qualitative as well as quantitative analysis of metal/semiconductor rectifying contacts (i.e., Schottky diodes) need to be addressed in view of their advantages over conventional p–n junction diodes.[7] The rectifying response of Schottky contacts of M/ZnO (M = Au, Ag, Pt, etc.) junctions has already been demonstrated by various groups.[8–10] Park et al.[8] witnessed improved rectifying behavior of Au/ZnO nanorod arrays when Au was used as a capping layer on the nanorod tips. In a similar way, it has become possible to fabricate Schottky devices by using single nanobelts/nanowires aligned between the two electrodes.[9] It is quite apparent that the surface and native defects (zinc or oxygen vacancies, interstitials, etc.) can directly influence the transport properties of Schottky diodes made from ZnO nanostructures.[11–13]

The effect of fast-moving ions has great relevance in tailoring the structural and morphological properties

(Received July 30, 2011; accepted February 7, 2012; published online March 17, 2012)

of nanostructures. Depending on the energy (keV or MeV regime) that ions carry, several important phenomena can take place: ion implantation, nanoparticle growth, splitting, and unidirectional growth (elongation).[14–16] In ZnO systems, ion beam-induced modification/reorganization of various native defects has also been discussed.[16,17] Nevertheless, the electrical properties of Schottky diodes made from ZnO nanostructures and subjected to energetic ion irradiation are rarely found in literature.

This work reports on the improved and unusual Schottky response of Ag/ZnO nanorod-based junctions. Randomly oriented nanorods (RON) of ZnO were irradiated by 80-MeV oxygen (O^{6+}) ions and later used for making Schottky junctions. Defect formation was monitored by photoluminescence (PL) spectroscopy and was correlated with the changes in the *I–V* curves as a consequence of carrier transport properties.

EXPERIMENTAL PROCEDURES

The production of ZnO RON, irradiation, and fabrication of Schottky junctions are discussed below.

Production of ZnO Nanorods

ZnO nanorods were prepared by using a cost-effective thermal annealing process.[18] To prepare an aqueous solution of polyvinyl alcohol (PVA), 5 wt.% PVA (Loba-Chemie, 99%) was subjected to constant stirring (~200 rpm) in double-distilled water for 2 h at constant temperature of 70°C. Considering a weight ratio of zinc acetate dihydrate (ZAD) to PVA of 1.5, ZAD [$Zn(CH_3COO)_2$, Merck, 99%] was transferred to aqueous PVA solution under vigorous stirring. Aqueous sodium hydroxide (NaOH, 0.6 M stock) was injected dropwise to the resulting solution until the pH became 8.5. This precursor was spin-cast onto cleaned Al_2O_3/Al substrates and then subjected to annealing in a constant air-flow muffle furnace for 1 h with surrounding temperature maintained at 750 ± 5°C. The spontaneous decomposition of ZAD to $Zn(OH)_2$ finally results in the formation ZnO nanorods.

Irradiation

The ZnO RON grown on Al_2O_3/Al substrates were irradiated in the Material Science chamber under high vacuum (pressure ~10^{-7} mbar) using 80-MeV O^{6+} ion beams (with low beam current of ~0.6 pnA, particle-nanoampere), available at the 15 UD tandem pelletron accelerator of Inter University Accelerator Centre, New Delhi. The ion fluence was measured by integrating the ion charge on the sample ladder, which was insulated from the chamber. The ion fluence was varied to 3×10^{10} ions/cm^2, 6×10^{10} ions/cm^2, and 9×10^{10} ions/cm^2. The fluence values were kept low as higher fluences would lead to nanorod agglomeration, as predicted in previous works.[16]

Characterization of ZnO Nanorods

The structural organization of the sample was inspected under scanning electron microscopy (SEM) in a JEOL JSM model 6390 LV instrument. Crystallographic analysis of the RON was performed by x-ray diffraction (XRD) measurements using a Rigaku D/max-2000 diffractometer employing Cu K_α radiation (λ = 1.54 Å). Room-temperature PL spectra were recorded by a PerkinElmer LS 55 spectrophotometer with a Xe line (λ_{ex} = 325 nm) as the excitation source.

Fabrication of Ag/ZnO RON Schottky Junctions

To explore the nature of electrical transport, the nanojunctions were characterized using a Keithley 2400 SourceMeter® via a two-probe method. In this regard, metallic contacts were fabricated by depositing two separate thin (~70 nm) Ag layers on the top surfaces of the nanorod-grown Al_2O_3/Al substrates by means of a thermal evaporation process using a vacuum coating unit (chamber pressure ~10^{-6} mbar). The effective contact area of the specimens under the probe lids was estimated to be ~1.45×10^{-7} m^2.

RESULTS AND DISCUSSION

Structural Characteristics

As can be found from Fig. 1a, RON of ZnO are clearly visible with inseparable structural organization. The approximate length of the RON is 2 μm to 3 μm, whereas the average diameter varies in the range of 30 nm to 70 nm. The XRD pattern of RON (Fig. 1b) suggests the development of hexagonal wurtzite phase of ZnO,[16] along with the characteristic peak of metallic Al. The existence of Al_2O_3 phase was also revealed in the form of poorly resolved peaks detected in the enlarged view of the diffraction pattern (inset of Fig. 1b).

Optical Emission and Alteration of Native Defects by Irradiation

It is expected that, in view of their high surface-to-volume ratio, nanoscale materials possess innumerable native point defects that are capable of influencing the emission response. Figure 2A depicts the room-temperature PL spectra (λ_{ex} = 325 nm) of virgin and 80-MeV oxygen ion irradiated ZnO RON samples. The PL spectra show emission in the visible region of the electromagnetic spectrum as a result of radiative emission preceded via various native defect states of ZnO such as zinc/oxygen vacancies, interstitials, and antisites.[18–21] Earlier, Gu et al.[19] observed the native defect state-mediated broad PL response from high-quality ZnO nanorods

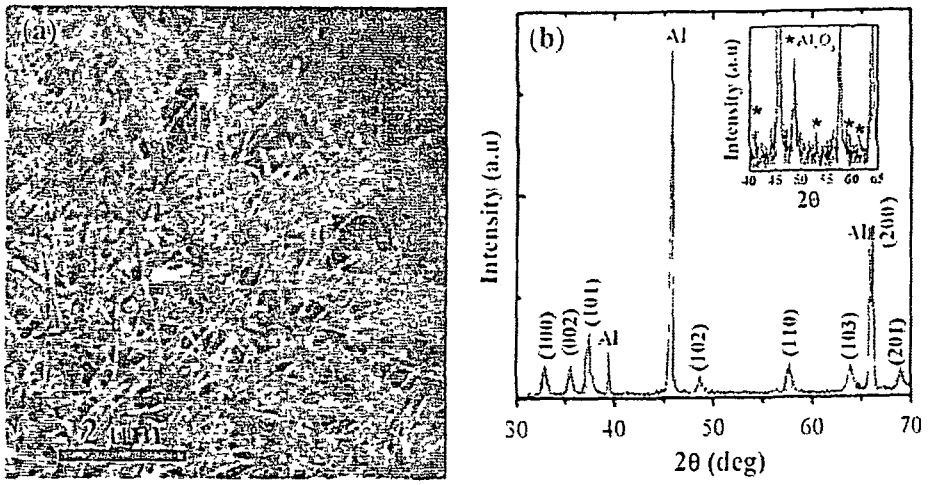

Fig. 1. (a) SEM image and (b) XRD pattern of RON of ZnO on the Al_2O_3/Al substrate. Inset of (b) shows a magnified part of the XRD pattern

grown using a catalyst-free, low-temperature oxidation method. It is worth mentioning here that the typical band-edge emission is not distinguishable in any of the PL spectra. Such an observation can be assigned to the excessively high contribution of the native defect states to the radiative emission, quenching the band-edge emission. The PL emission intensities of the RON irradiated with fluence of 3×10^{10} ions/cm^2 and 6×10^{10} ions/cm^2 were found to be enhanced as compared with the unirradiated one. The observed increase in emission intensity can be assigned to the dominance of creation over annihilation of native defects as a result of the bombardment by energetic ions.[16] However, upon irradiation at the highest fluence (9×10^{10} ions/cm^2), the luminescence response of the system is quenched. This luminescence quenching can be ascribed to collective annihilation of defects due to significant electronic energy loss leading to adequate migration of interstitials and fast structural ordering.[15,16]

For clear assessment of the contribution from independent native defects, Gaussian fitting was used to extract the different peak maxima associated with different defect types (Fig. 2B). The position and width of the fitted peaks were adjusted so that the empirical curve (red label) formed by the combination of the fitted peaks matched the experimental curve (black label). The PL spectrum of the unirradiated sample (Fig. 2Ba) shows three peaks, corresponding to neutral zinc interstitial (Zn_i at ~423 nm), singly ionized zinc interstitial (Zn_i^+ at ~446 nm), and singly ionized oxygen vacancy (V_O^+ at ~491 nm).[18,20,21] Among these emissions, the radiative response of Zn_i^+ defects was found to dominate the overall spectrum. Upon irradiation with fluence of 3×10^{10} ions/cm^2 (Fig. 2Bb), a sharp contribution from the neutral zinc vacancy (V_{Zn} at ~407 nm) as well as oxygen interstitials (O_i at ~526 nm) were observed.[20,21] Though the Zn_i and Zn_i^+ emission peaks remain intact, the V_O^+-related emission is suppressed. This could be accounted for by annealing out of a substantial amount of V_O^+ defects compared with other types of defects when the specimen was subjected to oxygen irradiation (equivalent to annealing in air).[22]

On the other hand, irradiation with fluence of 6×10^{10} ions/cm^2 (Fig. 2Bc) decreased the neutral V_{Zn}-related emission but led to the appearance of an emission peak due to singly ionized zinc vacancy (V_{Zn}^-) at ~472 nm.[21,23] Lastly, the V_{Zn}-related emission is completely quenched at the highest fluence (9×10^{10} ions/cm^2) while V_{Zn}^--related emission remains unaltered, as revealed in Fig. 2Bd. This indicates that the V_{Zn} defects created at fluence of 3×10^{10} ions/cm^2 are partly converted to V_{Zn}^- defects when a higher fluence (6×10^{10} ions/cm^2) is used. Finally, at 9×10^{10} ions/cm^2, all the V_{Zn} defects are transformed into V_{Zn}^- defects, leading to drastic quenching of V_{Zn}-related emissions. Also, as we move from low to high fluence, one can notice the increase of Zn_i-related emission over Zn_i^+-related emission. During irradiation, the electronic energy loss (S_e) is generally used to ionize the host material along the path of the ions.[24] In our study, the considerable magnitude of S_e (1.62×10^2 eV/Å) of the oxygen ions in the ZnO host is capable of ionizing Zn_i and the neutral V_{Zn} defects. As a result, there is conversion of V_{Zn} to V_{Zn}^- defects and Zn_i^+ to Zn_i defects along the trajectory of the ions. The probabilities of these conversions increase as more ions impact with the target material. At the highest fluence, V_{Zn} defects are converted to V_{Zn}^- defects, while Zn_i^+ defects get converted to Zn_i defects The formation and increase/decrease of various defect-related responses are summarized in Table I.

Transport Characteristics of Ag/ZnO RON Nanojunctions

The current–voltage (I–V) characteristics of the RON before and after irradiation were plotted by

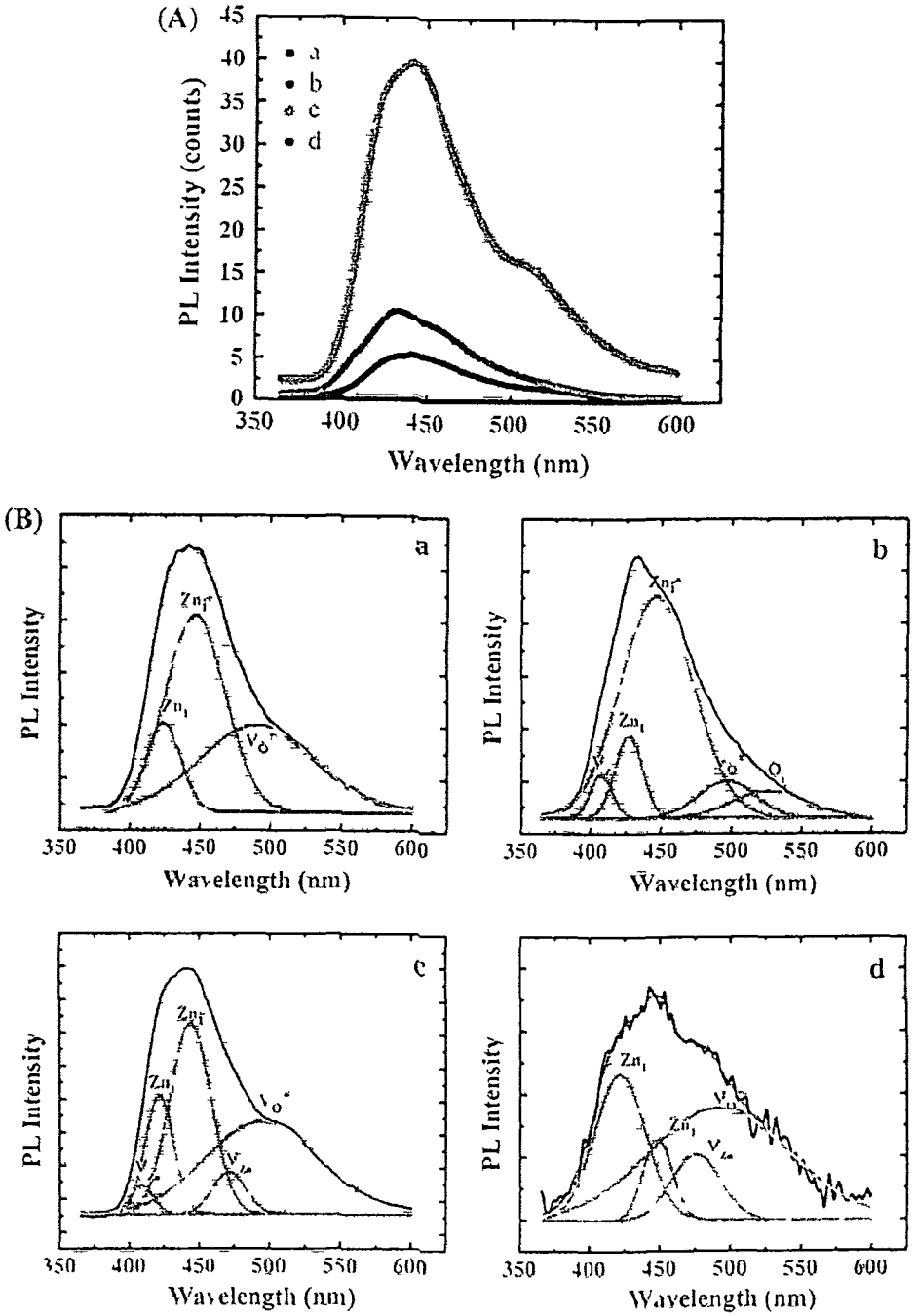

Fig 2 (A) Room temperature PL spectra of the nanorods (a) before, and after irradiation at fluence of (b) 3 × 10^{10} ions/cm^2, (c) 6 × 10^{10} ions/cm^2, and (d) 9 × 10^{10} ions/cm^2 (B) Respective Gaussian fits to the PL spectra (Color figure online)

using a computer-interfaced digital Keithley 2400 SourceMeter®, with vertical probes contacting the Ag contacts deposited on the RON (Fig 3a) The room-temperature I–V curves of the Ag/ZnO RON systems before and after irradiation exhibit excellent rectifying nature with very low leakage currents (Fig 3b) The Schottky contact formed between the Ag metallic contacts and the RON is the main reason for the rectifying response According to the Schottky diode equation, the forward diode current (for $V > 3kT/q$) is given by[25]

$$I = I_s \exp\left(\frac{qV_a}{\eta kT}\right) \quad (1)$$

where q is the electronic charge, V_a is the applied voltage, k is the Boltzmann constant, and T is the working temperature Here, η is the ideality factor

Table I. Modification of native defects due to irradiation (symbols ●, ○, ↑, and ↓ represent formation, suppression, increasing, and decreasing trends; respectively)

Fluence (ions/cm^2)	●	○	↑	↓
3×10^{10}	V_{Zn}, O_i	–	–	V_O^+
6×10^{10}	V_{Zn}^-	O_i	V_O^+	V_{Zn}
9×10^{10}	–	V_{Zn}	Zn_i	Zn_i^+

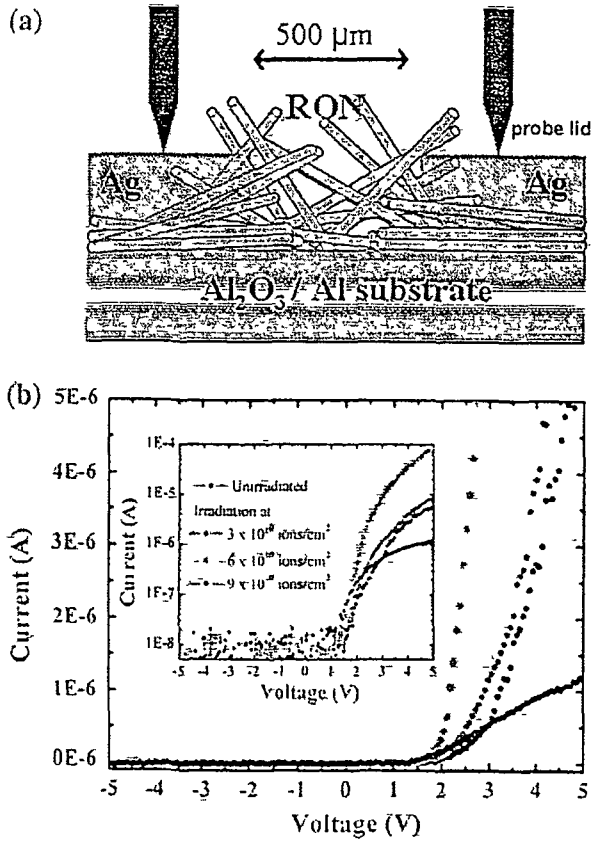

Fig 3. (a) Schematic diagram of the Ag/ZnO RON system on Al_2O_3/Al substrate. (b) Room-temperature I–V characteristics of the Schottky nanojunctions (Color figure online)

Qualitatively, η represents the departure from ideal diode behavior ($\eta = 1$). The reverse saturation current, I_s, can be written as

$$I_s = AA^*T^2 \exp\left(-\frac{q\phi_B}{kT}\right), \quad (2)$$

where A is the effective area of the metal–semiconductor contact, A^* is the Richardson constant, and ϕ_B is the Schottky barrier height. The η and ϕ_B of the RON before and after irradiation were calculated from the linear fit of the semilogarithmic I–V curve, depicted in the inset of Fig. 3b. For the unirradiated RON, η was found to be as high as 17.7, while ϕ_B has a value of 0.78 eV. The presence of a large number of surface/defect states within the band gap of ZnO is generally responsible for the nonideal character of a Schottky contact.[8,11,26] Earlier, in Au/ZnO systems, very high values of η between 20.5 and 38 were observed and the existence of an interfacial insulating layer or surface states at the metal–semiconductor junction was predicted.[27] In our study, the presence of various kinds of defects within the band gap of ZnO was evident from the PL spectra (Fig. 2A). Accordingly, mechanisms such as image-force barrier lowering (IFBL) and generation–recombination of carriers in the space-charge regions are responsible for the nonideal behavior of the junction with a high value of η.[7,11]

Upon 80-MeV O^{6+} ion irradiation of RON (with fluences of 3×10^{10} ions/cm^2 and 6×10^{10} ions/cm^2), the current under forward bias was found to be improved significantly with steep slopes (Fig 3b). The observed enhancement in current conduction is attributed to the irradiation-induced increase of defect concentration, as evident from the PL spectra (Fig. 2A). Again, ϕ_B of the nanojunctions using ZnO RON systems irradiated at fluences of 3×10^{10} ions/cm^2 and 6×10^{10} ions/cm^2 shows substantial enhancement, with respective values of 0.95 eV and 0.9 eV. The corresponding values of η were found to be 6.9 and 7.3, being smaller than for the unirradiated system ($\eta = 17.7$). It is known that V_O^+ and Zn_i defects act as donors, whereas V_{Zn}, O_i and O_{Zn} are regarded as acceptors in the ZnO system.[20] For unirradiated RON, the dominance of Zn_i-related defects and V_O^+ defects makes the system largely n-type and, therefore, show high IFBL effect.[13] However, for the RON subjected to irradiation at 3×10^{10} ions/cm^2, the formation of V_{Zn} and O_i-related defects was clearly evident (Table I). The formation of such acceptor-type defects compensates the n-type conductivity of the system, leading to a weak IFBL effect. Consequently, at this fluence, the ϕ_B of the Ag/ZnO RON junction is enhanced to 0.95 eV and η becomes 6.9. In contrast, irradiation at 6×10^{10} ions/cm^2 leads to simultaneous decrease of V_{Zn} and O_i defects, thus resulting in a slight improvement in the value of η up to 7.3. Lastly, at the highest fluence (9×10^{10} ions/cm^2), the substantial decrease of native defect concentration as compared with the unirradiated case (evident from the PL spectra, Fig. 2A; Table I) led to the noticeable lowering of forward bias current. In this situation, though the V_{Zn} defects are totally suppressed, the presence of V_{Zn}^- defects still maintains a higher value of ϕ_B (0.87 eV) and a moderate value of η (8.0).

Carrier Transport Mechanism and the Role of Irradiation Effect

To understand the nature of carrier transport for different voltage regimes, the I–V characteristics were also plotted on log–log scale (Fig. 4). Schottky

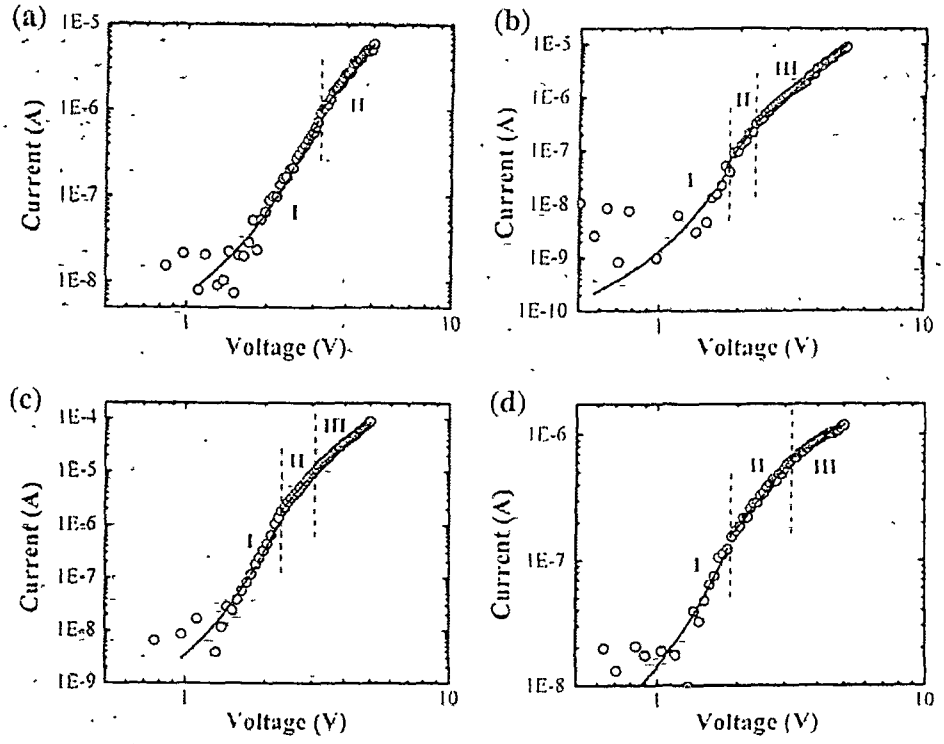

Fig. 4. Log–log plot of the *I–V* characteristics of the Ag/ZnO system with RON (a) before irradiation, and after irradiation at (b) 3×10^{10} ions/cm^2, (c) 6×10^{10} ions/cm^2, and (d) 9×10^{10} ions/cm^2.

Table II. The range of the different regions and the dominant transport mechanism

Fluence (ions/cm^2)	ϕ_B (eV)	η	Recombination Tunneling	SCLC/TCLC	
			Region I (V)	Region II	Region III
0 (unirradiated)	0.78	17.7	1.1–3.1	>3.2 V ($m \approx 4$)	–
3×10^{10}	0.95	6.9	0.6–1.8	1.8–2.2 V ($m \approx 7$)	>2.2 V ($m \approx 4$)
6×10^{10}	0.9	7.3	0.9–2.2	2.3–3.1 V ($m \approx 6$)	>3.1 V ($m \approx 4.3$)
9×10^{10}	0.87	8.0	0.7–1.8	1.8–3.2 V ($m \approx 2.7$)	>3.2 V ($m \approx 1.4$)

contacts using pristine RON exhibited two distinct regions of current conduction, as shown in Fig. 4a. Region I ($V < 3.1$ V) exhibits an exponential increase of current with respect to the applied voltage, following the relation $I \propto \exp(\alpha V)$, α being a system parameter. The η value of the system was calculated within this region where the conduction mechanism is dominated by recombination tunneling with electrons experiencing a series of tunneling events via local recombination sites.[28,29] Beyond 3.2 V (region II), the current follows a power law with the relation $I \propto V^m$, where $m = 4$, and the effective current transport is assigned to the space charge-limited conduction (SCLC) mechanism.[7,30] In the present case, as $m > 2$, the SCLC is in the mobility region where the carrier velocity depends on the electric field with an exponential distribution of traps within the band gap of ZnO.[31,32] This is why it is also termed as trap charge-limited current (TCLC).[31]

For the case of irradiated RON, the injected current exhibited three separate regions in the log–log scale *I–V* plots (Fig. 4b–d). The typical ranges responsible for transport mechanism are shown in Table II. For all the samples under study, current transport was dominated by the recombination tunneling mechanism characterized by the exponential current increase (region I). The current in region II can be described by a power law indicating the dominance of the TCLC mechanism, similar to the pristine case but with a different value of m (>2). Apart from these two conventional regimes, an extra zone (region III) appeared for the Schottky diodes based on irradiated RON (Fig. 4b–d; Table II). In this new region, the current conduction still obeys a power law but possesses lower values of m

and is expected to be mediated by the dominant SCLC mechanism. Moreover, governed by the TCLC transport mechanism, the Schottky contacts that use ZnO RON irradiated with fluences of 3×10^{10} ions/cm^2 and 6×10^{10} ions/cm^2 exhibit higher values of m (≥ 4) in region III (Fig 4b, c, Table II) At the highest fluence (9×10^{10} ions/cm^2), in region III, m has a value of 1 4 We suggest that the SCLC is in the ballistic region where the carrier velocity is independent of the field and scattering process, but depends on the injection velocity of the source [7 30] The appearance of the new region (III) for the Schottky contacts made from irradiated RON can be assigned to reorganization of defect/trap states within the band gap of ZnO induced by irradiation

CONCLUSIONS

The effects of 80-MeV O^{6+} ion irradiation on the optical emission and rectifying properties of ZnO RON nanojunctions have been studied Irradiation with fluences of 3×10^{10} ions/cm^2 and 6×10^{10} ions/cm^2 resulted in increase of the native defect concentration and, consequently, higher current conduction under forward bias Irradiation-induced formation of acceptor-type V_{Zn} and O_i defects was found to lower the IFBL effect, thus improving the Schottky responses of the irradiated RON This was characterized by a reduction of ideality factor from a value of 17 7 (unirradiated case) to 6 9 and 7 3 when irradiation was performed at fluence of 3×10^{10} ions/cm^2 and 6×10^{10} ions/cm^2, respectively The conduction process of the RON before and after irradiation is dominated by trap-assisted recombination tunneling and SCLC conduction in the mobility region with an exponential distribution of trap levels Conversely, irradiation with the highest fluence (9×10^{10} ions/cm^2) led to suppression of native defects, and hence current conduction under forward bias is decreased Here, the SCLC conduction is found to be in the ballistic region Although the current is lower, the estimated ideality factor of 8 0 remained lower than the corresponding value of the unirradiated specimen

ACKNOWLEDGMENTS

We extend our sincere gratitude to the pelletron group of IUAC, New Delhi for providing the high-quality oxygen beam under Project No UFUP 44314/2008 We also thank IUAC for sanctioning a follow-up Project No UFR-50307/2011 The cooperation received from the Material Science group is also acknowledged One of the authors (S B) acknowledges UGC, New Delhi, for providing a fellowship through the RGNF scheme

REFERENCES

1 M Law, J Goldberger, and P Yang, *Annu Rev Mater Res* 34, 83 (2004)
2 M S Gudiksen, L J Lauhon, J Wang, D C Smith, and C M Lieber, *Nature* 415, 617 (2002)
3 Y Huang and C M Lieber, *Pure Appl Chem* 76, 2051 (2004)
4 G C Yi, C Wang, and W I Park, *Semicond Sci Technol* 20, S22 (2005)
5 X Wang, C J Summers, and Z L Wang, *Nano Lett* 4, 423 (2004)
6 Z L Wang, *J Phys Condens Matter* 16, R829 (2004)
7 S M Sze and K K Ng, *Physics of Semiconductor Devices*, 3rd ed (New York Wiley, 2007)
8 W I Park, G -C Yi, J -W Kim, and S M Park, *Appl Phys Lett* 82, 4358 (2003)
9 C S Lao, J Liu, P Gao, L Zhang, D Davidovic, R Tummala, and Z L Wang, *Nano Lett* 6, 263 (2006)
10 L Wen, K M Wong, Y Fang, M Wu, and Y Lei, *J Mater Chem* 21, 7090 (2011)
11 S N Das, J -H Choi, J P Kar, K J Moon, T I Lee, and J -M Myoung, *Appl Phys Lett* 96, 092111 (2010)
12 K Cheng, G Cheng, S Wang, L Li, S Dai, X Zhang, B Zou, and Z Du, *New J Phys* 9, 214 (2007)
13 S Lee, Y Lee, D Y Kim, and T W Kang, *Appl Phys Lett* 96, 142102 (2010)
14 S O Kucheyev, J S Williams, C Jagadish, J Zou, C Evans, A J Nelson, and A V Hamza, *Phys Rev B* 67, 094115 (2003)
15 R Giulian, F Kremer, L L Araujo, D J Sprouster, P Kluth, P F P Fichtner, A P Byrne, and M C Ridgway, *Phys Rev B* 82, 113410 (2010)
16 S Bayan and D Mohanta, *Nucl Instrum Methods Phys Res B* 269, 374 (2011)
17 D C Agarwal, Amit Kumar, S A Khan, D Kabiraj, F Singh, A Tripathi, J C Pivin, R S Chauhan, and D K Avasthi, *Nucl Instrum Methods Phys Res B* 244 136 (2006)
18 S Bayan and D Mohanta, *J Appl Phys* 108, 023512 (2010)
19 Z Gu M P Paranthaman, J Xu, and Z W Pan, *ACS Nano* 3, 273 (2003)
20 B Lin, Z Fu, and Y Jia, *Appl Phys Lett* 79, 943 (2001)
21 S A M Lima, F A Sigoli Jr , M Jafelicci, and M R Davolos, *Int J Inorg Mater* 3, 749 (2001)
22 S S Tinchev, *Physica C* 256, 191 (1996)
23 K H Tam, C K Cheung, Y H Leung, A B Djurišic, C C Ling, C D Beling, S Fung, W M Kwok, W K Chan D L Phillips, L Ding and W K Ge, *J Phys Chem B* 110, 20865 (2006)
24 R L Fleischer, P B Price, and R M Walker, *J Appl Phys* 36, 3645 (1965)
25 S K Cheung and N W Cheung, *Appl Phys Lett* 49, 85 (1986)
26 P Klason, O Nur, and M Willander, *Nanotechnology* 19, 475202 (2008)
27 O Harnack, C Pacholski, H Weller, A Yasuda, and J M Wessels, *Nano Lett* 3, 1097 (2003)
28 A Bindal, R Wachnik, and W Ma *J Appl Phys* 68, 6259 (1990)
29 S Kishwar, K ul Hasan, N H Alvi, P Klason, O Nur and M Willander *Superlattices Microstruct* 49 32 (2011)
30 F Catalfamo T Yen, J Yun, and W A Anderson *J Electron Mater* 40, 433 (2011)
31 D I Son, C H You, J H Jung, and T W Kim, *Appl Phys Lett* 97, 013304 (2010)
32 T F Yen, A Haungs, S J Kim A Cartwright, and W A Anderson *J Electron Mater* 39 568 (2010)

Radiation Effects & Defects in Solids
Vol 166, No 11, November 2011, 884–893

Taylor & Francis
Taylor & Francis Group

Interplay of native defect-related photoluminescence response of ZnO nanosticks subjected to 80 keV Ar ion irradiation

S Bayan and D Mohanta*

Nanoscience Laboratory, Department of Physics, Tezpur University, PO Napaam, Tezpur, Assam 784 028, India

(Received 20 March 2011, final version received 7 June 2011)

We report on the effect of 80 keV Ar^+ ion irradiation on the luminescence response of zinc oxide (ZnO) nanosticks synthesized using a simple microemulsion route The formation of nanoscale rods was confirmed from the transmission electron microscopy, whereas the hexagonal wurtzite phase of the nanorods was detected in an X ray diffraction pattern The photoluminescence pattern of the nanorods was dominated by various native defect states of ZnO, which are responsible for the quenching of the typical band edge emission of ZnO Under Ar^+ ion irradiation at a fluence of 1×10^{13} ions/cm^2, the band edge emission was recovered owing to the suppression of oxygen vacancy defects In addition, the formation of new zinc vacancy and ionized zinc interstitial defects were also evident Conversely, the band edge emission was found to be quenched as a result of the creation of more oxygen vacancy (V_O) defects due to ion irradiation (fluence 1×10^{15} ions/cm^2) The nuclear energy loss of the Ar^+ ions in ZnO is responsible for the formation of point (vacancy-related) defects, while relatively small amount of electronic energy loss of the Ar^+ ion results in the ionization of the neutral zinc interstitial (Zn_i) defects The energy deposition scheme of the energetic ions has been elaborated with the help of theoretical modeling that explains the observed features quite satisfactorily

Keywords ZnO, ion irradiation, nanorods, photoluminescence

PACS 61 80Jh, 78 67Qa, 78 55Et

1. Introduction

In the recent decade, one-dimensional (1D) semiconductor nanostructures have been the focus of research owing to their potential application in optoelectronic and photonic devices (*1, 2*) In particular, zinc oxide (ZnO) is a promising candidate for the luminescent and display devices that work in the blue or ultraviolet (UV) region of the electromagnetic spectrum (*3–5*) The presence of various native defect states (oxygen/zinc vacancies, interstitials and antisites) within the band gap of ZnO has expanded the area of application to a vast number of components including gas sensors and photodetectors (*6, 7*) Advancement in the various processing techniques has led to the production of quality and cost-effective 1D ZnO nanostructures, namely, rods, wires,

*Corresponding author Email best@tezu ernet in

ISSN 1042-0150 print/ISSN 1029-4953 online

http //dx doi org/10 1080/10420150 2011 596838
http //www tandfonline com

needles, urchins, etc. (*8–10*). Compared with other binary compounds, ZnO offers the flexibility of extending the application to diverse fields while meeting economically viable synthesis strategies that rely on both quality and reproducibility.

Bombardment of semiconductor nanostructures with fast-moving ions can lead to the structural and morphological changes in the nanostructured systems. Depending on the energy of the projectile ions (keV or MeV scale), implantation, growth and elongation can take place (*11–13*). Ion beam-induced defects in ZnO have also been studied with different ions having energies in the keV or a few MeV range (*11, 14*). To be specific, the effect of low-energy ion irradiation on the emission response of various native defects of ZnO nanomaterials is rarely discussed in the existing literature. In the present work, we report on the consequence of 80 keV Ar^+ ion irradiation on the luminescence response arising due to various native defect states of ZnO nanoscale rods (nanosticks). In light of a theoretical model, we discuss how the nature of the energy deposition plays a vital role in the modification of native defects and, hence, on the radiative emission responses.

2. Experimental details

2.1. *Synthesis of ZnO nanosticks*

The ZnO nanorods were synthesized using a simple microemulsion route: 30 mL of hexane, 5.45 g *N*-cetyl-*N*, *N*, *N*,-trimethyl ammonium bromide (99.9% pure, Loba-Chemie) and 10 mL of *n*-butanol were stirred (~200 rpm) together for about half an hour resulting in a homogeneous white mixture. The mixture was divided into two equal parts, and aqueous zinc chloride ($ZnCl_2$) and sodium hydroxide (NaOH) were added to the two separate mixtures, thus producing two microemulsions. Finally, the two precursors were mixed steadily and continuous stirring was allowed for 8 h. The elongated ZnO nanostructures were obtained by following centrifugation, ultrasonication and annealing (~80°C) in sequence.

2.2. *Irradiation of ZnO nanosticks*

For the irradiation experiment, the ZnO nanorods were dispersed in polyvinyl alcohol (PVA) matrix to avoid agglomeration upon energetic irradiation. The ZnO nanorods dispersed in PVA matrix were casted on laboratory glass slides of size $1 \times 1\,cm^2$ and were subjected to 80 keV Ar^+ ion irradiation using the low-energy ion beam facility (LEIBF) available at Inter University Accelerator Centre, New Delhi. The beam current was kept at ~1 eμA, while the fluence varied as 1×10^{13} and 1×10^{15} ions/cm^2.

2.3. *Characterization tools*

The structural analysis of the as-synthesized product was performed by X-ray diffraction (XRD) measurements in a Rigaku D/max-2000 diffractometer employing Cu Kα radiation ($\lambda = 1.54$ Å). The transmission electron microscopy (TEM) study was carried out by a Jeol JSM-100 CX microscope working at a beam accelerating voltage of 80 kV. The optical absorption study was carried out by the UV–visible optical absorption spectroscopy (Shimadzu Corporation, Japan /UV2450). The room-temperature photoluminescence (PL) spectra were recorded by using a Perkin Elmer LS 55 spectrophotometer with Xe line ($\lambda_{ex} = 325$ nm) as the excitation source.

3. Results and discussion

3.1. *Development of ZnO nanosticks: microstructural and optical features*

The visible evidence of the as-synthesized nanosticks is obtained from the TEM image shown in Figure 1(a) As depicted in the micrograph, the diameter and the length of the nanorods vary within 20–30 and 175–200 nm range. The XRD pattern of the nanorods (Figure 1(b)) corresponds to the hexagonal wurtzite phase of ZnO with preferred orientation along (101) plane (JCPDS 36-1451) (*15*) The lattice parameters of the crystal lattice of the nanorod system were found to be $a = 3\ 25$ Å and $c = 5\ 23$ Å in agreement with the above-mentioned JCPDS data

As evident from the UV–visible absorption spectra (Figure 2(a)) of the nanosticks, an absorption peak is found at $\lambda \sim 362$ nm ($E = 3\ 43$ eV), which corresponds to the ground state exciton absorption in the ZnO nanosystem The enhancement in the ground state excitonic energy of the ZnO nanosticks compared with that of the bulk ($\lambda \sim 376$ nm, $E = 3\ 30$ eV) is attributed to the quantum confinement effect (*16*) The position of the ground state excitonic absorptions for the bulk and the nanosystems are shown by the arrow marks in Figure 2(a) The room temperature PL

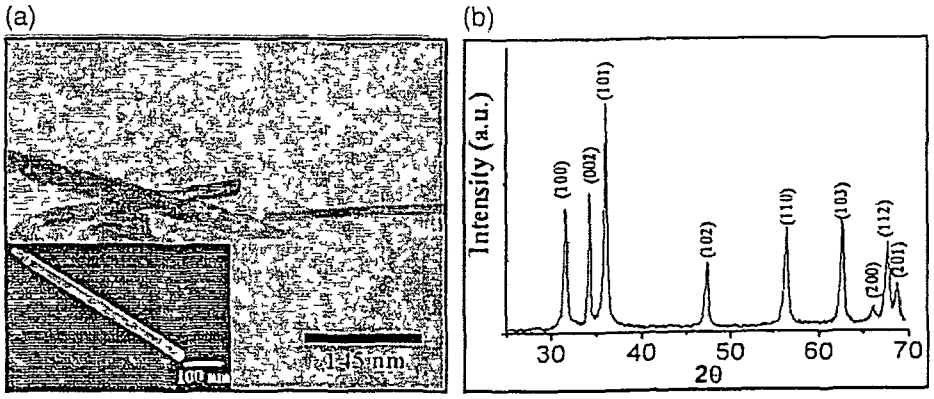

Figure 1 (a) TEM and (b) XRD pattern of the synthesized nanosticks Inset of (a) shows the dark field view of a single isolated nanorod

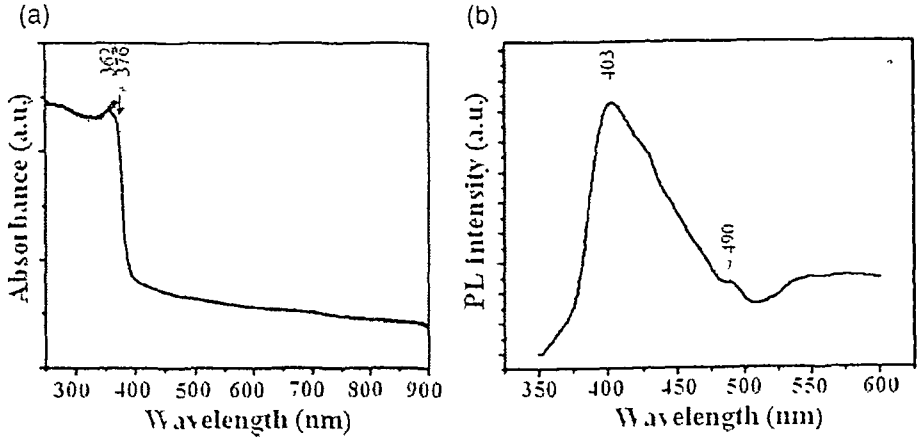

Figure 2 (a) UV–visible absorption spectra and (b) room temperature PL spectra of the unirradiated nanosticks

spectrum of the nanosticks, shown in Figure 2(b), depicts the presence of various defect-related emission of ZnO. The typical band edge emission of ZnO is found to become suppressed because of the presence of a large number of native defect states of different origins. The prominent central peak located at ~403 nm corresponds to the zinc vacancy (V_{Zn})-related defect response of ZnO, whereas the poorly resolved emission peaks at ~490 nm represent carrier recombination mediated via the oxygen vacancy (V_O^+)-related defects (*3, 17*). On the other hand, the broad region within 500–600 nm, in the emission spectrum, has arisen because of the presence of various defects: oxygen interstitial (O_i), double ionized oxygen vacancy (V_O^{++}), etc. (*3, 17*).

3.2. *Effect of 80 keV Ar^+ ion irradiation and interplay of defect emission*

The PL spectra of the ion-irradiated nanosticks are shown in Figure 3. Though the two emission spectra are dominated by the various defect-related emissions of ZnO, a clear variation in the emission pattern is visible in the spectra of the irradiated samples compared with the virgin one. Upon irradiation, the alteration of the emission spectra arises due to the substantial variation in the radiative process occurring via native defects. In order to distinguish the individual contribution of these defects and to compare with the pristine one, we took the Gaussian profile of different defect-related peaks of all the spectra for each case (Figure 4(a)–(c)).

The asymmetrically stretched PL spectrum of the unirradiated ZnO nanosticks depicts the presence of a prominent zinc interstitial (Zn_i) peak located at ~426 nm, apart from the above-mentioned V_{Zn}-related peak (Figure 4(a)). The two weak peaks at ~451 and 467 nm corresponded to the respective ionized zinc interstitial (Zn_i^+)- and zinc vacancy (V_{Zn}^-)-related defects (*3*). The singly ionized oxygen vacancy (V_O^+)- and oxygen interstitial (O_i)-related peaks have appeared at ~488 and 538 nm, respectively (*3, 17*). A poorly resolved emission peak at ~578 nm is found, which is ascribed to the doubly ionized oxygen vacancies (V_O^{++}) (*17*).

The nanosticks irradiated with a fluence of 1×10^{13} ions/cm^2 reveals a broad PL spectrum compared with the unirradiated one. The broadening of the PL spectrum arises due to the evolution of the ZnO-related band edge emission peak at ~375 nm (*3*). The V_{Zn} defect-related peak is still prominent, whereas the intensity of the Zn_i emission peak is lowered with respect to the former peak. Though the O_i defect emission is substantially quenched, the emission peaks corresponding to Zn_i^+ and V_{Zn}^- still exist. On the other hand, in the PL spectrum of samples irradiated with the fluence of 1×10^{15} ions/cm^2, the band edge emission is suppressed totally, whereas both Zn_i and Zn_i^+ defect-related emissions are enhanced by appreciable amounts Besides, the $V_{Zn}-$ and V_{Zn}^- related emission peaks are lowered compared with the interstitials (both neutral and ionized) Also, there is a development in the V_O^+-related emission, and as a result, the intensity of O_i-related emission shoots up.

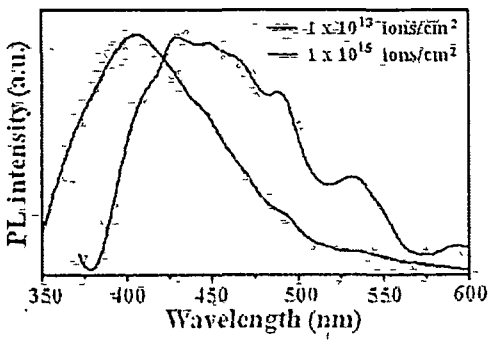

Figure 3. PL spectra of the nanosticks after ion irradiation at different fluences.

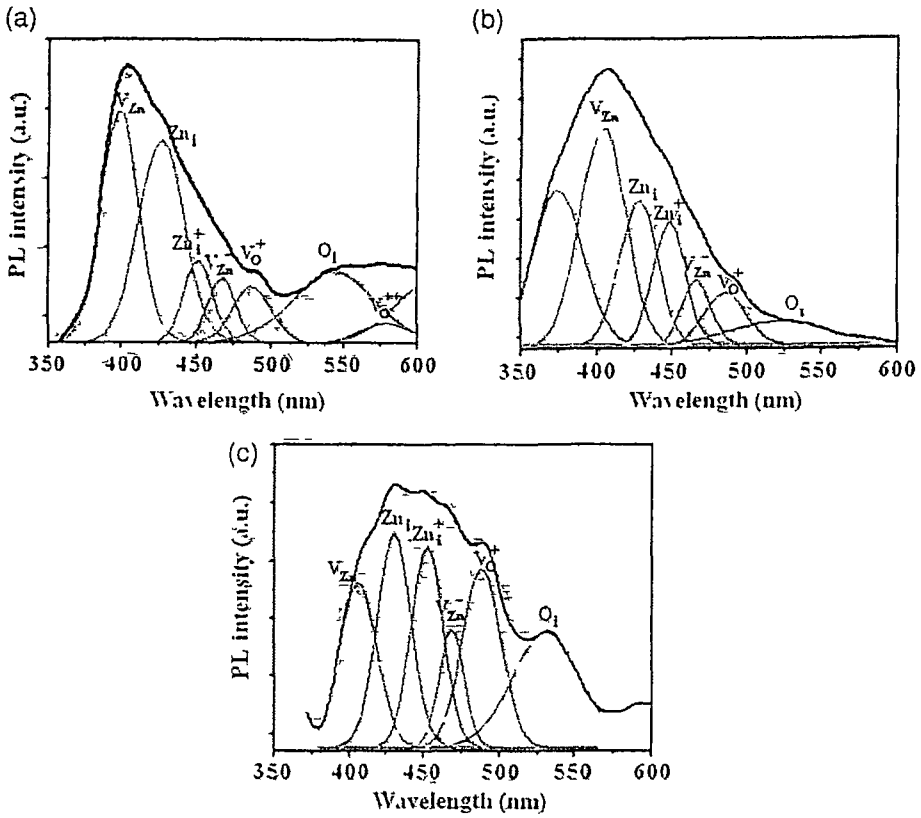

Figure 4 Gaussian fitting of the PL spectra of the nanosticks, recorded before (a) and after irradiation at 1×10^{13} ions/cm^2 (b) and 1×10^{15} ions/cm^2 (c)

Now it is apparent that there is a fluence-dependent variation in the emission responses of the defects. This variation is due to the irradiation-led creation and annihilation of the point defects in the nanosticks To account for the creation/annihilation of defects, the Zn- and O-related vacancy-to-interstitial emission intensity ratios have been calculated for the three spectra. As is evident from Figure 5, for the unirradiated ZnO nanorods, the V_{Zn}/Zn_i is just greater than unity (~1 14), representing thereby a nearly equal contribution to the PL emission by these defects Whereas upon irradiation with a fluence of 1×10^{13} ions/cm^2, a higher value of V_{Zn}/Zn_i ratio (~1 5) is ascertained that corresponds to the increase in V_{Zn} defects or decrease in Zn_i-related defects The increase in V_{Zn} is obvious and can be assigned to the irradiation led nuclear energy loss that can result in the knocking out of Zn atoms from its regular lattice site (*18*) The increase in V_{Zn} defects would also result in the increase in Zn_i On the contrary, it is possible that during irradiation, the Zn_i defects are formed but later converted to Zn_i^+ ones It can be seen in Figure 4 (a) and (b) that there is a variation in the intensity of the Zn_i and Zn_i^+ emission responses of the nanosticks before and after irradiation This is clearly evident from Figure 5, where the sharp rise in the Zn_i^+/Zn_i ratio of the nanorods irradiated at 1×10^{13} ions/cm^2, compared with the pristine one, hints at the increase in Zn_i^+ defects upon irradiation So, the decrease in Zn_i defects can be caused by the transformation of Zn_i to Zn_i^+ defects by ion impact As obtained from SRIM 2008 program (*19*), though the electronic energy loss (32 54 eV/Å, Table 1) by the Ar^+ ion during irradiation is smaller than the nuclear energy loss (87 07 eV/Å, Table 1), it is capable of ionizing a few atoms and it can result in the conversion of some Zn_i defects to Zn_i^+ defects In case of irradiation with the

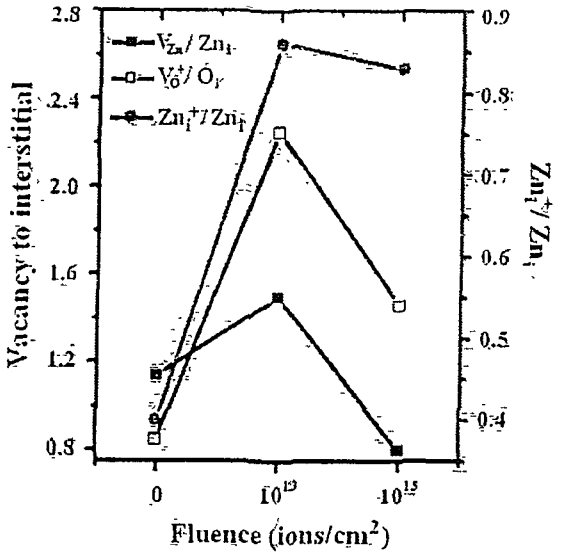

Figure 5. Zinc and oxygen vacancy-to-interstitial vs. fluence variation. Irradiation-dependent ionized zinc to neutral zinc interstitial response is also depicted in the graph.

Table 1. Electronic energy loss (S_e), nuclear energy loss (S_n) and projected range (R) of the 80 keV Ar^+ ion irradiation.

Material	Density (g/cc)	S_e (eV/Å)	S_n (eV/Å)	R (Å)
PVA	1.2	28.33	40.08	1172
ZnO	5.6	32.54	87.07	491

highest fluence (1×10^{15} ions/cm^2), the scenario is distinctly different owing to the suppression of some V_{Zn} defects as predicted by the lower value of V_{Zn}/Zn_i ratio (<1). As the Zn_i atoms are mobile even at room temperature (*20*), it is expected that during irradiation, several number of Zn_i atoms would migrate to the V_{Zn} defects, resulting in the reduction of the V_{Zn} defects.

On the other hand, the V_O^+/O_i ratio is found to be less than unity for the unirradiated case due to the dominance of O_i defects. Whereas the ratio becomes quite large after irradiation at a fluence of 1×10^{13} ions/cm^2, owing to the fact that O_i defects are being used in the annihilation of V_O^{++} defects during irradiation. The annihilation of V_O^{++} defects is responsible for the evolution of the band-edge emission peak of ZnO. Furthermore, V_O^+ defects are created when the nanorods are subjected to irradiation with a fluence of 1×10^{15} ions/cm^2, and eventually more O_i defects are formed. The simultaneous formation of V_O^+ and O_i defects at this fluence, results in acquiring a moderate value of V_O^+/O_i ratio for these nanoscale rods.

It has been observed that the nuclear energy loss related to the Ar^+ ion is responsible for the knocking out of atoms and the formation of V_{Zn} and V_O^+ defects, along with the annihilation of V_O^{++} defects by O_i atoms. The substantial amount of electronic energy loss by the Ar^+ ions also takes part in the event and converts the newly formed Zn_i to Zn_i^+ defects. However, it is evident that the Zn atoms are more affected during the irradiation event compared with the O atoms, whereas the O atoms are mainly affected at the highest fluence only. The origin of the defect establishment with regard to the creation and annihilation of vacancies and interstitials owing to Ar^+ ion irradiation must be explored, which requires suitable theoretical justification.

3.3. *Theoretical treatment on the observed phenomena*

In a system where the nanostructures are embedded in a matrix, both the matrix and the nanostructures will experience the impact of incoming ions during irradiation. As per the calculation obtained from the SRIM 2008 program, we predict that the 80 keV Ar^+ ions can traverse up to a distance of ~1172 Å (projected range, Table 1) within the PVA matrix. This suggests that the nanosticks located within this range only, would experience the impact of such ions. In order to visualize the events more clearly, we assume that the ion after traversing through the matrix encounters only one nanoscale rod to show its effect.

The total energy loss per unit length of the ion in PVA medium is S $(= S_e + S_n)$ with S_e and S_n being the electronic and nuclear energy losses. The initial energy of the ion before striking a nanorod surface is $(80 - Sz)$ keV, where z is the distance traversed by the ion from the surface of the PVA film to the nanorod surface (Figure 6). We consider three arbitrary values of z such as 5, 500 and 1000 Å, which correspond to the nanosticks positioned at the surface, middle and at the extreme end of the matrix but all within the projected range of the ion. Correspondingly, the initial energy of the ion before striking the nanorod will be 79.66, 45.8 and 11.6 keV, respectively. Using these values of the initial energy, the S_e, S_n and projected range (R) of the Ar^+ ion within the ZnO system have been calculated using the SRIM program (Table 2).

As far as the energy deposition by an ion is concerned, the energy of the ion decreases as it penetrates more atomic planes from the point of impact and can traverse to a distance equal to the projected range of the ion within the material. Now for the ions having energy in the keV scale, the deposited energy can be assumed in terms of some co-axial conical zones as shown in Figure 7. The maximum length of the axis of a cone will be equal to the projected range, whereas the maximum radius will be the distance between the point of impact and the spot where the deposited energy becomes close to zero.

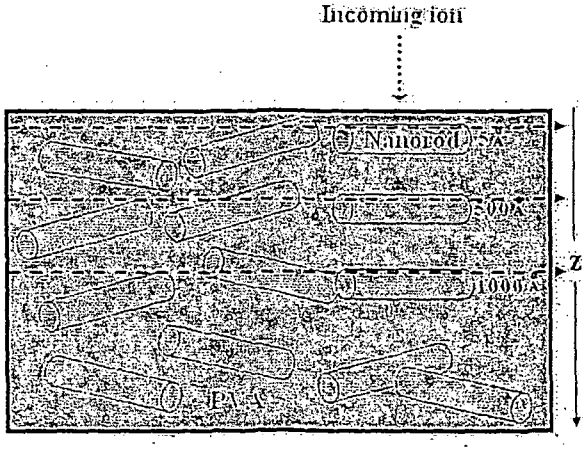

Figure 6. Scheme of the ZnO nanorods distributed within the matrix.

Table 2. Electronic energy loss (S_e), nuclear energy loss (S_n) and projected range (R) of the ZnO nanosticks situated at different positions in the PVA matrix.

z (Å)	$80 - Sz$ (keV)	S_e (eV/Å)	S_n (eV/Å)	R (Å)
5	79.66	32.5	87.1	489
500	45.8	24.6	94.1	289
1000	11.6	12.4	90.9	91

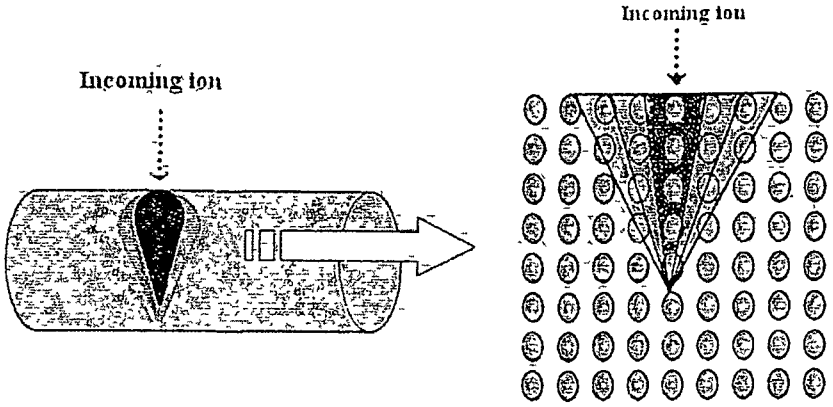

Figure 7. Schematic diagram of the conical zones created upon irradiation. (left) macroscopic and (right) atomistic views.

If x_i $(i = 1, 2, 3, \ldots)$ is the atomic percentage of each element of diameter d_i $(i = 1, 2, 3, \ldots)$ present in a nanorod of diameter D and length L, then the number of atoms present in the nanorod will be $N = 1.5fD^2L/\sum x_i d_i^3$, f being the packing fraction and $\sum x_i = 1$ (*21*).

Considering the volume of the cones to be v, the number of atoms present in a conical zone is given by

$$n = \frac{4Nv}{\pi D^2 L}. \tag{1}$$

Now, the total energy deposited by an ion within an effective region in the material will be equal to S_n times the projected range (R) of the ion within that material. So, the energy deposited per atom within a conical zone will be given by

$$\begin{aligned} E &= \frac{S_n R}{n}, \\ &= \frac{\pi D^2 L S_n R}{4Nv}. \end{aligned} \tag{2}$$

Next, using the various values of S_n and R (from Table 2) in the above equation, it can be found that the energy deposited per atom decreases as the volume of the cones increases from the center (Figure 8). This trend is maintained for all the nanosticks irrespective of their position within the matrix (i.e. whether nanorods are on the surface or in the interior). The atoms present within a cone having energy value greater than the displacement energies of Zn and O atoms are able to get displaced from their regular lattice site during the energy deposition process. The displacement energy of Zn in ZnO lattice is 18.5 eV and this energy corresponds to the imaginary cones having approximate volume of 17.5, 11.5 and 3.7 nm^3 for z-values of 5, 500 and 1000 Å, respectively. Whereas for O atoms the volume of the cones corresponding to its displacement energy (41 4 eV) is 7.6, 4.7 and 1.5 nm^3 for z values of 5, 500 and 1000 Å, respectively. Eventually, in acquiring displacement energy, the number of Zn atoms is larger than the O atoms according to Equation (1). Hence, upon irradiation, the Zn atoms are most affected irrespective of the position of the nanorods within the matrix and resulting in the variation of Zn-related defects.

In the above discussion, the overlapping of two or more energetic conical regions is not considered, which comes out to be an important aspect as one increases the fluence. With the increase in fluence, the nanorods will experience more ions, and as a result, there is chance of overlapping of the conical zones. At this situation, the atoms present in the overlapping region of two conical zones would possess more energy than the atoms beyond that region. As evident in the present

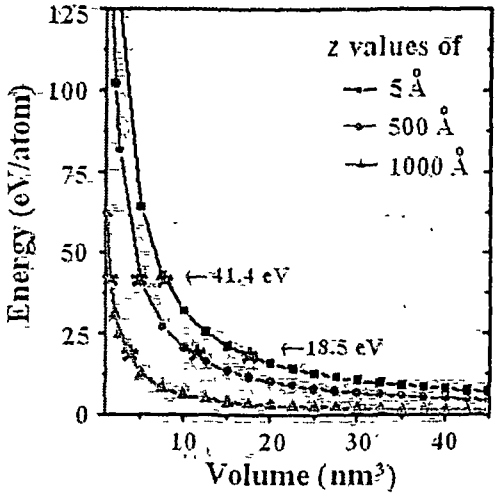

Figure 8. Variation of energy deposited per atom during irradiation and the volume of the cones.

system at a fluence of 1×10^{15} ions/cm^2, it is possible that the atoms present in the overlapping region acquire an energy equivalent to the displacement energy of O atoms and create more V_O^+ and O_i native defects.

4. Conclusions

ZnO nanorods, synthesized by using a simple microemulsion technique, were subjected to 80 keV Ar^+ ion irradiation in order to have variation in the emission pattern of ZnO. Though the emission responses of the nanorods before and after irradiation were dominated by different native defect states of ZnO, the band-edge emission of ZnO was recovered at 375 nm upon irradiation with a fluence of 1×10^{13} ions/cm^2. It was found that nuclear energy loss of the Ar^+ ion was used in the formation of V_{Zn} defects, whereas the electronic energy loss is responsible for the conversion of Zn_i atoms to Zn_i^+ defects. It is speculated that the energy deposition upon irradiation takes place in some co-axial conical regions, where the damage events at the Zn lattice sites is comparably-higher than the O sites owing to the less displacement energy of Zn in ZnO system. The overlapping of two or more conical regions at a higher fluence of 1×10^{15} ions/cm^2 is accountable for the evolution of more V_O^+ and O_i defects at that fluence. The irradiation-led variation in the emission patterns of ZnO can be useful and would form the basis of modern optoelectronic and display devices.

Acknowledgements

The authors sincerely thank the scientists involved in LEIBF of IUAC, New Delhi, for providing quality Ar beam. The financial support for the project UFUP 44314 is gratefully acknowledged. The authors are thankful to Ms M Devi for assisting in the irradiation experiment. The TEM facility obtained from SAIF, NEHU, is also acknowledged. One of the authors is thankful to UGC for the financial support of the RGNF fellowship.

References

(1) Zheng, M.J.; Zhang, L.D.; Li, G.H ; Zhang, X Y., Wang, X F *Appl. Phys Lett.* 2001, *79*, 839–841.
(2) Huang, X.; Li, J., Zhang, Y , Mascarenhas, A *J Am. Chem. Soc.* 2003, *125*, 7049–7055

(3) Lin, B , Fu, Z , Jia, Y *Appl Phys Lett* **2001**, *79*, 943–945
(4) Lima, S A M , Sigoli, F A , Jr , Jafelicci, M , Davolos, M R *Int J Inorg Mater* **2001**, *3*, 749–754
(5) Zeng, H , Yang, S , Xu, X , Cai, W *Appl Phys Lett* **2009**, *95*, 191904-1–3
(6) Roy, S , Basu, S *Bull Mater Sci* **2002**, *25*, 513–515
(7) Young, S J , Ji, L W , Chang, S J , Liang S H , Lam, K T , Fang, T H , Chen K J , Du, X L , Xue, Q K , *Sens Actuators A* **2007**, *135*, 523–529
(8) Willander, M , Nur, O , Bano, N , Sultana, K. *New J Phys* **2009**, *11*, 125020-1–16
(9) Ge, J , Tang, B , Zhuo, L , Shi, Z *Nanotech* **2006**, *17*, 1316–1322
(10) Bayan, S., Mohanta, D *J Appl Phys* **2010**, *108*, 023512-1–6
(11) Kucheyev, S O , Williams, J S , Jagadish, C , Zou, J Evans, C Nelson, A J , Hamza, A V *Phys Rev B* **2003**, *67*, 094115-1–11
(12) Bayan, S , Mohanta, D *Nucl Instrum. Methods B* **2011**, *269* 374–379
(13) Mohanta, D , Ahmed, G A , Choudhury, A , Singh F , Avasthi, D K , Boyer, G , Stanciu, G A *Eur Phys J Appl Phys* **2006**, *35*, 29–36
(14) Chattopadhyay, S , Dutta, S , Jana, D , Chattopadhyay, S , Sarkar, A , Kumar, P , Kanjilal, D , Mishra, D K , Ray, S K *J Appl Phys* **2010**, *107*, 113516-1–8
(15) Cao, B , Cai, W , Li, Y , Sun, F , Zhang, L *Nanotech* **2005**, *16*, 1734–1738
(16) Gu, Y , Kuskovsky, I L , Yin, M , O'Brien, S , Neumark, G F. *Appl Phys Lett* **2004**, *85*, 3834–3835
(17) Ye, J D , Gu, S L , Qin, F , Zhu, S M , Liu, S M , Zhou, X , Liu, W , Hu, L Q , Zhang, R , Shi, Y , Zheng, Y D *Appl Phys A* **2005**, *81*, 759–762
(18) Look, D.C , Hemsky, J W , Sizelove, J R *Phys Rev Lett* **1999**, *82*, 2552–2555
(19) Zeigler, J F , Zeigler, M D , Biersack, J P *SRIM (2008) – The Stopping and Range of Ions in Matter*, 2008 www srim org
(20) Rackauskas, S , Nasibulin, A G , Jiang, H , Tian, Y , Statkute, G , Shandakov, S D , Lipsanen, H , Kauppinen, E I *Appl Phys Lett* **2009**, *95*, 183114-1–3
(21) Bayan, S , Mohanta, D *J Mater Res* **2010**, *25*, 814–820

Defect mediated optical emission of randomly oriented ZnO nanorods and unusual rectifying behavior of Schottky nanojunctions

Sayan Bayan and Dambarudhar Mohanta[a)]
Nanoscience and Soft Matter Laboratory, Department of Physics, Tezpur University PO Napaam Tezpur, Assam 784 028, India

(Received 23 February 2011, accepted 1 August 2011, published online 12 September 2011)

We report on the interrelation of optical emission of randomly oriented ZnO nanorod system with the carrier transport properties of Ag/ZnO nanorod-based rectifying junctions The ZnO nanorods, exhibiting a hexagonal wurtzite phase, were fabricated by a cost-effective rapid thermal annealing process and at different annealing temperatures The photoluminescence spectra of the as grown samples have revealed various Zn and O related native defects (e g , vacancies, interstitials etc) located at ~400, 428, 491, and 535 nm As evident from the *I-V* characteristic curves, though all the Ag/ZnO nanojunctions show Schottky behavior, the nanorods grown at a temperature of 550 °C and 650 °C are characterized by very large ideality factors of respective values 35 4 and 33 2, apart from displaying unusually high reverse currents Whereas, the samples grown at 450 °C and 750 °C show usual rectifying nature having relatively lower ideality factors (18 4 and 12 2), along with low leakage-current under reverse biasing The enhancement or suppression of the reverse currents can be attributed to the eventual lowering or raising of the Schottky barrier heights which result from the variation in the native defect states of various ZnO nanorod systems Correlating optical events and electrical response through native defects would find scope in assessing figure of merit and sensitivity while making rectifying nanojunctions and single electron devices
 [doi 10 1063/1 3631792]

I. INTRODUCTION

Semiconductor nanostructured systems are regarded as building blocks for their extensive use in display and optoelectronic devices [1 2] In particular, one dimensional (1D) semiconductor nanostructures have gained a vast deal of interest due to their tunable emission property in the visible region of the electromagnetic spectrum [3 4] With the progress and development of advanced tools and techniques, it has been possible to fabricate high-quality 1D semiconductor nanostructures like nanorods, nanowires, nanoneedles, etc with varying aspect ratio [5–7] The quality, large scale processing capability, and cost decide the marketability and commercialization of the synthesized product Although optical properties are well known, the electrical properties are less addressed owing to the technical difficulty in obtaining quality nanoscale contacts

From the technology perspective, among the binary semiconductor materials, zinc oxide (ZnO) has immense application owing to its wide, direct band gap ($E_g = 3\ 37$ eV), and very large exciton binding energy ($E_b = 60$ meV) at room temperature (300 K) The luminescence response over a wide electromagnetic spectrum (UV-visible region) makes it a promising candidate for photonic/optoelectronic devices [7–10] The presence of Zn and O related various native defect states (vacancies, interstitials, antisites, etc) make it more interesting for obtaining selective emission patterns [10–12] As far as the metallic contacts with ZnO system are concerned, the fabrication of quality rectifying contacts (i e , the Schottky diodes) are proven to be vital as Schottky diodes usually exhibit faster switching response and lower turn-on voltages over conventional *p-n* junction diodes [13] The development of rectifying Schottky contacts fabricated using *M*/ZnO (*M* = Au, Ag, Pd, etc) systems have previously been reported by various groups [14 15] Further, the thermal stability of the contacts has been a major concern and it was reported that Ag/ZnO Schottky contacts are more stable over Au/ZnO counterparts [16 17]

The effect of surface and defect states on the transport property of the Schottky diodes of ZnO nanostructures has also been worked out [18–20] Nevertheless, the detailed study of the Schottky diode response of *M*/ZnO nanocontacts for varying native defects is rarely found in the existing literature In this work, we present a comprehensive study of the Schottky nanojunctions using randomly oriented ZnO nanorods, prepared under different annealing environment The variation of the Schottky barrier height and the ideality factor of the Schottky diodes with varying donor and acceptor defects of ZnO have been discussed Further, the correlation between the defects that are associated with optical transitions and the Fermi level positioning which influence the Schottky behavior are highlighted

II. EXPERIMENTAL

(a) Preparation of substrates Commercially available pure Aluminum (Al) substrates of size (~0 5 cm × 0 5 cm × 0 5 mm) were repeatedly washed with double distilled water and finally cleaned with ethanol and acetone in an ultrasonicator bath In order to develop an insulating layer of

[a)]Electronic mail best@tezu ernet in

Al_2O_3, the clean Al substrates were immersed in chromic acid solution for 36 h at room temperature

(b) Preparation of ZnO nanorods The ZnO nanorods were prepared by a rapid thermal annealing process, following our recent work.[21] Zinc acetate dihydrate (ZAD) [$Zn(CH_3COO)_2$, Merck, 99%] was transferred to an aqueous solution of 5wt. % polyvinyl alcohol (PVA) [Loba-Chemie, 99%] under constant stirring (~200 rpm) This was followed by the dropwise addition of aqueous sodium hydroxide (NaOH, 0 6 M stock solution) until the *p*H of the solution is raised to 9.0 The resulting precursor was then spin-casted on the Al-based Al_2O_3 substrates and was subjected to annealing in a constant air flow muffle furnace for 1 h The zone temperature was varied between 450 °C and 750 °C The samples prepared at working temperatures of 450 °C, 550 °C, 650 °C, and 750 °C are assigned as S_1, S_2, S_3, and S_4, respectively

The structural and optical properties of the samples were characterized by scanning electron microscopy (SEM), high resolution transmission electron microscopy (HRTEM), x-ray diffraction (XRD), and photoluminescence (PL) spectroscopy In order to study the electrical properties, the current vs voltage (*I-V*) characteristics were studied at room temperature by using a Keithley 2400 sourcemeter® via two probe method For exploring transport properties, metallic contacts were made (Figure 1) by depositing two thin Ag-layers (~70 nm) on the nanorod-grown Al_2O_3/Al substrates via thermal evaporation process using a vacuum coating unit (10^{-6} mbar) In order to avoid chances of short circuit along the vertical direction, the contacts were made horizontally on the top-surface of the specimens The effective contact area of the specimen under the probe lids was estimated to be ~1.5×10^{-7} m^2 The *I-V* characteristics were plotted for a minimum of three cycles for each of the Schottky junctions and any representative *I-V* curve is the outcome of the statistical average of the recorded cycles

III. RESULTS AND DISCUSSION

The formation of regular ZnO nanorods is confirmed from the SEM micrographs as shown in Figures 2(a) and 2(b) The diameter and length of the nanorods are found to vary between 40–70 nm and 2–3 μm, respectively As the nanorods synthesized at the lowest (S_1) and highest temperatures (S_4) are found to be in un-clustered form, it is expected that the nanorods of the other samples (S_2 and S_3) will also exhibit their independent existence The lattice fringes of the periodically arrayed crystal planes are clearly visible in the HRTEM

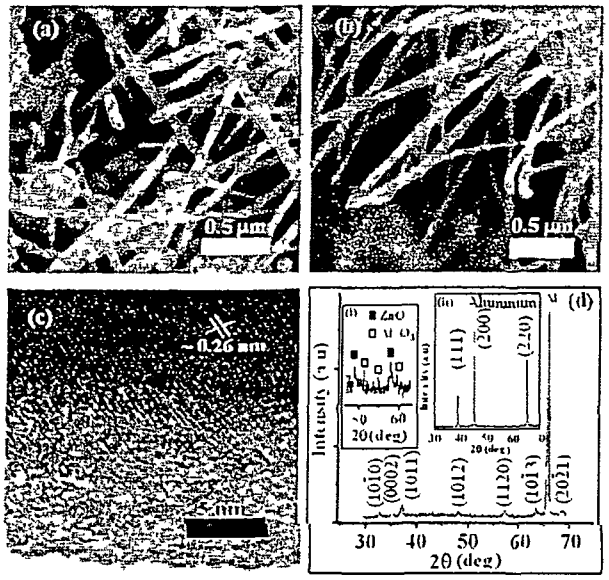

FIG 2 (a) and (b) SEM images of the nanorods of samples S_1 and S_4, (c) HRTEM image of a nanorod of sample S_1, and (d) XRD pattern of the sample S_1, with inset (i) magnified region and (ii) XRD pattern of metallic Al

image of the nanorods (Fig 2(c)) with an inter-planar spacing of 0 26 nm corresponding to (0002) planes of ZnO The XRD pattern of sample S_1 ensure the formation of hexagonal wurtzite phase of ZnO, apart from the existence of a characteristic peak of Al observable at a diffraction angle of 66 1° (Fig 2(d)) Poorly resolved Al_2O_3 peaks can be detected in the magnified diffraction pattern of the ZnO system (inset (i) of Fig 2(d)) [22] The XRD pattern of pure Al is also recorded (inset (ii) of Fig 2(d)) which is characterized by three sharp peaks representing (111), (200), and (220) planes of the face-centered cubic phase of Al unit cell In reference to the XRD pattern of metallic Al, the absence of the (111) and (200) peaks in sample S_1 ensure the development of a thin alumina layer (amorphous Al_2O_3) on the Al-substrate [21,23]

Figure 3 depicts a series of PL spectra obtained at room temperature for individual specimen under study The defects, though sample dependent, are found to be major contributor of the PL emission response The peak positions describing various kinds of zinc and oxygen related defects were discussed in earlier reports [24–26] The spectra of sample S_1 is dominated by the oxygen interstitial (O_i) defects (~535 nm),[12] whereas the luminescence peak (~490 nm), corresponding to the singly ionized oxygen vacancy (V_O^+) Ref 27 is also found Further, poorly resolved peaks arising due to the zinc related defects

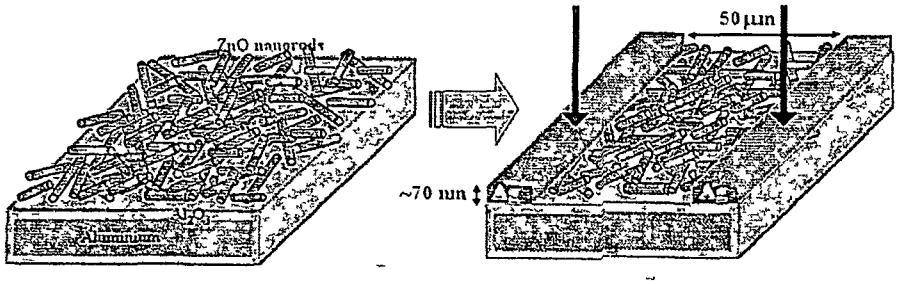

FIG 1 (Color online) Schematic diagram of randomly oriented ZnO nano rods supported by Al_2O_3/Al substrate Probe lids are shown by long vertical arrows

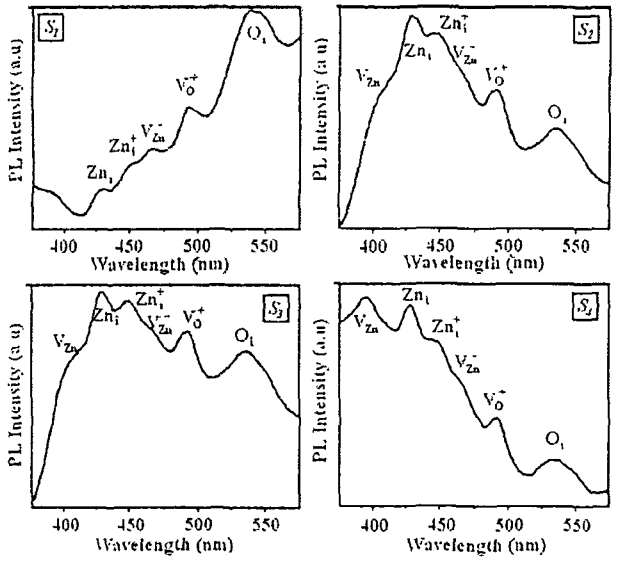

FIG. 3. Room temperature PL emission spectra of different samples corresponding to an excitation wavelength of 325 nm.

like neutral and singly ionized Zn interstitials (Zn_i at ~430 nm and Zn_i^+ at ~450 nm) Refs. 11, 12, 26, and 28 and ionized zinc vacancy (V_{Zn}^- at ~465 nm) Refs. 12 and 25 were also detected. Moreover, in the PL spectra of S_2 and S_3, the emission response due to the Zn interstitials (Zn_i and Zn_i^+), are found to be improved. Compared to S_1, the oxygen vacancy related emission (Zn_i^+ at ~490 nm) is also strengthened, along with the development of the neutral zinc vacancy related emission (V_{Zn}), located at ~400 nm[11,28] and that of the ionized vacancy (V_{Zn}^-) at ~465 nm. Finally, in the spectra of S_4, V_{Zn} related emission intensity gets enhanced and becomes comparable with the Zn_i related emission. Under rapid thermal annealing process, the formation of nanorods takes place via transferring of atoms from smaller particles to larger particles along [0001] direction of ZnO host lattice.[21] Since the atomic radius of oxygen is smaller than zinc, the energy required to transfer oxygen atoms will be lesser than that of zinc atoms. As substantiated in the PL spectra, the nanorods developed at the lowest temperature (450 °C), possess larger number of oxygen interstitial defects. When the working temperature is increased substantially, zinc atoms participate in the transfer process as a result of which zinc interstitial (Zn_i, Zn_i^+) and vacancy (V_{Zn}) related defects are created which strongly take part in the radiative emission process (cases S_2, S_3, and S_4). Since the annealing temperature of sample S_4, is quite larger than the melting point of Al (660 °C), it can be said that the growth of the nanorods (at that temperature) has taken place in a very unstable condition of the substrate. The instability at that temperature can affect the arrangement of Zn and O atoms of the nanorods and consequently, on different defect concentrations. Accordingly, the PL spectrum of this sample differs from that of S_2 and S_3, with a prominence and quenching of V_{Zn} and V_O^+ related defects, respectively.

Figure 4(a) shows the characteristic I-V curve of Ag/ZnO nanojunction made out of the sample S_1. The turn-on voltage of the sample was found to be ~3.2 V under forward bias. The breakdown occurred at ~−9.1 V when the junction was subjected to reverse bias. The nonlinear and rectifying behavior of the curve originates from the Schottky contact formed between randomly distributed ZnO nanorods and metallic Ag. Now, according to the thermionic model the forward diode current can be given by[13,29]

$$I = I_s\left[\exp\left(\frac{qV_a}{\eta kT}\right) - 1\right] \tag{1}$$

where, q is the electronic charge, V_a is the applied voltage, k is the Boltzman constant, and T is the working temperature. The dimensionless quantity, η, is called the ideality factor which determines the strength of the electrical contact for establishing a rectifying junction. The reverse saturation current, I_s, can be written as

$$I_s = AA^*T^2\exp\left(-\frac{q\phi_B}{kT}\right) \tag{2}$$

where, A is the effective area of the metal-semiconductor contact, A^* is the Richardson constant, and φ_B is the Schottky barrier height. For $V > 3kT/q$, the forward diode current can be written as[29]

$$I = I_s\exp\left(\frac{qV_a}{\eta kT}\right) \tag{3}$$

Referring to Schottky junction of S_1 and using the above equation, η and φ_B were estimated as 18.4 and 0.77 eV. Such

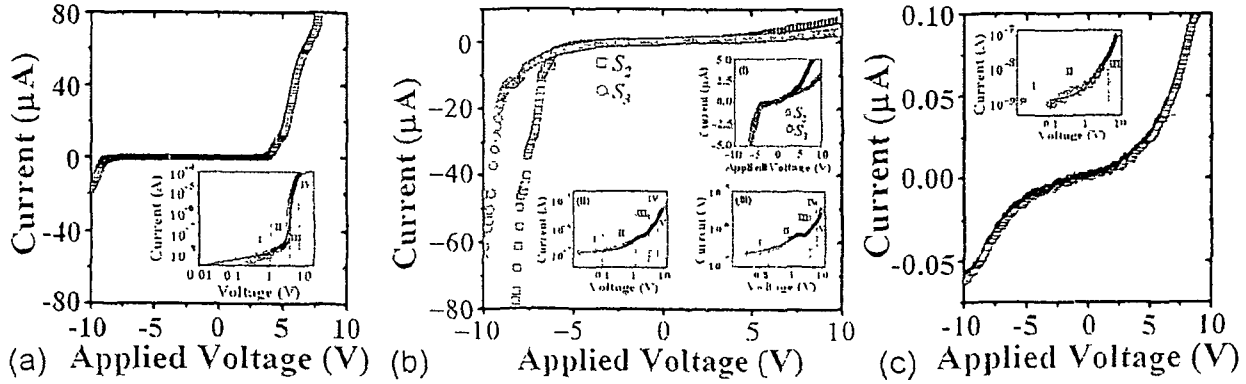

FIG 4. (Color online) Current-Voltage (I-V) characteristic curve of samples (a) S_1, (b) S_2 and S_3, and (c) S_4.

a high value of ideality factor, i e , the non-ideal behavior of the junction can largely be attributed to the atomic scale non-uniformity of the Schottky contacts which have aroused due to the intermediate states/surface states and defects[19] or due to the surface damage during the formation of the Ag layers on the nanorods [30] Previously, Allen and Durbin have ascribed high value of η to the significant electron tunneling owing to the formation of a layer of positively ionized oxygen vacancies with thickness comparable to a few atomic dimension at the interface separating the metal probe and the host ZnO [31] Similarly, the values of η between 20 5 and 38 were observed for Au/ZnO systems and were assigned to the existence of an interfacial insulating layer or the surface states at the junction [32 33] PL spectra, as discussed above, have also ensured the presence of various defect/surface states of zinc and oxygen, within the band-gap of ZnO Consequently, mechanisms such as barrier height reduction, tunneling current, generation, or recombination in the space charge region can be realized [31] All these key factors are mainly responsible for displaying the non-ideal character of the Ag/ZnO nanorod based Schottky contacts under investigation and thus, giving rise to a high value of η as 18 4 for S_1 The typical log-log I-V characteristics of the Schottky junction made out of S_1 is presented in the inset of Figure 4(a) Essentially, it depicts four independent regions highlighting the nature of carrier transport for different voltage regime of forward biasing The current response in the region I ($V < 1$ 2 V) is found to vary linearly with the bias voltage as per the conventional Ohms law ($I \propto V$) Thus, the tunneling assisted current transport mechanism is favored within the regime I The region II (1 2 V $< V <$ 4 6 V) shows an exponential growth of the current with the applied voltage following a relation $I \propto \exp(\alpha V)$, α being a constant which depends on the system under investigation The ideality factor of the sample was calculated within this region and the carrier transport is assigned to the recombination tunneling mechanism where the electron would experience a series of tunneling via local recombination sites [33–36] In the present context, the recombination centers are provided by the various native defects of ZnO thus facilitating recombination assisted tunneling conduction mechanism The region III (4 6 V $< V <$ 6 2 V) is characterized by a steep exponential growth of the current with biasing voltage and is also attributed to the multiple recombination tunneling events Finally, beyond 6 2 V (Region IV), the current follows a power law ($I \propto V^2$), which is recognized as the contribution owing to the space charge limited current (SCLC) conduction [35,36]

On the other hand, nanojunctions formed in the sample S_2 and S_3, show very large current flow under reverse bias (Fig 4b) Though the rectifying nature can be observed for both the samples (inset (i) of Fig 4b), the current under reverse bias is dominant The samples S_2 and S_3, were characterized by very high values of η, i e , 35 4 and 33 2, and φ_B of 0 64 and 0 63 eV, respectively Compared to S_3, the sample S_2 is governed by higher currents beyond a given bias voltage both in forward and reverse modes The log-log I-V characteristics of S_2 (inset (ii) of Fig 4(b)), exhibited five different distinguishable regions The current transport of region I ($V < 0$ 1 V) is dominated by tunneling current, whereas the transport property of region II (0 1 V $< V <$ 1.3 V), III (1 3 V $< V <$ 4 3 V), and IV (4 3 V $< V <$ 6 4 V) are dominated by the recombination tunneling mechanism to different extents Beyond $V >$ 6 4 V (region V), the transport process is governed by the SCLC mechanism Similarly, five independent regions, corresponding to different voltage ranges, are also observed in the log-log I-V plot of the Ag/ZnO nanorod based Schottky junction of S_3, shown in the inset (iii) of Fig 4(b) In contrast, as depicted in Figure 4(c), the junction obtained from the sample S_4, has a good rectifying response that exhibited very less leakage current in the reverse biasing mode The log-log I-V characteristics of S_4 (inset of Fig 4(c)) signifies the tunneling current in the region I ($V < 0$ 1 V), whereas the current transport through the recombination tunneling process is dominant within region II (0 1 V $< V <$ 2 3 V) Finally, the SCLC conduction becomes predominant over other mechanisms for biasing voltage beyond 2 3 V (region III) The η was calculated to be 12 2, while, φ_B assumed a value of 0 78 eV The values of η and φ_B for the four different samples are shown in Table I The large variation in the values of the ideality factors and barrier heights (φ_B) in the samples can be correlated to the image force barrier lowering (IFBL) effect, tunneling current etc The IFBL effect arises due to the potential associated with the image charges (contributed by the donor defects) which build up in the metal component of a Schottky junction as carriers approach the metal-semiconductor interface [13] Conversely, tunneling current occurs due to the variation of prime defects that exist even at the interface separating Ag layer and surfaces of the ZnO nanorod system

PL is associated with the carrier recombination emission whereas nature of carrier transport in an electrical junction is decided by how efficiently a physical contact is made In particular, if carriers are from impurity or defect related states then one can interrelate optical and electronic events simultaneously It has been established that in ZnO system, V_O^+ and Zn_i are donors, whereas V_{Zn}, O_i, and O_{Zn} act as acceptors [11] It is likely that the presence of these donors and acceptors in different concentration would change the Fermi level position within the bandgap [11] The variation of η and φ_B of the four different samples is shown in Figure 5(a) The ideality factor decreases with the increase in barrier height and vice-versa, which is in agreement with the earlier reports [15,19] Now, the variation of φ_B with the ratio of acceptor defect to donor defect, i e , zinc vacancy to interstitial (V_{Zn}/Zn_i) and oxygen interstitial to vacancy (O_i/V_O^+) of the four samples, is demonstrated in the Figure 5(b) It can

TABLE I Different physical parameters of the four samples synthesized under different annealing environment

Sample	Schottky barrier height (ϕ_B) in eV	Ideality factor (η)	Ratio of Zn vacancy to interstitial (V_{Zn}/Zn_i)	Ratio of O-interstitial to vacancy (O_i/V_O^+)
S_1	0 77	18 4	0 97	1 33
S_2	0 64	35 4	0 78	0 90
S_3	0 63	33 2	0 74	0 81
S_4	0 78	12 2	1 03	0 80

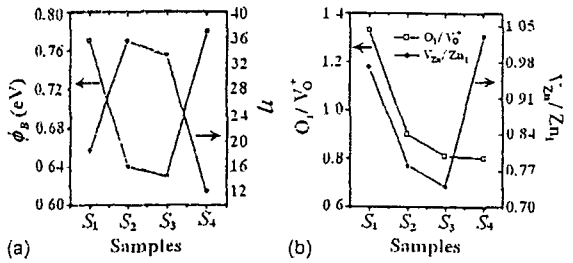

FIG. 5. (a) Comparison of ideality factor and Schottky barrier height and (b) variation of acceptor- to- donor defect contributions of different samples.

be observed that the O_i/V_O^+ ratio is significantly higher in S_1 which is due to the dominance of O_i defects over the other defects. The sample possesses a moderate Schottky barrier height and hence shows a typical *I-V* curve of a Schottky diode with less leakage current, whereas in S_2 and S_3, the large reverse current is found owing to the large electron flow from the metal to semiconductor under reverse bias. It has been observed in the PL spectra (Fig. 3) that Zn_i related defect emission get improved in these two samples and hence V_{Zn}/Zn_i ratio is lower in this case (Fig 5(b)). Now, the presence of Zn_i-donors will increase the *n*-type conductivity of the ZnO samples[20] and hence the Fermi level position in these samples will be closer to the conduction band compared to S_1. This implies that the Fermi level of S_2 and S_3 will lie just below the conduction band (depicted in Figure 6 (b)i) and hence the depletion region of the metal-semiconductor contact will be narrow in these two samples. As a result, under reverse bias when the semiconductor Fermi level gets below the equilibrium position, the electrons experience a no barrier situation and thus tunnel from metal to semiconductor in large quantity (Figure 6 (b)ii). Accordingly, a very high reverse current is predicted in S_2 and S_3. Again, the free electrons donated by the V_O^+ and Zn_i defect states increase the surface charge density, resulting in high IFBL effect.[15] Apparently, there is a reduction in the effective Schottky barrier height (0.64 and 0.63 eV for S_2 and S_3, respectively), along with the decrease in the barrier width, which defines the quality of an abrupt junction. Therefore, the large tunneling current in the reverse bias region of S_2 and S_3, is a consequence of the decrease in the barrier width owing to the Fermi level re-adjustment and large IFBL effect on account of the creation of many Zn_i-donor states.

As can be observed in Fig 5(b), the ratio of the acceptor-to-donor defect concentration (for O_i/V_O^+ as well as V_{Zn}/Zn_i) has a decreasing trend while moving from sample S_1 to S_3. Interestingly, though the O_i/V_O^+ ratio of S_4 follows the same tendency, the V_{Zn}/Zn_i ratio exhibits a reverse trend. Compared to S_2 and S_3, the V_{Zn}/Zn_i ratio of S_4 is found to be larger owing to the prominence of V_{Zn} related emission in S_4. Since the V_{Zn} defects are considered to be the compensating acceptors,[37] the dominance of the V_{Zn}-acceptors in S_4 will result in the lowering of *n*-type conductivity of the sample compared to S_2 and S_3. Hence, the Fermi level position of the nanorods of S_4 will be lower than the case of nanorods for S_2 and S_3 specimens. Also, the evolution of more V_{Zn} compensating acceptors will result in the decrease in surface charge density leading to a weak IFBL effect and that is why φ_B for the Ag/ZnO nanojunction of S_4 (0.78 eV) would be higher than S_2 and S_3 (Table I) Consequently, there is an adequate enhancement in the barrier

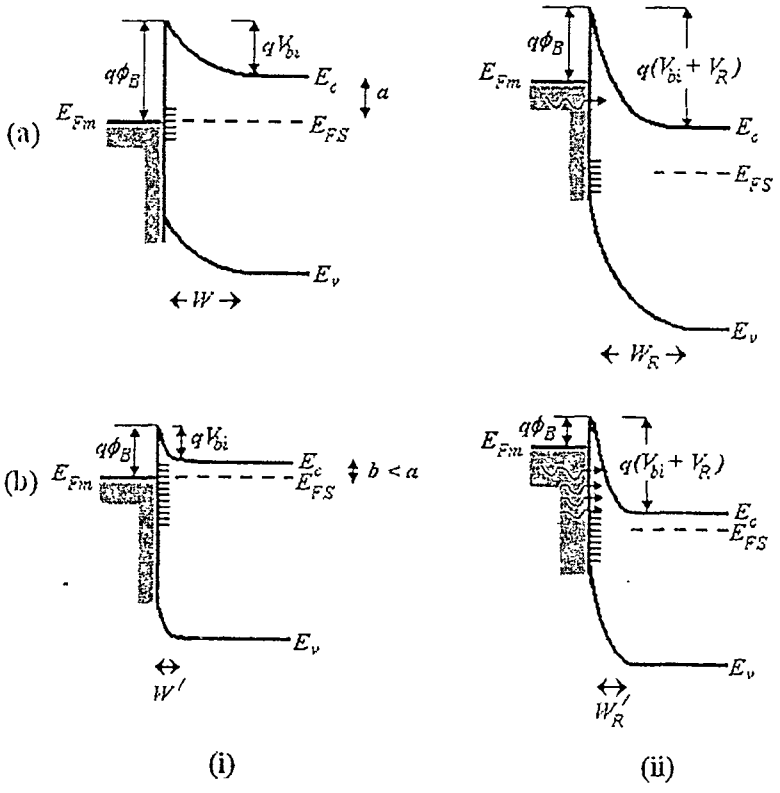

FIG. 6. Energy band diagram of the metal semiconductor junction formed by different ZnO nanorod samples (a) S_1, (b) S_2 and S_3; for (i) equilibrium and (ii) reverse biasing cases.

width of the Ag/ZnO nanojunction (using sample S_4), and hence, under a reverse bias, the free tunneling of electron is substantially hindered which has resulted in a small amount of leakage current

Therefore, the defects which are responsible for optical emission also control the electronic transport in a rectifying junction. The departure from the ideal Schottky behavior is found to be governed by the presence of defects at the interface of the nanojunctions In contrast to the Schottky junction of S_1, the recombination mediated tunneling is found to be initiated at a comparatively lower voltage for S_2, S_3 rectifying junction cases where the ideality factors were also found to be substantially high

IV. CONCLUSIONS

Randomly oriented ZnO nanorods were fabricated on Al_2O_3/Al substrates via a rapid thermal annealing process Then the Schottky behavior of the Ag/ZnO nanorod based junctions was studied. The current transport property of the Ag/ZnO nanojunction was found to be dependent on the nature of defects as predicted in the PL spectra The Ag/ZnO nanojunction has exhibited rectifying nature with very high ideality factor owing to participation of various native defect states of ZnO For the nanorods grown at 550 °C and 650 °C, it was observed that the current under reverse bias was larger than the current under forward bias The large reverse current is attributed to the large electron tunneling from the metal to the semiconductor side and because the Fermi level position in these ZnO systems is significantly affected by Zn_i-donor defect states Further, due to the significant contribution from V_O^{++} and Zn_i-donors, the IFBL effect becomes considerably high in these two systems (S_2, S_3), and therefore, effective barrier height as well as barrier width get suppressed On the other hand, the nanorods grown at 450 °C and 750 °C possess relatively higher barrier height owing to the enhanced contribution from the respective O_i and V_{Zn} acceptor states and as a result the leakage current is suppressed substantially The interplay of defects in optical emission and rectifying patterns would help in meeting challenges while fabricating miniaturized devices that require interlinking of optical and electronic circuits

ACKNOWLEDGMENTS

The authors thank IUAC, New Delhi, for sponsoring the project under Project No UFUP-44314/2008 The assistance of Mr U Das in performing the electrical measurements is also gratefully acknowledged

[1]M D Frogley, J F Dynes, M Beck, J Faist, and C C Phillips, Nature Mater 5, 175 (2006)
[2]R Held, T Vancura, T Heinzel, K Ensslin, M Holland, and W Wegscheider, Appl Phys Lett, 73, 262 (1998)
[3]M J Zheng, L D Zhang, G H Li, X Y Zhang, and X F Wang, Appl Phys Lett 79, 839 (2001)
[4]X Huang, J Li, Y Zhang, and A Mascarenhas, J Am Chem Soc 125, 7049 (2003)
[5]S K Pradhan, P J Reucroft, F Yang, and A Dozier, J Cryst Growth 256, 83 (2003)
[6]A Urbieta, P Fernández, and J Piqueras, Appl Phys Lett 85, 5968 (2004)
[7]M Willander, O Nur, N Bano and K Sultana, New J Phys 11, 125020 (2009)
[8]A van Dijken, E A Meulenkamp, D Vanmaekelbergh, and A Meijerink, J Lumin 87–89, 454 (2000)
[9]R Hauschild, H Lange, H Priller, C Klingshirn, R Kling, A Waag, H J Fan, M Zacharias, and H Kalt, Phys Status Solidi B 243, 853 (2006)
[10]Z G Wang, X T Zu, S Zhu, and L M Wang, Physica E (Amsterdam) 35, 199 (2006)
[11]B Lin, Z Fu, and Y Jia, Appl Phys. Lett 79, 943 (2001)
[12]S A M Lima, F A Sigoli, Jr M Jafelicci, and M R Davolos, Int J Inorg Mater 3, 749 (2001)
[13]S M Sze and K K Ng, *Physics of Semiconductor Devices*, 3rd ed (Wiley, New York, 2007)
[14]M W Allen, M M Alkaisi, and S M Durbin, Appl Phys Lett 89, 103520 (2006)
[15]S Lee, Y Lee, D Y Kim, and T W Kang, Appl Phys Lett 96, 142102 (2010)
[16]H Kim, H Kim, and D -W Kim, J Appl Phys 108, 074514 (2010)
[17]J C Simpson and F Cordaro, J Appl Phys 63, 1781 (1988)
[18]K Cheng, G Cheng, S Wang, L Li, S Dai, X Zhang, B Zou, and Z Du, New J Phys 9, 214 (2007)
[19]S N Das, J -H Choi, J P Kar, K J Moon, T Il Lee, and J M Myoung, Appl Phys Lett 96, 092111 (2010)
[20]H L Mosbacker, S El Hage, M Gonzalez, S A Ringel, M Hetzer, D C Look, G Cantwell, J Zhang, J J Song, and L J Brillson, J Vac Sci Technol B 25, 1405 (2007)
[21]S Bayan and D Mohanta, J Appl Phys 108, 023512 (2010)
[22]S Das A K Mukhopadhyay, S Datta, and D Basu, J Mater Sci Lett 22, 1635 (2003)
[23]A O Araoyinbo, M N A Fauzi, S Sreekantan, and A Aziz, Sains Malaysiana 38, 521 (2009)
[24]T Moe Børseth, B G Svensson, A Yu Kuznetsov P Klason, Q X Zhao, and M Willander, Appl Phys Lett 89, 262112 (2006)
[25]K H Tam, C K Cheung, Y H Leung, A B Djurišić, C C Ling, C D Beling, S Fung, W M Kwok, W K Chan, D L Phillips, L Ding, and W K Ge, J Phys Chem B 110 20865 (2006)
[26]L -L Zhang C -X Guo, J -G Chen, and J -T Hu Chin Phys 14, 586 (2005)
[27]J D Ye, S L Gu F Qin, S M Zhu, S M Liu, X Zhou, W Liu, L Q Hu, R Zhang, Y Shi, and Y D Zheng, Appl Phys A Mater Sci Process 81, 759 (2005)
[28]H Zeng, S Yang, X Xu, and W Cai, Appl Phys Lett 95, 191904 (2009)
[29]S K Cheung and N W Cheung, Appl Phys Lett. 49, 85 (1986)
[30]A Motayed, A V Davydov, M D Vaudin, and I Levin, J Appl Phys 100, 024306 (2006)
[31]M W Allen and S M Durbin, Appl Phys Lett 92, 122110 (2008)
[32]O Harnack C Pacholski, H Weller A Yasuda, and J M Wessels Nano Lett 3, 1097 (2003)
[33]P Klason O Nur and M Willander Nanotechnology 19 475202 (2008)
[34]A Bindal, R Wachnik, and W Ma, J Appl Phys 68, 6259 (1990)
[35]R Ghosh and D Basak, Appl Phys Lett 90, 243106 (2007)
[36]S Kishwar, K ul Hasan, N H Alvi, P Klason, O Nur, and M Willander, Superlattices Microstruct 49, 32 (2011)
[37]D C Look, C Coskun, B Claflin, and G C Farlow, Physica B 340–342, 32 (2003)

Eur. Phys. J. D 61, 463–468 (2011)
DOI: 10.1140/epjd/e2010-10457-7

THE EUROPEAN PHYSICAL JOURNAL D

Regular Article

Peacock feather supported self assembled ZnO nanostructures for tuning photonic properties

S. Bayan, U. Das, and D. Mohanta[a]

Nanoscience Laboratory, Department of Physics, Tezpur University, PO Napaam, 784028 Asam, India

Received 27 August 2010 / Received in final form 12 October 2010
Published online 3rd December 2010 – © EDP Sciences, Società Italiana di Fisica, Springer-Verlag 2010

Abstract. Barbules of the peacock feather have been used as the natural template for developing assemblies of zinc oxide (ZnO) nanospheres. The different colored barbules consisting of various photonic crystals (extracted from eye-pattern) were characterized in terms of the stop-bands identified in the respective Reflectance spectra. The stop-bands of the photonic crystals are found to get red-shifted after the loading of ZnO nanospheres and was reasoned to the modification of photonic band gap. The ZnO nanosphere decorated barbules show well defined photoluminescence response with dominant defect related emission of ZnO. The artificially grown inorganic structures on natural templates form a basis of new hybrid system that can help in exploiting photonic band gap engineering and light wave modulation with high selectivity.

1 Introduction

In recent years, with the significant advancement in the fabrication and processing methods, research interest has geared up in the field of photonics and optoelectronics. The photonic crystals and photonic band gap materials are attractive for precise modulation and propagation of electromagnetic waves [1,2]. A photonic crystal is a periodic dielectric structure (made of two different materials) in which em-waves are forbidden irrespective of their propagation directions and exhibits a photonic band gap (PBG). A PBG (or, stop-band) is the characteristic of a periodically arranged material-air gap alternate structure and is analogous to the electronic energy band gap (EBG) in semiconductors. Natural systems (e.g. *Ophiocoma wendtii*, *Morpho rhetenor* butterflies, peacock feather etc.) also possess remarkable photonic structures, better than artificially fabricated photonic crystals [3]. The central region of a male peacock feather generally appears blue. As one moves away from the core, one observes cyan, brown and green colors spreading in outward directions with spacings depending on the level of maturity and origin of feathers. Whatever the case may be, the chemical constituents which make up the barbules are same but their typical organization and orientation give rise to a series of diverse colors.

The peacock feather actually contains a 2D photonic-crystal structure composed of melanin rods connected by keratin in the cortex of differently colored barbules [4]. It was found that the variation in the lattice constant (rod spacing) and the number of periods (melanin rod stacks) along the direction normal to the cortex surface is mainly responsible for the typical appearance of a particular color [4]. On the other hand, it has been established that the infiltration or embedment of luminescent materials in the photonic crystals would lead to the inhibition of spontaneous emission, which is useful for solid-state lasers that require low threshold currents but high gains [5,6].

Zinc oxide (ZnO), a wide-direct band gap (E_g = 3.37 eV at 300 K) and high exciton binding energy (E_b = 60 meV) system, exhibits intense light emission features in the UV to visible range of the electromagnetic spectrum [7–9]. ZnO has always been a topic of significant interest for understanding various defect related emissions caused by zinc or oxygen vacancies or/and presence of anti-sites. There are also reports on the modification of the photonic band gap and the emission pattern of ZnO infiltrated photonic crystals [10,11]. Earlier, ZnO nanoparticles have been incorporated into the peacock feathers [12], but hardly there was any discussion on the aspect of photonic band gap engineering. In this work, a matured peacock feather (Indian Peafowl, *Pavo Cristatus*) collected from the Manas National Park, Assam (India), has been used as the base for synthesizing plentiful sub-micron size hexagonal ZnO nanospheres. The report also highlights on the tuning of photonic band gap of the inherent photonic crystals present in the peacock feather after ZnO embedment. A model is also encountered to correlate the experimental results with the theoretical predictions.

2 Experimental details

The ZnO decorated peacock feather was processed using a user-friendly physico-chemical reaction similar to the previous work [12]. 0.005 M zinc acetate dihydrate

[a] e-mail: best@tezu.ernet.in

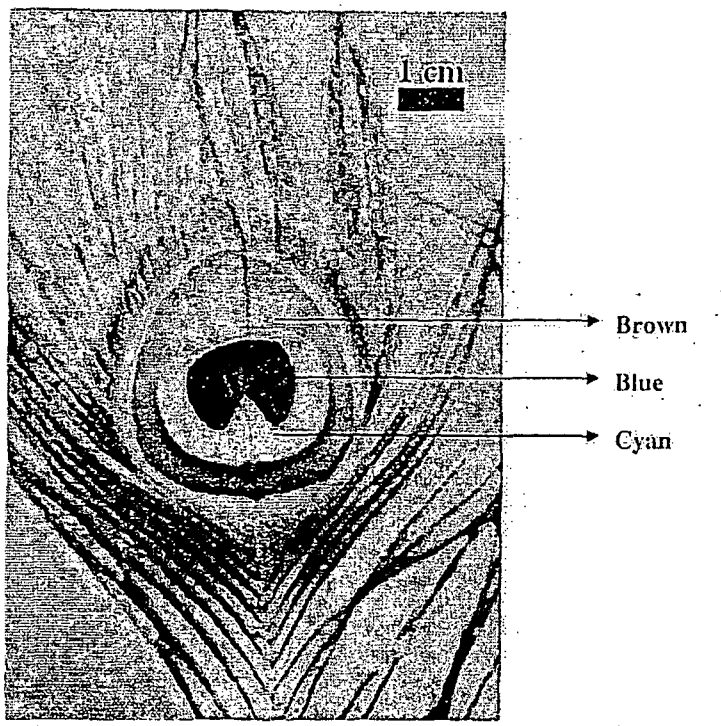

Fig. 1. (Color online) Optical image of the male peacock feather system used in the experiment.

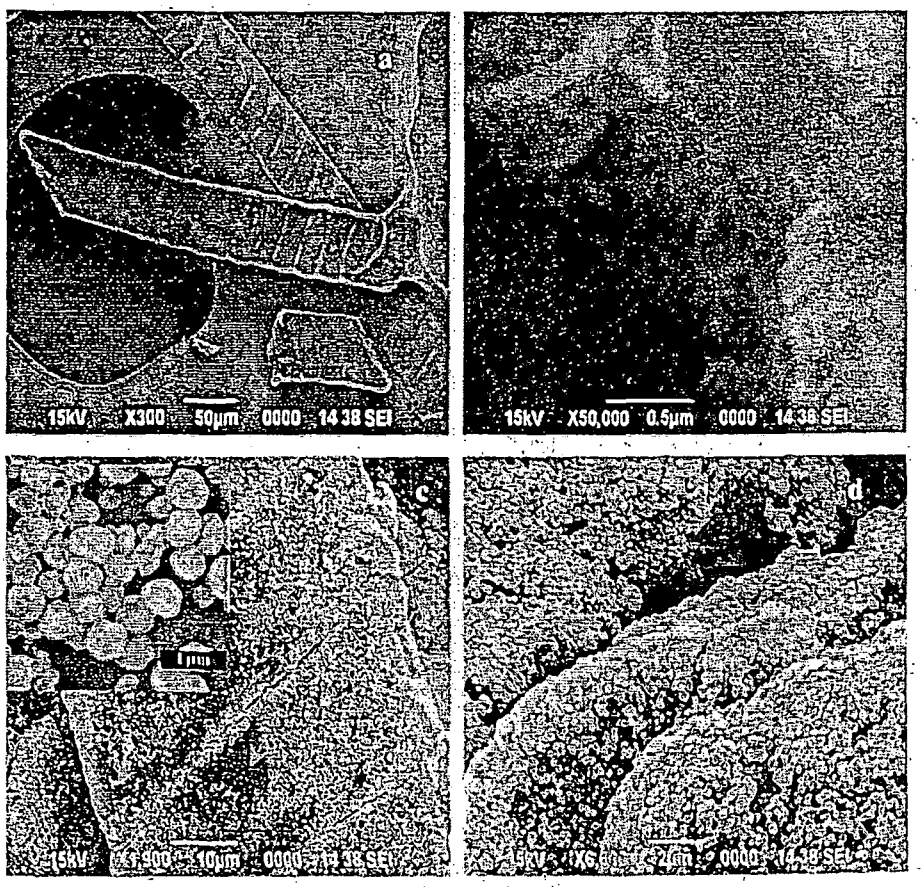

Fig. 2. (Color online) Scanning electron micrograph of blue barbules (a, b) before and (c, d) after developing ZnO nanospheres (inset in (c) depicts the hexagonal nanostructures at higher magnification).

($Zn(CH_3COO)_2$, Merck, 99.5%) and the peacock feather were put into 20 mL ethanol under continuous stirring at a moderate speed (~200 rpm) for 1/2 h. Then, 0.1 M aqueous sodium hydroxide (NaOH) in 5 mL ethanol was injected dropwise to the solution and stirred for another 1/2 h at a constant temperature of 70 °C. The resulting precursor was then placed in an ultrasonicator bath for 15–20 min to avoid abrupt coalescence of the as-grown structures. The carboxyl groups (COO^-) of aspartic ($HOOC\text{-}CH_2\text{-}CH(NH_2)\text{-}COOH$) and glutamic acid ($H_2N\text{-}CO\text{-}(CH_2)_2\text{-}CH(NH_2)\text{-}COOH$) residues in keratin provide the sites for the Zn^{2+} cations [12] and $Zn(OH)_2$ is produced after introducing NaOH in the system. Finally, upon control annealing (~80 °C) the product in air for 1/2 h, submicron ZnO structures were developed on the keratin layer of the barbules. Thus the barbules of the peacock feather can act as a natural template for self organized nanostructures.

The structural morphology of the resulting systems was characterized by scanning electron microscopy (SEM). The photonic band gap engineering aspects due to ZnO infiltration were studied by reflection and emission spectroscopy.

3 Results and discussion

As shown in the optical image (Fig. 1), the peacock tail feather has a central stem with an array of barbs on each side with barbules on each side of the barb. It can be observed that in the eye pattern, the barbules mainly appear in brown, cyan and blue. From the back side, the colors in the eye feather can not be seen as the stack of barbules emerged from the respective barbs directed upward in a precise manner.

Figure 2a shows the electron micrograph of the blue barbules of the eye pattern derived from the feather. The presence of the melanin rods along with the air gaps can be seen in the next micrograph (Fig. 2b). As evident from the SEM images, the barbules have a smooth surface before the infiltration of ZnO nanostructures. The homogeneous growth of hexagonal ZnO nanostructures is clearly visible on the surface of the barbules and can be observed in Figures 2c, 2d. It is possible that during ultrasonication process, some of the nanostructures have detached from the surface of the barbules and hence, a few parts of the barbules are left uncovered (as indicated by red arrows). Figure 2d gives a magnified side look of the nanostructures formed on 2–3 different barbules. The ZnO nanostructures are found to be close to uniform in size and hexagonal shape (inset Fig. 2c) with an average diameter varying within 250–270 nm.

Figure 3A shows the reflectance spectra of the blue barbules before and after ZnO embedment. The reflectance spectra of the blue barbules prior the development of ZnO, shows a prominent peak at ~470 nm (Fig. 3A(a)), indicating the presence of a photonic band gap (PBG). The reflectance peak in the blue region confirms the blue coloration of the barbules under visible

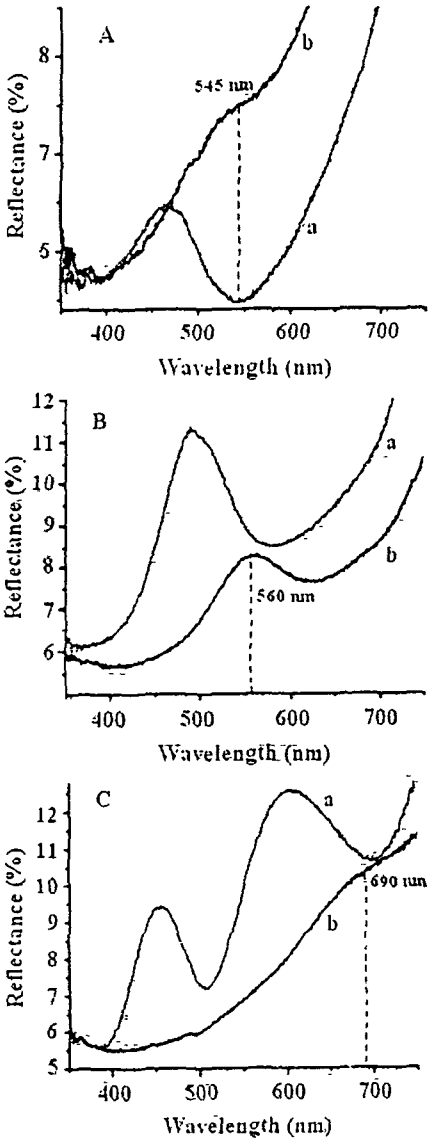

Fig. 3. (Color online) Reflectance spectra of (A) blue barbules, (B) cyan barbules, and (C) brown barbules with (a) before embedding, and (b) after ZnO loading.

light. Further, the effect of loading of ZnO nanostructures is clearly visible in the other reflectance spectrum as the peak becomes broad and red-shifted to ~545 nm (Fig. 3A(b)). The deposition of the ZnO nanospheres (of size of the order of visible wavelength) results in an appreciable change of the effective refractive index of the system and hence a modification in the PBG is expected. The reflectance peak after ZnO embedment is not sharp, which can be attributed to the non-uniform covering of the ZnO nanostructures. For instance, in some parts of the barbules, there could be some unoccupied empty space where no ZnO nanostructures exist or in some areas there might be overlapping stacks of ZnO arranged. Such uneven deposition of ZnO has considerably affected the symmetry of the reflectance peak.

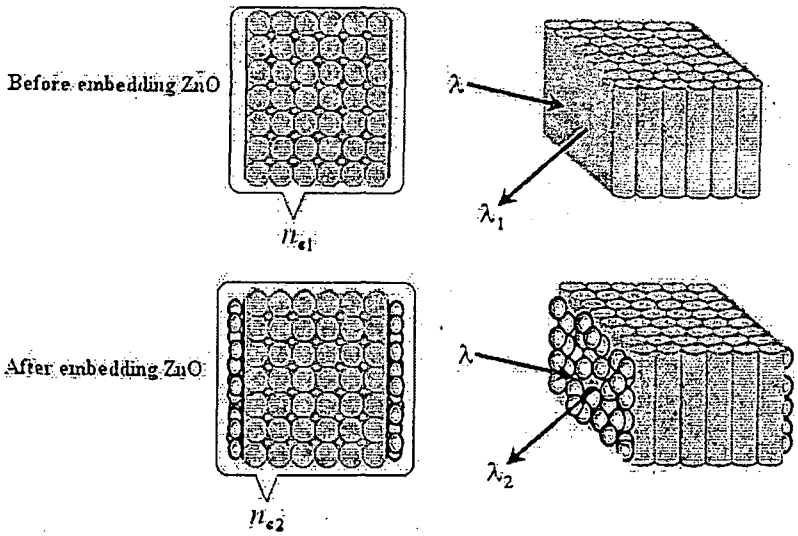

Fig. 4. (Color online) Schematic diagram depicting ZnO loading on the barbules and corresponding reflectance response.

The change in refractive index of the ZnO nanospheres attached to the surface of the blue barbules can be estimated using the fundamental equation $\lambda = 2Dn_e$ [11]. Here D is the lattice constant of the photonic crystals, and n_e as the effective refractive index of the system. If λ_1, λ_2 represent the wavelength maxima corresponding to the reflection, and n_{e1}, n_{e2} be the effective refractive indices before and after embedding ZnO on the barbules, then we can write,

$$n_{e2} = \frac{\lambda_2}{\lambda_1} n_{e1}. \quad (1)$$

As the internal structure of the melanin rods remained unaffected, D remains same before and after ZnO loading.

Now, the effective refractive index of the system before embedding ZnO, can be expressed as $n_{e1} = \sum_{i=1}^{3} f_i n_i$. Here n_1, n_2, n_3 are the refractive indices and f_1, f_2, f_3 are filling factors of the melanin-rods, air gaps and the keratin layer respectively, with the condition satisfying $f_1 + f_2 + f_3 = 1$ [13]. Then, we express

$$n_{e1} = n_3 - f_1(n_3 - n_1) - f_2(n_3 - n_2). \quad (2)$$

For calculating the filling factor, we take $f = \pi(r/D)^2$ where the structural parameters are taken as $r_{rod} = 60$ nm, $r_{air} = 37.5$ nm, with n_1, n_2, and n_3 being 1.54, 1, and 2 respectively and D as 140 nm for the blue barbules [4]. Hence, the effective refractive indices before and after ZnO infiltration i.e., n_{e1}, and n_{e2} are found to be 1.68 and 1.95. In order to justify that the ZnO assemblies are mainly responsible for the observed red-shift, the reflectance spectra of the cyan barbules were also studied with and without ZnO embedment (Fig. 3B). The reflectance spectrum of the ZnO embedded cyan barbules is also found to be red-shifted ($\Delta\lambda = 70$ nm) in a similar way to that of blue barbules (Tab. 1) and the effective refractive index of the system becomes ~1.91. In contrast, as far as melanin rod arrangement is concerned, the brown barbules are characterized by variable dimensions. It measures 150 and 185 nm along the directions parallel and perpendicular to the cortex surface thus exhibiting a rectangular lattice [4]. The effective refractive index of the brown barbules before embedding ZnO was 1.64. In the reflectance spectra (Fig. 3C(a)), along with characteristic peak of the brown barbules at ~600 nm, an extra peak was observed in the blue region (~450 nm) of the wavelength which is the result of the Fabry-Perot interference between the two surfaces of the photonic material [4]. On embedding the brown barbules with ZnO, the effective refractive index becomes 1.89 and the reflectance spectra also experiences a notable red-shift of $\Delta\lambda = 90$ nm w.r.t. the aforesaid 600 nm peak. The reflectance peak located in the blue region is now suppressed owing to covering of the barbules with ZnO nanospheres as a result of which Fabry-Perot interference principle is no longer valid.

Essentially, different colored barbules loaded with ZnO nanospheres results in the modification of the respective reflectance spectrum and hence stop-bands (of PBG) of the photonic crystals present in the barbules. Further, the ZnO nanospheres of the given size will be be responsible for efficient light scattering with light path length of the order of the thickness of the surface layer formed by the ZnO nanospheres. Thus controlled scattering events can be an alternative interpretation to the observed shift. A schematic diagram which illustrates the mechanism of changing reflectance spectra is shown in Figure 4. To clarify further, we must note that electron transport is regulated by the electronic energy gap that arises due to periodic potentials of the constituent atoms that make up the solid. In a similar way, photons with definite energy would experience a stop-band while propagating in the medium. In case of a peacock feather, the stop-bands arise because of the typical structural arrangement of the melanin rods, air gaps and keratin layers. But if ZnO is infiltrated in the air gaps then there is a chance of overlapping of EBG of ZnO and PBG of barbules, as a result

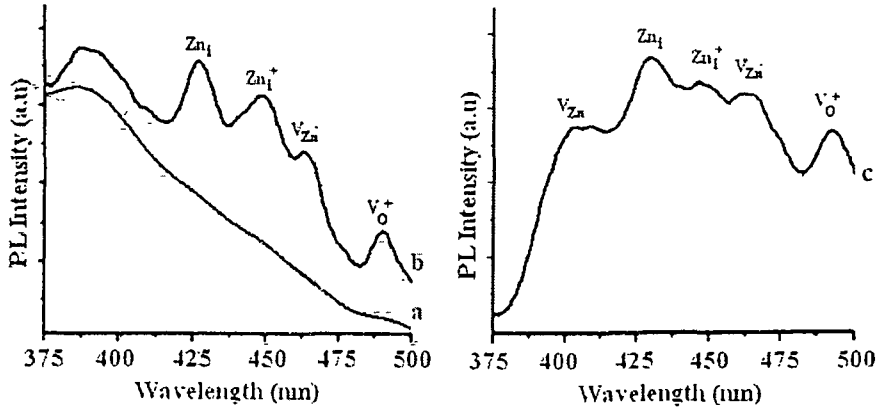

Fig. 5. (Color online) Room temperature photoluminescence spectra (λ_{ex} = 325 nm) of the blue barbules: (a) before, (b) after nanoscale ZnO embedment and that of (c) separately grown bare ZnO system.

Table 1. Physical parameters of the barbules.

Barbules	Lattice constant D (nm)	Before embedding ZnO		After embedding ZnO	
		Reflectance peak centre (nm)	Refractive index (n_{e1})	Reflectance peak centre (nm)	Refractive index (n_{e2})
Blue	140	470	1.68	545	1.95
Cyan	145	490	1.67	560	1.91
Brown	$D_{\parallel} \sim 150$, $D_{\perp} \sim 185$	450, 600	1.64	690	1.89

there will be substantial changes in the PL spectra of the peacock feather system (either band edge or defect related emission is suppressed depending on the range of PBG). In our case, ZnO intrusion into the air gaps was very unlikely as ZnO spheres are of larger dimension. Nevertheless, the effective refractive index would change as a result of ZnO loading.

Figures 5a, 5b show the room temperature photoluminescence spectra (λ_{ex} = 325 nm) of the blue barbules before and after ZnO loading. The barbules before infiltration of ZnO nanostructures show emission spectrum having a maximum in the ultra-violet region (~388 nm) (Fig. 5a). The effect of loading ZnO nanospheres can be clearly observed by the characteristic defect emissions as evident in the PL spectra shown in Figure 5b. Along with the emission response associated to the barbules peaking at ~388 nm, several other peaks are also observed which can be correlated with the defect related emission of ZnO. The peaks at ~426 nm and 449 nm arise due to the emissions via zinc interstitial related defects (Zn_i, Zn_i^+); respectively [14,15]. Further, the emission peaks at ~463 nm and 490 nm correspond to the zinc vacancy states (V_{Zn}^-) and oxygen vacancy states (V_O^+) [15,16]. To confirm the luminescence pattern, PL spectra of bare ZnO system (synthesized using the same protocol but without feathers), was also studied at the same excitation wavelength. (Fig. 5c). For the bare ZnO system, the peak at ~405 nm corresponds to the zinc vacancy states (V_{Zn}) [14], which was not found in the ZnO embedded feather system owing to the superimposition with the emission peak of the barbules (at ~388 nm). The band edge emissions in both the cases were not observed because of the presence of large number of defect states of ZnO. The alike PL spectra of bare ZnO and ZnO embedded feather system suggest that the defect related emission response of ZnO is not quenched by the photonic crystals composed of melanin rods and connected by keratin layers. It is now clear that the ZnO nanostructures are situated on the surface of the barbules having their independent existence and hence, the incorporation of ZnO nanostructures within the photonic crystals is less probable. In such a situation, the overlapping of the PBG of the photonic crystals and the electronic band gap of the defect states of ZnO nanostructures is not applicable. Decorating the surface of the natural feathers with nanoparticles without destroying the internal structure of the feathers would help in altering photonic band gap with high selectivity.

4 Conclusion

The self assembled ZnO nanostructures have been synthesized using a natural peacock feather as the supporting template and the PBG of the photonic crystals of the feather is shown to be altered, as evident from the reflectance spectra. To be specific, the change in the effective refractive index of the system after ZnO loading was accounted for the PBG modification of the different colored barbules. The similarity in the emission response, arising from different kinds of the defect states in bare ZnO as well as ZnO decorated peacock feather system was witnessed. The tunability of the PBG and emission in the

visible region from such artificially decorated natural hybrid systems can be potential candidates for nanoscopy, nanophotonics and other such optoelectronic devices.

We sincerely thank IUAC, New Delhi, for sponsoring the project UFUP-44314/2008.

References

1. S. Noda, A. Chutinan, M. Imada, Nature **407**, 608 (2000)
2. E. Yablonovitch, J. Opt. Soc. Am. B **10**, 283 (1993)
3. P. Vukusic, J.R. Sambles, Nature **424**, 852 (2003)
4. J. Zi, X. Yu, Y. Li, X. Hu, C. Xu, X. Wang, X. Liu, R. Fu, Proc. Natl. Acad. Sci. USA **100**, 12576 (2003)
5. S.G. Romanov, A.V. Fokin, R.M. De La Rue, Appl. Phys. Lett. **74**, 1821 (1999)
6. A. Blanco, C. López, R. Mayoral, H. Míguez, F. Meseguer, A. Mifsud, J. Herrero, Appl. Phys. Lett. **73**, 1781 (1998)
7. M Haupt, A. Ladenburger, R. Sauer, K. Thonke, R. Glass, W. Roos, J.P. Spatz, H. Rauscher, S. Riethmuller, M. Moller, J. Appl. Phys. **93**, 6252 (2003)
8. Y.-K. Tseng, C -J. Huang, H.-M. Cheng, I.-N. Lin, K.-S. Liu, I.-C. Cheng, Adv. Funct. Mater. **13**, 811 (2003)
9. X. Liu, X. Wu, H. Cao, R.P.H. Chang, J. Appl. Phys. **95**, 3141 (2004)
10. L.K. Teh, K.H. Yeo, C.C. Wong, Appl. Phys. B **87**, 297 (2007)
11. S.M. Abrarov, Sh.U. Yuldashev, T.W. Kim, S.B. Lee, H.Y. Kwon, T.W. Kang, J. Luminesc. **114**, 118 (2005)
12. J. Han, H. Su, C. Zhang, Q. Dong, W Zhang, D. Zhang, Nanotechnology **19**, 365602, 1 (2008)
13. R.D. Pradhan, I.I. Tarhan, G.H. Watson, Phys. Rev. B **54**, 13721 (1996)
14. L.L. Zhang, C.X. Guo, J.G. Chen, J.T. Hu, Chin. Phys. **14**, 586 (2005)
15. S.A.M. Lima, F.A. Sigoli, M. Jafelicci Jr., M.R. Davolos, Int. J. Inorg. Mater. **3**, 749 (2001)
16. J.D. Ye, S.L. Gu, F. Qin, S.M. Zhu, S.M. Liu, X. Zhou, W. Liu, L.Q. Hu, R. Zhang, Y. Shi, Y.D. Zheng, Appl. Phys. A **81**, 759 (2005)

Nuclear Instruments and Methods in Physics Research B 269 (2011) 374–379

Contents lists available at ScienceDirect

Nuclear Instruments and Methods in Physics Research B

journal homepage www.elsevier.com/locate/nimb

Effect of 80-MeV nitrogen ion irradiation on ZnO nanoparticles: Mechanism of selective defect related radiative emission features

S. Bayan, D. Mohanta *

Nanoscience Laboratory Department of Physics Tezpur University P O Napaam Tezpur Assam 784 028 India

ARTICLE INFO

Article history
Received 11 October 2010
Received in revised form 15 November 2010
Available online 20 November 2010

Keywords
ZnO
Ion irradiation
Nanoparticles
Emission

ABSTRACT

We report on the 80-MeV nitrogen ion irradiation on spherical ZnO nanoparticles fabricated by way of solid state mixing The structural and compositional analyses of the as-synthesized ZnO nanoparticles were done by X ray diffraction electron microscopy and energy dispersive spectroscopy studies As evident from the optical absorption spectra the energetic ion irradiation on the nanoparticle system is governed by evolution of new characteristic absorption features owing to modification in the electronic states Again in the luminescence spectra though the near band edge emission was not observable for pristine ZnO it was recovered (at ~385 nm) upon irradiation As far as the defect related emission is concerned a competition between the formation and annihilation of different defects (especially zinc vacancies and interstitials) at different ion fluences was realized Correlating the luminescence spectra and the theoretical investigation it can be understood that during irradiation the formation of zinc related defects are energetically favorable than the oxygen related counterparts Exploration of defect related radiative features corresponding to definite structural organization/modification would help in making next generation light emitting and display devices where a select emission response is desired

1 Introduction

Nanoscale semiconductor systems have gained significant importance due to their size-dependent optical electronic and catalytic properties of plentiful technological relevance [1 2] The wide band-gap semiconductor nanostructures in particular have emerged as a center of attraction for possible deployment in the field of optoelectronics and luminescence [3 4] Zinc oxide (ZnO) a wide direct band gap (3 37 eV at 300 K), have been found to be a promising candidate for optoelectronics and display devices as it shows intense light emission characteristics from UV to visible range in the electromagnetic spectrum [5–8] With the advancement in processing techniques like chemical vapor deposition laser ablation radio frequency/magnetron sputtering chemical bath deposition rapid thermal annealing, etc it has been possible to fabricate quality ZnO nanoparticles as well as asymmetric structures in the form of rods pillars flowers and urchins [9–11] Undoubtedly the concerned methods were pretty good for large scale production with controlled size distribution

In contrast a fast moving ion may lead to significant changes in the material leading to the track formation, implantation and other such effects [12] Bombardment of the nanoparticle systems with suitable energetic ions leads to permanent change in the structural and morphological features like nanoparticle growth [13] nanostructure elongation [14] ripple formation [15] etc Nanoparticle growth splitting and directed growth are reported for ions having energy in the MeV scale whereas ion implantation and ripple formation are observed on irradiat ng with ions carrying keV energies [13 15] Controlled irradiation of the semiconductor nanoparticles with light ions (e g N^{4+} Ar^{8+} etc) is expected to influence the luminescence patterns by introduction or rearrangement of the nanoscale crystal defects [16]

The present work reports on the fabrication of spherical ZnO nanoparticles by a cost-effective one-step solid-state reaction and their luminescence patterns due to the 80-MeV nitrogen ion impact at different fluences The luminescence response and the structural modification are being correlated followed by a relevant theoretical treatment

2 Experimental details

2 1 Synthesis of ZnO nanoparticles

ZnO nanoparticles were synthesized using a surfactant assisted solid state reaction method A mixture of zinc acetate dihydrate (ZAD) a cationic surfactant cetyl trimethyl ammonium bromide (CTAB 99 9% pure Loba-Chemie) and sodium hydroxide (NaOH) with a molar ratio of 1 0 3 2 were ground together in an agate mortar for ~45 min at room temperature The unidirectional soft

* Corresponding author Tel +91 3712 267007 fax +91 3712 267005
E mail address best@tezu e net in (D Mohanta)

0168-583X/$ - see front matter © 2010 Elsevier B V All rights reserved
doi 10 1016/j nimb 2010 11 044

grinding led to the excess heat release as the reaction was in progress. After ultrasonication, the product was washed repeatedly with deionised water and ethanol to remove any unreacted species. Finally the ZnO nanoparticles were obtained on drying the product ~70 °C in air for 2 h.

2.2. Irradiation of ZnO nanoparticles

Polymers being protecting materials against the agglomeration of nanoparticles, polyvinyl alcohol (PVA) matrix medium was selected to disperse ZnO nanoparticles. For the irradiation purpose, the ZnO nanoparticles-dispersed PVA films were casted on laboratory glass slides (1 × 1 cm^2). The samples were irradiated in the Material Science chamber under a high vacuum (pressure of ~10^{-6} mbar) condition and using 80 MeV-N^{4+} ion beams (with a beam current of ~1 pnA, particle-nanoampere), available at the 15UD tandem pelletron accelerator of Inter University Accelerator Centre, New Delhi. The ion beam fluence was measured by integrating the ion charge on the sample ladder, which was insulated from the chamber. The ion fluence was varied as 1.25×10^{11}, 5×10^{11}, 2×10^{12} and 8×10^{12} ions/cm^2.

2.3. Characterization techniques

The structural characterization of the ZnO nanoparticles were performed by X-ray diffraction (XRD) measurements recorded on a Rigaku D/max-2000 diffractometer employing Cu-K_α radiation (λ = 1.54 Å). Low resolution transmission electron microscopy (TEM) study was carried out by a JEOL JSM-100 CX microscope working at a beam accelerating voltage of 80 kV. In contrast, high resolution transmission electron microscopy (HRTEM) study was made with the help of a FEI, Tecnai S-twin electron microscope working under an accelerating voltage of 200 kV. The elemental analysis was performed through the energy dispersive X-ray spectroscope (EDS) attached with the scanning electron microscope (JEOL JSM: 6390 LV). The optical absorption study was performed by the UV–Visible absorption spectroscopy (UV 2450, Shimadzu Corporation). The room temperature photoluminescence spectra were revealed by using a PerkinElmer LS 55 spectrophotometer, having Xe lamp as the excitation source.

3. Results and discussion

3.1. Structural analysis

The TEM image of the as-synthesized ZnO nanoparticles are shown in Fig. 1(a). The average size of the nanoparticles is ~10–12 nm. The lattice fringes due to single crystalline planes are clearly observed in the HRTEM image of the ZnO specimen (Fig. 1(b)). The lattice spacing is found to be ~0.26 nm and it corresponds to the interplanar separation between the consecutive (0 0 2) planes of ZnO. The XRD pattern, shown in Fig. 1(c), shows hexagonal wurtzite structure of the ZnO nanoparticles (JCPDS 36-1451) [10]. No extra peak related to other byproducts e.g., $Zn(OH)_2$ was detected. The elemental constitution was obtained from the EDS spectra (Fig. 1(c)). In the EDS, the detection of a small peak corresponding to Br-element was noticed which might have arisen owing to the presence of a minor amount of CTAB surfactant used in synthesizing ZnO specimens.

3.2. Optical absorption spectra

As can be observed in the absorption spectra (Fig. 2), the pristine ZnO nanoparticle system before irradiation is characterized

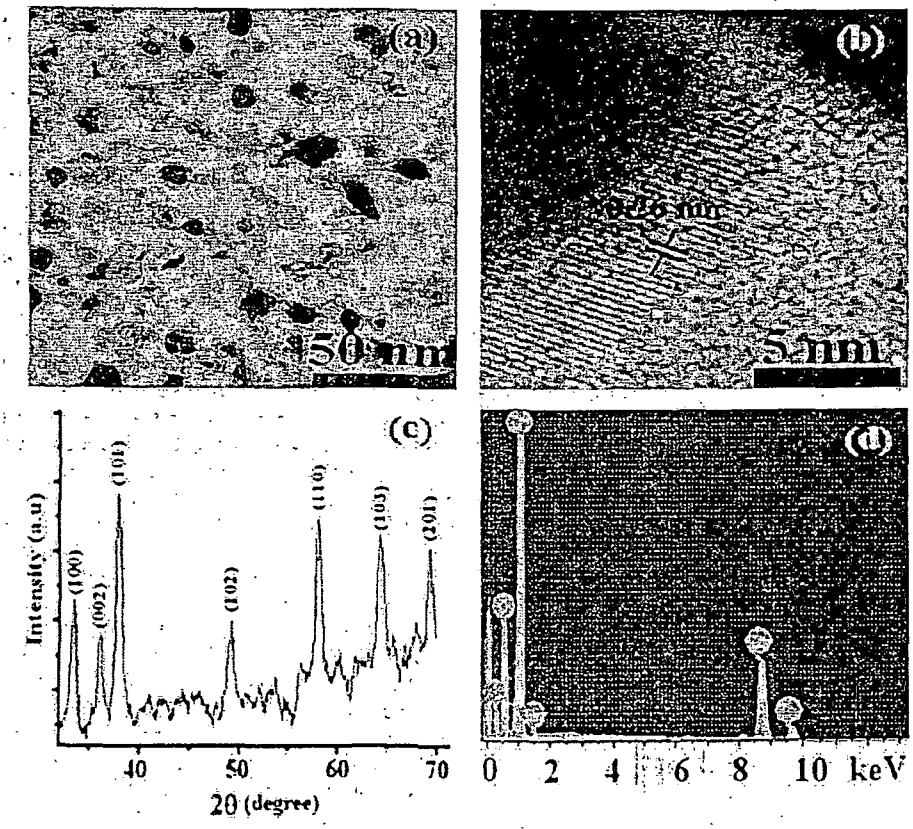

Fig. 1. (a) Low resolution TEM, (b) High resolution TEM, (c) XRD pattern, and (d) EDS spectra of the nanoparticle system.

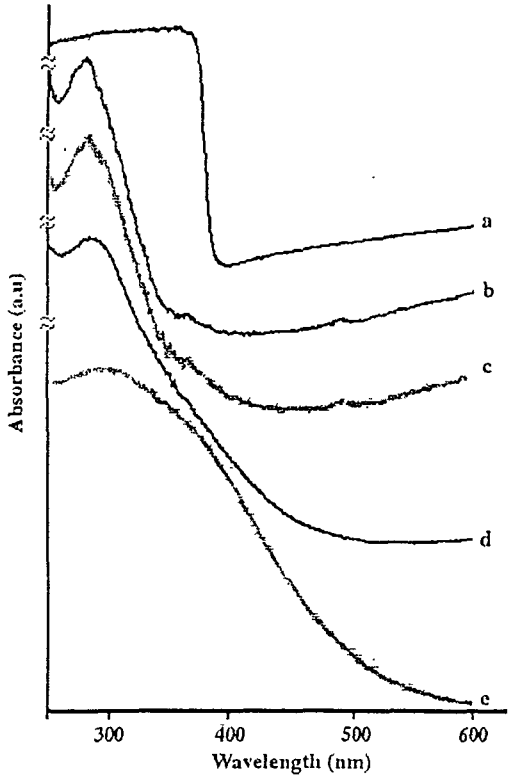

Fig. 2. Absorption spectra of ZnO nanoparticles (a) unirradiated and irradiated with fluence (b) 1.25×10^{11}, (c) 5×10^{11}, (d) 2×10^{12}, and (e) 8×10^{12} ions/cm^2; respectively.

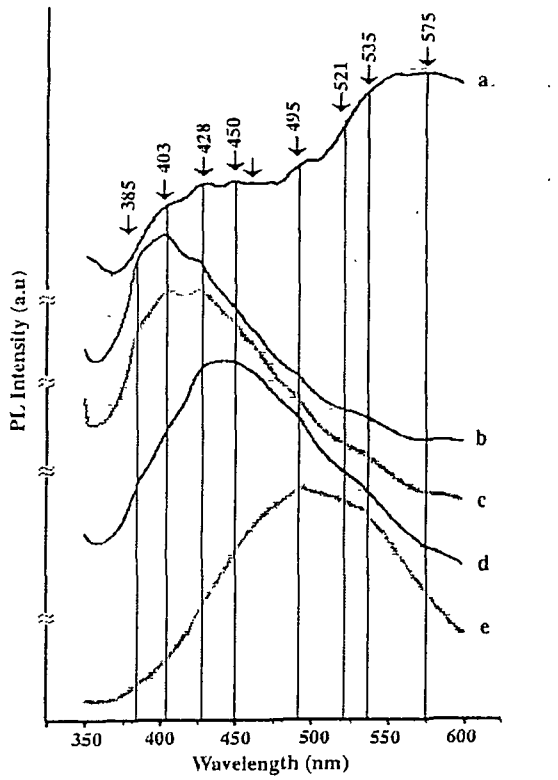

Fig. 3. Room temperature PL spectra of ZnO nanoparticles (a) un-irradiated and irradiated with a fluence of (b) 1.25×10^{11}, (c) 5×10^{11}, (d) 2×10^{12}, and (e) 8×10^{12} ions/cm^2; respectively.

by a band-edge absorption peak at ~360 nm (~3.44 eV). It signifies strong 1*s*-1*s* excitonic absorption near the vicinity of the band gap. On irradiation at a fluence of 1.25×10^{11} ions/cm^2, a new absorption peak is evolved at ~285 nm, while signature of the ground state absorption (~360 nm) gets quenched. The newly evolved peak and the trace of the ground state absorption peak are also visible for the specimen irradiated with a fluence of 5×10^{11} ions/cm^2. The unusual appearance of a new absorption peak at ~285 nm, can be assigned to the modification in the ground state electronic energy levels. Because of the instant rise in the electronic temperature during irradiation, the event can be treated as a case of abrupt annealing which can lead to structural reorganization and hence, modification in the electronic states. Again, at a fluence of 2×10^{12} ions/cm^2 the original ground state absorption has improved resulting in the broadening of the overall absorption spectra. Consequently, at the fluence of 8×10^{12} ions/cm^2, the spectrum (consisting of the two absorption peaks) was found to be optimally broadened.

3.3. Photoluminescence spectra

The photoluminescence spectra of the un-irradiated and irradiated ZnO nanoparticle systems under 325 nm excitation, is shown in Fig. 3. Typically, the un-irradiated ZnO system exhibits various defect related emissions. The visible impressions at ~403 nm, 428 nm and 450 nm correspond to the emission related to the Zn vacancy (V_{Zn}) and Zn interstitials (Zn_i, Zn_i^+, etc.); respectively [5–7]. The emission peak at ~495 and 575 nm can be ascribed to the oxygen vacancies (V_O^+, V_O^{++}, etc.) [8], while the larger wavelength side of the spectrum is dominated by other defects like complex defects (V_O:Zn_i at 516 nm), oxygen antisites (O_{Zn} at 521 nm) and oxygen interstitials (O_i at 535 nm) [5,6]. It is known that nanoparticles possess plentiful defects owing to large surface to volume ratio. Most of the surface defects are due to single and double ionized oxygen vacancies and it is expected that the radiative emission via these surface states can quench the band edge emission appreciably.

Upon irradiation with a fluence of 1.25×10^{11} ions/cm^2, the PL response gets improved with respect to V_{Zn} related emission, while the oxygen related emission response (V_O^+, V_O^{++}, V_O:Zn_i, O_{Zn}, etc.) is drastically reduced. Since the V_O related defect and band-edge emissions can be correlated [5], the band-edge emission at ~385 nm can be observable upon irradiation. The band-edge emission is found to be intact even in case of irradiation at a higher fluence (5×10^{11} ions/cm^2), while the emission response due to the Zn vacancy and interstitial related defects become comparable. Note that, V_{Zn}, Zn_i, V_O and O_i defects are generally encountered in ZnO nanostructures and owing to enormous energy deposition by irradiation events, their independent contribution to the luminescence pattern will be greatly affected. It is possible that the vacancy and interstitial related defects invariably compete and/or exchange each other. Further, Zn_i atoms are mobile even at the room temperature [17], there is a competition between the creation and annihilation of the V_{Zn} and Zn_i related defects. Towards this end, we observe comparable emission responses from these defects at a fluence of 5×10^{11} ions/cm^2. Moreover, at a moderate fluence of 5×10^{11} ions/cm^2, the host polymer matrix that supports ZnO nanosystems experiences significant C–C bond breakage leading to disruption in polymer chains. As revealed by the TEM images depicted in Fig. 4(a,b), the nanoparticles tend to overcome the polymer encapsulation (at $\sim 5 \times 10^{11}$ ions/cm^2), which was not observable in case of the sample irradiated at a lower fluence (1.25×10^{11} ions/cm^2).

On the other hand, upon irradiation at a fluence of 2×10^{12} ions/cm^2, the spectrum is found to be more symmetric with optimum Zn_i and Zn_i^+ related emission, whilst the intensity of the band-edge emission peak gets lowered. The suppression of the band-edge emission intensity is ascribed to the progressive development of the V_O^+ related emission. As found in the TEM image (Fig. 4(c)), at this fluence, the nanoparticles overcome the matrix encapsulation completely along with occasional instances of particle-coalescence. This facilitates in the recovery of the V_O^+ states as the oxygen vacancies normally stay on the surface of the nanoparticles. The nanoparticles just recovered from the matrix encapsulation becomes free standing but highly reactive and might cause coalescence with the neighboring nanoparticles. The coalescence of the nanoparticles under energetic ion irradiation can be assigned to the decrease in effective cohesive energy of the nanoparticles [18].

At 8×10^{12} ions/cm^2, the spectrum becomes more and more symmetric and peaking at the wavelength position as due to the V_O^+ related defect emission. In addition, the emission due to O_i defects can also be identified. The band-edge emission, at this fluence, is substantially quenched on account of dominancy of the aforesaid emissions. The extent to which nanoparticles will be recovered from the matrix encapsulation, depends on the amount of energy incident on the specimen. In this context, at the highest fluence (8×10^{12} ions/cm^2), the energy deposition is maximum and therefore, the matrix can be amorphized completely. The rapid mass transport between particles with interparticle separation relatively smaller than that of their dimension can result in particle coalesce/agglomeration. An agglomerated view of the irradiated nanostructures is evident from the electron micrograph, shown in Fig. 4(d).

3.4. Theoretical justification

In a ZnO nanoparticle embedded polymer matrix system, the incoming ions are expected to strike both the nanoparticles as well as the host matrix. An energetic ion while traversing through a solid loses its energy in two ways: (i) electronic energy loss due to inelastic collision of the incoming ion with the electrons of the solid, and (ii) nuclear energy loss due to the elastic collision with the atomic nuclei of the solid [12]. The electronic energy loss (S_e), nuclear energy loss (S_n), and the stopping range of the 80 MeV-N^{4+} ions in PVA and ZnO are shown in Table 1. It can be seen that both in ZnO and PVA cases, S_e dominates over S_n. As the energy deposited in the PVA film is very small compared to the incident energy (80 MeV) of the ion, the effective energy realized on the individual nanoparticles, to a good approximation will be ~80 MeV. Considering the average size of the nanoparticles as 10 nm, the amount of energy delivered to the nanoparticle by a single ion along its trajectory (i.e., along the diameter, D of the nanoparticle) is $S_eD = 11.91$ keV. According to the Thermal spike model [19], in the close vicinity of the projectile ion, the above mentioned energy would diffuse to the atomic subsystem (via electron–phonon coupling). As a result, local heating of the lattice takes place and eventually melting occurs. Later, the fast cooling of the system causes transient atomic disorder and thereby formation of innumerable defects. Since the energy deposited at the core is maximum and decreases gradually as one moves away from it, we speculate the development of several concentric cylindrical zones (each of length D), each of which representing a definite energy value (Fig. 5).

Now, if x_i ($i = 1,2,3,...$) is the atomic percentage of each element of diameter d_i ($i = 1,2,3,...$) present in the nanoparticle of diameter

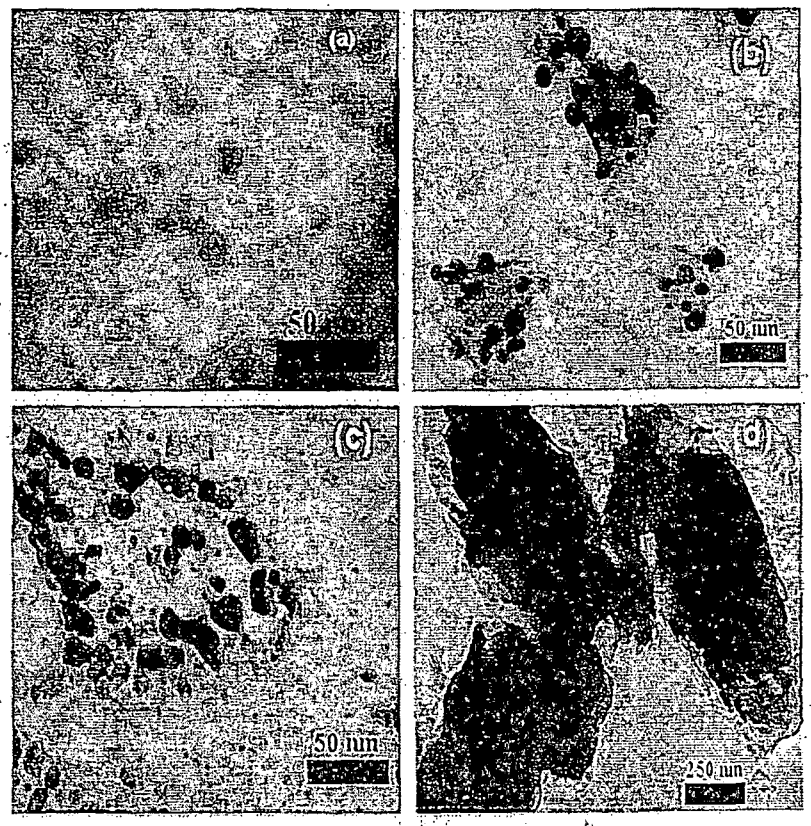

Fig. 4. TEM image of ZnO nanoparticles after irradiation with a fluence of (a) 1.25×10^{11}, (b) 5×10^{11}, (c) 2×10^{12}, and (d) 8×10^{12} ions/cm^2; respectively.

Table 1
Electronic energy loss (S_e), nuclear energy loss (S_n), and the stopping range of the 80 MeV-N^{4+} ions in PVA and ZnO.

Material	S_e (eV/nm)	S_n (eV/nm)	Projectile range (μm)
PVA	3.946×10^2	2.201×10^{-1}	129.42
ZnO	1.191×10^3	6.792×10^{-1}	47.18

D, then the total number of atoms present in the system can be given by:

$$N = \frac{f.D^3}{\sum x_i d_i^3}, \tag{1}$$

where f is the packing fraction and $\sum x_i = 1$ [18].

Considering the diameter of the cylinder as $\delta (< D)$, the number of atoms present in the cylindrical region can be expressed by:

$$n = \frac{3}{2}\left(\frac{\delta}{D}\right)^2 N. \tag{2}$$

From the basic understanding point of view the amount of energy deposited during the thermal spike event refers to the product of the electronic energy loss (S_e) and the electron–phonon coupling efficiency (g) [20,21]. So, the total energy deposited along the path of the projectile ion is gS_eD and the amount of energy received by each of the atoms in the cylindrical region of diameter δ will be

$$E = \frac{gS_eD}{\frac{3}{2}\left(\frac{\delta}{D}\right)^2 N} = \frac{2gS_eD^3}{3\delta^2 N} \tag{3}$$

Assuming $g = 0.4$ [21], the variation of the energy received by each atom of the cylindrical regions can be predicted (Fig. 6).

In ZnO lattice, the energy necessary to displace zinc and oxygen atoms from their regular positions to the interstitial positions are 18.5 and 41.4 eV; respectively [22]. In the plot (Fig. 6), these values corresponded to the cylindrical region of diameters (δ) 0.51 and 0.34 nm; respectively. Effectively, the Zn and O atoms present within the cylindrical zone of diameter ~0.51 and 0.34 nm can avail the above mentioned energy. As shown in Eq. (2), the number of atoms n, present in the cylindrical region is directly proportional to the square of δ. Thus the number of zinc atoms is larger than the number of oxygen atoms so as to acquire the effective displacement energies. Consequently, upon irradiation, the vacancy and interstitial related defects is likely to be larger in case of Zn atoms than O ones. Accordingly, the zinc related defects (vacancies, interstitials) can be dominant for the specimens irradiated with fluences of 1.25×10^{11}, 5×10^{11} and 2×10^{12} ions/cm^2 (Fig. 3).

In order to make out a clear picture on the contribution of defects responsible for a typical PL emission, we have plotted ion fluence vs. normalized intensity and is shown in Fig. 7. The intensity ratio of a definite defect related PL pattern corresponding to a given ion fluence and that of pristine one is taken as normalized intensity. As can be seen, lower fluences are accompanied by enhanced defect related emission response especially, the zinc related defects (V_{Zn} and Zn_i). It is expected that irradiation can inspire migration of a number of interstitial atoms to the vacancies. The competition between the creation and annihilation (formation of vacancies and migration of interstitials) of defects can be dependent on the ion fluence. The peak to peak ratio of V_{Zn} and Zn_i (i.e. V_{Zn}/Zn_i) has been calculated using the intensity profile of the PL patterns of Fig. 3, and is shown in the inset of Fig. 7. It is confirmed that before irradiation ($V_{Zn}/Zn_i = 0.8$), the Zn_i defects were the major contributors than V_{Zn}, whereas for irradiation at 1.25×10^{11} ions/cm^2 ($V_{Zn}/Zn_i = 1.12$), V_{Zn} defects have an increasing trend. Conversely, at a fluence of 5×10^{11} ions/cm^2, the V_{Zn}/Zn_i ratio becomes ~1.02, highlighting a competitive contribution from both the V_{Zn} and Zn_i defects. The competition among Zn-vacancy and interstitial related defects can be invoked as follows: (i) V_{Zn} decreases independently, (ii) Zn_i increases independently, and finally, (iii) both (i) and (ii) take place simultaneously. The conditions (i) and (ii) can be discarded as in a well defined system, a particular defect type has to increase/decrease at the cost of the other. Hence, the condition (iii) is most favorable. It can be clearly observed in Fig. 7 that at the third fluence (2×10^{11} ions/cm^2), Zn_i defects have higher normalized intensity than their V_{Zn} counterparts. This feature is continued up to the highest fluence, where the V_{Zn}/Zn_i ratio becomes 0.47 ensuring the dominance of Zn_i defects.

As the increased fluence variation is capable of promoting the migration of the Zn_i atoms, in principle, the zinc lattice sites are

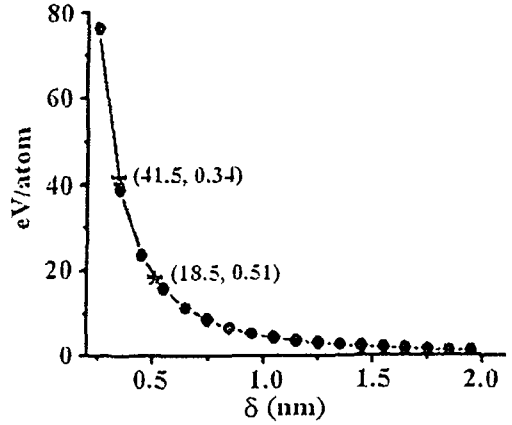

Fig. 6. Variation of energy received per atom present in the cylindrical region and the radii of the concerned cylinders.

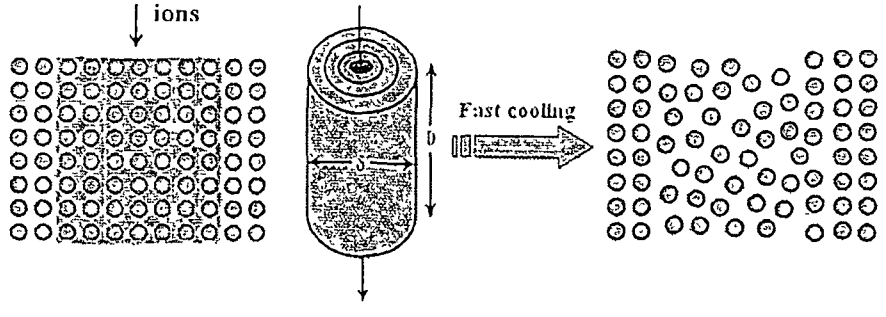

Fig. 5. A scheme of energy deposition in concentric cylindrical regions along with defect formation upon fast cooling

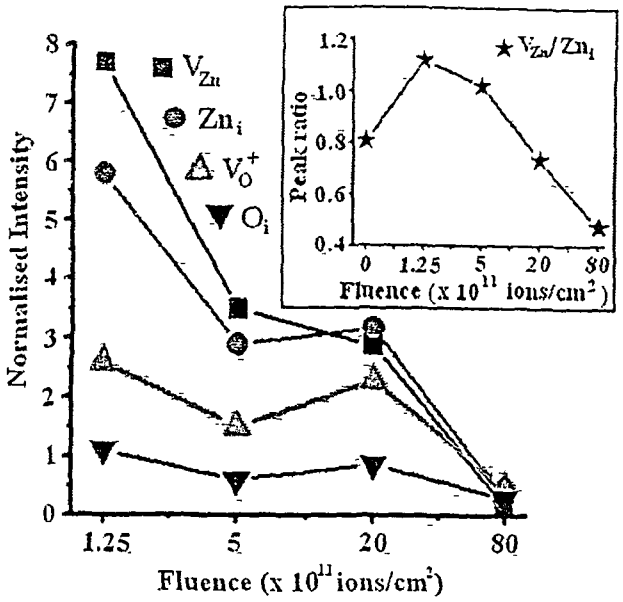

Fig. 7. Normalized emission intensity of different defects vs. fluence. Inset being the variation of the V_{Zn}/Zn_i before and after irradiation at different fluences.

believed to be most affected. On the other hand, the extent of recovery from the matrix encapsulation depends largely on the ion fluence variation which could lead to the substantial improvement in V_0^+ related emission. At the highest fluence (8×10^{12} ions/cm^2), the nanostructure clustering owing to particle–particle coalesce is found to be responsible for quenching the overall emission intensity.

4. Conclusion

Structural and optoelectronic modification of the solid-state derived ZnO nanoparticles are studied with special reference to 80-MeV nitrogen ion irradiation. After irradiation, the absorption pattern was found to be altered owing to the modification of electronic states. On irradiation, the band-edge emission of the nanoparticle system was recovered while suppressing the oxygen vacancy (V_0^{++}) related emissions. The defect dominated radiative emission patterns were modified at different fluences due to the competition among various defects (V_{Zn}, and Zn_i), stimulated by the irradiation events. Owing to the less energy required to displace the zinc atoms from their respective lattice sites the zinc related defects are found to be more prominent than oxygen ones, upon irradiation. The ion irradiated ZnO nanostructures, with a variation in luminescence feature, can form the basis of modern nanoscale luminescent/display devices.

Acknowledgements

The authors extend their sincere gratitude to Mr. U. Das for assisting in the synthesis process. The authors also thank the accelerator group of IUAC, New Delhi; for providing good quality nitrogen beam against UFUP project no. 44314/2008. The cooperation received from SAIF, NEHU, Shilong and SINP, Kolkata in undertaking electron microscopy are gratefully acknowledged.

References

[1] X. Peng, L. Manna, W. Yang, J. Wickham, E. Scher, A. Kadavanich, A.P. Alivisatos, Nature 404 (2000) 59.
[2] J. Hu, L.-S. Li, W. Yang, L. Manna, L.-W. Wang, A.P Alivisatos, Science 292 (2001) 2060.
[3] R.N. Bhargava, V. Chhabra, T. Som, A. Ekimov, N. Taskar, Phys. Status Solidi B 229 (2002) 897.
[4] L. Grocholl, J. Wang, E.G. Gillan, Chem. Mater. 13 (2001) 4290.
[5] B. Lin, Z. Fu, Y. Jia, Appl. Phys. Lett. 79 (2001) 943.
[6] S.A. M Lima, F.A. Sigoli Jr., M. Jafelicci, M.R. Davolos, Int. J. Inorg. Mater 3 (2001) 749.
[7] L.-L. Zhang, C.-X. Guo, J.-G. Chen, J.-T. Hu, Chin. Phys. 14 (2005) 586.
[8] J.D. Ye, S.L. Gu, F. Qin, S.M. Zhu, S.M. Liu, X. Zhou, W. Liu, L.Q. Hu, R. Zhang, Y. Shi, Y.D. Zheng, Appl. Phys. A 81 (2005) 759.
[9] M. Willander, O. Nur, N. Bano, K. Sultana, New J. Phys. 11 (2009) 125020.
[10] J. Ge, B. Tang, L. Zhuo, Z. Shi, Nanotechnology 17 (2006) 1316.
[11] S. Bayan, D. Mohanta, J. Appl. Phys. 108 (2010) 023512.
[12] G.K. Mehta, Nucl. Instrum. Methods Phys. Res., Sect. A 382 (1996) 335.
[13] Y.K. Mishra, D K. Avasthi, P.K. Kulriya, F. Singh, D. Kabiraj, A. Tripathi, J.C. Pivin, I.S. Bayer, A. Biswas, Appl. Phys. Lett. 90 (2007) 073110.
[14] D. Mohanta, G.A. Ahmed, A. Choudhury, F. Singh, D.K. Avasthi, G. Boyer, G.A. Stanciu, Eur. Phys. J. Appl. Phys. 35 (2006) 29.
[15] J. Lian, W. Zhou, Q.M. Wei, L.M. Wang, L.A. Boatner, Rodney C. Ewing, Appl. Phys. Lett. 88 (2006) 093112.
[16] S. Bayan, U. Das, D Mohanta, Phys. Status Solidi A 207 (2010) 1859.
[17] S. Rackauskas, A.G. Nasibulin, H. Jiang, Y. Tian, G. Statkute, S.D. Shandakov, H. Lipsanen, E.I. Kauppinen, Appl. Phys. Lett. 95 (2009) 183114.
[18] S. Bayan, D. Mohanta, J. Mater. Res. 25 (2010) 814.
[19] C. Dufour, Z.G. Wang, E. Paumier, M. Toulemonde, Bull Mater Sci. 22 (1999) 671.
[20] G. Szenes, Z.E. Horváth, B. Pécz, F. Pászti, L. Tóth, Phys. Rev. B 65 (2002) 045206.
[21] G. Szenes, F. Pszti, Á. Péter, A.I Popov, Nucl. Instrum. Methods Phys. Res., Sect. B 166–167 (2000) 949.
[22] D.C. Look, J.W. Hemsky, J.R. Sizelove, Phys. Rev. Lett. 82 (1999) 2552.

Directed growth characteristics and optoelectronic properties of Eu-doped ZnO nanorods and urchins

S. Bayan and D. Mohanta[a)]
Nanoscience Laboratory, Department of Physics, Tezpur University, P.O. Napaam, Assam 784028, India

(Received 22 April 2010; accepted 8 June 2010; published online 27 July 2010)

Inexpensive fabrication of europium (Eu^{3+})-doped zinc oxide (ZnO) nanoparticles, nanorods, and urchin systems obtained by rapid thermal annealing is being reported. The polyvinyl alcohol films containing a reactant mixture [$Zn(CH_3COO)_2$, $Eu(CH_3COO)_3$, and NaOH] were casted on Al-foils followed by thermal annealing at 80, 300, and 650 °C. Gradual change-over from spherically symmetric nanoparticles to nanorods along with urchin like structures are obtained under different annealing environment. The nanorods and urchins are expected to have grown as a result of spontaneous decomposition of $Zn(OH)_2$ followed by unidirectional growth. The nanorods are dislodged from the regular urchin structures at a high annealing temperature of 650 °C because of the loss of the crystalline substrate support. The as-received ZnO products possessed hexagonal wurtzite structure for all the annealing cases-as evident from the x-ray diffraction patterns. The photoluminescence study on the samples has revealed dominant defect related emissions compared to the near band edge emission. The band edge emission (~382 nm) is recovered in the urchin systems whereas Eu^{3+} related transitions observed at ~591 nm ($^5D_0 \rightarrow {}^7F_1$) and ~613 nm ($^5D_0 \rightarrow {}^7F_2$) remained intact with structural modification. © *2010 American Institute of Physics.* [doi:10.1063/1.3462396]

I. INTRODUCTION

In recent years, the semiconductor nanostructured materials are being considered as the potential candidates for the photonic and optoelectronic applications because of their size dependent modification in electronic structures.[1–3] Among them, there has been a considerable interest in the elongated semiconductor nanostructured systems owing to tunable emission in the visible region. Earlier, doping with suitable optically active impurities such as transition metal ion[4,5] and trivalent rare-earth ion[6–8] in semiconductor nanosystems was investigated in great detail.

Zinc oxide (ZnO), a wide-direct band gap (E_g =3.37 eV) semiconducting material has a very high exciton binding energy (E_b=60 meV) at room temperature. It exhibits its intense light emission features from the UV to visible range in the electromagnetic spectrum.[9–11] In view of the defect related emission caused by zinc/oxygen vacancies or/and presence of antisites, ZnO is being considered as a technologically important system. Varieties of structures of ZnO such as wires, rods, needles, shells, urchins, and flower like structures can be found in the literature.[12–14] Also numerous reports on rare-earth doped ZnO nanostructured systems are available. In europium doped ZnO nanoparticles, a broadband room temperature emission was previously observed by Bhargava *et al.*[15] White light emission response by europium doped ZnO urchins and nanoparticles have also been reported.[8] Similarly, the cathodoluminescence of terbium doped ZnO nanocrystals was studied in different annealing environments.[16] However, the mechanism that governs a specific nanostructure type has not been well addressed. In this work, we report on the structural evolution of europium doped ZnO nanoscale products as a result of rapid thermal annealing. The experimental evidence on the development of rods and urchins are encountered by relevant theoretical justifications. Further, the origin and nature of luminescence patterns are highlighted.

II. EXPERIMENTAL

The europium doped ZnO nanostructures were synthesized using a simple rapid thermal annealing process. Following our previous report,[17] polyvinyl alcohol (PVA) was chosen as the supporting matrix for embedding ZnO nanoparticles. 5 wt % PVA (Loba Chemie, lmw, degree of polymerization 1700–1800) matrix was prepared by stirring (~200 rpm) vigorously for 1.5 h while maintaining a temperature of ~70 °C, well below the glass transition temperature of PVA. As a result, a transparent viscous solution is obtained. Europium acetate [$Eu(CH_3COO)_3$, Central Drug House, 99.9%] and zinc acetate dihydrate [$Zn(CH_3COO)_2$, (Merck, 99%)] were mixed in a weight ratio of 0.04 and transferred to the aqueous solution of PVA. Then, 0.6 M aqueous sodium hydroxide (NaOH) was added dropwise under continuous stirring environment for 1 h. The *p*H of the final precursor was 9.0. Aluminum substrates of size 1 $\times 2$ cm^2 and thickness ~300 μm, were cleaned using ethanol and acetone in an ultrasonicator bath and finally washed with distilled water. Then, the resulting precursor was spin-casted onto the clean substrates followed by annealing at 80 °C, 300 °C, and 650 °C for 0.5 h in a muffle furnace having a provision for constant air flow. The respective samples are named as S_1, S_2, and S_3.

The structural and optical properties of Eu-doped ZnO nanostructures were characterized by high resolution scan-

a)Electronic mail best@tezu.ernet.in.

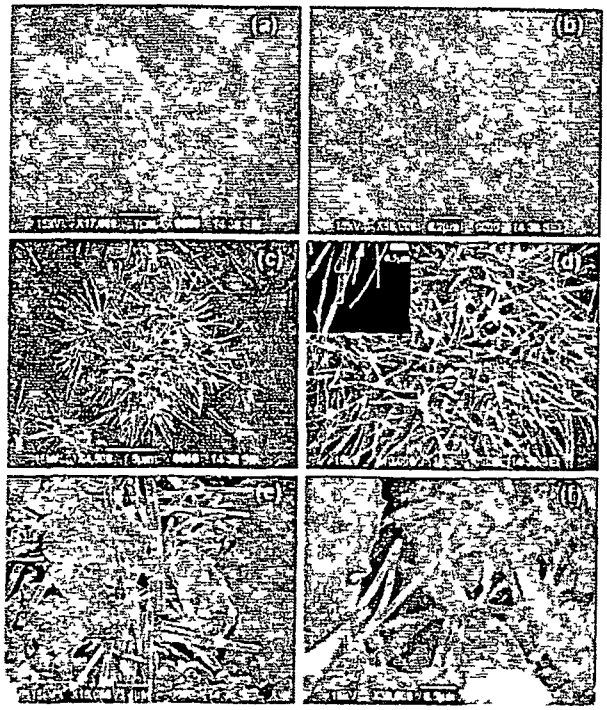

FIG 1 (Color online) SEM images at different magnifications of Eu doped ZnO systems (a) and (b) annealed at 80 °C (c) and (d) annealed at 300 °C with inset at higher magnification and (e) and (f) annealed at 650 °C

ning electron microscopy (SEM), x-ray diffraction (XRD), optical absorption, and emission spectroscopy tools

III RESULTS AND DISCUSSION

The experimental conditions facilitating development of typical nanostructures are discussed in conjunction with theoretical justification The optoelectronic properties of synthesized samples are detailed on the basis of the nature of distribution and organization of the nanostructures

A. Development of Eu-doped ZnO nanostructures

As shown in Fig 1, the formation of ZnO nanostructures is clearly visible from the electron micrographs The sample annealed at 80 °C [Figs 1(a) and 1(b)] shows the development of spherical ZnO nanoparticles with a variation in average diameter ~120–200 nm The particles are uniformly distributed in the PVA matrix without any signature of undesired clustering or agglomeration

The sample annealed at a temperature of 300 °C, showed unusual growth of urchin like nanostructures In this case, no trace of the PVA matrix was found as PVA decomposes at a temperature of ~230 °C It can be observed that the urchins are composed of a large number of independent nanorods, of different orientations but originated from the same base (pointed by red arrows) The average length and diameter of the nanorods are found to be 4–5 μm and 120–200 nm respectively As the diameter of the rods [inset of Fig 1(d)] is nearly equal to the diameter of the particles [Fig 1(b)], it was expected that the growth of the nanorods took place by unidirectional assimilation of individual ZnO nanoparticles Note that upon annealing the specimen at 650 °C, in addition to growth of nanorods, the Al substrate develops an amorphous layer (forming Al_2O_3 layer) [18] As a result, the urchin like structures are not well supported The constituent nanorods, therefore, fall randomly onto the substrate [Figs 1(e) and 1(f)] It can also be noticed that there is no substantial variation in the length and diameter of the rods corresponding to the annealing temperatures, i e , 300 and 650 °C The rods which make up the urchins preserve their structure at both the annealing temperatures

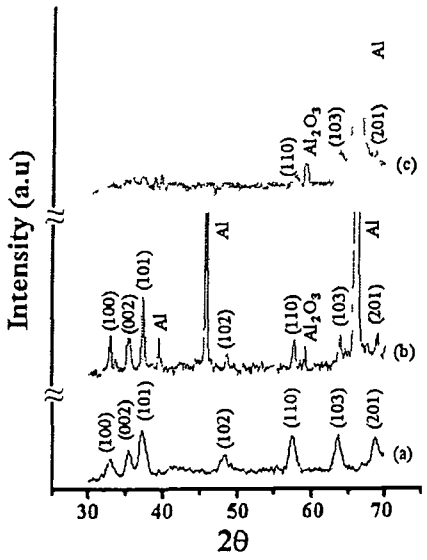

FIG 2 (Color online) XRD pattern of the Eu-doped ZnO nanostructures annealed at (a) 80 °C, (b) 300 °C, and (c) 650 °C

We have also studied XRD patterns of various nanostructured ZnO Eu samples the results of which are shown in Fig 2 The diffraction pattern corresponds to the hexagonal wurtzite structure of ZnO with preferred orientation along (101) plane [Figs 2(a) and 2(b)] Any extra peak corresponding to the byproducts (e g , Eu_2O_3, $Zn(OH)_2$, etc) was not detected A close look on Figs 2(a) and 2(b) reveals that there is a decrease in full width half maxima of the (002) peak from 0 023 rad to 0 011 rad for the samples annealed at 80 °C and 300 °C, respectively Ge *et al* have observed similar kind of situation based on reflux time dependent growth of the nanoparticles along [0001] direction resulting to nanorods [19] So, in this present study also it can be inferred that on annealing at 300 °C, the growth of the nanoparticles occurs along the [0001] direction and as a result the nano rods are formed as supported by the SEM micrographs The diffraction planes for metallic Al is visible in case of samples annealed at 300 °C because of the removal of PVA [18] A small peak observed at ~59° is ascribed to the formation of Al_2O_3 [18] At 650 °C, the Al surface gets oxidized (forming Al_2O_3) and this is the reason why the peaks of ZnO are not clearly distinguishable in the XRD pattern of the sample heated at that temperature [Fig 2(c)] This is also evident from the SEM images where the part of amorphized debris can be seen clearly The compositional analysis was per formed on the sample annealed at 300 °C the results of which are depicted in the energy dispersive spectra (EDS) in

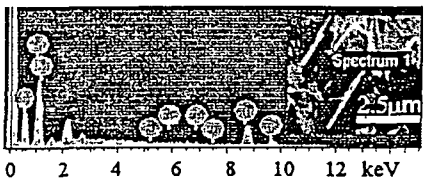

FIG. 3. (Color online) EDS spectra of the Eu-doped ZnO nanorods (sample S_2). Inset being the spot where the spectrum was captured.

Fig. 3. The EDS was taken at a specific site of a single nanorod (labeled by a red cross). Apparently visible peaks due to Zn, O, and Eu elements were detected. Consequently, the synthesized nanorods/urchins confirm the presence of Eu^{3+} in the host ZnO.

B. Growth mechanism of Eu-doped ZnO nanorods and urchins

When the PVA dispersed nanoparticle system was heated at 300 °C, owing to the decomposition of PVA (at ~230 °C), the nanoparticles gradually lose support from the matrix. In this situation, the growth phenomena of the nanoparticles can be described by the Ostwald ripening.[20] Considering two nanoparticles of radii R_1 and R_2 (where $R_2 > R_1$) the Young–Laplace equation[20] can be written as

$$\mu_1 = 2\gamma\frac{\Omega}{R_1}, \tag{1}$$

$$\mu_2 = 2\gamma\frac{\Omega}{R_2}, \tag{2}$$

where μ_1 and μ_2 are the chemical potentials (work per atom) of the respective particles. γ and Ω being the surface energy and atomic volume of ZnO.

The difference in chemical potentials between the particles will be given by[20]

$$\Delta\mu = 2\gamma\Omega\left[\frac{R_2 - R_1}{R_1R_2}\right] = kT\ln\frac{P_{R_1}}{P_{R_2}}. \tag{3}$$

Here P_{R_1} and P_{R_2} are the vapor pressures of the two particles, with k and T being the Boltzmann constant and the temperature of the environment. The above equation represents the change in chemical potential of an atom transferring from particle of radius R_1 to R_2. The chemical potential of a system increases with the temperature and hence with the external supply of heat. Now, on increasing chemical potential, the term in the parenthesis will tend to increase for fixed values of γ and Ω.

$$\text{So, } \left[\frac{R_2 - R_1}{R_1R_2}\right]_{\text{After heating}} > \left[\frac{R_2 - R_1}{R_1R_2}\right]_{\text{Before heating}} \Rightarrow (R_2 - R_1)_{\text{After heating}} > (R_2 - R_1)_{\text{Before heating}}$$

$$\text{or } (R_1R_2)_{\text{After heating}} < (R_1R_2)_{\text{Before heating}}.$$

The above two conditions are valid only if the numerical value of R_2 tend to increase while R_1 decreases. Given the total number of atoms in a nanoparticle is constant, such a situation can be realized only if mass transport takes place from smaller particle (radius R_1) to the larger one (radius R_2). Since the surrounding matrix is lost above the decomposition temperature, interparticle mass transport is highly favorable that results in particle growth. The role of cohesive energy in particle–particle coalescence under energetic ion irradiation was investigated by our group recently.[21]

Now we need to address upon the nature of growth process. From the crystallographic point of view, the nanoparticle growth will occur at the unit cell level along preferential directions. However, as the surface energy of ZnO is different along different directions of the unit cell, particle growth would not occur in all directions equally. According to the calculations of Fujimara *et al.*,[22] surface energy per mole along different directions varies as $\gamma_{[0001]} < \gamma_{[11\bar{2}0]} < \gamma_{[10\bar{1}0]}$.

Following Eq. (3) after heat treatment, $(R_2 - R_1)/R_1R_2 = \Delta\mu/2\Omega\gamma$. Thus, we obtain $\Delta R_{[0001]} > \Delta R_{[11\bar{2}0]} > \Delta R_{[10\bar{1}0]}$. In other words, the growth of the nanoparticles along [0001] direction (along c-axis) is energetically favorable owing to minimum surface energy and hence, the formation of elongated nanostructures is expected (Fig. 4). Growth along the direction [0001] results in the vanishing of (002) plane as it is known that plane with higher growth rate disappears quicker.[23] This is also predicted by the XRD results where the full width at half maxima of the (002) peak for the urchin system decreases as discussed above. In the formation of urchin structures, the distribution and arrangement of the nanoparticles in the PVA matrix play important roles. In a

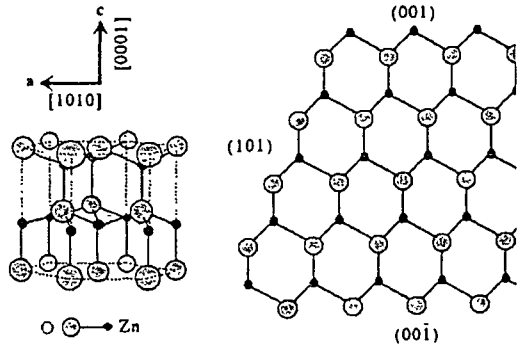

FIG. 4. Schematic of ZnO crystal structure and configuration model of the stack of zinc and oxygen atoms.

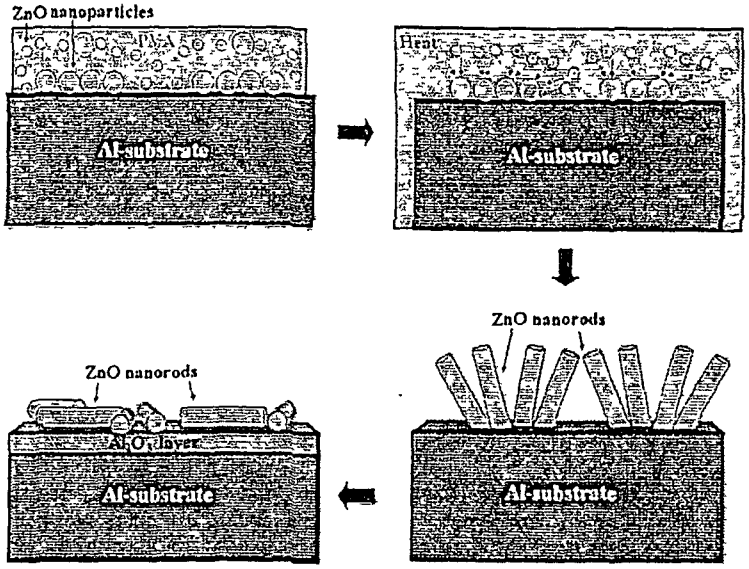

FIG 5 (Color online) The growth mechanism of the nanoparticles leading to nanorods and urchins.

way, the nanoparticles lying close to the surface of the Al substrate may act as seed particles. At the interface separating the substrate and the PVA film, due to substantial difference in thermal conductivities a temperature gradient can be realized. This temperature gradient will enforce the seed particle clustering as a result of creation of thermal hot spots [indicated by red arrow in Fig. 1(c)]. These hot spots are believed to be the base of the nanorods and the urchins (Fig. 5). The formation of the urchins can be understood with the reference of the lattice parameter also. The lattice parameter for ZnO system along the *c*-axis (the growth direction) is 5.206 Å and for Al 4.049 Å.[24] A substantial lattice mismatch would prevent in forming vertically aligned nanorods, and that is why randomly oriented rods resulting urchin like structures are obtained in most cases. On heating at 650 °C, the base of the nanorods that make up urchins is lost as a result of which nanorods fly apart and fall randomly on to the substrate surface (Fig. 5).

C. Optoelectronic transitions in Eu-doped ZnO nanostructures

Figure 6 represents the UV-visible optical absorption spectra of the Eu-doped ZnO nanostructures (S_1, S_2, and S_3). The specimen S_1 (containing spherical nanoparticles) shows an absorption peak at ~356 nm (3.48 eV), which is assigned to the ground state excitonic state. The ground state excitonic peak exhibits a redshift in ~90 meV in case of the systems heated at 300 °C (specimen S_2) and 650 °C (specimen S_3) compared to S_1. The observed redshift, therefore, supports particle growth (possibly, one directional to form nanorods). No significant shift in the absorption peak of S_3 compared to S_2 was found [Figs. 6(b) and 6(c)] indicating the fact that annealing at 650 °C neither facilitates further growth of particles nor leads to agglomeration of the nanorods.

The photoluminescence (PL) spectra of the Eu-doped ZnO nanostructures (λ_{ex}=325 nm) are shown in Fig. 7. Each of the PL spectra is composed of various defect related emissions [Figs. 7(a)–7(c)]. Note that all the spectra are characterized by peaks located at approximately same wavelength positions. The 382 nm peak [Fig. 7(b)] is attributed to the near band edge emission of ZnO.[25] The impressions at ~400 nm and 467 nm corresponded to the emissions related to the zinc vacancy states (V_{Zn}, V_{Zn}^{-}); respectively.[25,26] Further, the peaks at ~429 and 452 nm arise due to the respec-

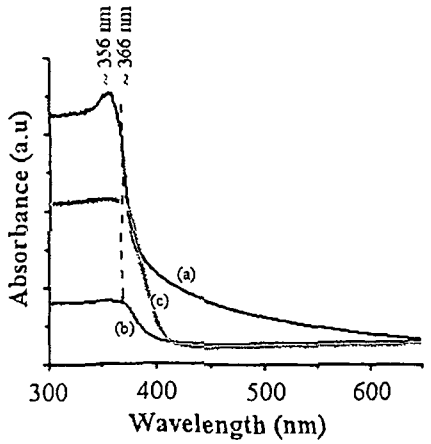

FIG 6 (Color online) UV-visible spectra of the Eu-ZnO nanostructures annealed at (a) 80 °C, (b) 300 °C, and (c) 650 °C

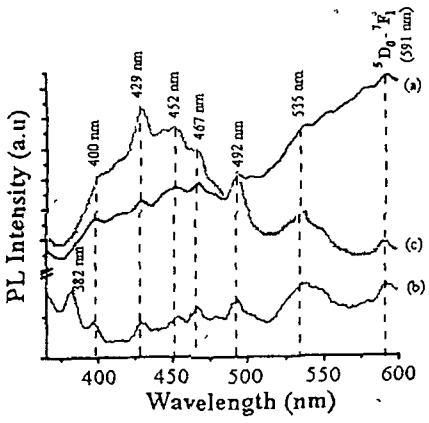

FIG 7 (Color online) PL spectra (λ_{ex}=325 nm) of the Eu-ZnO nanostructures annealed at (a) 80 °C, (b) 300 °C, and (c) 650 °C

tive emissions via zinc interstitial related defects (Zn_i, Zn_i^+).[26,27] On the other hand, the 492 and 535 nm peaks are identified as emissions related to the oxygen vacancy (V_o^+) and interstitial (O_i) defects.[26,28] Note that the oxygen related emissions are dominant in case of S_1 than S_2 and S_3, whereas the zinc related emissions are dominant in S_3 [Figs. 7(a)–7(c)]. Apart from these peaks, the emission at ~592 nm is ascribed to the transition related to Eu^{3+} cations ($^5D_0 \rightarrow {}^7F_1$).[8]

It can be observed that the overall PL intensity of the urchin system (S_2) gets quenched. As the growth of the nanoparticles takes place in order to form the nanorods, the defect state concentration responsible for the characteristic emission also decreases. As a result, the band edge emission at ~382 nm is recovered for the urchin systems under 325 nm excitation [Fig. 7(b)]. In contrast, for sample S_3 upon annealing at 650 °C, the overall PL intensity of the system is regained [Fig. 7(c)]. It is quite clear that the isolated nanorods exhibit better emission patterns than a bunch of randomly oriented nanorods (urchins). Though the availability of independent defect states (nonradiative centers) are comparable in both S_2 (urchins) and S_3 (isolated nanorods) systems, the later exhibited improved defect related emission response. The dimension (length and diameter) of the nanorods being same (for S_2 and S_3 systems), it is the structural organization that matters the most for a typical radiative emission. It is expected that the bunching of the closely spaced nanorods toward the core of the urchins would suppress the defect related emissions appreciably. The nanorods gradually separate from each other as we move from the core to the tips. It is possible that most of the emission occurred as a result of $e-h$ recombination along the c-axis of the individual nanorods. Earlier, radiative recombination emission along the c-axis was assigned to the enhanced band edge emission whereas the defect related emission was claimed to have originated from the curved surface of the nanorods.[29] Accordingly, for the urchins, the defect related emission gets quenched but the band edge emission is favored at large [Fig. 7(b)]. In contrast, the isolated nanorods (S_3) which were fallen onto the Al-base display better defect related emission because of the fact that the radiative process along c-axis is hindered but along a-axis is geometrically favored. Consequently, even though the band edge emission (~382 nm) is suppressed, the overall defect related emission response is improved [Fig. 7(c)].

In order to avoid band-to-band transition (~382 nm), we also took PL spectra corresponding to $\lambda_{ex}=405$ nm (Fig. 8). The oxygen interstitial defect related emission (centered at ~535 nm) is found to be prominent for the specimen S_1 and is characterized by a broad spectrum [Fig. 8(a)]. The oxygen vacancy related peak ~492 nm is still intact. In addition, the peak observed at ~613 nm, is being ascribed to the Eu^{3+} related emission due to $^5D_0 \rightarrow {}^7F_2$ transitions.[15] The most important aspect of the Eu^{3+} related emission is that it gets quenched with the decrease in defect related emission. So, it can be ascertained that the emission due to $^5D_0 \rightarrow {}^7F_1$ and $^5D_0 \rightarrow {}^7F_2$ transitions take place due to the energy transfer from the host ZnO via the defect states. On exciting the systems with energy lower than the band gap of the material,

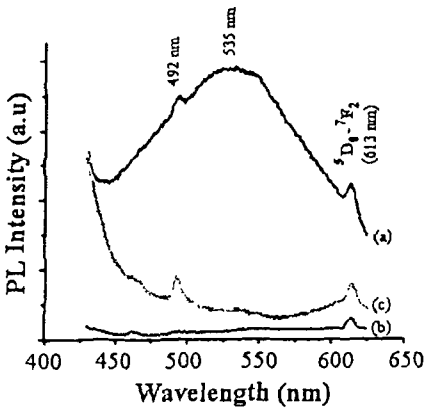

FIG. 8. (Color online) PL spectra ($\lambda_{ex}=405$ nm) of the Eu:ZnO nanostructures annealed at (a) 80 °C, (b) 300 °C, and (c) 650 °C.

the intensity of the Eu^{3+} related emissions increases (Fig. 8) as the defect related emission (in our case, oxygen vacancies and oxygen interstitials) gets enhanced. The emission spectra corresponding to $\lambda_{ex}=325$ and 405 nm, for S_3 are represented in Fig. 9. The peak at ~613 nm is found to be asymmetrically stretched toward the lower-end wavelength side which might have arisen due to the presence of an inherent peak at ~591 nm [pointed by a blue arrow in Fig. 9(b)]. The oxygen vacancies and interstitials capture the photoexcited electrons and transfer some of them to the $^5D_3$ level of Eu^{3+} cations which is then followed by a nonradiative transition from the $^5D_3$ level to the $^5D_0$ level and later resulting in the $^5D_0 \rightarrow {}^7F_1$ and $^5D_0 \rightarrow {}^7F_2$ transitions (Fig. 10).

IV. CONCLUSION

To conclude, Eu^{3+}-doped ZnO nanostructured systems in the form of particles, rods, and urchins are achieved under different annealing environments. It was found that one directional (along [0001]) growth of the particles has led to the formation of nanorods, followed by the evolution of urchin like structures. The nature of growth process was discussed in conjunction with a brief theory. Though the defect related emission of ZnO was dominant, the band edge emission has been recovered in the urchin system. The Eu^{3+} related tran-

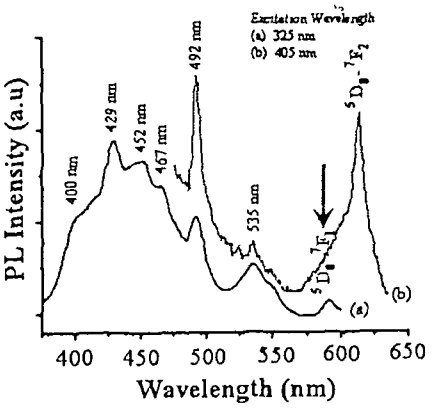

FIG. 9 (Color online) Comparison of the PL spectra at excitation at 325 and 405 nm of the Eu:ZnO nanorods (sample S_3).

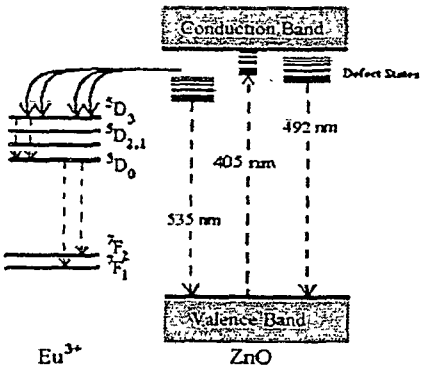

FIG. 10. Scheme of energy transfer mechanism in Eu:ZnO nanostructures.

sitions are also noticed, which generally occurred via the energy transfer mechanism through the defect states (especially, oxygen vacancies and oxygen interstitials). The intensity of the Eu^{3+} related emission was found to vary with the structure type and annealing environment.

ACKNOWLEDGMENTS

The authors thank IUAC, New Delhi for sponsoring the project under Project No. UFUP-44314/2008. The useful discussion with Mr. U. Das is also gratefully acknowledged.

[1]X. Peng, L. Manna, W. Yang, J. Wickham, E. Scher, A. Kadavanich, and A. P. Alivisatos, Nature (London) 404, 59 (2000).
[2]J. Hu, L.-S. Li, W. Yang, L. Manna, L.-W. Wang, and A. P. Alivisatos, Science 292, 2060 (2001).
[3]C. B. Murray, D. J. Norris, and M. G. Bawendi, J. Am. Chem. Soc. 115, 8706 (1993).
[4]R. N. Bhargava, D. Gallagher, X. Hong, and A. Nurmikko, Phys. Rev. Lett. 72, 416 (1994).
[5]M. Tanaka, J. Lumin. 100, 163 (2002).
[6]R. N. Bhargava, J. Lumin. 70, 85 (1996).
[7]S. Okamoto, M. Kobayashi, Y. Kanemitsu, and T. Kushida, Phys. Status Solidi B 229, 481 (2002).
[8]S. S. Ashtaputre, A. Nojima, S. K. Marathe, D. Matsumura, T. Ohta, R. Tiwari, G. K. Dey, and S. K. Kulkarni, J. Phys. D 41, 015301 (2008).
[9]M. Haupt, A. Ladenburger, R. Sauer, K. Thonke, R. Glass, W. Roos, J. P. Spatz, H. Rauscher, S. Riethmuller, and M. Moller, J Appl. Phys. 93, 6252 (2003).
[10]Y.-K. Tseng, C.-J. Huang, H.-M. Cheng, I.-N. Lin, K.-S. Liu, and I.-C. Cheng, Adv. Funct. Mater. 13, 811 (2003).
[11]X. Liu, X. Wu, H. Cao, and R. P. H. Chang, J. Appl. Phys. 95, 3141 (2004).
[12]T.-C. Lin, C.-Y. Wang, L.-H. Chan, D.-Q. Hsiao, and H. C. Shih, J. Vac. Sci. Technol. B 24, 1318 (2006).
[13]S. Gao, H. Zhang, R. Deng, X. Wang, D. Sun, and G. Zheng, Appl Phys. Lett. 89, 123125 (2006).
[14]W. Bai, K. Yu, Q. Zhanga, F. Xua, D. Penga, and Z. Zhua, Mater. Lett. 61, 3469 (2007).
[15]R. N. Bhargava, V. Chhabra, T. Som, A. Ekimov, and N. Taskar, Phys. Status Solidi B 229, 897 (2002).
[16]K. E. McBean, M. R. Phillips, and E. M. Goldys, Microsc. Microanal. 12, 327 (2006).
[17]D. Mohanta and A. Choudhury, Opt. Mater. 29, 342 (2006).
[18]S. Das, A. K. Mukhopadhyay, S. Datta, and D. Basu, J. Mater. Sci. Lett. 22, 1635 (2003).
[19]M. Y. Ge, H. P. Wu, L. Niu, J. F. Liu, S. Y. Chen, P. Y. Shen, Y. W. Zeng, Y. W. Wang, G. Q. Zhang, and J. Z. Jiang, J. Cryst. Growth 305, 162 (2007).
[20]G. Cao, *Nanostructures & Nanomaterials: Synthesis, Properties & Applications* (Imperial College Press, London, 2004).
[21]S. Bayan and D. Mohanta, J. Mater. Res. 25, 814 (2010)
[22]N. Fujimura, T. Nishihara, S. Goto, J. Xu, and T. Ito, J. Cryst. Growth 130, 269 (1993).
[23]H. Zhang, D. Yang, Y. Ji, X. Ma, J. Xu, and D. Que, J. Phys. Chem. B 108, 3955 (2004).
[24]V. A Lubarda, Mech. Mater. 35, 53 (2003).
[25]B. Lin, Z. Fu, and Y Jia, Appl. Phys. Lett. 79, 943 (2001).
[26]S. A M. Lima, F. A. Sigoli, Jr., M. Jafelicci, and M. R. Davolos, Int. J. Inorg. Mater. 3, 749 (2001).
[27]L.-L. Zhang, C.-X. Guo, J.-G. Chen, and J.-T. Hu, Chin. Phys. 14, 586 (2005).
[28]J. D. Ye, S. L. Gu, F. Qin, S. M. Zhu, S. M. Liu, X. Zhou, W. Liu, L. Q. Hu, R. Zhang, Y. Shi, and Y. D. Zheng, Appl. Phys. A: Mater. Sci. Process. 81, 759 (2005).
[29]N. E. Hsu, W. K. Hung, and Y. F. Chen, J. Appl. Phys. 96, 4671 (2004).

Phys. Status Solidi A 207, No. 8, 1859–1863 (2010) / DOI 10.1002/pssa.200925525

physica status solidi a
www.pss-a.com
applications and materials science

Development of Tb-doped ZnO nanorods: Effect of nitrogen ion irradiation on luminescence and structural evolution

S. Bayan, U. Das, and D. Mohanta*

Nanoscience Laboratory, Department of Physics, Tezpur University, P. O. Napaam, Assam-784028, India

Received 12 October 2009, revised 23 December 2009, accepted 1 January 2010
Published online 26 February 2010

Keywords: ion irradiation, nanorods, ZnO, luminescence, solid-state fabrication

*Corresponding author: e-mail best@tezu.ernet.in, Phone: 91 3712 267007 5558, Fax: 91 3712 267007

In this work, we present surfactant (cetyl-trimethylammonium bromide, CTAB) assisted solid-state fabrication and characterization of hydroxyl-free ZnO and Tb-doped ZnO nanorods. 80-MeV nitrogen ion irradiation (fluence upto 8×10^{12} ions/cm^2) was performed to explore irradiation induced modification in the structural and optical properties of the nanorods. In the asymmetrically broadened photoluminescence (PL) spectra of the irradiated samples, the band-edge emission (~370 nm) is found to be suppressed due to the dominance of the defect related emissions. Apart from ZnO defect related emissions (within 405–535 nm) due to zinc/oxygen vacancies, interstitial, *etc.*, we have adequately identified the Tb-related $^5D_3 \rightarrow F_J$ and $^5D_4 \rightarrow F_J$ transitions at ~490 and 548 nm, respectively. At the highest fluence (8×10^{12} ions/cm^2), the nanorod structural ordering is lost, which is characterized by a luminescence quenching. The nitrogen irradiation at the chosen energy/fluence and selective Tb related transitions are promising for precise control over tunability in the specific luminescence.

1 Introduction Owing to increasing demands of display and optoelectronic devices, intensive research efforts are being pursued worldwide on various aspects of semiconductor nanostructured systems [1–3]. High-quality semiconductor nanocrystals can be processed by a wide variety of physical and chemical routes. Doping with suitable optically active impurities has its own importance when a specific emission is desired. In recent years, the fabrication of binary semiconductor nanocrystals doped with either transition-metal ions [4, 5], or rare-earth ions [6, 7] has gained a great deal of interest within the research community. Zinc oxide (ZnO), a wide direct band gap (3.37 eV at 300 K) semiconductor, exhibits intense light emission characteristics from the UV to the visible range in the electromagnetic spectrum [8–10]. With the advent of processing routes, it has been possible to produce not only good-quality spherical ZnO nanoparticles (quantum dots) of narrow size distribution but also nanostructures of a large variety *e.g.* rods, needles, strips, shells, urchin and flower-like structures [11, 12].

On the other hand, bombardment of the nanocrystal systems with energetic ions is an interesting concept to reveal in-depth information with regard to structural and morphological evolution during ion–nanomatter interaction. Attempts have been made so far that highlight ion-induced nanoparticle growth [13], nanostructure elongation [14, 15], ripple formation [16] and other such effects. While nanoparticle growth, splitting and directed growth are reported for ion energy in the MeV scale, ion implantation [17] and ripple formation are observed for ions carrying energy in the keV scale. The effect of controlled ion irradiation on asymmetrically shaped nanostructures could reveal many exciting properties that include surface polishing, polarized light emission, tunability in the trapped related emission, *etc.* In particular, irradiation-related study on rare-earth-doped elongated systems is rarely discussed in the existing literature. In this report, we present cost-effective, one-step solid-state fabrication of quality Tb-doped ZnO nanorods and explore their structural and luminescence responses after 80-MeV nitrogen ion irradiation.

2 Experimental details

2.1 Synthesis of ZnO and Tb/ZnO nanorods

ZnO nanorods were synthesized using a simple solid-state reaction approach. A mixture of zinc acetate dihydrate (ZAD), a cationic surfactant cetyl-trimethyl ammonium

bromide (CTAB, 99.9% pure, Loba-Chemie), and sodium hydroxide (NaOH) with a molar ratio of 1:0.4:3 were ground together in an agate mortar for ~1 h at room temperature. The unidirectional soft grinding was accompanied by the abrupt decomposition and excess heat release while the reaction was in progress. After ultrasonication, the product was washed repeatedly with deionized water and ethanol and finally dried in air (~70 °C) for 2 h.

For preparing Tb-doped ZnO nanorods, at first, terbium oxide (Tb_4O_7, 99.9% pure, Otto) was converted to terbium acetate. 0.5 gm of terbium oxide was reacted with a 0.4 mL of conc. nitric acid (maintaining pH ~ 7 by dropwise addition of sodium hydroxide solution) resulting in a white precipitate. In order to remove unwanted byproducts, the product was subjected to repeated washing with distilled water. Finally, the product was treated with 0.4 mL glacial acetic acid to give rise to terbium acetate [$Tb(CH_3COO)_3$]. The Tb-doped ZnO nanorods were developed by adding as-received terbium acetate in the reactant-mixture (weight ratio Tb/Zn = 0.02) followed by unidirectional grinding.

2.2 Irradiation of the nanorods Nontoxic and transparent polyvinyl alcohol (PVA) matrix medium was selected to disperse ZnO nanorods. ZnO nanorod-dispersed PVA films were casted on laboratory glass slides (1 × 1 cm^2) for the irradiation experiment. The samples were irradiated in the Material Science chamber under a high vacuum (pressure of ~10^{-6} mbar) condition and using 80 MeV-N^{4+} ion beams (with a beam current of ~1 pnA, particle-nanoampere), available at the 15UD tandem pelletron accelerator of Inter University Accelerator Centre, New Delhi. The ion-beam fluence was measured by integrating the ion charge on the sample ladder, which was insulated from the chamber. The ion fluence was varied in the range of 5×10^{11}–8×10^{12} ions/cm^2.

The structural and optical properties of undoped and Tb-doped ZnO nanorods were characterized by X-ray diffraction (XRD), scanning electron microscopy (SEM), transmission electron microscopy (TEM), absorption and emission spectroscopy tools. The results are discussed with a specific objective to understand irradiation-induced effects on Tb-doped ZnO nanorod systems.

3 Results and discussion Figure 1 illustrates the XRD patterns of the pure and Tb-doped ZnO nanorods. In consistency with the other reports [7, 8], the diffraction peaks corresponded to the hexagonal wurtzite structure of ZnO with preferred orientation along the (101) plane (Fig. 1A). The XRD pattern of the Tb-doped system is similar to the undoped one and no extra peak was detected that might correspond to other byproducts or reactant species (*e.g.* TbO_2, Tb_2O_3, Tb_4O_7, *etc.*). Since terbium crystallizes into hexagonal closed-packed structure, it can easily be accommodated into the hexagonal ZnO host lattice ($a = 3.257$ Å, $c = 5.233$ Å). As shown in the magnified version of Fig. 1A (*i.e.* Fig. 1B), the characteristic XRD patterns reveal a uniform shift in the diffraction peaks

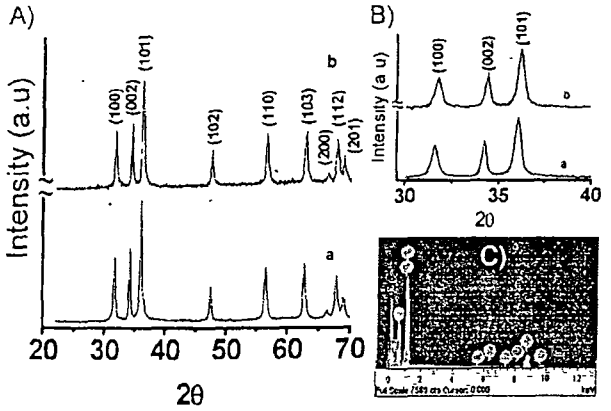

Figure 1 (online colour at: www.pss-a.com) (A) is the XRD pattern of (a) undoped ZnO nanorods, and (b) Tb-doped ZnO nanorods. (B) represents the magnified view of (A) that is shown in the selected diffraction angle range. (C) corresponds to the EDS spectra of Tb-doped ZnO nanorods.

towards larger angle in the case of Tb-doped ZnO nanorods ($a = 3.250$ Å, $c = 5.197$ Å) with respect to its ZnO counterpart. This may be attributed to the lattice mismatch aroused due to the incorporation of the larger-sized Tb^{3+} cations (1.18 Å) into the Zn^{2+} site (0.74 Å) of the host lattice. A similar kind of shift of the diffraction peaks towards larger diffraction angle on doping with rare-earth elements was reported by Zhang et al. [18]. It is necessary to make an in-depth analysis on the structural modification due to Tb doping. Applying the Williamson–Hall model [19], given by: $\beta \cos\theta = 0.9\lambda/D + 4\varepsilon \sin\theta$, one can obtain the average crystallite size (D) and microstrain (ε) for a system of interest. Here, β is the full width at half maxima (FWHM) at Bragg's angle (2θ), with λ being the X-ray wavelength ($CuK_\alpha = 1.54$ Å). Since the expression represents the equation of a straight line, the lattice strain can be calculated from its slope, whereas the intercept on the y-axis gives the crystallite size. Accordingly, the values of lattice parameter, microstrain and average crystallite size for undoped and Tb-doped ZnO nanorods can be estimated (using Figs. 2a and b) and are presented in Table 1. The microstrain experienced by the Tb-doped ZnO system is about eight times more than its undoped counterpart. The substantial increment in strain

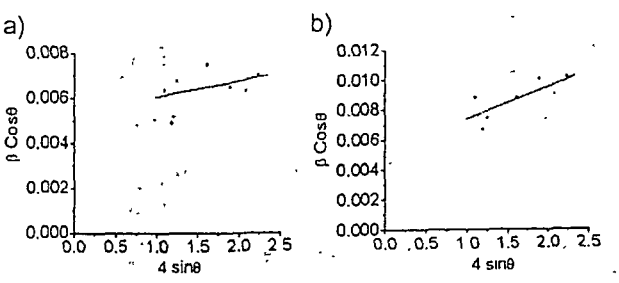

Figure 2 (*online colour at: www.pss-a.com*) Williamson–Hall plot of (a) undoped and (b) Tb-doped ZnO nanorods.

Table 1 Lattice parameter, microstrain and crystallite size of undoped and Tb-doped ZnO nanorods.

sample	microstrain	crystallite size (nm)	lattice parameter (Å)
ZnO	6.87×10^{-4}	28.84 ± 0.11	$a = 3.257$, $c = 5.233$
Tb/ZnO	2.11×10^{-3}	29.16 ± 0.03	$a = 3.250$, $c = 5.197$

value is assigned to the inevitable chemical incompatibility arising due to Tb incorporation into the ZnO host. The presence of Tb in doped ZnO nanorod system was also verified from the energy-dispersive spectra (EDS). Zinc and terbium atoms corresponding to the lowest ground-state energy were found to be located at the same position (Fig. 1C).

The visible evidence of nanorods was obtained from SEM (JEOL-JSM6390LV) and TEM (JEOL JSM-100 CX) studies which are presented in Figs. 3a and b. The average length and diameter of the nanorods are found to be ~600 and ~75 nm, respectively. The diameter of the nanorods at the extreme ends is found to be considerably smaller than the central parts. Since the decomposition of hydroxides into oxides is accompanied by a strong heat of reaction, the nanoparticle growth is expected to be slow during the initiation and termination of the final product (nanorods). The nanorods are found to be surface polished and resemble with the structure of solid-cylindrical ballpoint pens.

Figure 4 depicts the UV-visible absorption spectra of both the irradiated and unirradiated samples of Tb-doped ZnO nanorods. The un-irradiated nanorods (Figs. 4a and b) show long tailing and two prominent peaks at ~365 nm (~3.4 eV) and ~270 nm (~4.59 eV). The 365-nm peak is attributed to the excitonic ground-state ($n = 0$), whereas the 270 nm corresponds to the first ($n = 1$) excited excitonic state. The ground-state excitonic energy (~3.4 eV) is enhanced compared to the free exciton energy in the bulk (~3.30 eV) owing to 1D confinement of carriers [20]. The ground-state excitonic energy (3.4 eV), in our case, is comparatively smaller than the reported value (3.53 eV) where the nanorods are considered in the strong quantum confined regime. However, the first excited-state (4.59 eV) is consistent with the reported one [20]. The presence of long tailing due to significant inhomogeneity in the sample is found to be suppressed for ion-irradiated samples (Figs. 4c and d), though the ground-state excitonic absorption position is found to be undisplaced. This clearly indicates that controlled nitrogen irradiation could bleach out the undesired species at best along with improved surface passivation and without affecting the ground-state excitonic feature. Conversely, the excited-state absorption peak of irradiated nanorods was shifted to 285 nm (Figs. 4c–e). So, there is an appreciable redshift of ~235 meV in the first excitonic excited-state absorption of irradiated specimens, compared to the pristine one. It is now clear that a metastable-state is created between the ground-state and the first excited-state as a result of nitrogen ion irradiation. This newly generated state could be due to the improved symmetric distribution of the nanorods owing to recovery from matrix encapsulation which is otherwise suppressed in a given matrix. The excited-state excitonic absorption feature is found to be more prominent with increased ion fluence. In contrast, the ground-state absorption that was sharp in the case of the unirradiated nanorod specimen becomes broad owing to relaxed ground-state absorption. At the highest fluence (8×10^{12} ions/cm^2) the ground-state absorption becomes featureless followed by a long tailing. We have thus shown that with the proper selection of fluences, energetic nitrogen beam can improve not only the quality but also help in preserving ground-state and excited-state carrier population of elongated nanosystems (nanorods) under investigation.

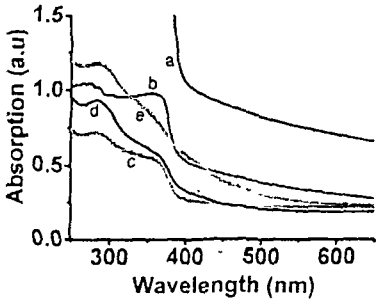

Figure 4 (online colour at: www.pss-a.com) UV-visible spectra of (a) unirradiated undoped ZnO; (b) unirradiated Tb-doped ZnO nanorods, and Tb-doped ZnO nanorods irradiated with a fluence of (c) 5×10^{11}, (d) 2×10^{12} and (e) 8×10^{12} ions/cm^2; respectively.

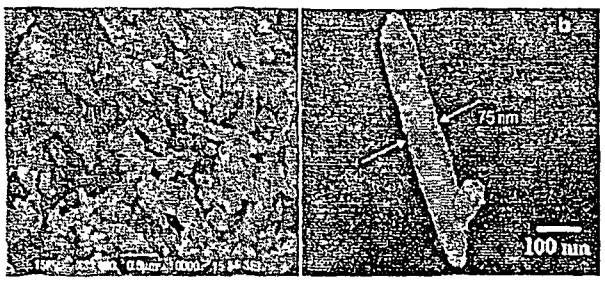

Figure 3 (a) SEM image of Tb-doped ZnO nanorods, and (b) TEM image of a fully grown isolated nanorod of diameter ~75 nm.

The PL spectra of the nanorods ($\lambda_{ex} = 325$ nm) before and after irradiation are shown in Fig. 5A. In the asymmetrically broadened PL spectra, the defect-related emissions dominate the band-edge emission of ZnO and hence the band-edge emission (~370 nm, dashed line) is only poorly resolved. The central maxima at ~405 nm are ascribed as the emission from zinc vacancies present in the ZnO lattice [21]. The asymmetric nature of the luminescence patterns is ascribed to the presence of other inherent emission peaks (due to distributed defect states on the surface and in the interior of a given nanostructured system) at higher wavelengths owing to the asymmetric geometry of the nanosystems. In particular, the impression at ~430 nm is the emission due to the presence of zinc interstitials [21]. The zinc-interstitial-related emission becomes more prominent

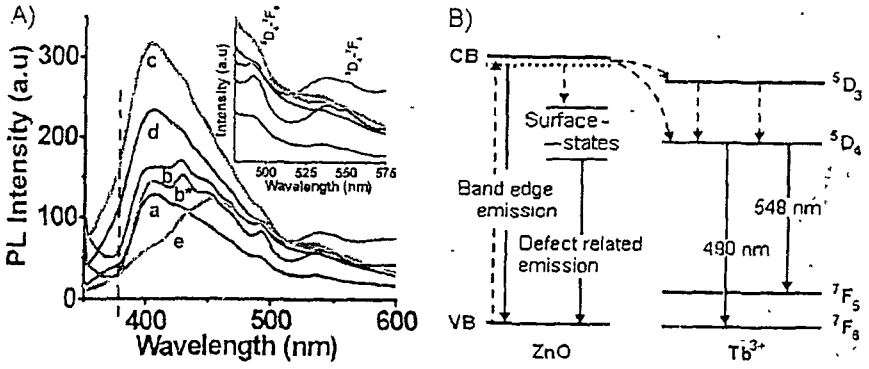

Figure 5 (online colour at: www.pss-a.com) A Room-temperature PL spectra of (a) unirradiated undoped ZnO, (b) unirradiated Tb-doped ZnO nanorods, and Tb-doped ZnO nanorods irradiated with a fluence of (c) 5×10^{11}, (d) 2×10^{12} and (e) 8×10^{12} ions/cm^2, respectively. The label 'b*' corresponds to as synthesized Tb-doped ZnO, whereas 'b' represents nanorods after repeated washing and dispersing in PVA. B: Scheme of various transitions involved in Tb-doped ZnO nanosystem.

for Tb-doped ZnO nanorod system (Figs. 5Ab,b*). Further, for irradiated Tb/ZnO samples, this emission gets suppressed owing to the improvement in zinc-vacancy-related emission (~405 nm). A feebly resolved peak at ~490 nm of the undoped nanorods (Fig. 5Aa) is attributed to the blue emission of ZnO [21]. The same peak corresponding to the Tb-doped ZnO nanorods gets enhanced (Figs. 5Ab,b*) because of the superimposition of the Tb^{3+}-related $^5D_4$–$^7F_6$ transition that occurs almost in the same wavelength range [22]. Another weakly resolved band centered at ~535 nm was seen for undoped nanorods, which corresponds to the oxygen-vacancy-related green emission [23, 24]. This peak becomes distinct and broad in the spectrum of Tb-doped ZnO nanorods as a result of the overlapping emission pattern arising due to the transition ($^5D_4$–$^7F_5$) of Tb^{3+} at ~548 nm with the aforesaid green emission [25]. The probable transition events are also shown in schematic Fig. 5B.

The PL spectra of the irradiated nanorod samples exhibit significant alteration. The PL response of the nanorods, irradiated with a fluence of 2×10^{12} ions/cm^2 is more intense than the unirradiated nanorods, but irradiation with a fluence of 5×10^{11} ions/cm^2 exhibits the highest PL intensity (Figs. 5Ab–d). Note that the central peak-to-blue, and central peak-to-green emissions are found to be enhanced for irradiated Tb-doped ZnO nanorods, upto a fluence of 2×10^{12} ions/cm^2 (Table 2). It is expected that upon ion irradiation the nanorods overcome the PVA matrix encapsulation allowing recovery of free excitons and resulting in the enhancement of defect-related emission. The Tb^{3+}-related emission peaks are still in view after irradiation (Figs. 5Ac–e). This indicates that the Tb^{3+}-related peak appears due to the energy transfer from the deep level states to the $^5D_4$ energy level of Tb^{3+} cations (Fig. 5B). While returning from the conduction band, most of the photoexcited electrons relax in the defect states, and transfer their energy to the $^5D_4$ energy level of Tb^{3+} resulting in the $^5D_4$–$^7F_6$ and $^5D_4$–$^7F_5$ transitions. The visual evidence of recovery from matrix encapsulation can also be seen in the electron micrographs (Figs. 6a and b). In contrast, the same sample that was irradiated with a fluence of 8×10^{12} ions/cm^2, the PL intensity decreases drastically along with a redshift in the PL spectra (Fig. 5Ae). This indicates that at this fluence, the nanorods get completely dislodged from the supporting matrix, leading to agglomeration events (Figs. 5Ae and 6c,d) The agglomeration leads to the suppression of the zinc vacancy and zinc interstitial related emissions. The agglomerated system is characterized by a disordered phase where the quantum confinement effect would no longer be valid. However, the Tb-related emission peak remained intact even if the structural ordering was lost. The agglomerated nanosystem (corresponding to a fluence of 8×10^{12} ions/cm^2) is found to have a symmetric peak at ~455 nm.

Taking PL maxima into consideration, the variation in the symmetry factor *vs.* ion fluence can be plotted (Fig. 7). The improvement in the symmetry factor (δ/Δ, δ is the magnitude of the lower-end asymmetry and Δ is the FWHM) from 0.28 to 0.48 was observed while fluence was varied from 5×10^{11} to 8×10^{12} ions/cm^2. Thus, one can adequately improve the symmetry factor without retaining structural ordering for overexposed samples. It is believed

Table 2 Characteristic PL response *vs.* ion fluence variation for Tb/ZnO nanorods.

fluence (ions/cm^2)	energy absorbed (J/cm^2)	central peak position (nm)	relative PL intensity	
			central-to-blue	central-to-green
) (undoped)	0	405	2.3	4.2
) (Tb-doped)	0	405	1.7	1.9
5×10^{11}	6.4	405	2.5	4.0
2×10^{12}	25.6	405	2.8	4.9
8×10^{12}	102.4	405 (455[a])	0.7	1.0

[a] Though the central position is shifted to 455 nm, the original central peak at 405 nm (corresponding to zinc vacancy) remains intact

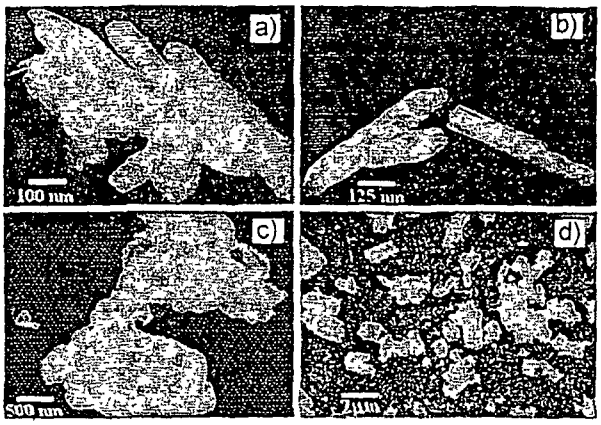

Figure 6 TEM image of the Tb/ZnO nanorods after irradiation with a fluence of (a) 5×10^{11}, (b) 2×10^{12} and (c) 8×10^{12} ions/cm^2; respectively. An overview of the agglomerated nanorods (case 'c') at lower magnification is shown in (d).

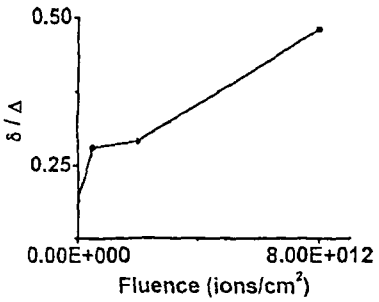

Figure 7 (online colour at: www.pss-a.com) Symmetry factor *vs.* ion fluence variation

that with controlled nitrogen ion irradiation, one can recover not only band-edge emission but also improve the defect-related tunable and selective emissions.

4 Conclusions By adopting a user-friendly surfactant-assisted growth process, one can produce high-quality Tb-doped ZnO nanorods. The excitonic ground-state and excited-state absorption features are evident in the optical absorption spectra. Nitrogen ion irradiation, at selected fluences, has a direct impact on defect-related emission owing to significant surface modification. Recovery of the nanorods from the polymer matrix due to ion irradiation enables the suppression of the non-radiative emission and improvement of the radiative emission via surface traps. The Tb-related $^5D_4$–$^7F_5$ and $^5D_4$–$^7F_6$ transitions are found to be overlapped with the respective blue and green bands of the luminescence patterns. The quantitative aspects correlating structural modification and luminescence patterns, applicable for rare-earth-doped irradiated ZnO nanorods might form the basis of nanoscale luminescent/display devices and are currently being investigated by our group.

Acknowledgements The authors are thankful to the accelerator group of IUAC, New Delhi for providing the good-quality nitrogen beam against UFUP project no. 44314/2008. The authors also extend sincere thanks to SAIF, Shillong for providing the TEM facility

References

[1] X. Peng, L. Manna, W. Yang, J. Wickham, E. Scher, A. Kadavanich, and A. P. Alivisatos, Nature 404, 59 (2000).
[2] J. Hu, L.-S. Li, W. Yang, L. Manna, L.-W. Wang, and A. P. Alivisatos, Science 292, 2060 (2001).
[3] C. B. Murray, D. J Norris, and M. G. Bawendi, J. Am. Chem. Soc. 115, 8706 (1993).
[4] R. N. Bhargava, D. Gallagher, X. Hong, and A. Nurmikko, Phys. Rev. Lett. 72, 416 (1994).
[5] M. Tanaka, J. Lumin. 100, 163 (2002).
[6] S. Okamoto, M. Kobayashi, Y Kanemitsu, and T. Kushida, Phys. Status Solidi B 229, 481 (2002).
[7] A. Ishizumi and Y. Kanemitsu, Appl. Phys. Lett. 86, 253106 (2005).
[8] M. Haupt, A. Ladenburger, R. Sauer, K. Thonke, R. Glass, W. Roos, J. P. Spatz, H. Rauscher, S Riethmuller, and M. Moller, J. Appl. Phys. 93, 6252 (2003).
[9] Y.-K. Tseng, C.-J. Huang, H.-M. Cheng, I.-N. Lin, K.-S. Liu, and I -C. Cheng, Adv. Funct. Mater. 13, 811 (2003).
[10] X. Liu, X. Wu, H. Cao, and R. P. H. Chang, J. Appl. Phys. 95, 3141 (2004).
[11] A. B. Djurišiæ, Y. H. Leung, K. H. Tam, L. Ding, W. K. Ge, H. Y. Chen, and S. Gwo, Appl. Phys. Lett. 88, 103107 (2006).
[12] S. Gao, H. Zhang, R Deng, X. Wang, D. Sun, and G. Zheng, Appl. Phys. Lett. 89, 123125 (2006)
[13] Y. K. Mishra, D. K. Avasthi, P. K. Kulriya, F. Singh, D. Kabiraj, A. Tripathi, J. C. Pivin, I. S. Bayer, and A. Biswas, Appl. Phys. Lett. 90, 073110 (2007).
[14] S. M. Kluth, J. D Fitzgerald, and M. C Ridgway, Appl. Phys Lett. 86, 131920 (2005)
[15] D Mohanta, G. A. Ahmed, A. Choudhury, F. Singh, D K. Avasthi, G. Boyer, and G. A. Stanciu, Eur. Phys. J. Appl. Phys. 35, 29 (2006).
[16] J. Lian, W. Zhou, Q. M. Wei, L. M. Wang, L. A. Boatner, and R. C Ewing, Appl. Phys. Lett. 88, 093112 (2006).
[17] P. G. Kik and A. Polman, J. Appl. Phys. 88, 1992 (2000).
[18] L.-L. Zhang, C.-X. Guo, J.-J. Zhao, and J.-T. Hu, Chin. Phys. Lett. 22, 11225 (2005).
[19] G. K. Williamson and W. H. Hall, Acta Metall. 1, 22 (1953).
[20] Y. Gu, Igor, L. Kuskovsky, M. Yin, S. O'Brien, and G F. Neumark, Appl. Phys. Lett. 85, 3833 (2004).
[21] B. Lin, Z. Fu, and Y. Jia, Appl. Phys. Lett. 79, 943 (2001)
[22] Z.-B. Fang, Y.-S. Tan, X.-Q. Liu, Y.-H. Yang, and Y.-Y. Wang, Chin. Phys. 13, 1330 (2004).
[23] F. A. Kroger and H. J. Vink, J. Chem. Phys. 22, 250 (1954).
[24] K. Vanheusden, W. L. Warren, C. H. Seager, D. R. Tallant, J. A. Voight, and B. E. Gnade, J. Appl. Phys. 79, 7983 (1996)
[25] K. E. McBean, M R. Phillips, and E. M. Goldys, Microsc Microanal. 12, 327 (2006).

Role of cohesive energy on the interparticle coalescence behavior of dispersed nanoparticles subjected to energetic ion irradiation

Sayan Bayan and Dambarudhar Mohanta[a)]
Nanoscience Laboratory, Department of Physics, Tezpur University, PO Napaam, Assam 784028, India

(Received 14 August 2009; accepted 21 December 2009)

The present work reports on the conditions of nanoparticle growth and splitting under energetic ion irradiation. Cohesive energy that determines the thermal stability of a given nanoparticle system was calculated by extending surface area difference (SAD) and liquid drop model (LDM). Based on the size-dependent cohesive energy calculations, the interparticle coalescence mechanism is discussed for a ZnS-based nanoparticle system with special reference to a variety of matrices. The interparticle separation is found to play key role in particle–particle coalescence leading to nanoparticle growth or partial evaporation that results in splitting.

I. INTRODUCTION

Matrix-encapsulated metal/semiconductor nanostructures are considered technologically important assets for displaying size-dependent optoelectronic properties in the nanoscale regime. In recent years, size-selective quality nanostructure formation and modification by energetic ion beams using ion implantation,[1] ion beam mixing,[2] etc. have gained interest for obtaining better control over growth and recrystallization processes. It was demonstrated in previous studies that the energetic ion irradiation could play a major role in tailoring size, shape, and distribution of the nanostructures.[3,4] This is because the energy deposited during irradiation leads to either particle growth or splitting of the nanostructures. Ion-induced particle melting and growth are generally attributed to the Ostwald ripening process.[5] In contrast, nanoparticle fragmentation into still smaller particles was considered to be the result of the ion hammering effect.[6]

The cohesive energy of a material system is the amount of energy required to separate out its constituent neutral atoms. It is an important physical quantity as it is directly related to the melting temperature of the crystalline material.[7] In earlier studies, the size-dependent cohesive energy of the nanoparticles was computed using different models such as surface area difference (SAD) model[8,9] and liquid drop model (LDM).[10,11] Though each of these models has its own merits and limitations, they adequately relate the cohesive energy, the melting temperature, and the onset temperature (temperature at which atoms escape from the nanoparticle surface). The models can also be extended to explain the particle splitting or coalescence under ion-irradiation events. It is expected that ion irradiation will increase the internal energy of the nanoparticle system as a result of which cohesive energy will be suppressed. The reduction in interatomic cohesion results in competition with regard to particle evaporation, growth, and splitting, which in fact depends on the interparticle separation of the nanoparticles within the matrix host. To this end, we propose here a model that highlights the mechanism of nanoparticle growth/splitting under energetic ion irradiation. Using an expansion of the LDM model, we show how cohesive energy of the nanoparticles is strongly influenced by the irradiation condition and matrix encapsulation leading to particle coalescence or splitting.

II. THEORETICAL TREATMENT

Based on the Linderman criterion of melting, Tateno[7] has shown that the melting point of a bulk material can be expressed in terms of its cohesive energy:

$$T_{mB} = \frac{sE_B\eta^2}{3k_BZ} \quad . \tag{1}$$

Here, s is the exponent of the repulsive part of the interaction potential (proportional to r^{-s}) between the constituent atoms separated by a distance r, E_B is the bulk cohesive energy, k_B is the Boltzmann constant, and Z is the covalency of the atoms. The characteristic function η is defined as the ratio of the atomic displacement at T_{mB} to the interatomic separation at equilibrium.

Nanda et al.[11] have correlated the melting point with the cohesive energy per coordination number for both the nanoparticles and the bulk given by

a)Address all correspondence to this author.
e-mail: best@tezu.ernet.in
DOI: 10.1557/JMR.2010.0119

$$\frac{E_{np}}{N} = C_1 T_m + C_2$$
$$\frac{E_B}{N} = C_1 T_{mB} + C_2 \quad , \tag{2}$$

where T_m and E_{np} are the melting point and the cohesive energy of the nanoparticles, respectively N is the coordination number per atom, and C_1, C_2 are respective constants for a given crystal structure

Let us consider a system of spherical nanoparticles of average diameter D that are embedded in a suitable host matrix Further, we assume that the nanoparticles are composed of multielements The atomic percentage of each element of diameter d_i ($i = 1, 2, 3,$) in each of the nanoparticle is x_i ($i = 1, 2, 3,$) such that $\Sigma x_i = 1$ Defining f as the packing factor, the total number of atoms that make up each of the nanoparticles can be represented by[9]

$$n = \frac{f D^3}{\sum x_i d_i^3} \tag{3}$$

According to the LDM,[11] the cohesive energy of a nanoparticle represents the difference of the bulk cohesive energy per atom (E_B) and the surface energy of the nanoparticle The cohesive energy per atom can be expressed as

$$E_{np} = E_B - \frac{\pi D^2 \gamma_{np}}{n} \quad , \tag{4}$$

where γ_{np} is the surface energy per unit area of the nanoparticle of diameter D containing n number of atoms

Now, the size-dependent cohesive energy per atom of the nanoparticles embedded in a dielectric matrix of surface energy per unit area γ_{mx}[11] can be reformulated as

$$E_{np} = E_B - \frac{\pi D^2}{n}(\gamma_{np} - \gamma_{mx}) \tag{5}$$

Compared with the nanostructured systems (interparticle separation close to the dimension of the particles), the embedded nanoparticles are unique in the sense that they do not experience grain-boundary effects that generally act as major source of weak link resistivities (Fig 1) Moreover, nanoparticles dispersed in desired matrices were shown to be useful candidates for optoelectronic,[12,13] photocatalytic,[14] and photovoltaic applications [15] In addition, an embedded system would provide a suitable scheme where ion–matter interaction at the nanoscale level can be studied, in great detail

It is known that a projectile ion (with $S_e > S_n$, where S_e and S_n represent electronic and nuclear energy losses, respectively), at first, excites the electronic subsystem of the target material. This results in the instantaneous rise of the electronic temperature ($\sim 10^5$ K) within a time

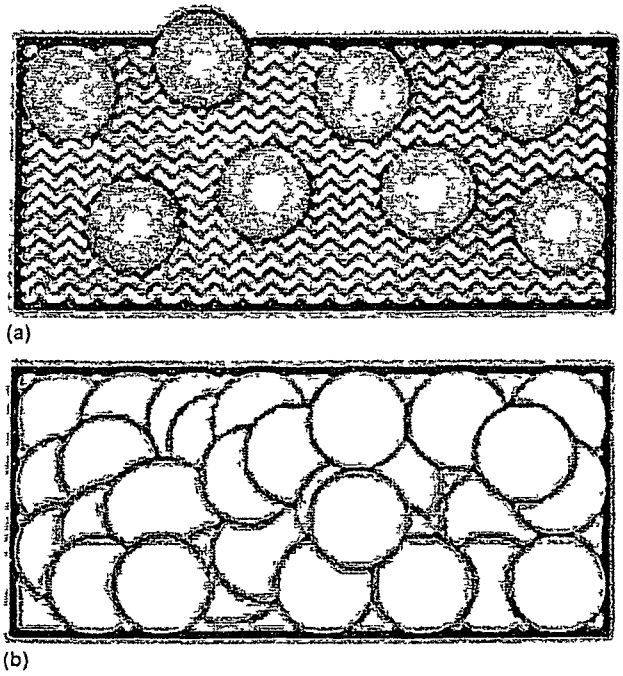

FIG 1 Schematic of nanosystems (a) Nanoparticles dispersed in a matrix and with large interparticle separation (b) Nanostructures with interparticle separation close to the particle size

scale of 10^{-15} s Later, within a timescale of 10^{-12} s, the electronic energy is translated to the lattice causing an increment in the kinetic energy of the atoms and hence, lattice temperature rise ($\sim 10^3$ K) [16] The deposited energy is believed to be uniform throughout the specimen If F is the number of ions incident per unit area (i e , fluence), then the number of ions received by each of the nanoparticle of diameter D is $F\pi D^2/4$ The energy deposited per atom of the nanoparticle is $(F\pi D^2 E)/4n$, where E is the energy carried by the projectile ion As the irradiation process would increase the internal energy of the nanoparticles, the cohesive energy of the particles will be suppressed by this amount of energy In reality, however, all of the incident energy E is not delivered to the sample containing nanoparticles, only a fraction of it is deposited because of the finite thickness of the target sample Therefore, the new cohesive energy of the nanoparticles embedded in a matrix of thickness z can be expressed as

$$E_c = E_{np} - E_i = E_{np} - \frac{F\pi D^2}{4n} S_e z$$
$$= E_{np} - \frac{F\pi D^2}{4n}\left(\frac{dE}{dz}\right)_e z \tag{6}$$

The second term on the right-hand side of Eq (6) is dependent on F and should increase with the increase in ion fluence As a result of the enormous energy deposition caused by irradiation, the internal energy of the

system would increase, making the nanoparticles thermodynamically unstable. At a critical fluence, the irradiation energy can be comparable to the cohesive energy of the nanoparticle such that the effective cohesive energy (E_c) would be vanishingly small. At higher fluences, the irradiation energy will dominate the cohesive energy of the nanoparticles, making $E_c < 0$. The negative effective cohesive energy signifies that the atoms would dislodge and fly out of the nanoparticle surface, leading to particle fragmentation. Nevertheless, if the particles are closely spaced (interparticle separation is comparable to or smaller than the particle dimension), then mass exchange would result in particle growth.

Ions traversing through the matrix create ion tracks of several nanometers diameter.[17] If a sufficient number of tracks are created between any two adjacent nanoparticles, then the medium separating the particles (i.e., interparticle spacing) would become amorphized with weakly bonded constituents. The diffusion-led mass transport among adjacent nanoparticles, followed by rapid solidification, results in particle growth.[5,18,19] This is analogous to the coalescence of the nearby islands during the growth of thin films.[20]

In a previous study, the nanoparticle size reduction as a result of progressive evaporation was supported by SDE model.[21] For large interparticle separation, it is unlikely that the particles in the molten state would coalesce and grow. Under continued irradiation conditions, the particles would reach the onset point, forcing atoms to escape from the nanoparticle surface. As a result of such partial evaporation events, the particle size can be drastically reduced. It is now apparent that the growth and the fragmentation of nanoparticles under irradiation are accompanied by the decrease of cohesive energy but highly dependent on the interparticle spacing. To visualize it more clearly, consider two nanoparticles, each of diameter D and separated by a distance R (Fig. 2). Upon melting, to minimize the surface energy the molten species condense and acquire a spherical shape. As irradiation has to proceed along a certain direction (e.g., z direction), uniformly dispersed nanoparticles will pass through the molten phase, giving rise to regular oblate ellipsoids [Figs. 2(a) and 2(b)]. The three sides of a regular oblate are a, b, and c such that $a > b = c$. Now, as the mass is conserved in the irradiation process, we can write

$$\frac{4}{3}\pi\left[\frac{D}{2}\right]^3 \rho = \frac{4}{3}\pi a b^2 \rho' \quad ,$$

or

$$a = \frac{1}{8}\left(\frac{D^3}{b^2}\right)\frac{\rho}{\rho'} \quad , \quad (7)$$

where ρ and ρ' ($<\rho$) are the density of the system before and during irradiation. In the case of complete melting,

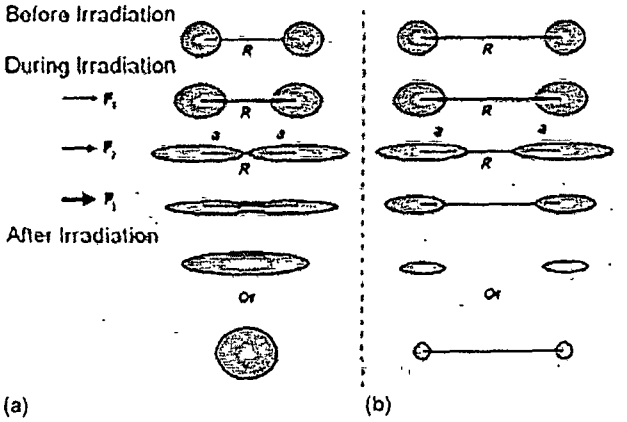

FIG. 2. Different stages of nanoparticle melting. (a) Growth ($R \leq 2a$), and (b) fragmentation ($R > 2a$) under energetic ion irradiation. (Fluence $F_3 > F_2 > F_1$).

the two oblates will be in the closest proximity if the sum of the two equatorial radii (along the z direction) of the two oblates is equal to R. Such a situation can facilitate exchange of atoms with great ease. In principle, upon coalescence, two or more particles can grow into an independent particle of larger size [Fig. 2(a)].

Therefore,

$$2a = \frac{1}{4}\left(\frac{D^3}{b^2}\right)\frac{\rho}{\rho'} \geq R \quad ,$$

is the growth condition for the nanoparticles subjected to ion irradiation. In other words, the equatorial diameter of the oblates should be at least equal or larger than the interparticle separation between the two nanoparticles of interest. On the other hand, when $2a < R$, it is unlikely that the molten particles would exchange mass for coalescence, rather evaporation-led particle splitting would occur under continual irradiation. environment [Fig. 2(b)].

III. RESULTS AND DISCUSSION

We apply our model to ZnS nanoparticles (hexagonal wurtzite structure) that are dispersed independently in four varieties of matrices, namely, polyvinyl alcohol (PVA), amorphous SiO_2, borosilicate glass, and alumina (α-Al_2O_3). The physical properties of the materials under study are presented in Table I. We consider the typical energy of the incident ion to be ~100 MeV, and the fluence varied between 1×10^9 and 1×10^{12} ions/cm^2. Since we are interested in the deposited energy, the electronic energy loss corresponding to given ion energy and for a particular dispersed system plays vital role in deciding particle growth and splitting. Note that the electronic energy loss for a pure ZnS film and a matrix are drastically different from each other. For instance, a 100 MeV chlorine ion experiences a S_e value of ~261 and 497 eV/Å for PVA and ZnS, respectively.[22] In other

words, with more and more ZnS particle dispersion into the PVA matrix, the S_e value will gradually shift from 261 to 497 eV/Å. In the present work, for simplicity, we consider S_e values corresponding to 50% volume dispersion of ZnS nanoparticles in a specified matrix of thickness $z = 1$ μm. The S_e values are computed using SRIM program and are listed in Table II.[22]

Figure 3 depicts a comparison between the irradiation energy received and the cohesive energy for different sized nanoparticles, corresponding to a given matrix. As shown, with the increase of fluence (1×10^9 to 1×10^{12} ions/cm^2), the deposited energy per atom increases from several meV/atom to tens of eV/atom. As a general trend, the irradiation energy (E_i) corresponding to a particular

TABLE I. Physical properties of the materials used in the present study.

Materials	Melting point (K)	Density (g/cm^3)	Thermal conductivity (W/m·K)	Dielectric constant	Surface energy per unit area (eV/m^2) × 10^{19}
ZnS	1458	4.09	27	8.9	0.356
PVA	503	1.19–1.31	0.2	1.9–2	0.023
a-SiO_2	1883	2.2	1.3	4.2	0.187
Borosilicate glass	1094	2.24	0.88–1.09	4.6–5.2	3.437
α-Al_2O_3	1373	3.97	40	4.5	1.437

TABLE II. Electronic energy loss (S_e) of 100 MeV chlorine ion beam in host materials and dispersed systems.

Material	ZnS	PVA	ZnS in PVA	a-SiO_2	ZnS in a-SiO_2	Borosilicate glass	ZnS in borosilicate glass	α-Al_2O_3	ZnS in α-Al_2O_3
S_e (eV/Å)	497	261	249	359	432	423	540	640	571

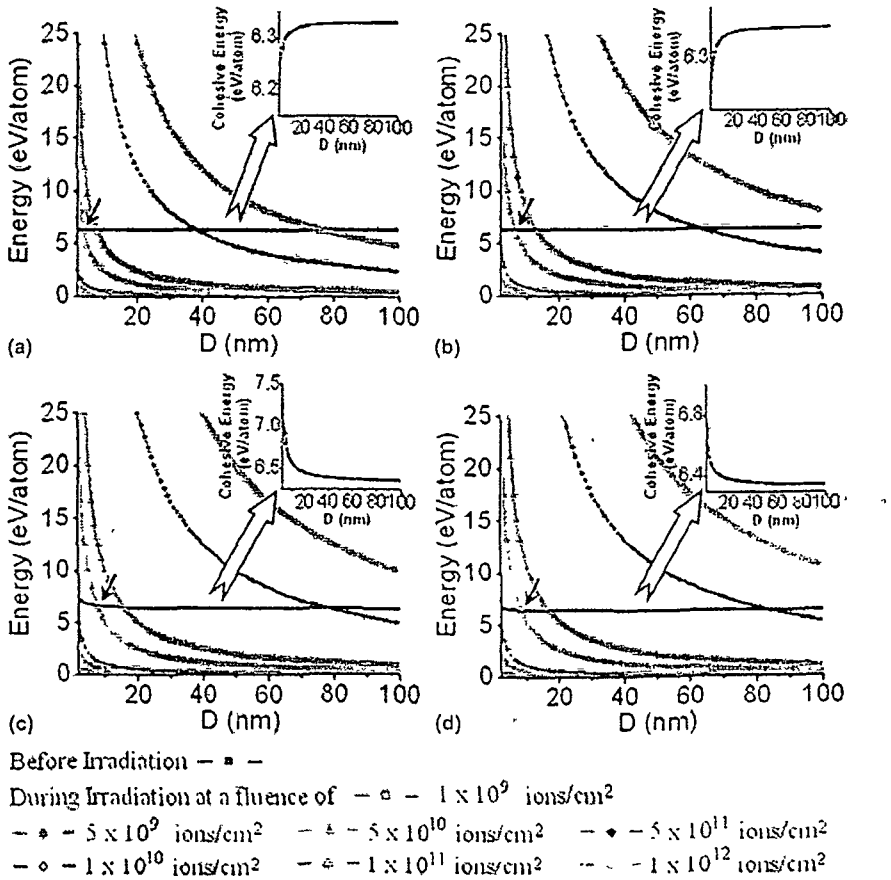

FIG. 3. Plots of irradiation energy versus size of ZnS nanoparticles embedded in (a) PVA, (b) a-SiO_2, (c) borosilicate glass matrix, and (d) α-Al_2O_3 with fluence variation from 1×10^9 to 1×10^{12} ions/cm^2. Insets being magnified version of the cohesive energy versus nanoparticle size (shown by flat open arrow).

fluence was found to decay exponentially with the increase of particle size. The horizontal line at ~6.4 eV/atom (highlighted in the insets of Fig. 3) actually describes the size-dependent cohesive energy characteristic of nanoparticles for a definite matrix encapsulation. In all the cases, it is seen that the irradiation energy (up to a fluence $\sim 1 \times 10^{10}$ ions/cm^2) is completely dominated by the respective cohesive energy. Conversely, at the fluence of 5×10^{10} ions/cm^2, the irradiation energy deposited on the particles dominates the corresponding cohesive energy. However, the critical size at which the irradiation energy dominates the cohesive energy would vary with the nature of the surrounding matrix. Corresponding to the fluence of 5×10^{10} ions/cm^2, the critical sizes for PVA, a-SiO_2, glass, and α-Al_2O_3 are 3.88, 6.31, 7.54, and 8.33 nm, respectively (see solid arrow in Fig. 3). Thus, for a ZnS-dispersed a-SiO_2 system, the particles having size $\leq$6.31 nm can participate in the initial melting process, while bigger particles, to a large extent, would not qualify for melting because of a relatively large cohesive energy. Moreover, for a particular host matrix, the critical size is found to increase with the increase in ion fluence (Fig. 4, Table III). On plotting, we notice a linear relationship between ion fluence and the critical size (Fig. 5, Table III).

Since the surface energy of borosilicate glass and α-Al_2O_3 (Table I) is greater than the surface energy in the ZnS system, the ZnS nanoparticles embedded in these two matrices show superheating effects as predicted by Jiang et al. in Pb/Al nanoscale system.[23,24] In these matrices, cohesive energy and hence the melting point of the nanoparticles increases with the decrease of particle size. As shown in the insets of Fig. 3, as a result of strong interatomic bonding in the nanoscale regime the effective cohesive energy has an increasing trend from the bulk value of ZnS (i.e., 6.33 eV/atom[25]). The reduced thermal vibration of the interface atoms separating the nanoparticle and the surrounding matrix triggers superheating characteristics.[23] For particles of ~2 nm size, the cohesive energies of ZnS/borosilicate and ZnS/α-Al_2O_3 systems are found to be as large as 7.4 and 6.8 eV/atom, respectively. With an increase in particle size, cohesive energy drops exponentially until it attains the bulk value.

The traces for the effective cohesive energy (E_c) versus nanoparticle size for different matrices are shown in Fig. 4. It is clear that for the nanoparticles of finite size, with the increase in ion fluence, the E_c value decreases substantially. In addition, at a low fluence (e.g., 1×10^9 ions/cm^2) the superheating nature is clearly visible for nanoparticles encapsulated in borosilicate and α-Al_2O_3

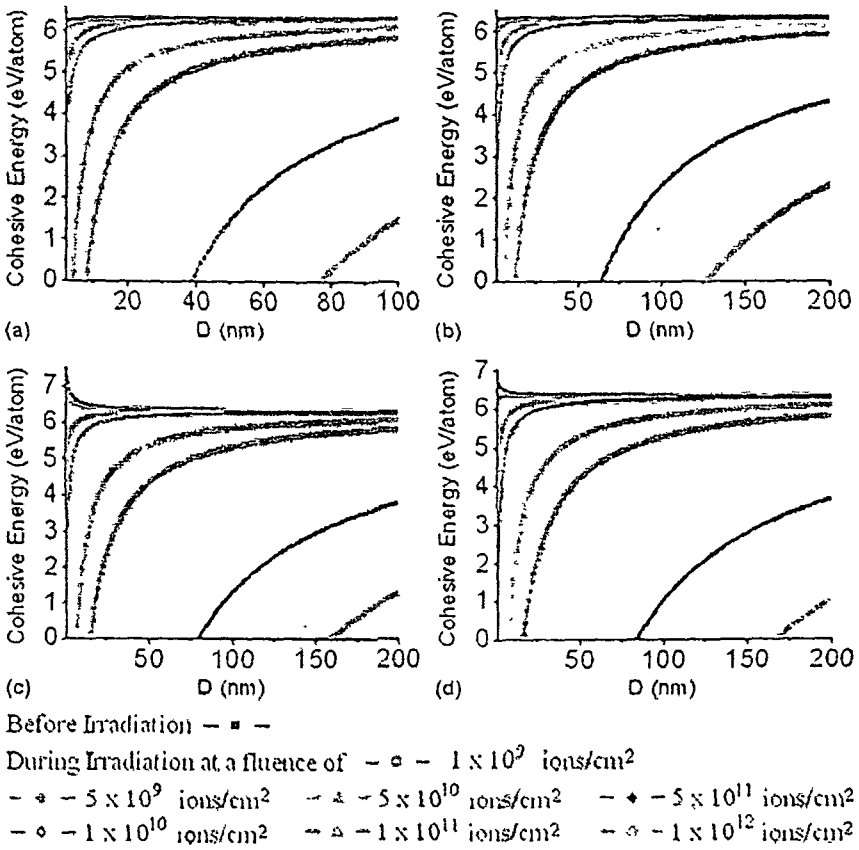

FIG. 4. Size-dependent effective cohesive energy response during irradiation of nanoparticles embedded in (a) PVA, (b) a-SiO_2, (c) borosilicate glass matrix, and (d) α-Al_2O_3.

TABLE III. Critical nanoparticle size (nm) versus corresponding fluence (ions/cm^2).

Fluence (ions/cm^2)	ZnS in PVA	ZnS in a-SiO_2	ZnS in borosilicate glass	ZnS in α-Al_2O_3
5×10^{10}	3.88	6.31	7 54	8.33
1×10^{11}	7.75	12.81	15.72	16.77
5×10^{11}	38.43	63.61	78.78	83.45
1×10^{12}	76.14	126.46	158.21	167.45

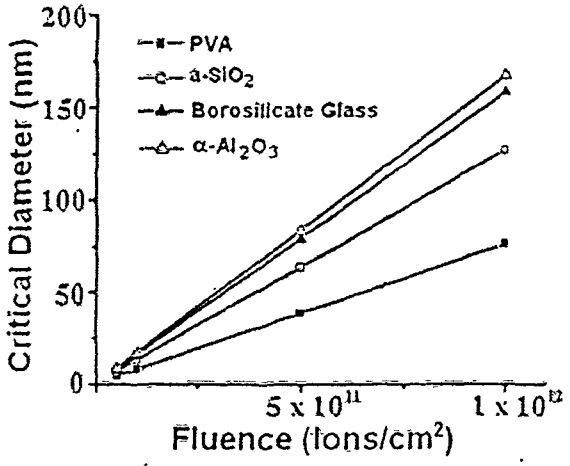

FIG. 5. Fluence dependent variation of critical nanoparticle size in different matrices.

matrices. Also, note that the cohesive energy dominates the irradiation energy up to a fluence of 1×10^{10} ions/cm^2 even for the ZnS/PVA system, which possesses the lowest cohesive energy (Fig. 3). This accounts for radiation-resistant behavior of the embedded nanoparticles. Beyond this value of fluence, the physical condition is decided by the irradiation energy irrespective of the nature of matrix. The E_c value slowly reduces to zero from the bulk value at the corresponding critical size of the nanoparticles (Fig. 4, Table III). A vanishing E_c represents no interactive force between the atoms that constitute the nanoparticle, and the negative values (not shown) would lead to conditions of flying out of atoms (partial evaporation) from the nanoparticle surface. If two identical nanoparticles (with sizes larger than interparticle spacing) are completely melted ($E_c \approx 0$) at a finite fluence, then it is likely that they will coalesce when interparticle-diffusion-led mass transport satisfies $2a \geq R$ [Fig. 2(a)]. As a result, two particles will grow into an independent nanoparticle of bigger size. However, when the interparticle separation is relatively large than the particle dimension ($2a < R$), interparticle mass transport will not be favorable. In this case, each particle would undergo independent evaporation, leading to size reduction [Fig. 2(b)].

To strengthen our arguments, we now discuss how the matrix could play vital role in the particle coalescence process. As evident from the plots shown in Figs. 4(a)–4(d), the fluence required to melt the ZnS nanoparticles is highly dependent on particle size. The growth process would occur through particle coalesce in the matrix medium, which is amorphized as a result of creation of ion tracks. For nanoparticles of definite size, melting followed by coalescence would certainly depend on the fluence, which is again dependent on the nature of the host matrix. The matrix with lower thermal conductivity would dissipate heat at a slower rate from the point of ion impact to the surroundings. Since the critical size corresponding to a given fluence is maximum for a matrix of larger thermal conductivity, controlled growth can be achieved in a matrix of lower thermal conductivity (Tables I and III). Essentially, the particle growth in PVA matrix will start at relatively higher fluence compared with a-SiO_2. In our previous experimental work on PVA-encapsulated CdS, ZnS, and ZnO nanoparticle systems, we noticed that the light ions (chlorine, oxygen) of energy 80 to 100 MeV can initiate nanoparticle growth at a fluence of 1×10^{11} ions/cm^2.[26,27] On the other hand, the growth of metallic nanoparticles (e.g., Ag, Au, etc.) in a-SiO_2 by MeV irradiation was found to occur at a significantly larger fluence ($\sim 10^{13}$ ions/cm^2). Note that because of a value of cohesive energy of ZnS (6.33 eV/atom) that is larger than that of the metallic systems ($E_c^{Ag} \approx 2.95$ eV/atom; $E_c^{Au} \approx 3.81$ eV/atom), the former has higher melting point ($T_m^{ZnS} \approx 1458$ K) as compared to the metallic systems ($T_m^{Au} \approx 1337$ K). However, excessively high thermal conductivity of the metallic systems (e.g., ~318 W/m·K, for Au) allows them to grow at a comparatively higher fluence.

It is now clear that the nature of matrix also governs the growth kinetics apart from the interparticle separation and size dispersion. We infer that because of the larger difference in thermal conductivity (with respect to ZnS) for PVA than a-SiO_2, the former requires relatively higher fluence for complete amorphization through the creation of ion tracks allowing melted particles to approach and coalesce. For example, for a track of diameter ~10 nm, the fluence required to cover the whole sample area (1 × 1 cm), is 1×10^{12} ions/cm^2.[19] Such conditions assist in the interparticle coalesce without hindrance, but fluence beyond this value would lead to unavoidable overlapping ion impacts on the specimen. The spontaneous particle–particle coalesce followed by rapid solidification results in large sized particles. Ideally, a coalescence-led recrystallization process could result in a spherical shape because of minimum surface energy. However, there can be instances where particles can facilitate in the formation of oblate and elongated nanostructures.[28] The departure from the spherical symmetry can be attributed to the fact that the coalescence form, because of the abrupt change in elasticity, is unable to regain its minimum energy configuration prior to instant solidification. Hence, it is now evident that the

nanoparticle growth is bound to occur in particles of size comparable with the interparticle separation The fluence at which growth will initiate is decided by the nanoparticle size, type, and the nature of the surrounding matrix Conversely, in the case of nanoparticles with large interparticle separation, fragmentation will occur as a result of partial evaporation

IV. CONCLUSIONS

To summarize, our model suggests that under energetic ion irradiation, particle growth or fragmentation can be initiated by the suppression of the effective cohesive energy Particle growth occurs through interparticle mass transport during irradiation On the other hand, particle splitting can be ensured in samples with large interparticle spacing The dispersing media (matrix) and the particle size would decide the fluence at which coalesce of particles can be achieved The embedded nanoparticle system with relevant size dispersion and exposure to radiation can be used in future photonic and optoelectronic components In addition, as a consequence of ion–matter interaction, any fluence $\leq 1 \times 10^{12}$ ions/cm^2 is recommended to observe and control nanoparticle coalescence in a designated host matrix

ACKNOWLEDGMENT

The work was carried under the project UFUP-44314/2008 The authors thank the sponsoring agency (IUAC, New Delhi) for the financial support

REFERENCES

1 P G Kik and A Polman Exciton-erbium interactions in Si nanocrystal-doped SiO_2 *J Appl Phys* **88**, 1992 (2000)
2 P Gangopadhyaya, R Kesavamoorthy, K G M Nair, and R Dhandapani Raman scattering studies on silver nanoclusters in a silica matrix formed by ion beam mixing *J Appl Phys* **88**, 4975 (2000)
3 S M Kluth, J D Fitz Gerald, and M C Ridgway Ion irradiation-induced porosity in GaSb *Appl Phys Lett* **86**, 131920 (2005)
4 S Talapatra, J-Y Cheng, N Chakrapani, S Trasobares, A Cao, R Vajtai M Bhuang, and P M Ajayan Ion irradiation induced structural modifications in diamond nanoparticles *Nanotechnology* **17**, 305 (2006)
5 Y K Mishra, D K Avasthi, P K Kulriya, F Singh D Kabiraj, A Tripathi, J C Pivin, S Bayer, and A Biswas Controlled growth of gold nanoparticles induced by ion irradiation An in situ x ray diffraction study *Appl Phys Lett* **90**, 073110 (2007)
6 A Berthelot, S Hemon, F Gourbilleau C Dufour E Dooryhee, and E Paumier Nanometric size effect on irradiation of tin oxide powder *Nucl Instrum Methods Phys Res Sect B* **146**, 443 (1998)
7 J Tateno An empirical relation on melting temperature of some ion c crystals *Solid State Commun* **10**, 61 (1972)
8 W H Qi and M P Wang Size effect on the cohesive energy of nanoparticle *J Mater Sci* **21**, 1743 (2002)
9 W H Qi Generalized surface-area-difference model for cohesive energy of nanoparticles with different compositions *J Mater Sci* **41**, 5679 (2006)
10 C Bre'chignac, H Busch Ph Cahuzac, and J Leygnier Dissociation pathways and binding energies of lithium clusters from evaporation experiments *J Chem Phys* **101**, 6992 (1994)
11 K K Nanda, S N Sahu, and S N Behera Liquid-drop model for the size-dependent melting of low dimensional systems *Phys Rev A* **66**, 013208 (2002)
12 P Nemac and P Maly Temperature study of trap-related photoluminescence decay in CdS_xSe_{1-x} nanocrystals in glass *J Appl Phys* **87**, 3342 (2000)
13 M Ando, Y Kanemitsu, T Kushida, K Matsuda, T Saiki and C W White Sharp photoluminescence of CdS nanocrystals in Al_2O_3 matrices formed by sequential ion implantation *Appl Phys Lett* **79**, 539 (2001)
14 H D Jang S-K Kim, and S -Jin Kim Effect of particle size and phase composition of titanium dioxide nanoparticles on the photocatalytic properties *J Nanopart Res* **3**, 141 (2001)
15 H-C Huang, G L Huang, H L Chen, and Y-D Lee Immobilization of TiO_2 nanoparticles on carbon nanocapsules for photovoltaic applications *Thin Solid Films* **511**, 203 (2006)
16 G K Mehta Materials modification with high energy heavy ions *Nucl Instrum Methods Phys Res Sect A* **382**, 33 (1996)
17 *Nuclear Tracks in Solids*, edited by R L Fleischer, P B Price and R M Walker (University of California Press, Berkeley, CA, 1975)
18 B Joseph, J Ghatak, H P Lenka, P K Kuiri, G Sahu, N C Mishra, and D P Mohapatra Effect of 100 MeV Au irradiation on embedded Au nanoclusters in silica glass *Nucl Instrum Methods Phys Res Sect B* **256**, 659 (2007)
19 S K Srivastava, D K Avasthi, and E Pippe Swift heavy ion induced formation of nanocolumns of C clusters in a Si based polymer *Nanotechnology* **17**, 2518 (2006)
20 J A Venables G D T Spiller and M Hanbucken Nucleation and growth of thin films *Rep Prog Phys* **47**, 399 (1984)
21 K K Nanda Bulk cohesive energy and surface tension from the size dependent evaporation study of nanoparticles *Appl Phys Lett* **87**, 021909 (2005)
22 J F Zeigler, M D Zeigler, and J P Biersack SRIM (2008)—The stopping and range of ions in matter www srim org (2008)
23 Q Jiang, Z Zhang, and J C Li Superheating of nanocrystals embedded in matrix *Chem Phys Lett* **322**, 549 (2000)
24 Z Zhang, Z C Li, and Q Jiang Modelling for size dependent and dimension dependent melting of nanocrystals *J Phys D* **33**, 2653 (2000)
25 J E Jaffe R Pandey, and M J Seel Ab initio high-pressure structural and electronic properties of ZnS *Phys Rev B* **47**, 6299 (1993)
26 D Mohanta, S S Nath, A Bordoloi A Choudhury S K Dolui and N C Mishra Optical absorption study of 100-MeV chlorine ion-irradiated hydroxyl-free ZnO semiconductor quantum dots *J Appl Phys* **92**, 7149 (2002)
27 D Mohanta, N C Mishra, and A Choudhury SHI induced grain growth and grain fragmentation effects in polymer-embedded CdS quantum dot systems *Mater Lett* **58**, 3194 (2004)
28 P Kluth, R Giulian D J Sprouster C S Schnohr A P Byrne D J Cookson and M C Ridgway Energy dependent saturation width of swift heavy ion shaped embedded Au nanoparticles *Appl Phys Lett* **94**, 113107 (2009)